Experimentelle Physik

# Intrinsic background reduction by cryogenic distillation for the XENON1T dark matter experiment

Inaugural-Dissertation
zur Erlangung des Doktorgrades der Naturwissenschaften
im Fachbereich Physik
der Mathematisch-Naturwissenschaftlichen Fakultät
der Westfälischen Wilhelms-Universität Münster

vorgelegt von
Michael Murra
aus Lingen
–2018–

| | |
|---|---|
| **Dekan:** | **Prof. Dr. Gerhard Wilde** |
| **Erster Gutachter:** | **Prof. Dr. Christian Weinheimer** |
| **Zweiter Gutachter:** | **Prof. Dr. Anton Andronic** |
| **Tag der mündlichen Prüfung:** | _____ |
| **Tag der Promotion:** | _____ |

# Abstract

The XENON Dark Matter Project is world leading in the field of direct dark matter detection. Its goal is to detect the scattering interactions of Weakly Interacting Massive Particles, one class of well motivated candidates, in liquid xenon dual phase time projection chambers.

The dominant background in the currently operating XENON1T experiment, the first ton-scale detector with a total xenon mass of 3200 kg, originates from the decay of the radioactive intrinsic contaminants $^{85}$Kr and $^{222}$Rn. Both have to be reduced to unprecedented low levels. This was achieved with the XENON1T cryogenic distillation column.

The upgrade to the final distillation column (Phase-2) for XENON1T is described in this work. Its characterization yielded that the krypton concentration on the order of a few ppb (parts per billion, 1 ppb = $10^{-9}$ mol/mol) in commercially available xenon is reduced by a factor of $\mathrm{F_{red}} = (6.4^{+1.9}_{-1.4}) \cdot 10^5$. Furthermore, it produced ultra-pure xenon with concentrations below 48 ppq (90 % C.L.) (parts per quadrillion, 1 ppq = $10^{-15}$ mol/mol). This is a factor of 4 lower than the required concentration in XENON1T of $^{\mathrm{nat}}\mathrm{Kr/Xe} = 200$ ppq and allows for the purification of the raw xenon with only one pass through the column. Worldwide, only the initial prototype of this column (Phase-1) produced lower concentrations ($< 26$ ppq (90 % C.L.)).

A novel online krypton removal technique was developed where the gaseous phase of the detector system is continuously purified with the distillation plant in a closed loop. This produced the lowest krypton concentration of $(360 \pm 60)$ ppq ever achieved in a liquid xenon based dark matter detector, sufficiently low for the first science run. Due to this new application, the first science run was started two month in advance, leading to the best sensitivity in the extremely competitive field of direct dark matter detection worldwide.

After the successful krypton removal, the main background source in XENON1T originates from radon emanation. In the scope of this thesis, the first successful radon removal operation using a cryogenic distillation column was demonstrated at XENON100, the predecessor of XENON1T, yielding a column reduction factor of $R_{\mathrm{C}} > 73$ (95 % C. L.). Furthermore, the novel online removal technique was applied for radon reduction in XENON1T as well, resulting in a decrease by $(20.8^{+8.8}_{-10.1})$%. Based on these results, a new high-flux radon distillation column can be designed for the upcoming XENONnT experiment.

# Zusammenfassung

Das XENON Dark Matter Project ist weltweit führend auf dem Gebiet der direkten Suche nach Dunkler Materie. Das Ziel ist die Wechselwirkung von Weakly Interacting Massive Particles, einer Klasse von vielversprechenden theoretischen Teilchen, nachzuweisen. Dies soll über die Streuung an flüssigem Xenon in Zeitprojektionskammern geschehen.

Der Hauptuntergrund in dem aktuell laufenden XENON1T Experiment, welches eine Masse von 3200 kg Xenon nutzt, entsteht durch den Zerfall von den radioaktiven Verunreinigungen $^{85}$Kr und $^{222}$Rn im Xenon selbst. Beide müssen vor bzw. während des Betriebes auf noch nie zuvor erreichte niedrige Niveaus reduziert werden. Das konnte mit der Hilfe einer kryogenen Destillationssäule für XENON1T erreicht werden.

Der Umbau auf die finale Destillationssäule (Phase-2) für das XENON1T Experiment wird in dieser Arbeit beschrieben. Bei der Charakterisierung der Säule wurde herausgefunden, dass die Kryptonkonzentration in der Größenordnung von einigen ppb (parts per billion, 1 ppb = $10^{-9}$ mol/mol) in kommerziell verfügbarem Xenon um einen Faktor von $\mathrm{F_{red}} = (6.4^{+1.9}_{-1.4}) \cdot 10^5$ durch die Säule reduziert werden kann. Weiterhin enthält das gereinigte Xenon einen Kryptonanteil von weniger als 48 ppq (90 % C.L.) (parts per quadrillion, 1 ppq = $10^{-15}$ mol/mol). Das ist 4 mal weniger als das benötigte Level in XENON1T von $^{\mathrm{nat}}$Kr/Xe = 200 ppq, wodurch eine einmalige Reinung des gekauften Xenon durch die Destillationsanlage genügt. Weltweit wurde eine geringere Sauberkeit nur durch den Prototypen dieser Säule (Phase-1) erreicht ($< 26$ ppq (90 % C.L.)).

Eine neue online Krypton Reinigungsmethode wurde entwickelt, bei der die Gasphase des XENON1T Detektors kontinuierlich von der Destillationssäule in einem geschlossenen Kreislauf gereinigt wird. Damit konnte die niedrigste jemals gemessene Krypton in Xenon Konzentration von $(360 \pm 60)$ ppq in einem Flüssigxenon basiertem Dunkle Materie Experiment erzeugt werden. Diese war zu diesem Zeitpunkt ausreichend gering, um die ersten wissenschaftlichen Daten aufzuzeichnen. Durch diese neue Methode konnte außerdem der Startzeitpunkt der Messungen um zwei Monate vorverlegt werden, was später dazu führte, dass XENON1T das weltweit sensitivste Experiment im hart umkämpften Feld der Dunklen Materie Suche werden konnte.

Nachdem Krypton erfolgreich entfernt werden konnte, bleibt als Hautquelle für den Untergrund in XENON1T das Radon. Im Rahmen dieser Arbeit wurde zum ersten Mal eine kryogene Destillationssäule eingesetzt, um Radon induzierten Untergrund zu reduzieren. Dies wurde zunächst am XENON100 Experiment, dem Vorgänger von XENON1T, durchgeführt. Hier konnte ein Reduktionsfaktor der Säule von $R_{\mathrm{C}} > 73$ (95 % C. L.) bestimmt werden. Später wurde die oben erwähnte online Reinigungsmethode bei XENON1T auch bei Radon eingesetzt, was zu einer Reduzierung des Untergrundes von $(20.8^{+8.8}_{-10.1})$% führte. Basierend auf diesen Tests kann eine neue Hochfluss Radon Destillationssäule für das zukünftige XENONnT Experiment designt werden.

# Contents

# 1 Introduction

An overwhelming number of independent observations in the past decades from a cosmological to an astronomical scale lead to the assumption that our universe is dominated by two unknown constituents - dark energy and dark matter. Dark matter is a new kind of non-luminous matter that is so far not detectable by any interaction except its gravitational one. The XENON Dark Matter Project is active in the field of direct dark matter detection in the form of Weakly Interacting Massive Particles (WIMPs). It aims to measure energy depositions in a xenon dual-phase time projection chamber (TPC) that originates from the scattering process of WIMPs with xenon nuclei. The currently operating XENON1T experiment utilizes a total of 3200 kg of liquid xenon. Its science runs did not yield any evidence for the existence of dark matter, but set the most stringent limits on spin-independent scatter cross sections worldwide.

For such large detector volumes the intrinsic background, introduced by radioactive contaminants such as $^{85}$Kr and $^{222}$Rn within the xenon, dominates the final background level and, thus, the sensitivity of the detector. These radioactive noble gases can be removed with a cryogenic distillation column by exploiting the difference in vapor pressure with respect to xenon.

The development of the XENON1T distillation column was divided into three phases: It started with a single-stage distillation setup (Phase-0), where the proof of principle to separate krypton from xenon on the unprecedented level of parts per quadrillion (ppq) was demonstrated for the first time. The next phase (Phase-1) was the construction of a multi-stage package column with a total height of 3 m allowing for the investigation of thermodynamic stability as well as separation performance. In order to safely reach the required separation efficiency for XENON1T, the final version (Phase-2) was extended to a total height of 5.5 m. After the successful characterization in Münster, the system was integrated in XENON1T and operated in a variety of new applications. The upgrade to the Phase-2 system and its application are the main topic of this work.

The important pieces of evidence and properties of dark matter, as well as the WIMP as a dark matter candidate are summarized in chapter 2. Moreover, the working principle, the advantages of a liquid noble gas detector, and the most important background sources, divided into external and intrinsic backgrounds, are reviewed for XENON100 as well as for XENON1T.

The basic concept of noble gas separation and the design of the distillation column based on the McCabe-Thiele method are presented in chapter 3 along

with the technical realization. Additionally, the integration as a XENON1T subsystem is shown.

In chapter 4, the characterization of the Phase-2 column is discussed with emphasis on the thermodynamic stability and reduction capability.

The distilllation plant was also utilized for the removal of helium from the xenon storage system ReStoX before the initial filling of the XENON1T cryostat. This application is explained in chapter 5.

During the helium removal campaign it was found that krypton is removed as well. Consequently, a new online krypton removal technique was developed in order to decrease the krypton level in XENON1T while the detector was filled and operational. The concept and technical realization as well as the modeling of the krypton evolution over time is discussed in chapter 6.

The main background source after decreasing the krypton level originates from radon emanation. Since radon is a noble gas as well, cryogenic distillation is feasible to further reduce this source of background. This was successfully demonstrated for the first time using XENON100 as a testbed. Furthermore, the final Phase-2 distillation system was modified in such a way that continuous online radon removal could be tested at XENON1T as well. The radon removal campaigns are described in chapter 7.

Finally, a summary and outlook are given in chapter 8 at the end of this thesis.

# The XENON Dark Matter Project 2

The XENON Dark Matter Project aims to detect interactions of the ever elusive dark matter within liquid xenon dual-phase time projection chambers (TPCs). An initial search was performed with the XENON10 experiment, where 14 kg out of 25 kg xenon were used as the active target. With an active target of 62 kg (161 kg total mass), the successor XENON100 set competitive limits on spin-dependent and spin-independent dark matter interactions with xenon nuclei.

The currently operating XENON1T experiment is the first liquid xenon detector on the ton-scale featuring the lowest achieved background. So far, no dark matter signatures were found, but the next-generation detector XENONnT with a total mass of around 8 t is under development.

At the beginning of this chapter, the most compelling evidence for the existence of dark matter is briefly summarized along with the most favoured candidate, the weakly interacting massive particle (WIMP). Furthermore, the approach for an earthbound direct detection is presented.

The working principle of a liquid xenon TPC are presented together with potential sources of background and their reduction. This is followed by a brief introduction of the most recent stages of the XENON project: XENON100 as well as XENON1T. For both detectors, the background requirements and achievements are discussed, leading to the requirement of a cryogenic distillation column for XENON1T that removes the intrinsic radioactive backgrounds $^{85}$Kr and $^{222}$Rn in order to reach the desired sensitivity.

At the end of the chapter, the required performance for such new distillation system is discussed.

## 2.1 Dark Matter

An overwhelming number of independent observations in the past decades from a cosmological to an astronomical scale lead to an image of our universe where it is dominated by two components whose exact nature is still widely unknown: dark energy and dark matter. While dark energy resembles an almost uniformly distributed energy density responsible for the accelerated expansion of the universe, dark matter is a new kind of non-luminous matter that is so far not perceivable by any interaction except its gravitational one.

This section will introduce evidence for dark matter from a large to a small scale, such as the cosmic microwave background, gravitational lensing, and

rotation curves of galaxies along with the most common candidate particle, the WIMP. Furthermore, the principle of its direct detection is discussed.

### 2.1.1 Evidence

One of the most compelling pieces of evidence for the existence of dark matter arises from the precise measurements of the temperature anisotropies at the level of μK in the cosmic microwave background (CMB) by WMAP [1] and Planck [2].

These fluctuations are directly linked to the matter distribution at the point of recombination in the early universe about 380 000 years after the big bang, and therefore give access to the energy density of the universe during this period of time. By expanding the fluctuations in terms of spherical harmonics, an angular power spectrum can be obtained. Here, the power of the anisotropies is given in terms of a multipole moment. Such a spectrum from the Planck mission is presented in figure 2.1.

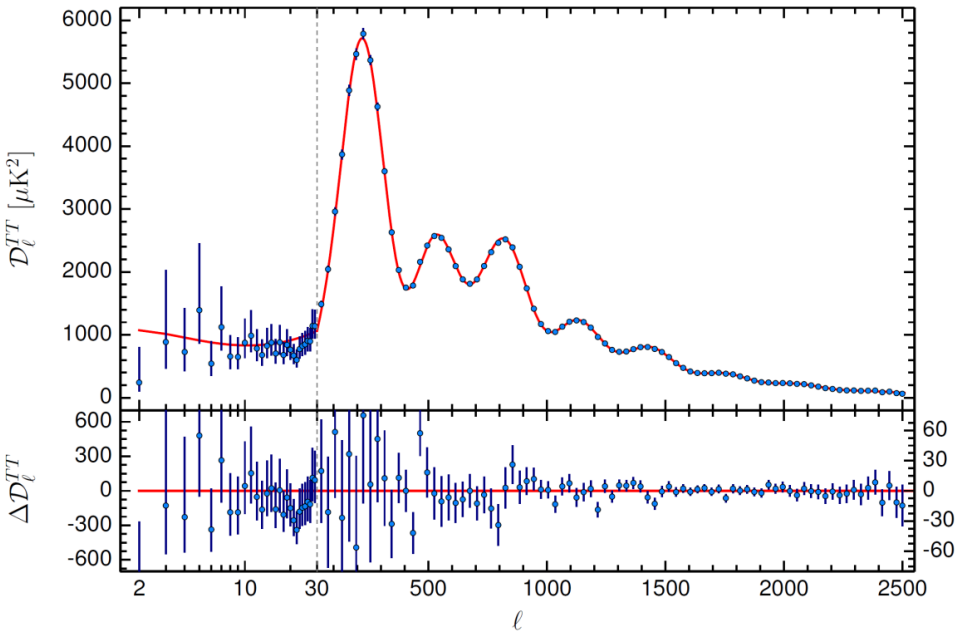


Figure 2.1: **The temperature power spectrum of the cosmic microwave background measured by Planck:** The variations in temperature fluctuations $D_\ell^{TT}$ in dependence of the multipole moment $\ell$ are shown. The data is described by the best-fit for the ΛCDM model. The bottom shows the residuals $\Delta D_\ell^{TT}$ with respect to the model, while the error bars show $\pm 1\,\sigma$ uncertainties. Figure from [3].

The spectrum is best described within the cosmological standard model, called Λ cold dark matter (ΛCDM) model, where Λ refers to the cosmological constant required to explain the current accelerated expansion of the universe [3]. Cold dark matter density perturbations in the gravitational potential formed oscillations of the baryon-photon plasma before recombination. This lead to a characteristic oscillation pattern in the CMB power spectrum called acoustic peaks. The fractions of baryonic and dark matter can be computed with the

relative height of these acoustic peaks. From these calculations, a flat universe was found with an energy density distribution of $\Omega_{DM} = 0.259$ (dark matter), $\Omega_b = 0.049$ (baryonic matter) and $\Omega_\Lambda = 0.692$ (dark energy) [3].

Another phenomenon pointing to the existence of dark matter is gravitational lensing as predicted by Albert Einstein in general relativity [4]. Spacetime can be curved around a massive object referred to as lens. Light that is emitted by a source is deflected by the lens depending on its mass. The observer on Earth in the line of sight will see a distorted image of the source under study due to the bent light trajectories. A two-dimensional basic scheme is shown in figure 2.2.

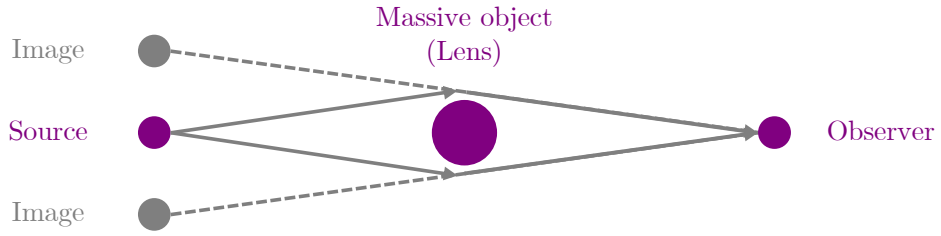


Figure 2.2: **Basic scheme of gravitational lensing:** The light emitted by a source in the line of sight with a massive object, the lens, is deflected due to spacetime curvature. Therefore, the observer potentially reconstructs a distorted image or even several objects.

With the help of known sources, the gravitational potential of the lens, for example a galaxy cluster, can be reconstructed from the degree of light deflection giving access to the amount of matter inside the bending object. When determining the mass of the luminous matter within several clusters with X-ray measurements, discrepancies in the quantity of mass were found. These can be resolved with the existence of dark matter within the objects.

The method above was also applied to galaxy-cluster collisions with high mass to light ratios ($\mathcal{O}(100)$) in order to reconstruct the center of mass after intermixing of the objects. Classically, the diffuse gas clouds, which represent the bulk amount of ordinary matter within the two clusters, would slow down due to friction. The point-like stellar components pass each other without collision and only interact gravitationally. From this assumption, the center of mass would follow the gas distribution. However, it was still found in the center of the respective cluster, clearly displaced from the location of the ordinary matter. This paradox can be solved by including the existence of dark matter halos around both clusters following their original trajectories independent of the collision. Furthermore, an upper limit for the strength of the self-interaction of dark matter can be obtained from these studies [5]. This phenomenon is shown in figure 2.3 for the Bullet Cluster, a system of two galaxy clusters, which collided about 150 million years ago [6]. More of these systems were found, as discussed in [7].

Additional evidence can be found on smaller scale structures by measuring the rotation velocity of spiral galaxies. The rotation velocity $v(r)$ of stars with large radii $r$ orbiting the galactic center is expected to follow Newtonian dynamics

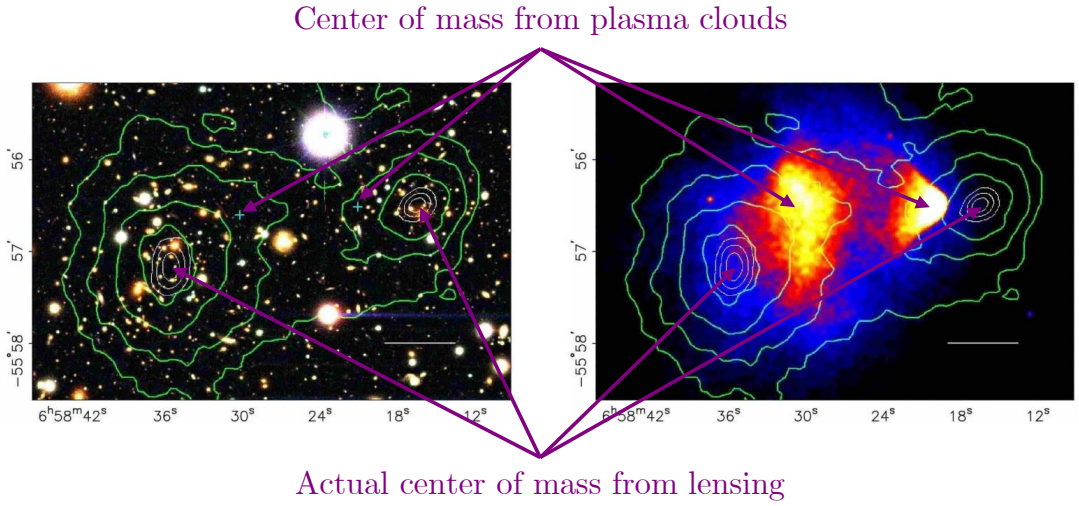


Figure 2.3: **The bullet cluster:** In the left panel, a color image of the merging cluster 1E0657-558 taken by the Magellan telescope is visualized. In the right panel, an x-ray image of the same cluster taken by the Chandra X-ray Observatory is shown. The blue +s (left panel) correspond to the center of mass location resulting from the plasma clouds (color-coded area on right panel). They are clearly displaced from the actual center of mass shown in green contours in both panels measured via weak gravitational lensing. Figure taken from [6].

with

$$v(r) \sim \frac{1}{\sqrt{r}}, \tag{2.1}$$

as most of the luminous mass is located there.

However, the measured velocities stay approximately constant for increasing distances from the galactic center. This can be explained by adding a uniformly distributed dark matter halo to the given model [8]. Consequently, the observed velocity distribution can be represented by a composition of the galactic disk, the galactic gas, and the dark matter halo, as shown in figure 2.4 for the galaxy NGC 6503 [8]. Recently, a galaxy lacking dark matter was found [9]. This may falsify theories that try to explain the observations with a modification of the Newtonian dynamics (MOND), where galaxies without dark matter signatures cannot exist [10]. Several properties for a dark matter candidate can be concluded from the observations above. This is discussed in the next section.

### 2.1.2 Weakly interacting massive particles

Possible candidate particles of this kind of new non-baryonic matter do not interact electromagnetically, leading to a class of neutral particles. The interaction with baryons can only be on the scale of the weak interaction or even below since no dark matter disks such as baryonic disks in galaxies were found. Additionally, dark matter must be stable on the scale of the age of the universe since its influence can still be measured. Most of the dark matter should have propagated with non relativistic velocities (referred to as cold) when structure

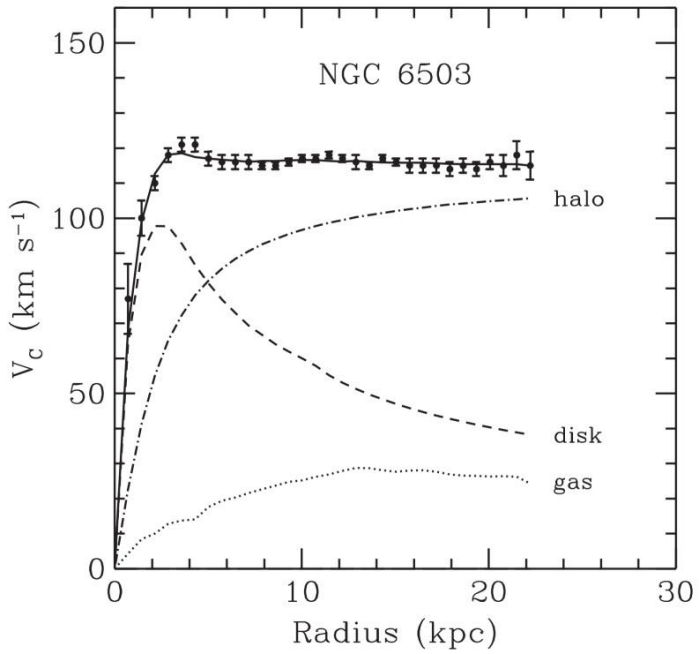


Figure 2.4: **Rotation curve of the spiral galaxy NGC 6503:** The approximately constant circular rotation velocities at large radii with respect to the galactic center can be explained by adding a dark matter halo to the galactic disk and gas. Figure taken from [8].

formation started, in order to allow clumping and formation of galaxies and clusters driven by gravitation. The observed structures predicted in a cold dark matter model agree with numerical N-body simulations of the formation [11].

From the standard model of particle physics, only the neutrino would fulfill these constraints. Neutrinos are considered to be hot dark matter due to their relativistic velocities and can be ruled out as the sole constituent of dark matter. First off, their velocity is too high for the structure formation in the early universe, shown with N-body simulations in [12]. Secondly, the neutrino abundance was determined to be $\Omega_\nu h^2 < 0.0067$ (95 % C.L.) with the help of the CMB measurements combined with large-scale structure data. Thus, standard model neutrinos are not abundant enough to compose a significant fraction of dark matter [13].

Another hypothetical class of neutrinos are sterile neutrinos. While sterile neutrinos are used to explain the smallness of the standard model neutrinos, they would be considered as warm or cold dark matter for relativistic velocities only during early times or non relativistic velocities at all times, respectively. Typical masses for this type of particle range from one to tens of keV [14].

Another representative for a cold dark matter candidate is the WIMP, a stable and neutral particle with a mass ranging from below GeV/$c^2$ to several TeV/$c^2$. It naturally arises in certain theories beyond the standard model, chiefly supersymmetry (SUSY). SUSY was designed to address the gauge hierarchy problem and the unification of weak, strong and electromagnetic forces as two examples [15]. A supersymmetric partner is postulated for each standard model particle. This partner differs by a spin of 1/2, such that fermions would have a

supersymmetric boson partner and vice versa. The new symmetry must be broken in order to allow higher masses for the supersymmetric particle with respect to its partner. Otherwise, SUSY particles should have been found in collider experiments already, which is not the case. Therefore, a multiplicative quantum number, called R-parity, is introduced to the model, where standard model constituents feature an R-parity of 1 and SUSY particles of $-1$. Consequently, the lightest stable supersymmetric particle (LSP) cannot decay into standard model particles because R is a conserved quantity. This gives rise to a WIMP-like particle [15].

In the minimal supersymmetric standard model (MSSM), the standard model is extended only by a minimum set of new supersymmetric partners. Here, the LSP is the superposition of the partners of the standard model bosons and is called neutralino. If the neutralino was a Majorana particle and interacted on the weak scale, dark matter would have been produced in a simple and predictive manner as a thermal relic of the big bang after freeze-out, as visualized in figure 2.5.

In the early universe - in thermal equilibrium (indicated by (1) in figure 2.5) - dark matter particles $\chi$ were allowed to annihilate into standard model components $SM$ and vice versa:

$$\chi + \chi \longleftrightarrow SM + SM. \tag{2.2}$$

After dropping below a certain temperature $T$ due to expansion and thus, cooling of the universe, the mean energy was not sufficient anymore to create dark matter particles. Consequently, the process in equation (2.2) was no longer allowed and the production rate of dark matter was suppressed exponentially, following a Boltzmann distribution with $e^{-m_\chi/T}$ (indicated by (2) in figure 2.5). With further expansion of the universe, the probability for two dark matter particles to meet and annihilate decreased, until freeze-out. Here, the dark matter abundance was asymptotically approaching a constant as a result (indicated by (3) in figure 2.5). This thermal relic density can be expressed by

$$\Omega_\chi h^2 = \frac{3 \cdot 10^{-27}\,\mathrm{cm}^3/\mathrm{s}}{\langle \sigma_\mathrm{A} v \rangle}, \tag{2.3}$$

where $\langle \sigma_\mathrm{A} v \rangle$ is the thermally averaged WIMP annihilation cross section. For a 100 GeV WIMP with an interaction strength on the the weak-scale, equation (2.3) naturally leads to the correct relic density as determined by the CMB measurements. This makes the WIMP a well motivated dark matter candidate. Detailed derivations and calculations can be found in [15]. The described phenomenon is often referred to as the *WIMP miracle*.

Since the XENON Dark Matter Project is aiming to probe the existence of WIMPs, the possible detection principles are discussed in the following. The main focus is on direct detection.

### 2.1.3 Direct detection

In principle, three promising strategies exist in order to test the particle dark matter hypothesis, namely production at collider experiments as well as indirect

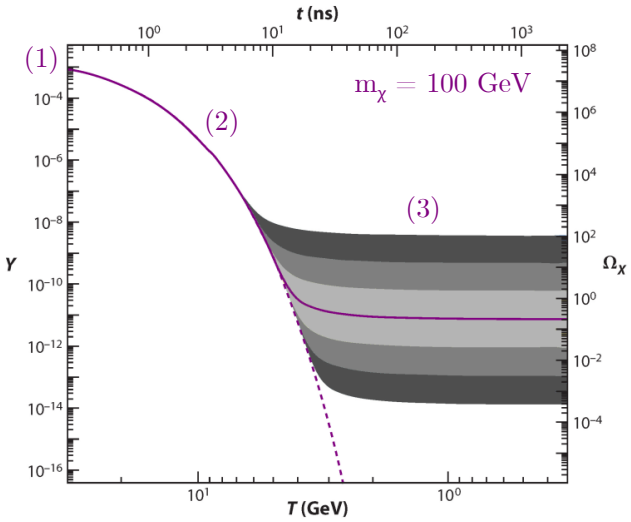


Figure 2.5: **Freeze-Out:** The comoving number density Y (left) and resulting thermal relic density (right) of a 100 GeV dark matter particle as a function of temperature T (bottom) and time t (top). The solid purple contour is for an annihilation cross section that yields the correct relic density, and the grey shaded regions are for cross sections that differ by 10, $10^2$, and $10^3$ from this value. The dashed purple contour is the number density of a particle that remains in thermal equilibrium. Figure and caption based on [16].

and direct detection. In figure 2.6, the possible coupling of a dark matter particle $\chi$ to a standard model particle SM is illustrated. Each direction of reading this diagram corresponds to one of the strategies.

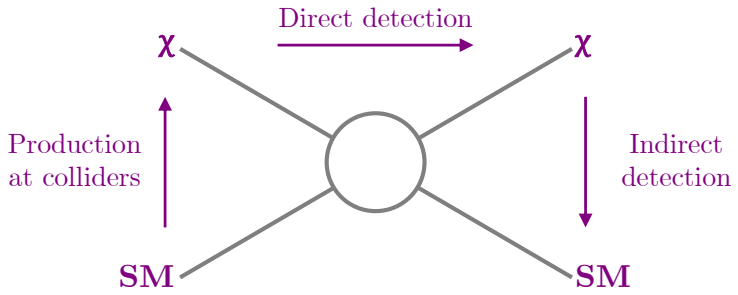


Figure 2.6: **Possible dark matter detection channels.** Figure based on [17].

In collider experiments, dark matter may be produced by collisions of standard model particles (from bottom to top in figure 2.6) and may be detected via missing transverse momentum in the collision products [18–20].

In the segment of indirect detection, experiments try to measure the standard model annihilation products of a dark matter pair (from top to bottom in figure 2.6). Especially in places with high gravitational potential such as near black holes, the dark matter density is expected to be increased, leading to a higher probability for dark matter annihilation [21–28].

The third option is direct detection, where a dark matter particle scatters off

standard model particles (from left to right in figure 2.6). Energy is deposited in form of recoil energy in sensitive low background detectors.

The event rate per detector mass and per recoil energy $E_\mathrm{r}$ can be derived as

$$\frac{dR}{dE_\mathrm{r}} = \frac{\rho_0 \cdot \sigma_0 \cdot F^2(q^2)}{2 \cdot m_\chi \cdot \mu_\mathrm{r}^2} \cdot \int_{v_\mathrm{min}}^{v_\mathrm{esc}} \frac{f(\boldsymbol{v})}{v} \mathrm{d}^3 v, \tag{2.4}$$

neglecting earth's motion around the sun. This would introduce an annual modulation to the WIMP velocity $v$ with respect to the target. The local dark matter density $\rho_0$ of about $0.3\,\mathrm{GeV/cm^3}$ can be obtained from rotation velocities in our galaxy. The WIMP mass is denoted as $m_\chi$, and $\mu_\mathrm{r}^2$ is the reduced mass of the WIMP/nucleus system. The WIMP scattering cross section is defined as $\sigma_0$. The form factor of the target nucleus $F(q^2)$ corresponds to the Fourier transformation of the charge distribution within the nucleus for small momentum transfers. The overall WIMP velocity distribution $f(\boldsymbol{v})$ is most commonly assumed to be a Maxwellian velocity distribution.

A minimum velocity

$$v_\mathrm{min} = \sqrt{\frac{E_\mathrm{r} \cdot m_\mathrm{A}}{2 \cdot \mu_\mathrm{r}^2}}, \tag{2.5}$$

with $m_\mathrm{A}$ being the mass of the nucleus, is required to create a measurable recoil, which is taken into account for the integration over all velocities. WIMPs with a velocity greater than the escape velocity $v_\mathrm{esc} \approx 570\,\mathrm{km/s}$ of the galaxy are also neglected.

For the case of a coherent WIMP scattering, a spin-independent (SI) cross section can be written as

$$\sigma_\mathrm{0,SI} = \sigma_\mathrm{p} \cdot \frac{\mu_\mathrm{r}^2}{\mu_\mathrm{p}^2} \cdot \left(Z \cdot f^\mathrm{p} + (A - Z) \cdot f^\mathrm{n}\right)^2 . \tag{2.6}$$

The nucleon cross section is defined as $\sigma_\mathrm{p}$. The parameter $\mu_\mathrm{p}^2$ denotes the reduced mass of the WIMP/nucleon system. The contributions of the protons and neutrons to the total coupling strength are given by $f^\mathrm{p,n}$. For the commonly used assumption $f^\mathrm{p} = f^\mathrm{n}$, the spin-independent cross section scales with $A^2$.

A WIMP could also couple to the spin of the target nucleus. Then, the spin-dependent (SD) cross section can be stated as

$$\sigma_\mathrm{0,SD} = \frac{32}{\pi} \cdot \mu_\mathrm{r}^2 \cdot G_\mathrm{F}^2 \cdot \left[a_\mathrm{p} \cdot \langle S^\mathrm{p} \rangle + a_\mathrm{n} \cdot \langle S^\mathrm{n} \rangle\right]^2 \cdot \frac{J+1}{J}. \tag{2.7}$$

Here $G_\mathrm{F}^2$ denotes the Fermi coupling constant, $J$ is the total nuclear spin, $a_\mathrm{p,n}$ are the effective proton and neutron couplings, and $\langle S^\mathrm{p,n} \rangle$ stand for the expectation value for proton and neutron spin content, respectively. Equations (2.4) to (2.7) are based on [17], where further discussions and derivations can be found.

In general, the induced recoil energy by the WIMP scattering within the detector material can produce three types of elementary excitation: ionization, phonons, and scintillation photons. Current experiments usually exploit two of the three detection channels (charge, heat, and light) in order to discriminate

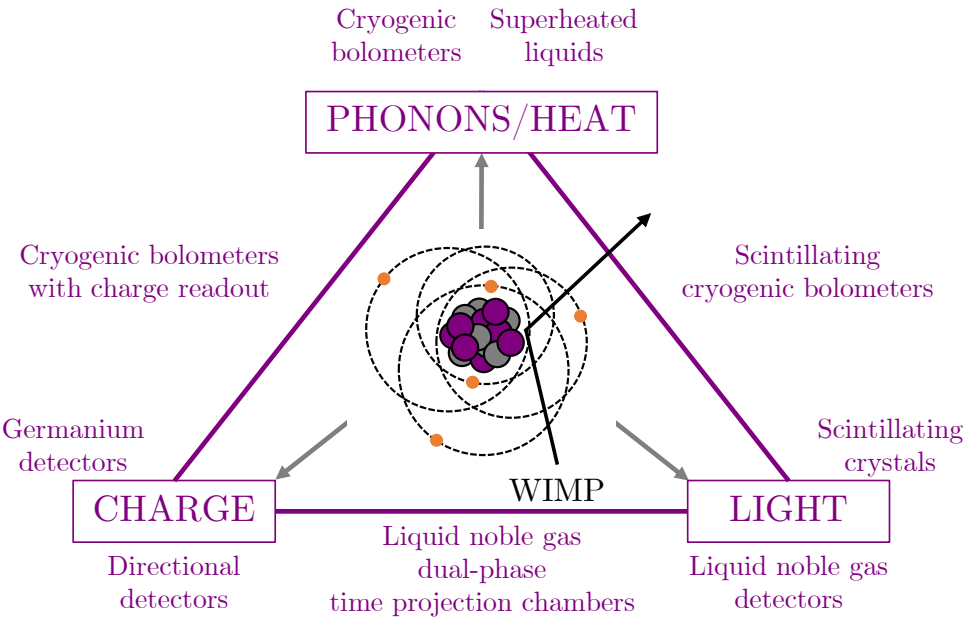


Figure 2.7: **Direct WIMP detection technologies:** The recoil energy introduced by a WIMP-nucleon scatter process can create heat, charge and light within the detector material. Potential technologies are shown exploiting one or two detection channels. Figure based on [17].

background events from possible WIMP signals. Figure 2.7 illustrates several detector technologies with their respective detection channels.

One way to measure light and charge signals from a WIMP induced interaction is the usage of a liquid noble gas, such as xenon, in a dual-phase time projection chamber.

## 2.2 Liquid xenon dual-phase time projection chamber

Liquid xenon features several properties that make it favourable as a dark matter detector material, such as a high atomic number of $A \sim 131$. Since the spin-independent cross section is proportional to $A^2$ as presented in equation (2.6), xenon is more sensitive to low energy recoils compared to other materials like argon, germanium or silicon, as visualized in figure 2.8. For increasing recoil energies, the interaction rate for WIMPs with xenon is suppressed due to the form factor $F(q^2)$, which is further discussed in [17].

Additionally, the natural xenon isotope composition is made of about half even and half odd isotopes, giving access to investigate spin-dependent interactions as shown in equation (2.7). Among the isotopes, only $^{136}$Xe is radioactive and a potential candidate for double beta decay searches. The $2\nu\beta\beta$ decay features a half-life on the order of $10^{21}$ y [29]. The event rate from the $2\nu\beta\beta$ decay in the region of interest is low enough to not interfere with the current dark matter search. However, this may change when moving to larger ton-scale detector

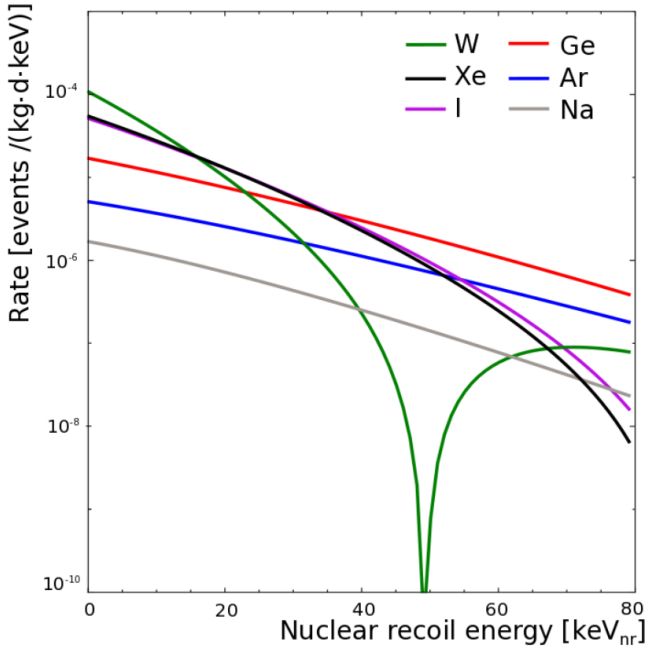


Figure 2.8: **Differential event rate for WIMP-nucleon scattering:** The expected rate is shown for the direct detection of a $100\,\mathrm{GeV/c^2}$ WIMP with a cross section of $10^{-45}\,\mathrm{cm^2}$ in experiments using tungsten (green), xenon (black), iodine (magenta), germanium (red), argon (blue) and sodium (grey) as target materials. Figure taken from [17].

masses. Due to the high charge number of $Z = 54$, xenon has a high stopping power for low energy gammas, such that they cannot penetrate deeply into a liquid xenon target. This self-shielding capability can be exploited for background reduction by fiducialization, where a quiet central detector region can be defined. A high liquid density of $\sim 3\,\mathrm{g/cm^3}$ in combination with a boiling point of 178 K at a pressure of 2 bar [30] allows for building compact detectors with large target masses and comparably simple cryogenic systems.

Scintillation light in liquid xenon is produced in two processes. In both cases light is emitted by an excited dimer ($Xe_2^*$). Therefore, xenon is transparent for its own scintillation light with a wavelength of about 178nm [31]. The first process starts with an excited xenon atom ($Xe^*$) following an energy deposition:

$$\begin{aligned} Xe^* + Xe &\rightarrow Xe_2^* \\ Xe_2^* &\rightarrow 2Xe + h\nu. \end{aligned} \tag{2.8}$$

The second process needs ionized xenon atoms ($Xe^+$):

$$\begin{aligned} Xe^+ + Xe &\rightarrow Xe_2^+ \\ Xe_2^+ + e^- &\rightarrow Xe^{**} + Xe \\ Xe^{**} &\rightarrow Xe^* + \text{heat} \\ Xe^* + Xe + Xe &\rightarrow Xe_2^* + Xe \\ Xe_2^* &\rightarrow 2Xe + h\nu. \end{aligned} \tag{2.9}$$

A part of the ionization component in equation (2.9) can be separated and drifted away before recombination, when an external electric field is applied.

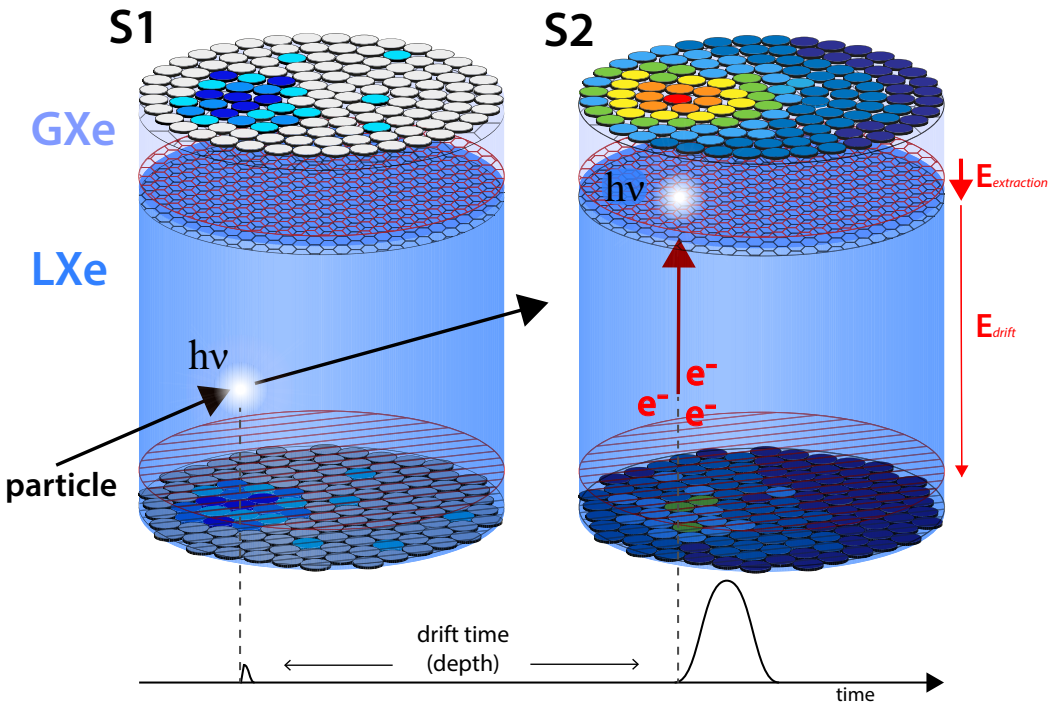


Figure 2.9: **Working principle of a xenon dual-phase time projection chamber:** On the left, the prompt S1 signal from the scintillation process is shown. On the right, the process for S2 creation is visualized. A full 3D reconstruction is possible by exploiting the drift time between the two signals as well as the S2 hit pattern in the top PMT array. Figure taken from [32].

Therefore, a dual-phase time projection chamber allows an independent measurement of a light as well as a charge signal.

The typically cylindrical detector is made of polytetrafluoroethylene (PTFE) as a frame for high reflectivity. The top and bottom plane are covered with arrays of Photomultiplier Tubes (PMT). The inner part is filled with liquid xenon (LXe) to a certain level, with a gaseous xenon (GXe) phase above. A schematic of a dual-phase TPC highlighting the two signal measurement processes of light and charge is illustrated in figure 2.9.

When an incoming particle deposits energy in form of a recoil within the LXe, light and charge are produced according to the scintillation and ionization processes described in equations (2.8) and (2.9). The light is promptly detected by the top as well as the bottom PMTs, as indicated in the left part of figure 2.9. It is referred to as the S1 signal. A fraction of the created electron-ion pairs is separated by the drift field $E_{drift}$ between two meshes, called cathode (negative potential, red mesh in the bottom in figure 2.9) and gate (ground potential, black mesh in the top in figure 2.9). The electrons follow the field lines upwards until they reach the edge of the liquid phase around gate level. From here, the electrons are extracted by a second electric field $E_{extraction}$ between gate mesh and anode (positive potential, red mesh in the top in figure 2.9) and are accelerated into the GXe where secondary scintillation light can be produced due

to electroluminescence. This light signal is referred to as the S2. The process is shown in the right part of figure 2.9.

By exploiting the time difference between the S1 and S2 signal for a constant drift velocity of the electrons, the depth and, therefore, the z-coordinate of the interaction point within the detector can be calculated. Additionally, the x- and y-position of the interaction can be determined using the localized hit pattern of the top PMT array created by the S2 signal. Consequently, a full 3D position reconstruction along with the time stamp of the interaction can be achieved. This gives access to the definition of a fiducial volume utilizing the self-shielding power of LXe. The background induced from the outside of the detector or from the detector materials themselves can be suppressed.

The dual signal also allows for the differentiation between two different recoil processes of the xenon atom: While most of the background components such as $\gamma$- and $\beta$-particles scatter off the electronic shell of the xenon atom, referred to as electronic recoil (ER), heavier particles such as WIMPs or neutrons can interact with the nucleus itself, referred to as nuclear recoil (NR). ER and NR create different signatures for the light and charge signal. This difference can be exploited using the ratio of the S2 over S1 signals where one has:

$$\left(S2/S1\right)_{\mathrm{NR}} \; < \; \left(S2/S1\right)_{\mathrm{ER}}. \tag{2.10}$$

Thus, electronic recoils can be discriminated from nuclear recoil events, which is schematically depicted in figure 2.10.

The different background sources and their reduction is the topic of the next section.

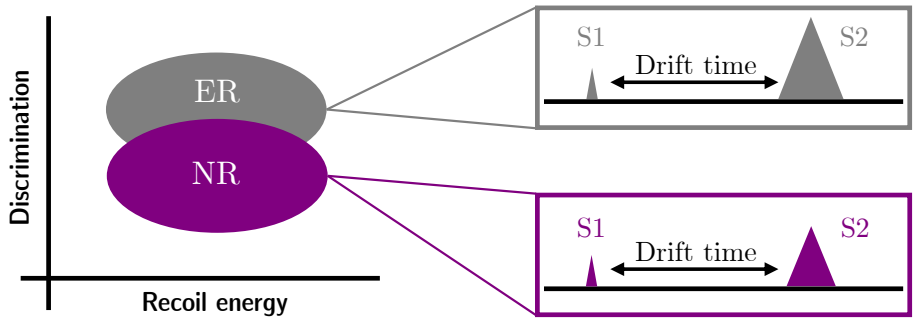


Figure 2.10: **Discrimination of nuclear and electronic recoils:** The smaller ratio of S2 over S1 for nuclear recoils (NR, purple) compared to electronic recoils (ER, grey) can be used for background discrimination. Figure based on [17].

## 2.3 Background sources and reduction

For the dark matter search, a low event rate is expected. This requires a sufficiently low background in order to reach the best possible sensitivity with the detector used. The most common sources of background for a liquid xenon based

Table 2.1: Common background sources in xenon dark matter detectors with energy ranges and mitigation strategies. Note that $\gamma$-sources produce a continuous spectrum with a full absorption peak due to Compton scattering. Table based on [33].

| Background component | Source | Interaction type | Mitigation strategy |
|---|---|---|---|
| Environmental $\gamma-$ radiation | $^{137}$Cs | $\leqslant$661.2 keV ER | Material selection, passive shielding |
| | $^{40}$K | $\leqslant$1460.8 keV ER | |
| | $^{60}$Co | $\leqslant$1173.2 keV ER | |
| | | $\leqslant$1332.5 keV ER | |
| | U/Th decay chains | $\leqslant$2.6 MeV ER | |
| Muons | Cosmic rays | ER | Underground detectors, active veto |
| | | Activation of target | |
| Cosmogenic neutrons | Spallation | NR (multiple) | Active veto (Water Cherenkov, LXe) |
| Radiogenic neutrons | ($\alpha$, n)-reactions | NR (multiple) | |
| | Spontaneous fission | NR (multiple) | |
| Neutrinos | Solar | ER, NR | |
| Internal backgrounds | $^{85}$Kr | $\leqslant$687 keV ER ($\beta$) | Cryogenic distillation |
| | | $\leqslant$173 keV ER ($\beta$) | |
| | | $\leqslant$514 keV ER ($\gamma$) | |
| | $^{222}$Rn | $\leqslant$6 MeV ($\alpha$) | Material selection, cryogenic distillation |
| | (+ daughters) | $\leqslant$1.6 MeV ER ($\beta, \gamma$) | |
| | $^{136}$Xe | $\leqslant$2458 keV ER ($2\nu\beta\beta$) | |

dark matter detector are summarized in table 2.1, along with their interaction type, energy and possible mitigation strategies.

One type of external background is coming from $\gamma$-radiation. In an interaction of $\gamma$-rays with matter, the photoelectric effect is the dominant process for $\gamma$-energies up to a few hundred keV, while the Compton scattering is most probable for higher energies up to several MeV. With further increasing energies, pair production is more likely to occur [34]. In all three cases energy is deposited within the target material xenon, creating signals that can be in the range of a few keV, the region of interest for the dark matter search. A typical $\gamma$-spectrum in the TPC features a full energy absorption peak with a continuous spectrum before the peak due to the Compton scattering.

The most common $\gamma$-sources are coming from the natural decay chains of $^{238}$U and $^{232}$Th contained within the surrounding detector area and the detector materials themselves, featuring several $\alpha$- and $\beta$-decaying daughter nuclei with $\gamma$-lines from tens of keV up to 2.6 MeV. Additional material isotopes are $^{40}$K, $^{60}$Co and $^{137}$Cs, originating from PMTs or stainless steel.

First off, in order to avoid $\gamma$-induced background from the start, the detector components must be selected in terms of high radio-purity following screening campaigns [35, 36]. Furthermore, ambient radiation can be shielded by lead, which features a high $Z$ and, therefore, a high stopping power, or by large water

tanks for a full coverage of the detector system.

Second off, the self-shielding effect of liquid xenon as discussed in section 2.2 can be used to further reduce the remaining $\gamma$-background by defining a fiducial volume. Additionally, electronic recoils induced by $\gamma$-rays, can be discriminated from nuclear recoils as explained in section 2.2. Multiple simultaneous events generated from Compton scattering can be rejected as well due to the low interaction probability of the WIMP.

Another type of external background are free neutrons that can mimic a WIMP signal by inducing nuclear recoil events within the fiducial volume. They can be created via spallation reactions of cosmic muons with the surrounding material, reaching energies of up to several GeV [37]. The so-called cosmogenic neutrons are moderated by the detector shielding down to energies of MeV and create NR-like events in the dark matter search region. Additionally, so-called radiogenic neutrons are generated with energies of a few MeV as a result of $(\alpha, n)$-reactions and spontaneous fission from natural radioactivity. Multiple NR-like scatter events induced by free neutrons, as in the case for electronic recoils, can be rejected by the analysis. The rejection power increases with larger target masses, as multiple interactions are more likely.

In order to reduce the muon flux and therefore the muon-induced neutron production, the experimental setup is typically localized in deep underground laboratories. The XENON Dark Matter Project, for example, is operated in Laboratori Nazionali del Gran Sasso (LNGS) in Italy at an average depth of 3600 meters water equivalent (mwe), resulting in a muon flux reduced by a factor of $10^6$ [38].

Additional mitigation can be achieved with large water shields that double as Cherenkov detectors [39]. These detectors allow an active muon veto where simultaneous events in the water and in the TPC can be rejected.

Additionally, solar neutrinos become an external background source for large scale detectors with masses on the multi ton-scale. They can induce electronic as well as nuclear recoil events, but are not yet a limiting factor for XENON1T. Therefore, they will not be discussed here. Further discussions can be found in [17].

Internal backgrounds are most critical contributors to the final background level, especially for increasing liquid xenon target masses. As mentioned in section 2.2, the decay rate of the double beta decay isotope $^{136}$Xe with a half-life of $2 \times 10^{21}$ y is too low to significantly contribute to the final background of current experiments such as XENON1T [40]. Cosmic activation of xenon can lead to artificial radioactive xenon isotopes, where $^{127}$Xe has the longest lifetime with 36 d. This activation can be avoided by storing the xenon long enough underground before starting the experiment.

Electronegative impurities or radio-active isotopes of other noble gases constitue a significant group of intrinsic contaminants. While electronegative impurities such as $H_2$, $O_2$, $N_2$, $CO/CO_2$ or $H_2O$ do not contribute to the background for the dark matter search, they do capture free electrons and absorb scintillation light, reducing the drift-length of the electrons and the light yield. Therefore, the xenon has to be continuously circulated through a purification system with hot metal getters outside the detector, reducing these impurities down to a required

level of 1 ppb[1] (oxygen equivalent) [41]. Further information on the XENON1T purification system is shown in section 3.3.

Radioactive noble gases, namely $^{85}$Kr as well as $^{220}$Rn and $^{222}$Rn, cannot be removed by getters. $^{85}$Kr is a β-emitter with an endpoint energy of 687 keV and a half-life of 10.76 yr, as illustrated in the decay scheme in figure 2.11. In 0.4 % of the cases, a β-decay with an endpoint of 173 keV can occur, followed by a 514 keV-γ. A delayed coincidence analysis of these subsequent decays can be used to identify $^{85}$Kr in the TPC and allows for the estimation of the krypton in xenon content. Krypton creates electronic recoils homogeneously throughout the detector volume, rendering fiducial volume cuts ineffective. Although ER events can be discriminated from NR events, a small fraction of leakage events can infiltrate the dark matter search region. The relatively long half-life requires the krypton to be removed before starting the experiment.

The isotope $^{85}$Kr is anthropologically produced in uranium and plutonium fission and is released to the atmosphere by nuclear weapon tests and nuclear reprocessing plants. The abundance of $^{85}$Kr in natural krypton is typically stated as

$$\frac{^{85}\mathrm{Kr}}{^{\mathrm{nat}}\mathrm{Kr}} \sim 10^{-11} \qquad [42]. \tag{2.11}$$

Since xenon is extracted from air by fractional distillation based on the Linde cycle, a small portion of natural krypton is contained within the xenon, typically at the level of ppm[2], but xenon with a $^{\mathrm{nat}}$Kr/Xe ratio ∼10 ppb can be purchased from industrial vendors. Meanwhile, current dark matter experiments require concentrations at the ppt[3] level and below. This can be achieved with a cryogenic distillation column. Since krypton comes from the atmosphere, it needs to be removed just once before the dark matter search. The achieved krypton level in XENON100 as well as the required and achieved concentration for XENON1T are discussed in sections 2.4 and 2.5, respectively. The krypton removal at the XENON1T experiment is one of the main parts of this thesis and is explained in detail in chapter 6.

In contrast to krypton, the radon isotopes $^{220}$Rn and $^{222}$Rn are continuously emanated from detector materials. While $^{220}$Rn with a half-life of 56 s does not live long enough to deeply penetrate large scale liquid xenon detectors, $^{222}$Rn has a half-life of 3.8 d and can homogeneously disperse inside the TPC. The vast amount of deposited energy by its α-decay of 5.59 MeV can easily be rejected for the dark matter search. However, subsequent β-decays in the decay chain, in particular $^{214}$Pb which is a β-emitter with an endpoint energy of 1.02 MeV and a half-life of 26.8 min, create low energy background events similar to krypton. The $^{222}$Rn decay chain is depicted in figure 2.12.

As in the case for γ-induced background reduction, one approach for mitigation of radon is the selection of materials with a low radon emanation [45]. An additional strategy is the development of a continuous radon removal system based on cryogenic distillation.

The first successful operation for radon removal using a cryogenic distillation

[1] 1 ppb (parts per billion) = $10^{-9}$ mol/mol
[2] 1 ppm (parts per million) = $10^{-6}$ mol/mol
[3] 1 ppt (parts per trillion) = $10^{-12}$ mol/mol

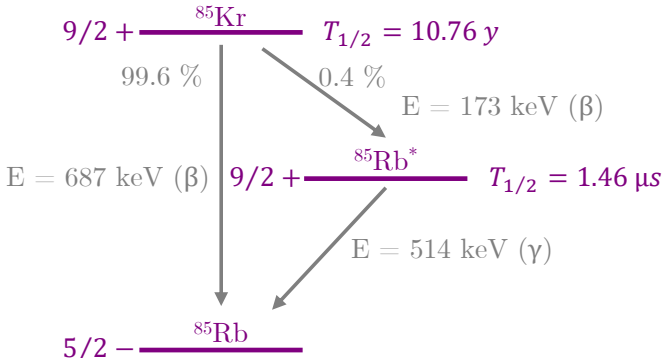


Figure 2.11: **Decay scheme of** $^{85}$Kr**:** With a branching ratio of 99.6 % it disintegrates via β-emission into $^{85}$Rb with an endpoint energy of 687 keV and a half-life of 10.76 yr. In 0.4 % of the cases, a β-decay with an endpoint of 173 keV followed by a 514 keV-γ can occur. The 1.46 µs half-life of the $^{85}$Rb* allows to tag krypton events by a coincidence analysis of the subsequent decays. Numbers taken from [43].

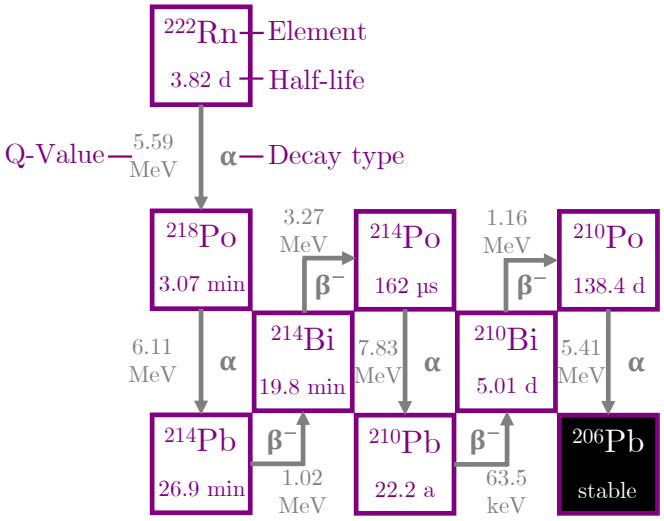


Figure 2.12: **Decay chain of** $^{222}$Rn**:** The α-decays from $^{222}$Rn and $^{218}$Po can be used to monitor the radon in xenon content in the TPC. The β-emitter in the chain can create leakage events in the region of interest for the dark matter search, especially $^{214}$Pb with an endpoint energy of 1.02 MeV. The subsequent decays of $^{214}$Bi and $^{214}$Po allow for a coincidence analysis to cross check the radon in xenon content. Decay channels with a branching ratio <0.1 % are omitted. Numbers taken from [44].

column is another major part of this thesis and is presented in section 7.1. Since XENON100 was used as a test bed for this operation, it is briefly introduced in the next section.

## 2.4 XENON100

The XENON100 dual-phase time projection chamber is made of a cylindrical PTFE structure with 30.5 cm height and a diameter of 30.6 cm and is filled with 62 kg LXe. The TPC is housed in a double-walled stainless steel cryostat and is surrounded by a 99 kg LXe active scintillator veto for background rejection.

In order to reduce external background sources the cryostat is passively shielded, going from inside to outside, by a 5 cm layer of OFHC (oxygen-free high conductivity) copper, followed by a 20 cm layer of polyethylene, 20 cm lead and 20 cm water. Additionally, the shield is purged with boil-off $N_2$ to suppress radon induced background [46].

An electric field for the electron drift of 530 V/cm is applied inside the LXe between the cathode and the gate while an extraction-field of 12 kV/cm is applied in the gaseous phase between the gate and anode [47].

178 square 1″ Hamamatsu R8520-AL PMTs with a low radioactivity and high quantum efficiency are installed with 80 PMTs in the bottom array and 98 PMTs in the top. The top light sensors are arranged in concentric circles in order to improve the resolution of the radial event reconstruction. The bottom ones are packed as close as possible for the highest possible light yield. In addition, 64 PMTs that were originally used for the XENON10 detector are used in the active veto. In XENON100, the depth z can be measured with a precision of 0.3 mm, while the uncertainty of x and y is lower than 3 mm in each direction [47]. A picture showing the top and bottom PMT arrays as well as the fully assembled TPC are visualized in figure 2.13.

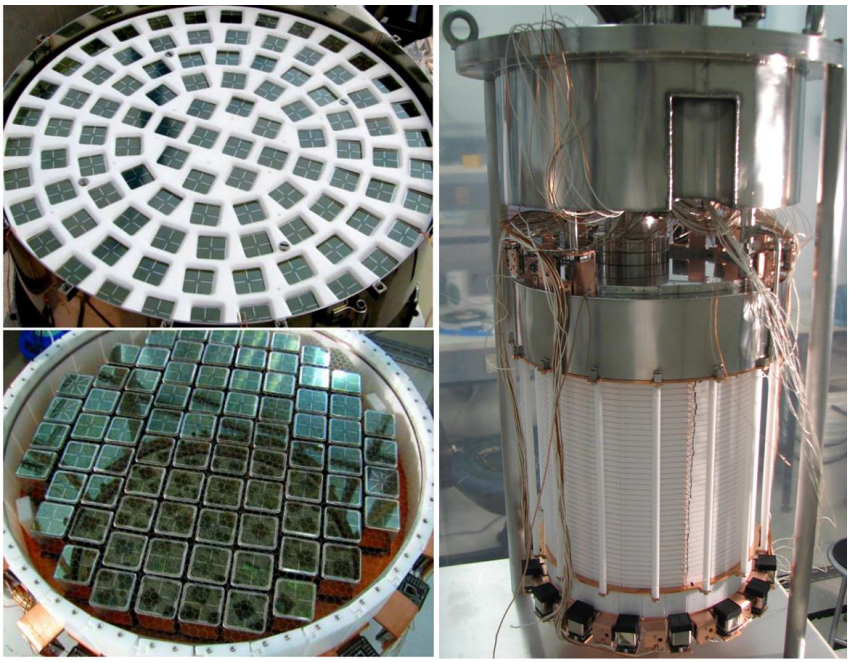

Figure 2.13: **XENON100 TPC:** On the left are the top and bottom PMT arrays, while on the right the fully assembled detector is shown. Pictures from [48].

In total, 477 live days from three science runs, resulting in an exposure of 48 kg × yr from January 2010 until January 2014, were analyzed, yielding no

evidence for dark matter. The combination of all three runs with an improved analysis resulted in a limit on the spin-independent elastic WIMP-nucleon scattering cross section of

$$\sigma_{\mathrm{SI}} < 1.1 \cdot 10^{-45}\mathrm{cm}^2, \tag{2.12}$$

for a WIMP mass of $50\,\mathrm{GeV/c^2}$ (90 % C.L.) [47].

The average total electromagnetic background before electron recoil rejection was around $5 \times 10^{-3}\,\mathrm{events/(keV \cdot kg \cdot day)}$[4]. The different levels of the intrinsic contaminants $^{85}$Kr and $^{222}$Rn along with their contribution to the total background throughout the science runs SR1, SR2 and SR3 are briefly summarized in the following. All stated numbers are taken from [49].

The natural krypton in xenon concentration was determined in two ways: First off, by the extraction of gas samples into pipettes that were measured offsite with a rare gas mass spectrometer (RGMS) [50] (see also section 4.2). Second off, by a delayed coincidence (DC) analysis of the second decay branch via an excited $^{85}$Rb state as shown in figure 2.11 [49].

Table 2.2: Overview of the $^{\mathrm{nat}}$Kr concentrations in XENON100 using RGMS. Numbers taken from [49].

| Period | Date | $^{\mathrm{nat}}$Kr/Xe [ppt] |
|---|---|---|
| SR1 | 02 Jun 2010 | 340 ± 60 |
| SR2 | 17 Nov 2011 | 13.8 ± 2.4 |
| SR3 | 14 Dec 2012 | 0.71 ± 0.24 |
| | 09 Jan 2013 | 0.95 ± 0.22 |
| | 21 Oct 2013 | 8.7 ± 1.5 |
| | 22 Dec 2013 | 11.1 ± 1.9 |

The results of several RGMS measurements are summarized in table 2.2. At the start of science run 1 (SR1), the level was $(340 \pm 60)$ ppt, which was later on reduced with several cryogenic distillation campaigns down to the lowest concentration of $(0.71 \pm 0.24)$ ppt at the beginning of the third science run (SR3). However, due to leaks this low level was not maintained for a long period of time leading to an average concentration of $(6.3 \pm 1.0)$ ppt during SR3.

Table 2.3: Comparison of the $^{\mathrm{nat}}$Kr concentrations in XENON100 obtained from delayed coincidence analysis (DC) for a fiducial volume of 34 kg and the run-average from rare gas mass spectrometer (RGMS) measurements. Numbers taken from [49].

| Period | DC [ppt] | RGMS [ppt] |
|---|---|---|
| SR1 | $370^{+60}_{-50}$ | 340 ± 60 |
| SR2 | $15^{+10}_{-7}$ | 11.0 ± 1.7 |
| SR3 | $18^{+14}_{-9}$ | 6.3 ± 1.0 |

[4] Sometimes the rate is given in milli Differential Rate Unit (mDRU), $1\,\mathrm{mDRU} = 1 \times 10^{-3}\,\mathrm{events/(keV \cdot kg \cdot day)}$

The run-averaged concentrations for the DC analysis with a fiducial volume of 34 kg as well as RGMS measurements are presented in table 2.3. The combination of both yield run-averaged concentrations of $340^{+60}_{-50}$ ppt, $12^{+8}_{-5}$ ppt and $12^{+9}_{-6}$ ppt for SR1, SR2 and SR3, respectively.

In the case of $^{222}$Rn, the level in xenon is most commonly given as the activity per one kilogram of xenon. This activity concentration can be obtained by $\alpha$-event selection in a defined fiducial volume. In addition, the daughter nuclide $^{218}$Po, which undergoes an $\alpha$-decay with a half-life of about 3.07 min, can be used as a cross check. Furthermore, a delayed coincidence analysis with $^{214}$Bi and $^{214}$Po (BiPo analysis) from the radon decay chain can be applied. However, the activity concentration found from the $^{218}$Po analysis is about 86 % and the one from the BiPo analysis is about 50 % of the expected events compared to the $^{222}$Rn $\alpha$-counting [49, 51]. In the case of $^{218}$Po, acceptance losses originating from the selection criteria are negligible due to the high energy signature of the $\alpha$-events. Ionized radon daughters plating out onto the cathode due to convection and drift in the electric field can resolve the mismatch. This was also observed and studied in [52, 53]. Events occurring at the cathode due to the plate out effect are shadowed resulting into losses in the S1 signal and thus into a lower acceptance of $^{218}$Po and BiPo events. Especially for the $^{214}$BiPo events the effect is assumed to be enhanced due to the increased chance of ionized daughters to plate out with every decay in the radon chain.

The main contributor to the electronic recoil background in the dark matter region of interest from the radon decay chain is the $\beta$-emitter $^{214}$Pb as discussed in section 2.3. It is the daughter nuclide of $^{218}$Po. Therefore, the estimated activity concentration of $^{218}$Po can be used as an upper limit of the $^{214}$Pb contribution, while the $^{214}$BiPo results can be utilized as lower limit.

The obtained radon levels from the three analysis channels $^{222}$Rn, $^{218}$Po and $^{214}$BiPo are presented in table 2.4 including periods with leaks. From the overall analysis it can be concluded that in average the radon emanation from detector materials is around 40 µBq/kg.

Table 2.4: Average rates for radon induced background in XENON100 with the help of $\alpha$-event selection ($^{222}$Rn and $^{218}$Po) and delayed coincidence analysis of $^{214}$Bi and $^{214}$Po. The leak period of SR1 ends on 07 Feb 2010, and the leak period of SR3 lasts from 27 Jun 2013, to 01 Dec 2013. Numbers taken from [49].

| Period | $^{222}$Rn [µBq/kg] | $^{218}$Po [µBq/kg] | $^{214}$BiPo [µBq/kg] |
|---|---|---|---|
| SR1 | 48.0 ± 0.4 | 41.0 ± 0.4 | 24.8 ± 0.6 |
| SR1 (aft. leak) | 38.3 ± 0.4 | 33.4 ± 0.4 | 20.5 ± 0.6 |
| SR2 | 64.3 ± 0.4 | 52.2 ± 0.3 | 32.8 ± 0.5 |
| SR3 | 68.3 ± 0.4 | 59.0 ± 0.3 | 36.9 ± 0.5 |
| SR3 (bef. leak) | 41.8 ± 0.9 | 37.1 ± 0.9 | 22.9 ± 1.2 |
| SR3 (dur. leak) | 76.7 ± 0.4 | 66.1 ± 0.4 | 41.1 ± 0.6 |

For both isotopes $^{85}$Kr and $^{222}$Rn, conversion factors can be determined with the help of Monte Carlo studies [40] in order to translate the impurity level into a differential background event rate per mass, energy and time. For krypton a

factor of 0.039 mDRU/ppt can be calculated, assuming $^{85}\mathrm{Kr}/^{\mathrm{nat}}\mathrm{Kr} = 2 \times 10^{-11}$, while for radon a conversion factor of 0.029 mDRU/(μBq/kg) is found from simulation. The transformed rates are summarized in table 2.5 for krypton as well as radon for all three science runs along with the total ER background in the 34 kg fiducial volume.

Table 2.5: Estimated average ER background induced by the $^{222}$Rn chain and $^{85}$Kr (below 100 keV, before applying ER/NR discrimination) in all three XENON100 science runs. Delayed coincidence analyses were performed for a 34 kg fiducial volume. The total ER background rate including materials is presented for comparison. Numbers taken from [49].

| Source | Methode | Induced ER rate [$10^{-3}$ events/(keV · kg · day)] | | |
|---|---|---|---|---|
| | | SR1 | SR2 | SR3 |
| $^{222}$Rn | $^{222}$Rn | 1.392 ± 0.012 | 1.865 ± 0.012 | 1.981 ± 0.012 |
| | $^{218}$Po | 1.189 ± 0.012 | 1.514 ± 0.009 | 1.711 ± 0.009 |
| | $^{214}$BiPo | 0.719 ± 0.017 | 0.951 ± 0.015 | 1.070 ± 0.015 |
| $^{85}$Kr | DC | 14 ± 2 | 0.6 ± 0.4 | 0.7 ± 0.5 |
| | RGMS | 13.2 ± 2 | 0.43 ± 0.07 | 0.25 ± 0.04 |
| Total | - | 17.8 ± 2.7 | 5.3 ± 0.6 | 5.3 ± 0.7 |

In SR1, the high krypton concentration lead to a contribution of about 75 % to the total background of $(17.8 \pm 2.7) \times 10^{-3}$ events/(keV · kg · day) and was one order of magnitude larger than radon (6 %).

Krypton was removed by cryogenic distillation before SR2 and SR3 yielding similar total background rates of about $5.3 \times 10^{-3}$ events/(keV · kg · day). In contrast to SR1, the dominant background originated from external sources such as the materials with about (60-65) %. With about 30 % radon was the dominant intrinsic background.

The self-shielding property of liquid xenon for target masses on the ton-scale as in XENON1T allows to define a fiducial volume that reduces material backgrounds to a negligible level. Consequently, the background is dominated by intrinsic contaminants. However, due to the increased mass in the inner volume, the krypton and radon levels need to be reduced further to reach comparable background rates and below. The basic features of the XENON1T TPC as well as background requirements are briefly discussed in the next section.

## 2.5 XENON1T

The XENON1T experiment is located in Hall B of LNGS featuring a total xenon mass of about 3200 kg. It is the first operating liquid xenon detector with a target mass above the ton-scale. The cylindrical dual-phase time projection chamber inside a double-walled vacuum cryostat has a height of approximately 97 cm and a diameter of 96 cm enclosing around 2000 kg of liquid xenon. The surrounding 1200 kg are utilized as passive shield.

The cryostat is installed in the center of a 10 m wide and 10 m tall water tank housing about 700 t of pure water, for the shielding of environmental radioactivity.

Additionally, the water tank is equipped with 84 PMTs as part of an active Cherenkov muon veto [39].

An electric field for the electron drift of about 117 V/cm is applied between the cathode and the gate while an extraction-field >10 kV/cm is applied in the gaseous phase between the gate and anode [54]. Higher drift fields along the liquid xenon were not possible due to high voltage issues, but the actual field strength is sufficient to drift electrons and to achieve a reasonable ER/NR-discrimination.

In total, 248 Hamamatsu R11410-21 PMTs of 76.2 mm diameter with a low radioactivity [55] and high quantum efficiency (34.5 % at 178 nm in average at room-temperature [56]) are installed with 121 PMTs in the bottom array and 127 PMTs in the top. The top light sensors are arranged in concentric circles in order to improve the x-y-resolution of event reconstruction. At the bottom the PMTs are packed as tightly as possible to maximize scintillation light collection efficiency [41]. Both PMT arrays as well as the TPC are shown after assembly in figure 2.14.

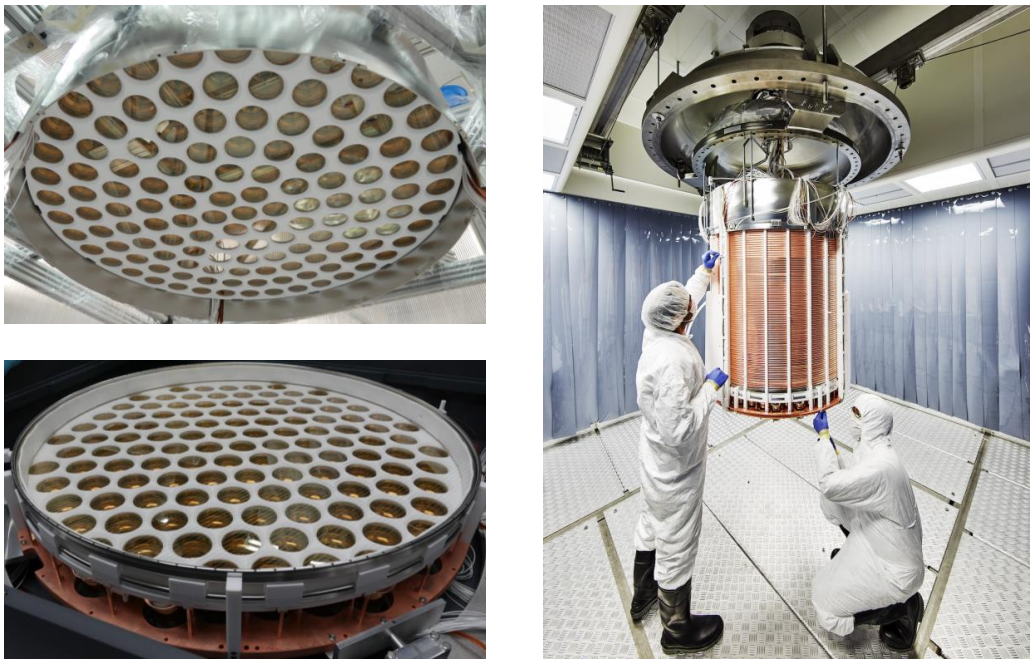

Figure 2.14: **XENON1T TPC:** On the left are the top and bottom PMT arrays, while on the right the fully assembled detector is shown. Pictures from [41].

A service building next to the water tank houses the xenon storage, cryogenic plant, purification loop, distillation column, data acquisition, as well as the slow control system. All subsystems are explained in detail in [41] while some of the relevant systems for this thesis are briefly presented in section 3.3.

With the help of extensive Monte Carlo simulations [40], the required impurity levels for krypton and radon were calculated to 0.2 ppt and 10 µBq/kg, respectively. These are needed to reach a projected sensitivity for a spin-independent WIMP-nucleon scattering cross section of $1.6 \times 10^{-47}\,\mathrm{cm}^2$ at a WIMP mass of $50\,\mathrm{GeV/c}^2$ with an exposure of 2.0 tonne × yr. The total expected ER background as the sum of external and internal background sources

in a 1 tonne fiducial volume and in a (1–12) keV energy range is simulated to be $(1.80 \pm 0.15) \times 10^{-4}$ events/(keV · kg · day). The different contributions expected are summarized in table 2.6 showing that intrinsic backgrounds with 91.1 % are dominant.

Table 2.6: Summary of the predicted ER backgrounds in XENON1T from MC simulations, evaluated in 1 tonne fiducial volume and in (1–12) keV energy range. 10 µBq/kg of $^{222}$Rn, 0.2 ppt of $^{nat}$Kr, and the natural abundance of $^{136}$Xe are assumed. Table and caption based on [40].

| Source | Background $[(\text{keV} \cdot \text{kg} \cdot \text{day})^{-1}]$ | Fraction [%] |
|---|---|---|
| Materials | $(7.3 \pm 0.7) \cdot 10^{-6}$ | 4.1 |
| $^{222}$Rn | $(1.54 \pm 0.15) \cdot 10^{-4}$ | 85.4 |
| $^{85}$Kr | $(7.7 \pm 1.5) \cdot 10^{-6}$ | 4.3 |
| $^{136}$Xe | $(2.3 \pm 0.3) \cdot 10^{-6}$ | 1.4 |
| Solar neutrinos | $(8.9 \pm 0.2) \cdot 10^{-6}$ | 4.9 |
| Total | $(1.80 \pm 0.15) \cdot 10^{-4}$ | 100 |

The nuclear recoil background in the corresponding nuclear recoil equivalent energy region (4, 50) keV is composed of $(0.6 \pm 0.1)$ (tonne · yr)$^{-}1$ from radiogenic neutrons, $(1.8 \pm 0.3) \times 10^{-2}$ (tonne · yr)$^{-}1$ from coherent scattering of neutrinos, and less than 0.01 (tonne · yr)$^{-}1$ from muon-induced neutrons [40].

After commissioning in summer 2016, a first science run (SR0) with 34.2 live days was performed, acquiring data between November 2016 and January 2017 [54]. Followed by that, a second science run (SR1) lasted from January 2017 until February 2018. The combined analysis of both runs with 278.8 live days and a fiducial volume of $(1.30 \pm 0.01)$ tonne yielded no dark matter signal, but resulted in the most stringent exclusion of the spin-independent WIMP-nucleon scattering for WIMP masses greater 6 GeV/c$^2$ with a minimum of $4.1 \times 10^{-47}$ cm$^2$ for a 30 GeV/c$^2$ (90 % C.L.) WIMP [54]. The exclusion curve is visualized in figure 2.15. It features a $1\sigma$ under-fluctuation for masses below 8 GeV/c$^2$ and an over-fluctuation at higher masses. However, the result is compatible with the background-only hypothesis. Limits from other experiments such as XENON100, LUX and PandaX are illustrated as well for comparison.

The mean of the natural krypton concentration within the LXe target was $(0.66 \pm 0.11)$ ppt, whereas the lowest achieved concentration was $(0.36 \pm 0.06)$ ppt. The details of the reduction with the help of cryogenic distillation are presented in chapter 6. The purity reached is the lowest in a running dark matter experiment so far and is sufficiently low for XENON1T as radon is the dominant background.

With the help of in-situ $\alpha-$spectroscopy, the radon activity concentration was determined to be $(13.3 \pm 0.8)$ µBq/kg. In combination with the delayed coincidence analysis of BiPo events, the contribution from $^{214}$Pb can be constrained to $(0.8\text{–}1.9) \times 10^{-4}$ events/(keV · kg · day) in the low energy range of interest for WIMP searches [54]. During the second half of SR0 the modified krypton distillation column was utilized in inverse mode to reduce the radon background further by about 20 %. This is presented in chapter 7.

The total electronic recoil background was found to be $(2.24^{+0.23}_{-0.12}) \times 10^{-4}$ events/(keV · kg · day) [54], compatible with the Monte Carlo

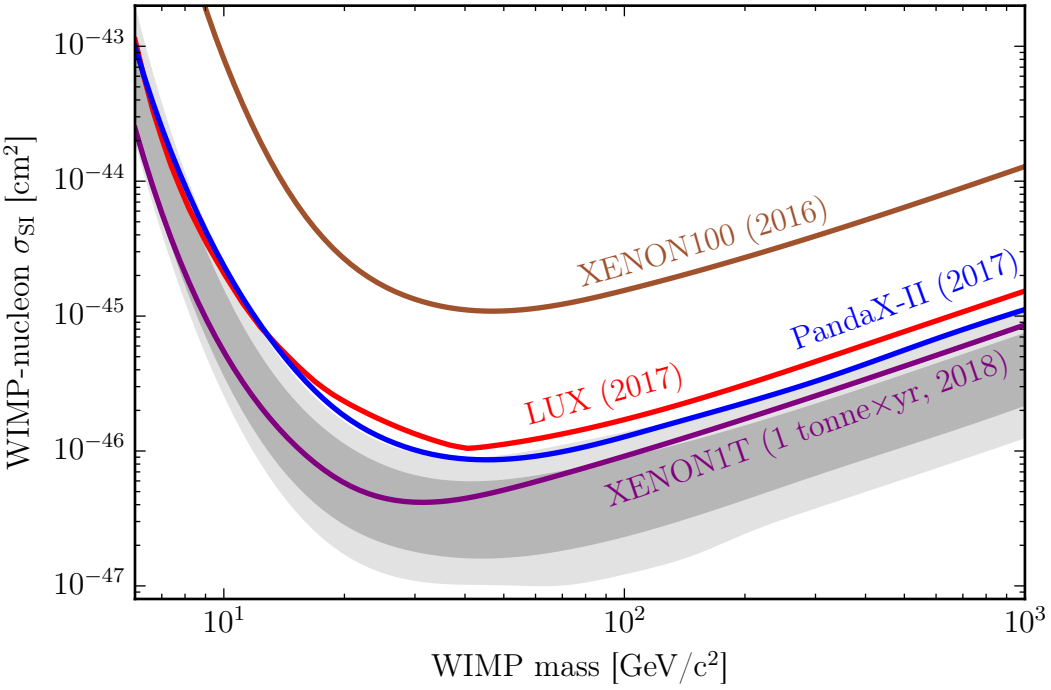


Figure 2.15: **Exclusion limits:** The exclusion limits from different dark matter experiments for given WIMP masses and corresponding WIMP-nucleon cross sections $\sigma_{SI}$ are visualized. The results from a one tonne-year exposure of XENON1T yielded the most stringent limit. The grey shaded areas highlight the one and two sigma sensitivity bands. Figure based on [57].

prediction of $(2.3 \pm 0.2) \times 10^{-4}$ events/(keV · kg · day) [40] for the krypton and radon values measured. This is the lowest background ever achieved in a dark matter experiment for WIMP searches.

One key subsystem of XENON1T is the cryogenic distillation plant. It was originally designed to reduce the krypton induced background in the liquid xenon allowing to meet the strict background requirements. Later on it was modified to also remove parts of the radon induced background. The key requirements for the XENON1T column in terms of krypton removal are briefly summarized in the following section.

### 2.5.1 Requirements for the distillation system

Commercially available xenon comes most commonly with a $^{nat}$Kr/Xe ratio of several hundreds of ppb up to a few ppm. On special request, companies do provide purer xenon with a krypton concentration on the order 10 ppb at significantly increased cost.

In order to reach a sub-ppt level as required by XENON1T a reduction of krypton by a factor of $10^4$ to $10^5$ is necessary.

The existing distillation column for XENON100, based on the distillation system of XMASS [58], was designed for a reduction factor of $10^3$ at a process speed of 0.6 kg/h. The plant was able to provide output concentrations around

1 ppt, but only after several rounds of purification of the same xenon batch as mentioned before. It would require 32 weeks of continuous operation to purify the 3200 kg of target material. However, several rounds of distillation would be required to reach the desired purity. Additionally, the system never provided concentrations below 0.2 ppt such that a pure xenon would not be guaranteed after an extensive cleaning procedure over the course of at least a year or more. Therefore, a new distillation plant was needed for the XENON1T experiment that can also serve for the next-generation experiment XENONnT. The target mass is planned to be purified in about 6 weeks of operation, corresponding to a throughput of 3 kg/h. During operation, 99 % of the distilled xenon must be recovered and used as detector material, while 1 % is stored as krypton-enriched off-gas. The separation factor for one purification cycle has to be in the range of $10^4$ to $10^5$, featuring purified output concentrations below 0.2 ppt.

The development of the distillation column was divided into three phases: It started with a single-stage distillation setup (Phase-0), where the proof of principle to separate krypton from xenon on the sub-ppt level was shown with a $^{83m}$Kr tracer method [59, 60].

The next phase (Phase-1) was the construction of a multi-stage test setup with a smaller total height compared to the final version allowing to investigate different aspects of the thermodynamic stability as well as the separation performance [60, 61]. It produced the worldwide lowest krypton in xenon concentration measured with RGMS to be below 26 ppq[5] (90 % C.L.). The reduction factor was proven to be greater than $5.6 \times 10^3$ (90 % C.L.) [60, 61]. In order to safely reach the required separation efficiency, the final version (Phase-2) was extended in height. Additionally, the collection efficiency of the condenser stations was optimized compared to the Phase-1 system. The upgrade from Phase-1 to Phase-2 column is part of this thesis. The basic idea of noble gas separation and the design of the distillation column based on the McCabe-Thiele method along with the technical realization are presented in the next chapter. Additionally, the integration as a XENON1T subsystem is shown.

[5] 1 ppq (parts per quadrillion) = $10^{-15}$ mol/mol

# The Phase-2 distillation column 3

Cryogenic distillation is utilized for the XENON1T experiment to remove radioactive contaminants like $^{85}$Kr and $^{222}$Rn inside the xenon. In the first part of this chapter, the design of the XENON1T distillation system based on the McCabe-Thiele method is briefly reviewed. Unless stated otherwise, the following equations and explanations concerning the principle of cryogenic distillation and the McCabe-Thiele method can be found in [62,63]. A more detailed description of the design can be found in [60,61,64]. In the second part, the main components of the system will be briefly introduced. The main focus will be the upgrade from the Phase-1 to the Phase-2 column along with the main improvements. At the end, a short overview about the two slow control systems used in Münster (LabVIEW) and at XENON1T (General Electrics) will be given followed by the integration of the final system within the XENON1T infrastructure.

Parts of this chapter are published in [61] by the XENON collaboration, where Stephan Rosendahl and the author of this thesis are corresponding authors.

## 3.1 McCabe-Thiele design

The principle of cryogenic distillation is based on the difference of vapour pressures of two components in an ideal binary mixture, like krypton or radon in xenon. In a single distillation stage made of a static liquid xenon reservoir in equilibrium with a gaseous phase above, a more volatile contaminant (Krypton) would be enriched in the gaseous xenon phase, while a less volatile contaminant (Radon) would be accumulating in the liquid xenon phase. The enhancement/depletion in the gaseous phase can be described by the relative volatility $\alpha$, deduced from Raoult's law. It is the ratio between the vapour pressure of the noble gas contaminant $P_{\mathrm{ng}}$ and the one of xenon $P_{\mathrm{Xe}}$:

$$\alpha = \frac{P_{\mathrm{ng}}}{P_{\mathrm{Xe}}}. \tag{3.1}$$

Table 3.1 summarizes the relative volatilities of different noble gases like helium, argon, krypton and radon with respect to xenon at a temperature of $-98\,^{\circ}\mathrm{C}$. In a single distillation stage an enhancement of the krypton concentration by a factor of about 10 in the gaseous phase is expected following the concept of relative volatility. This assumption was verified in Münster with the Phase-0 setup: A single-stage distillation system was realized, containing liquid xenon

Table 3.1: Relative volatilities of different noble gases with respect to xenon at −98 °C [30].

| Noble gas | Vapour pressure [bar] | Relative volatility $\alpha$ |
|---|---|---|
| Helium | $\gg 100$ | $\gg 50$ |
| Argon | $\approx 100$ | $\approx 50$ |
| Krypton | 20.9 | 10.4 |
| Xenon | 2.0 | 1 |
| Radon | 0.2 | 0.1 |

with a gaseous phase above. Such a system allowed the investigation of the dynamics of a distillation process in a volume with a single liquid-gas interface and steady state mass flow at very low concentrations of krypton in xenon in the ppq range [59]. This allowed the first measurement of the relative volatility at such low concentrations of krypton in xenon, yielding that $\alpha \approx 10$ is consistent with Raoult's law even at this level of impurity. According to the relative volatility, radon will be enriched in the liquid xenon phase by a factor of $\approx 10$. This was tested and verified in a boil-off experiment, resulting into a depletion factor greater 4 in the gaseous phase depending on the extraction flow [65].

Both cases confirmed that a single distillation setup is not enough to achieve reduction factors of $10^4$ - $10^5$ for krypton nor $10^2$ for radon. Therefore, distillation plants consist of a series of distillation stages to successively reduce the impurities to the desired level.

In the following, the design of a distillation column is presented based on the McCabe-Thiele method [62]. The calculations are applicable for high volatile contaminants such as helium, krypton or argon. In connection to this, a modified McCabe-Thiele approach for the low volatile radon is discussed afterwards. A typical distillation column, as sketched in figure 3.1, features three parts, namely the feeding section, where the raw xenon gas is injected to the tower, the stripping section below, where the more volatile contaminant is depleted and the rectifying section above, where the more volatile contaminant is enriched.

Starting from the reboiler stage in the stripping section, the liquid xenon is evaporated and a gaseous stream flows upwards at a flow rate of $V'$. Assuming that the vapour will condense on Plate 1, the generated liquid phase on this stage will have the same composition as the vapour from the reboiler stage, and will therefore have a higher concentration of the contaminant compared to the starting mixture due to the higher volatility. By repeating this procedure for several stages, the fraction of the contaminant in the xenon will successively increase. On top of the tower, the concentration is at its maximum. While most of the vapour is partially liquefied with the help of the re-condenser and fed back to the column with a flow rate $L$, a small fraction of the gas is removed as enriched off-gas at a flow rate $D$. In contrast, the impurity is lowest at the bottom inside the reboiler, where the purified xenon is extracted with a flow rate $B$. Such an operation with a partial reflux is called rectification. The stripping section and the rectifying section are connected by the feeding section, where xenon is injected at a flow rate $F$. It is added to either the up-streaming vapour

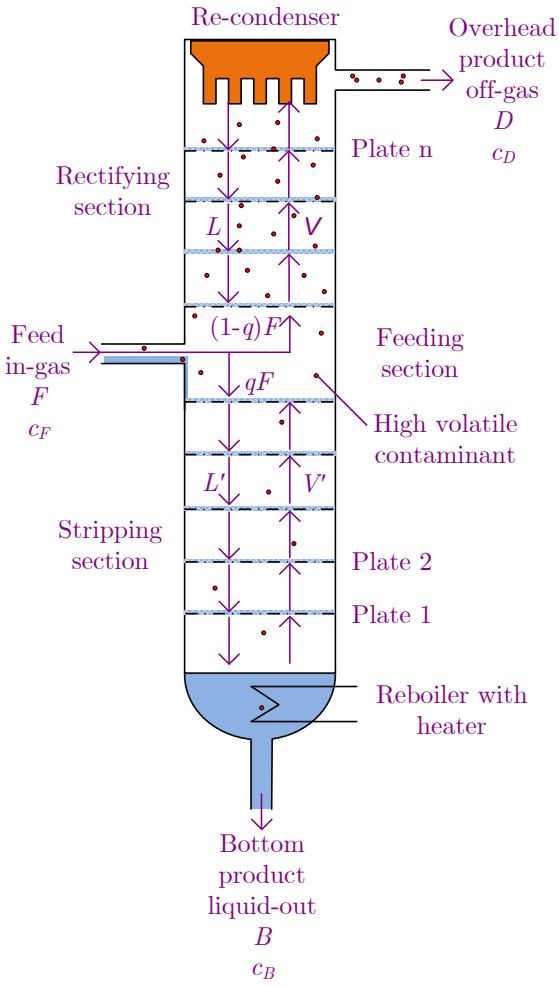


Figure 3.1: **Distillation column with partial reflux:** In this diagram, the typical construction of a distillation column using several distillation plates and partial reflux is shown. It consists of three parts, the stripping section, the feeding section and the rectifying section. $L$ and $L'$ are the down-going liquid streams while $V$ and $V'$ are the up-going gaseous streams in the different parts. Both are connected to the feeding stream $F$. The enriched off-gas stream $D$ is extracted from the top, while the purified xenon is extracted from the bottom with a flow rate $B$. The concentrations of the more volatile noble gas inside the xenon of the feed and the two extraction flows are given by $c_F$, $c_D$ and $c_B$, while $q$ defines the state of matter of the injected xenon. Figure and caption based on [61].

$V$ in the rectifying section or to the down-streaming liquid flow $L'$. This depends on the state of the injected matter (gaseous or liquid), denoted by the caloric factor

$$q = (L' - L)/F. \tag{3.2}$$

For the following calculations a saturated liquid feed at the boiling point ($q = 1$) is assumed. As consequence, the injected xenon is added to the down-streaming

liquid flow $L'$. Depending on the requested xenon purity at the bottom (purified xenon, liquid-out) and at the top (enriched xenon, off-gas) the number of theoretical plates[1] $n_{\mathrm{TP}}$ can be determined using the McCabe-Thiele method [62]. In this method, the concentrations of the more volatile noble gas in the gaseous xenon phase ($y_{\mathrm{ng}}$) and in the liquid xenon phase ($x_{\mathrm{ng}}$) are plotted against each other in an equilibrium diagram.

For constant temperature and pressure, the system drifts to equilibrium based on the concept of vapour pressure as described above. For each local concentration $x_{\mathrm{ng}} = 1 - x_{\mathrm{Xe}}$ of the contaminant in the liquid phase, there is a certain equilibrium concentration $y_{\mathrm{ng}}$ in the vapour phase. For very low concentrations with $x_{\mathrm{ng}} \cdot (\alpha - 1) \ll 1$ this relation can be expressed by

$$y_{\mathrm{ng}} = \frac{P_{\mathrm{ng}} \cdot x_{\mathrm{ng}}}{P_{\mathrm{ng}} \cdot x_{\mathrm{ng}} + P_{\mathrm{Xe}} \cdot x_{\mathrm{Xe}}} \tag{3.3}$$

$$= \frac{\alpha \cdot x_{\mathrm{ng}}}{1 + (\alpha - 1) \cdot x_{\mathrm{ng}}} \tag{3.4}$$

$$\approx \alpha \cdot x_{\mathrm{ng}}, \tag{3.5}$$

and is called equilibrium line.

By heating from the bottom and cooling from the top, upward gaseous and downward liquid flows are introduced to the column and as consequence, the equilibrium inside the system is disturbed due to the mass flow. As a result of that, the actual concentration of the contaminant in the gaseous phase related to the concentration in the liquid phase is described by operation lines for each of the three sections. Between the equilibrium line and operation lines a forcing concentration gradient is ensured, driving the system toward the equilibrium via mass transfer between the ascended gaseous stream and the descended liquid stream.

During stable operation, the incoming feed flow $F$ requires to be equal to both outgoing flows $B$ and $D$ yielding the total mass balance

$$F = D + B. \tag{3.6}$$

Combining the flows with the different concentrations of the more volatile noble gas inside the xenon in the feed $c_F$, in the off-gas $c_D$ and in the liquid-out $c_B$, equation (3.6) can be expressed in terms of the number of contaminant atoms

$$F \cdot c_F = D \cdot c_D + B \cdot c_B. \tag{3.7}$$

The amount of xenon that is fed back at the top as liquid with respect to the outgoing flux $D$ is defined as the reflux ratio. In the same manner, a second ratio can be found at the bottom:

$$R = \frac{L}{D} \qquad \text{and} \qquad R' = \frac{L'}{B}. \tag{3.8}$$

A high reflux ratio $R$ is mandatory for a high separation performance. For the XENON100 column as well as the XMASS column [58] a ratio of $R = 191$

[1] One theoretical plate equals one distillation stage.

worked well for krypton removal and was not the limiting factor in terms of separation efficiency. For this reason, the same ratio was chosen for the initial design calculations of the XENON1T system. For comparison, in industrially used distillation plants, reflux ratios $< 10$ will be found. Otherwise the costs of energy and operation would be uneconomical.

For each of the three sections in the system, a particle balance can be formulated using the respective flows in the sections. From these, the three operation lines can be obtained:

$$\text{Stripping line:} \qquad y_{\text{ng}} = \frac{R'}{R'-1} \cdot x_{\text{ng}} - \frac{c_B}{R'-1} \tag{3.9}$$

$$\text{Rectiying line:} \qquad y_{\text{ng}} = \frac{R}{R+1} \cdot x_{\text{ng}} + \frac{c_D}{R+1} \tag{3.10}$$

$$\text{Feeding line:} \qquad y_{\text{ng}} = \frac{q}{q-1} \cdot x_{\text{ng}} - \frac{c_F}{q-1}. \tag{3.11}$$

A complete derivation of the formulas above can be found in [60, 64].

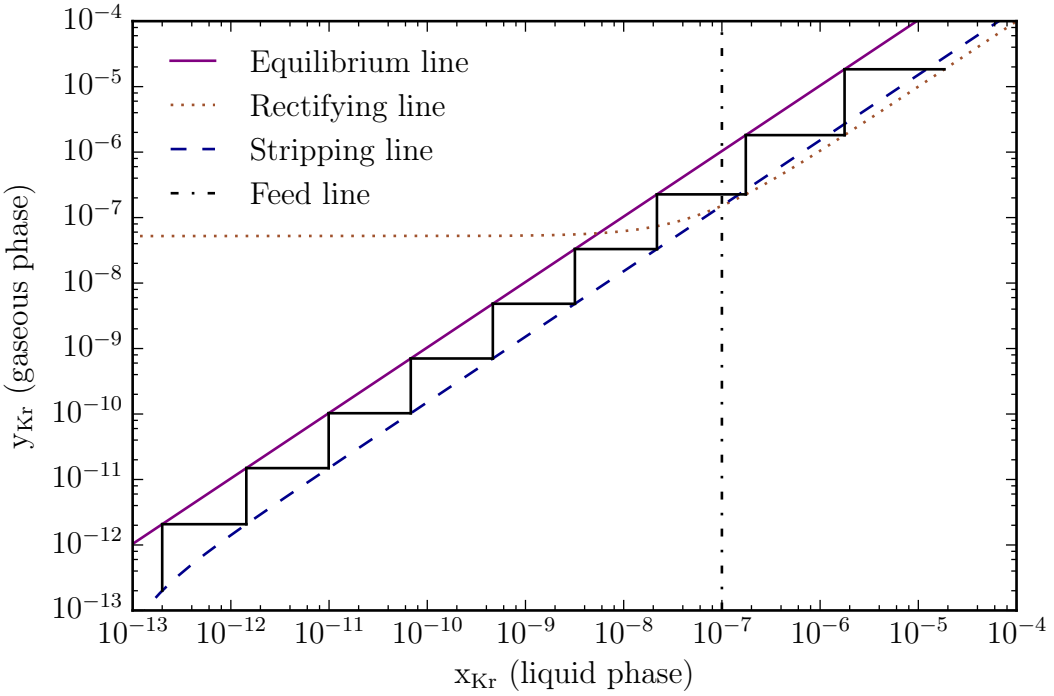


Figure 3.2: **McCabe-Thiele diagram for the XENON1T requirements:** The concentration of the krypton in the gas phase $y_{\text{Kr}}$ in relation to the concentration in the liquid phase $x_{\text{Kr}}$ is visualized. The equilibrium line (solid purple line) as well as the operation lines for the different sections, namely rectifying (blue dashed line), stripping (brown dotted line) and feed line (black dash-dotted line) of the column are drawn and allow for the determination of the number of theoretical stages (black solid line) needed to meet the XENON1T requirements. Figure and caption based on [61].

In figure 3.2, the McCabe-Thiele diagram for the XENON1T krypton distillation column for a saturated liquid feed ($q = 1$) with a flow rate of $F = 3\,\text{kg/h}$

and an input concentration of $c_F = 100\,\text{ppb}$ is visualized. Since the off-gas rate was fixed to maximal 1 % of the feed flow, it follows $D = 0.03\,\text{kg/h}$ and thus $B = 2.97\,\text{kg/h}$. With equation (3.6) and equation (3.7) and with the required krypton in xenon concentration of XENON1T of $c_B = 200\,\text{ppq}$, the off-gas concentration can be calculated to be $c_D = 10\,\text{ppm}$. With equation (3.5) to equation (3.11) all flows and concentrations for $q = 1$ can be derived:

$$\begin{array}{lll} F = 3\,\text{kg/h} & B = 2.97\,\text{kg/h} & D = 0.03\,\text{kg/h} \\ c_F = 100\,\text{ppb} & c_B = 200\,\text{ppq} & c_D = 10\,\text{ppm} \\ R = 191 & L = 5.73\,\text{kg/h} & V = 5.76\,\text{kg/h} \\ R' = 2.94 & L' = 8.73\,\text{kg/h} & V' = 5.76\,\text{kg/h} \end{array} \tag{3.12}$$

The equilibrium line is drawn as solid purple line in figure 3.2. The stripping section, valid for the bottom part of the column, is depicted as the blue dashed line and the rectifying line, valid for the top part, is indicated as brown dotted line. The feeding line describes the intersection between the other two operation lines and simplifies to a vertical line for a liquid feed with $q = 1$ as shown by the black dash dotted line. The number of black steps in the diagram indicates the number of theoretical stages and can be determined by taking the liquefaction processes and the related vapour compositions into account. A liquid mixture with the krypton content $x_{\text{Kr}}$ features a vapour phase with an enhanced krypton concentration $y_{\text{Kr}}$, which is streaming up to the next stage (vertical line) where it gets liquefied again (horizontal line).

In total, 9 theoretical distillation stages can be drawn for a saturated liquid feed to achieve a reduction factor of $\sim 10^4 - 10^5$. This allows to purify xenon with the highest commercially available purity (∼ppm) in a single pass through the column. For a saturated vapour feed ($q = 0$), the diagram changes slightly and 10 stages are required to reach the same separation. This can be found in [60, 64].

From the experimental point of view, a series of multiple connected single distillation stages is not practical. For this reason, a structured package material (Laboratory package, type EX, Sulzer AG) inside a package tube is utilized, featuring a large surface for good liquid-gas exchange through the full height of the tower. The effective exchange is equivalent to a certain number of theoretical single distillation stages. This height-equivalent of one theoretical plate (HETP) denotes the amount of required package material to realize one distillation stage. Together with the number of plates $n_{\text{TP}}$ derived from the McCabe-Thiele diagram, the total height $h$ of the package tube can be calculated:

$$h = \text{HETP} \cdot n_{\text{TP}}. \tag{3.13}$$

The HETP-value is determined empirically based on a standard mixture, typically such as Benzene/Toluene at concentrations at least in the percentage range, and varies for different gas compositions and system parameters. Typical values for the Sulzer EX package type are (2 - 8) cm [66]. Furthermore, the partial pressure of krypton in the injected krypton-xenon mixture is very low, due to its low feed concentration $c_F \sim 100\,\text{ppb}$. The investigations on the single-stage distillation setup (Phase-0) confirmed the separation process on the ppq

scale for krypton and xenon to be in agreement with the expectations from the relative volatility [59]. However, for this concentration regime the McCabe-Thiele approach was not validated for larger distillation plants. Due to these uncertainties it was decided to first realize a smaller distillation column, using 1 m of package material (Phase-1 column) [60, 64] and increase the amount of material afterwards, if needed (Phase-2 column). The HETP value was measured to be in the range of (9.2 - 24) cm using the Phase-1 column, being much higher than derived from the standard mixtures [60].

### Low volatile contaminant radon

Radon as the less volatile noble gas compared to xenon is enriched in the liquid xenon phase and thus in the reboiler in the bottom part of the distillation plant. The idea of radon removal by cryogenic distillation is based on trapping $^{222}$Rn in the liquid xenon reservoir until disintegration. This is possible due to its comparable short half-life of $T_{1/2} = 3.8\,\text{days}$. As consequence, there is no extraction of enriched xenon at the bottom ($B = 0$) of the system as it is the case for krypton and thus radon removal is a xenon-loss free operation. Consequently, the xenon flow mass balance is given by

$$F = D. \tag{3.14}$$

While the relation of the equilibrium line stays the same (equation (3.5)), but with $\alpha = 0.1$ as shown in table 3.1, the total particle balance as presented in equation (3.7) has to be modified:

$$F \cdot c_F = D \cdot c_D + \cancel{B \cdot c_B} + c_B \cdot \lambda_{\text{Rn}} \cdot M_{\text{Xe,reboiler}}. \tag{3.15}$$

Here, $\lambda_{\text{Rn}} = 7.55 \times 10^{-3}\,\text{h}^{-1}$ denotes the decay constant of $^{222}$Rn and $M_{\text{Xe,reboiler}}$ is the mass of xenon inside the reboiler. The last term effectively describes an out-going mass flow of radon particles from the system by decay and is the equivalent to the out-going mass flow $c_B \cdot B$ in the krypton case. The decay of radon particles in the other parts of the distillation system can be neglected due to the short residence time compared to the decay time.

When fixing $F$, $c_F$, and $c_D$ by design, the mass of radon particles in the reboiler $c_B \cdot M_{\text{Xe,reboiler}}$ requires to be calculated with above formulas in order to conserve the particle mass balance:

$$c_B \cdot M_{\text{Xe,reboiler}} = \frac{c_F \cdot F - c_D \cdot D}{\lambda_{\text{Rn}}}. \tag{3.16}$$

For the calculation of the McCabe-Thiele diagram, either the concentration $c_B$ or the mass in the reboiler $M_{\text{Xe,reboiler}}$ has to be fixed.

While the definition of the reflux ratio in equation (3.8) at the top of the system does not change, the ratio at the bottom becomes infinity due to $B = 0$. As consequence, the rectifying (equation (3.10)) and feed (equation (3.11)) lines are the same as in the krypton case, but the stripping line has to be changed to

$$\text{Stripping line:} \qquad y_{\text{Rn}} = x_{\text{Rn}} - \frac{c_B \cdot \lambda_{\text{Rn}} \cdot M_{\text{Xe,reboiler}}}{L'}. \tag{3.17}$$

In the following, a McCabe-Thiele diagram for a possible radon distillation column for XENONnT is discussed. The motivation on how to choose the design parameters is presented in chapter 7. A high feed flow of $F = 72\,\mathrm{kg/h}$ is required with a feed concentration of $c_F = 1.04 \times 10^{-24}\,\mathrm{mol/mol}$ corresponding to a radon activity of $10\,\mu\mathrm{Bq}$ per kilogram xenon. With a desired depletion of a factor 100 at the top and an enrichment of a factor 1000 at the bottom with respect to the feed concentration, follows $c_D = 1.04 \times 10^{-26}\,\mathrm{mol/mol}$ and $c_B = 1.04 \times 10^{-21}\,\mathrm{mol/mol}$. The reflux ratio $R$ determines the amount of xenon that needs to be re-liquefied and send back to the column and is therefore directly proportional to the required cooling power at the top condenser. For high purification flows and large $R$, this cooling can start to become an issue. Therefore, a minimal reflux ratio $R_{\mathrm{min}}$ has to be estimated for the radon column design to minimize the needed cooling power. The Underwood equation can be utilized to calculate the reflux ratio that results in the operation line with minimal slope:

$$R_{\mathrm{min}} = \frac{1}{\alpha - 1} \cdot \left( \frac{c_D}{c_F} - \alpha \cdot \left( \frac{1 - c_D}{1 - c_F} \right) \right) = 0.1 \tag{3.18}$$

Several McCabe-Thiele diagrams for a liquid feed ($q = 1$) and the given concentrations above were constructed with varying reflux ratios starting with $R = 0.05$ up to $R = 5$. For $R < 0.1$ no diagrams can be constructed since the rectifying line starts to go below the equilibrium line and no stages can be drawn anymore. This is in agreement with the calculated $R_{\mathrm{min}}$ from the Underwood equation. For $R = 0.11$ a total number of 16 stages is required to meet the desired purity level. The number of stages decreases with increasing $R$ up to $R = 0.5$. Here, 7 theoretical stages can be drawn. With further increase of the reflux, the number of stages can be reduced to 6 for $R = 5.0$. The reduction by one stage between $R = 0.5$ and $R = 5.0$ would require a ten times higher cooling power. Therefore, a reflux ratio of $R = 0.5$ was chosen for the design. All other required parameters to create the diagram for the chosen reflux ratio are presented in the following:

$$\begin{aligned}
F &= 72.0\,\mathrm{kg/h} & B &= 0.0\,\mathrm{kg/h} & D &= 72.0\,\mathrm{kg/h} \\
c_F &= 1.04 \times 10^{-24} & c_B &= 1.04 \times 10^{-21} & c_D &= 1.04 \times 10^{-26} \\
R &= 0.5 & L &= 36.0\,\mathrm{kg/h} & V &= 108.0\,\mathrm{kg/h} \\
R' &= \infty & L' &= 108.0\,\mathrm{kg/h} & V' &= 108.0\,\mathrm{kg/h} \\
M_{\mathrm{Xe,reboiler}} &= 9.4\,\mathrm{kg}.
\end{aligned} \tag{3.19}$$

The resulting McCabe-Thiele diagram is visualized in figure 3.3. The solid purple equilibrium line in contrast to the case of krypton is below the operation lines due to $\alpha = 0.1$. The stripping line from the bottom part, where in this case radon is enriched, is indicated by the blue dashed line, while the rectifying line from the top, where radon is depleted, is drawn as brown dotted line. The operation lines are intersected by the black dash dotted feed line, which is a vertical line due to $q = 1$. In contrast to krypton, the concentration $c_B$ in the liquid, visualized for better understanding by the green dotted vertical line, is located at the right border of the diagram. The concentration $c_D$ in the gas,

drawn as red dotted horizontal line, is located at the left border. Consequently, the bottom of the distillation column corresponds to the right and the top to the left part of the diagram. In total, 7 theoretical distillation stages can be drawn, where 3 stages below and 4 stages above the feed section are required to achieve the desired enrichment and depletion factors of 1000 and 100, respectively. The height of the distillation tower can be calculated from the HETP value as in the case of krypton. However, this value is rather unknown so far for radon in xenon. This will be estimated from distillation tests at XENON100 in chapter 7 within this thesis. Additionally, one should be conservative when choosing the final height of the package material to allow some safety margin.

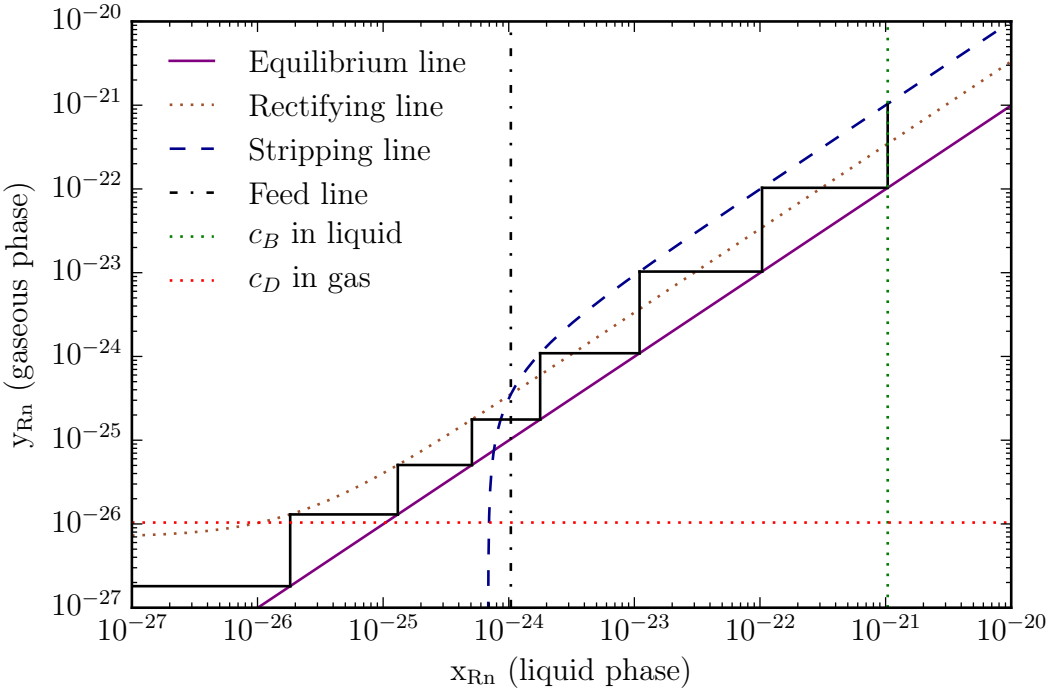


Figure 3.3: **McCabe-Thiele diagram for a possible radon distillation system with R = 0.5:** The solid purple equilibrium line is below the stripping line, visualized by the blue dashed line, and the rectifying line, drawn as brown dotted line. The operation lines are intersected by the black dash dotted feed line, which is a vertical line due to $q = 1$. The green dotted vertical line represents the concentration $c_B$, while the red dotted horizontal line gives the concentration $c_D$. The bottom of the column corresponds to the right and the top of the system to the left part of the diagram.

## 3.2 Experimental setup

The experimental setup of the Phase-2 distillation plant as depicted in figure 3.4 is presented in this section. The reboiler, containing the liquid xenon reservoir, and the input condenser, which liquefies the incoming raw xenon, are located in the bottom of the system. The inlet pipe of the raw xenon and the outlet pipe of the purified xenon are connected by a plate heat exchanger in order to cool down the warm raw xenon gas using the cold purified xenon gas. The package tube in the middle, housing the large surface structured package material, is connected to the reboiler at the bottom and to the top condenser at the top, which re-liquefies up-streaming xenon to allow for a high reflux ratio. Additionally, the krypton-enriched xenon is partially extracted at the top. From the input condenser, the xenon can be fed either in liquid-only form, in gas-only form or in both forms simultaneously at different heights to the package tube. Everything is housed inside an evacuated outer vessel structure in order to avoid any heat losses and freezing of water on the main components outer surfaces. The inlet flow as well as the purified outlet flow are regulated by flow controllers (1479B, MKS Instruments) allowing flows up to 20 slpm. The off-gas line of the Phase-2 plant is equipped with two flow controllers (1479B, MKS Instruments) in parallel with a maximum flow rate of 0.1 slpm and 10 slpm, respectively.

In general, all parts such as gas routing pipes or the vessels of both condensers and reboiler were either made from electro-polished stainless steel (alloy 316L and 316LN) or from oxygen-free, high conductivity (OFHC) copper in order to guarantee a high xenon purity. The components were connected by metal-to-metal sealed VCR connections or CF flanges, while the fittings for the VCR connections were orbitally welded to the pipes to achieve optimal leak-tightness and clean weld seams. Welding examples can be found in [60]. In addition, the package material as well as all other components made from stainless steel were cleaned in an ultrasonic bath, using a special cleaning agent (Henkel, P3 Almeco 36) and deionized water. The copper was cleaned using citric acid and deionized water in an ultrasonic bath. The package tube was assembled in a clean-room (ISO 14644-7) to avoid any contamination after the cleaning procedure. Before filling the column with xenon, the system can be evacuated and baked out. The package tube can be baked to 100 °C with a heating tape mounted to the tube inside the insulation vacuum vessel, while other components of the setup e.g., the cryo coolers, only withstand a maximum heating of 50 °C. After the bake-out, gaseous xenon can be circulated through the column and a hot metal getter (SAES, PS4-MT15-R-2) in a closed loop to further reduce remaining impurities. In the following, the four main components including their upgrades are presented. While the reboiler stayed the same as in Phase-1, the package tube was enlarged from about 1 m to about 2.8 m. In addition, both condensers were slightly modified for higher gas collection efficiencies.

### Reboiler: Liquid xenon reservoir

The reboiler is located at the bottom of the distillation plant, housing the high purity liquid xenon as visualized in figure 3.5. It is made of a cylindrical stainless steel vessel closed on both sides with CF flanges with a diameter of 250 mm and

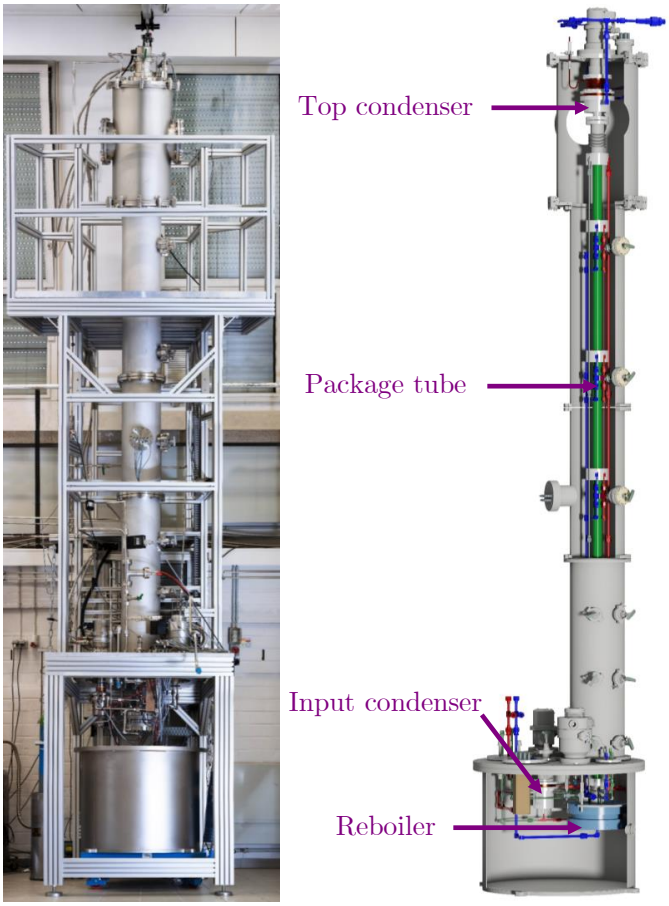


Figure 3.4: **Phase-2 setup during commissioning at WWU Münster:** The final height is about 5.5 m. The system was transferred and remounted at the underground laboratory LNGS in Italy. Figure and caption from [61].

a height of 75 mm. This translates into a maximum storage of up to 31 of liquid xenon. The bottom of the vessel is funnel-shaped in order to drain liquid xenon more efficient into the outlet pipe, which is connected to the heat exchanger.

While the top flange is connected to the package tube, the vessel itself is fixed by four rods to the insulation vessel. By slightly varying the height of these rods, the alignment of the package tube can be optimized. This is necessary to allow an equally distribution of the down-rinsing liquid xenon inside the tube. This feature especially becomes of crucial importance for the Phase-2 compared to the Phase-1 due to the longer package tube .

The temperature in this location is measured via a silicon diode (DT-670D-CU, Lakeshore) and in addition, via a PT1000 sensor as coverage. In order to evaporate some xenon to guarantee a counter gaseous flow to the down-going liquid flow as described in section 3.1, 2×2 heater cartridges of 150 W each are installed inside the bottom flange, where one pair is actively heating and one pair is used as backup.

The liquid xenon level can be measured in two redundant ways: Four PT1000 temperature sensors are installed at different heights inside the vessel, which change temperature when touching the liquid xenon. In addition, the differential

pressure inside the reboiler between two pipes that are guided into the vessel is measured. One stops at the top and one towers to the bottom as depicted by the yellow pipes in figure 3.5. Depending on the liquid level, the hydrostatic pressure will change and thus the differential pressure. More details on the calibration of the liquid level can be found in [64].

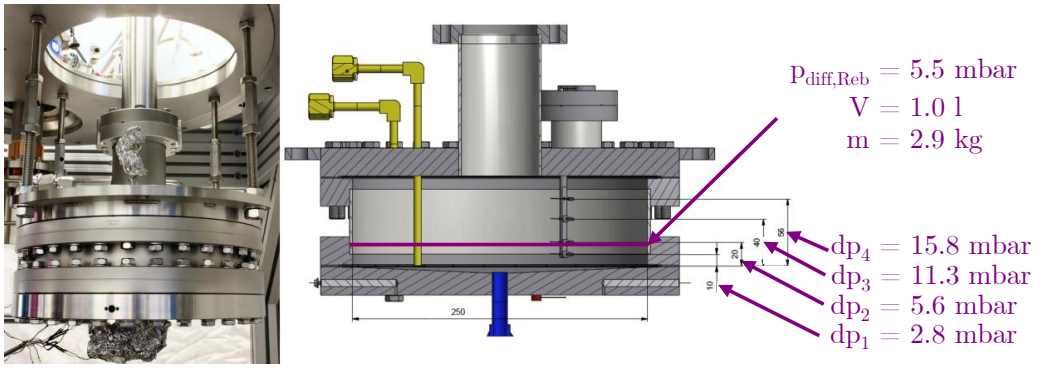


Figure 3.5: **Reboiler, housing the liquid xenon reservoir:** On the left picture, the mounted reboiler is shown. On the right, a technical drawing is skeched, indicating the determination of the liquid level inside the reboiler using the differential pressure as well as the PT1000 method. Figure taken from [64]

.

## Package tube: Large surface

In order to provide a large surface for an enhanced separation, structured package material (Laboratory package, type EX, Sulzer AG) is utilized, featuring a surface of 1500 $m^2/m^3$ [66]. The package tube of the Phase-1 column, consisting of four tubes with a diameter of 44.3 mm and a height of 300 mm each, was enlarged by three additional pieces with same diameter, two with a length of 590 mm and one with a length of 650 mm. In total, 51 pieces of package material with a diameter of 39 mm and a height of 53 mm each were stacked into the tubes. Each piece was rotated by 90° with respect to the previous one, resulting in a height of 2703 mm of package. This resulted into a surface of 4.8 $m^2$. The new tube segments as well as the package material are pictured in figure 3.6. The seven segments are connected via special-made CF flanges that each feature a feed and diagnostic port. In addition, at each connection, a PT1000 sensor is installed in order to monitor the temperature along the tube. This is important during the cooling process of the package while filling and to verify stable operation during distillation.

One pipe connects the top feed port to the gas outlet of the input condenser, which is used for the gaseous feed, while another pipe connects the rest of the six possible liquid feed ports at different heights to the liquid-out line of the input condenser. These feed ports can also be used as gaseous feeds. In contrast to the Phase-1 system, all feed ports valves are equipped with potentiometers (Hybritron 3541H-I-102 L, 1 kOhm, Mexico Bourns) to read-out the position of the valve during operation. The valve design was based on the custom-made

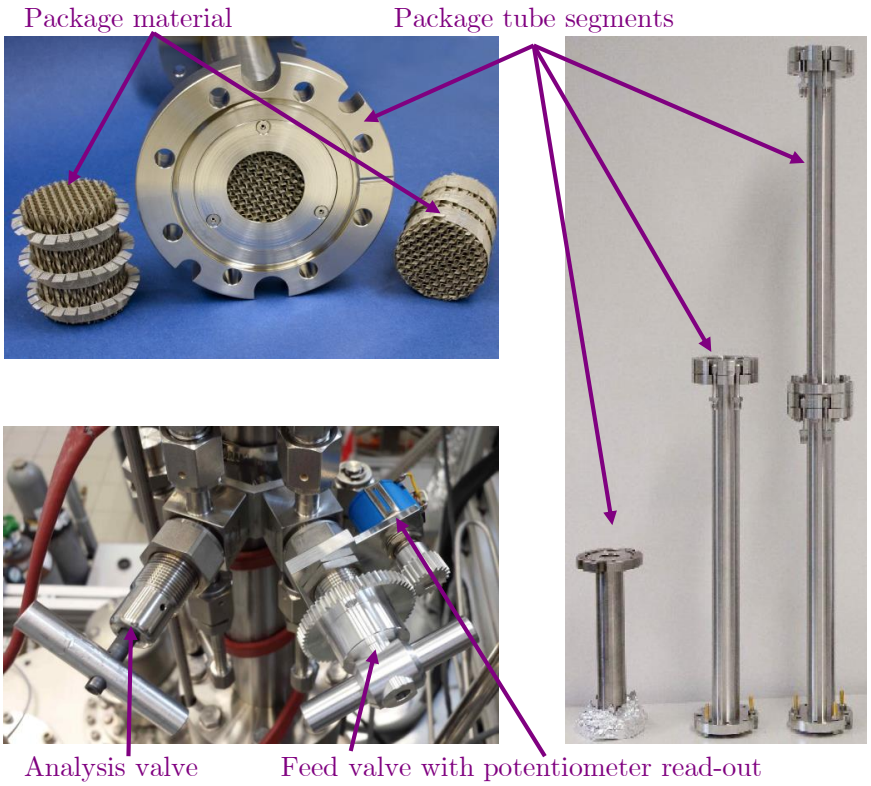


Figure 3.6: **Package tube:** Top left: Two pieces of the package material are shown along with a filled package segment. Bottom left: A pair of analysis and feed valve with the new potentiometer read-out are displayed. Right: The new package tube segments after assembly in the clean-room are pictured.

cold valve of the gaseous feed line in Phase-1 as described in [60, 64]. A picture is shown in figure 3.6. The top analysis port is linked via an additional pipe to the reboiler in order to measure the differential pressure along the whole column with a differential pressure sensor (221B Baratron, MKS Instruments). A fourth pipe connects six diagnostic ports to a feed-through port of the insulation vessel flange. This pipe can provide gas samples during the distillation process and allows the measurement of the separation performance online by an RGA (see section 4.2). For the Phase-2 system, capillaries with a diameter of 1 mm and a length of 5 mm were integrated into the analysis valves. This was the smallest possible size to be machined in our workshop. The idea was to reduce the gas velocity during extraction of the gas sample and thus to not disturb the krypton concentration at different heights of the column during operation as well as the extraction of reproducible samples. This was investigated in [67] and it was found that the holes in the capillaries were still too big.

Two heating belts are wrapped around the package tube giving the possibility of a bake-out of up to 100 °C before starting the filling process.

A stainless steel bellow (NG 75/10, 6 bar max inner pressure at −100 °C, SKODOCK group) is installed between package tube and top condenser in order to compensate the shrinking of the stainless steel tube and slight miss-alignment of the their position to each other, when cooling from room temperature to liquid

xenon temperatures of about −100 °C.

## Top condenser: Liquefaction of xenon

The cooling tower at the top of the system, referred to as top condenser, allows to liquefy up-streaming gaseous xenon in order to create a reflux of down-rinsing liquid xenon, fed back to the package tube. The funnel-shaped stainless steel vessel with a diameter of 125 mm and a height of 66 mm is connected to a Gifford-McMahon (GM)-type refrigerator (CP 140T, Leybold) over a lamellar structured piece of OFHC copper. The copper block is utilized as a gasket at the same time. The cooling fins enlarge the surface of the condensation of the incoming xenon. While the available cooling power at liquid xenon temperatures for the Phase-1 system was measured to be around 210 W [64], the cooling power at this temperature range after assembly of the Phase-2 was about 6 % lower due to the higher heat load from a longer package tube. A detailed investigation can be found in [67]. In addition, a spiral copper pipe linked to the copper block as shown in figure 3.7 provides the possibility of additional cooling by liquid nitrogen and was successfully tested in [60], but was not required to reach stable operation of the Phase-1 and Phase-2 columns.

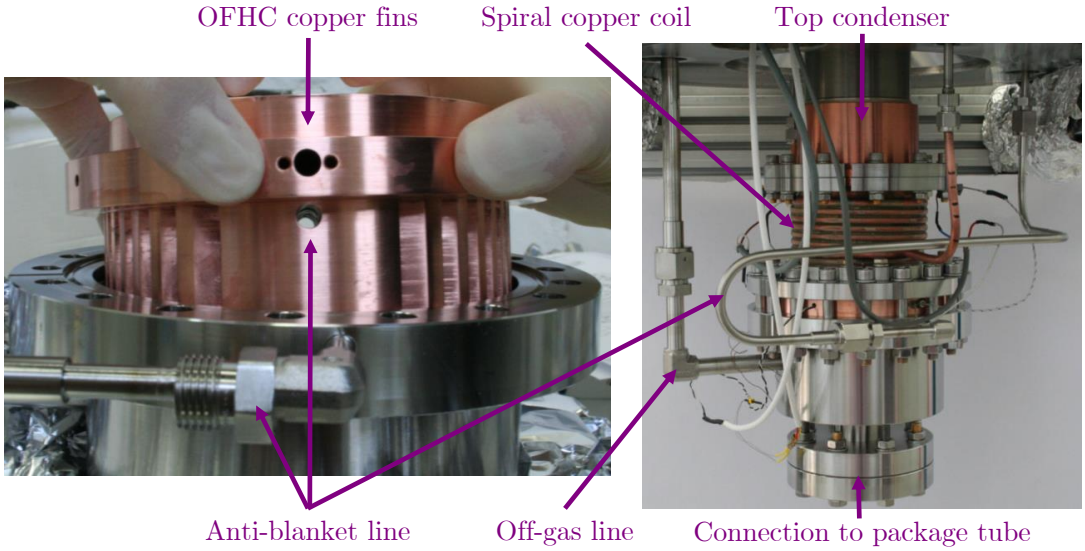


Figure 3.7: **Upgrade of top condenser:** Left: Modified copper fins with hole to avoid blanket effect. Right: Mounted top condenser with new anti-blanket effect line.

For the temperature monitoring and the cooling power control, a Si-diode (DT-670D-DI, Lakeshore) is installed to the copper along with 2×2 heater cartridges of 150 W each, where one of the pair is used for heating and one pair is used as backup.

At the top, the vessel features a port for the extraction of the krypton-enriched xenon gas as off-gas. For the initial top condenser of Phase-1, it turned out that the position of the extraction port at the vessel is not optimal and lead to the so-called blanket effect [60], when processing raw xenon with high impurities such as helium, argon, oxygen and nitrogen: A distillation run, processing

xenon off-gas from previous tests with the Phase-1 column, is visualized in figure 3.8. While the column pressure (figure 3.8 bottom) increased after the start of the distillation process, the temperature, measured in the copper at the top condenser, (figure 3.8 top) was decreasing. This phenomenon cannot be explained by thermodynamics since temperature and pressure in the system are correlated, but can be explained by the high amount of contaminants inside the xenon itself. Since lighter gases as helium, argon, oxygen or nitrogen are also accumulating at the top of the system, a layer of these contaminats can cover the copper fins of the condenser. Thus, the cooling power of the cold-head cannot be efficiently transferred to the xenon gas anymore, indicated by the decrease in temperature while the pressure increased. As consequence, the distillation process was forced to be stopped. All details are presented in [60].

By drilling a horizontal hole in the copper fins and move the extraction port of the condenser vessel to the top of the vessel as pictured in figure 3.7, these layers of lighter gases can be removed efficiently. In order to enhance this collection efficiency, an additional flow controller (10 slpm, 1479B, MKS Instruments, normally-open for safety reasons) was installed in parallel to the existing off-gas flow controller allowing for extraction flows of up to 10 slpm. This vessel modification was also applied to the input condenser as the same phenomenon was expected in this part as well.

During commissioning in Münster as well as at LNGS, highly contaminated xenon was distilled several times. In one distillation run after the commissioning of the Phase-2 column at LNGS, xenon with a $O_2$/Ar concentration of about 1300 ppm ($O_2$ and Ar cannot be distinguished by the gas chromatograph used [68, 69]) and a $N_2$ concentration of about 2600 ppm were successfully processed [68]. The extraction flow of the off-gas was increased from 1 % to 10 % to reach a thermodynamically stable operation.

These studies indicate that the modifications of the gas collection in both input and top condenser were successful and enable the processing of xenon with a high content of impurities other than krypton. Furthermore, this allows the XENON collaboration to purchase higher contaminated xenon, reducing significantly the price for the target material. This is important as the major cost of XENON1T and the upcoming XENONnT originates from the xenon acquirement.

## Input condenser: Liquefaction and pre-separation stage

The second cooling tower in the system, the input condenser, also referred to as pre-separator, is located in the bottom of the distillation plant and features the same design as the top condenser. The smaller funnel-shaped vessel (d = 100 mm, h = 93mm) is linked to a smaller refrigerator (CP 50, Leybold) as shown in figure 3.9. Again, the temperature in this location is measured via a silicon diode (DT-670D-CU, Lakeshore). The condenser provides around 95 W cooling power at a temperature of −100 °C. Measurements of the available cooling power for different temperatures after assembly of Phase-2 can be found in [67]. A cooling power of 94.3 W is required to provide a fully liquid feed at a flow rate of 3 kg/h. In order to allow also higher distillation speeds, the inlet line containing the warm xenon and the return line containing the cold purified xenon from the

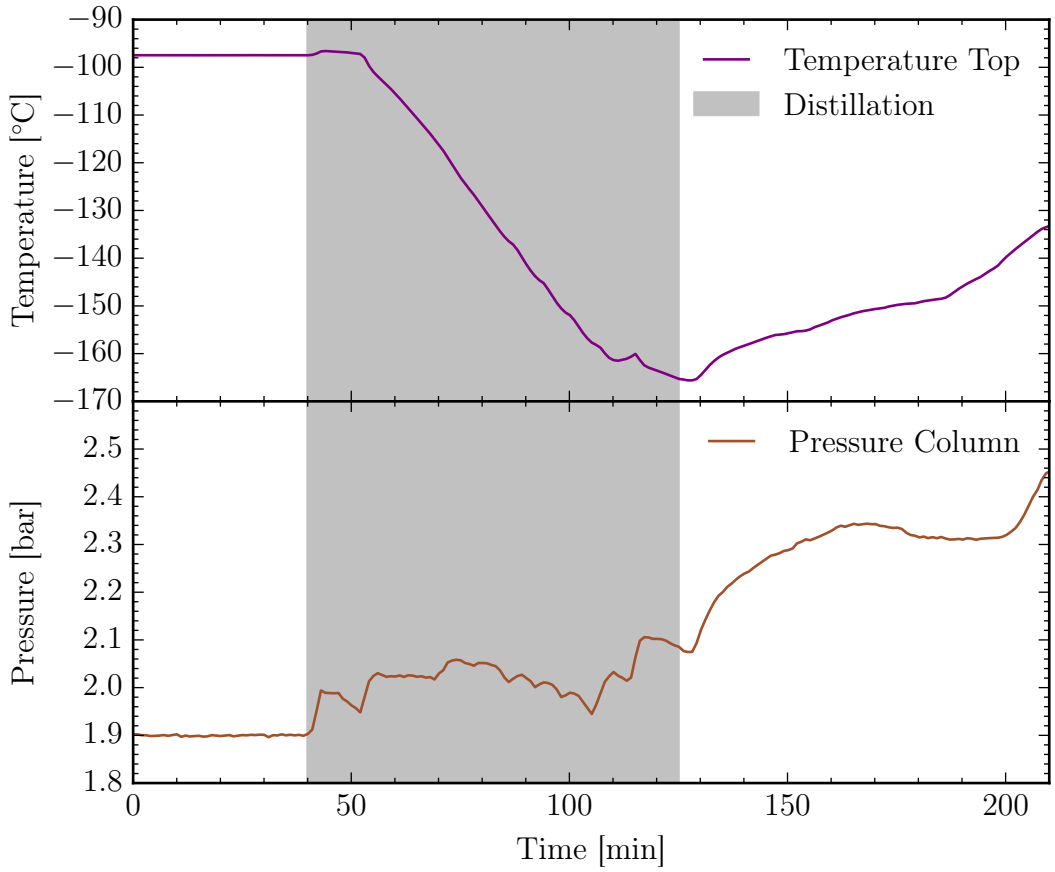


Figure 3.8: **Blanket effect:** Top: Temperature at top condenser. Bottom: Pressure inside the column. The temperature decreased drastically during a distillation operation with the Phase-1 system processing highly contaminated xenon, while the pressure even slightly increased. This hints towards a blanket of lighter gases covering the copper fins, reducing the effective cooling power. Data from [60].

reboiler are connected to a plate heat exchanger as mentioned above (GEA Wtt GBS 100M-20R). Like that, a gaseous and liquid feed can be provided by the combination of the heat exchanger and the cooling tower.

By extracting a fraction of the incoming xenon as gas and feed it directly to the top of the column, while the rest is liquefied in the input condenser, a first separation between krypton and xenon is achieved. Therefore, the input condenser can be employed as a first distillation stage and is called pre-separator as a result. A hole was drilled horizontally into the copper fins and the extraction port was moved to the most possible height of the vessel, similar to the top condenser, in order to avoid any blanket effect and ensure stable operation over a long-term distillation run. The gas flow is controlled by a custom-made cold valve, same as the analysis and feed valves, giving the possibility to read the actual position via a potentiometer. A detailed investigation about the flow coefficiencies for different valve positions can be found in [64]. In order to inject the liquid xenon from the input condenser into the package tube via one of the six possible feed positions, an over-pressure needs to be established between

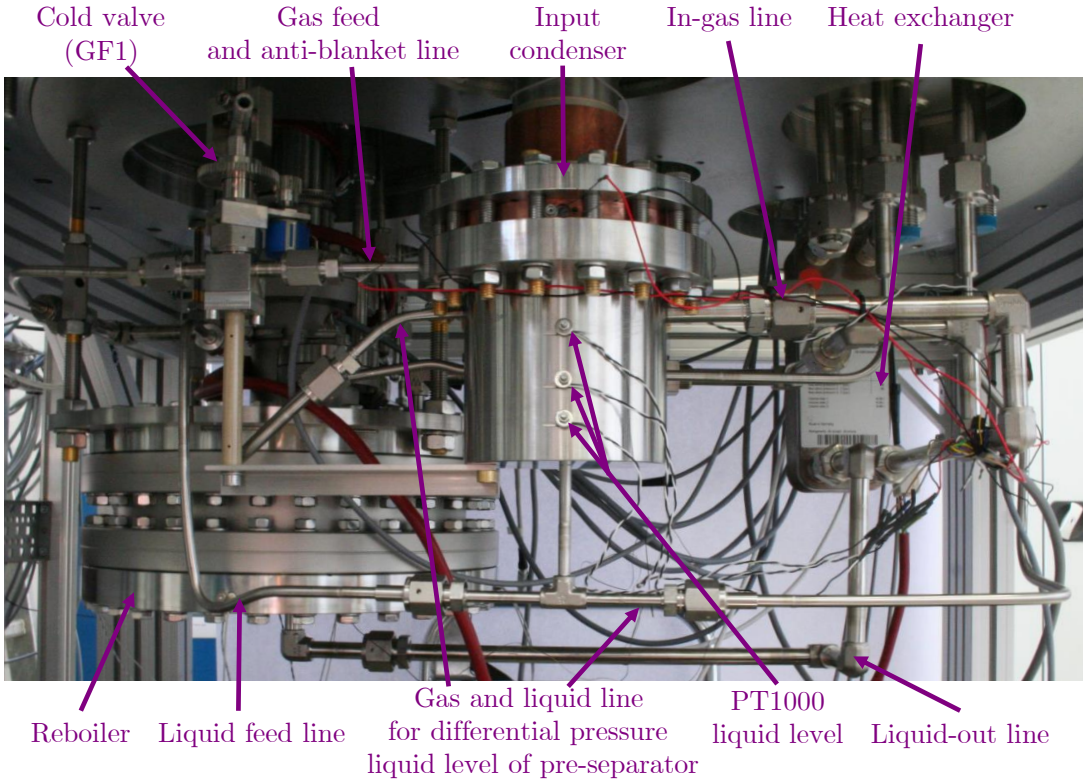


Figure 3.9: **Bottom part of the distillation system:** The heat exchanger, reboiler and input condenser are pictured along with several feed pipes.

pre-separator and tube, depending on the height of the respective feed.

For the Phase-1 system, the liquid level inside the pre-separator was determined using three PT1000 sensors connected to the outside of the vessel. This allowed only a rough estimation of the filling height. For the Phase-2 system, the input condenser was equipped with a differential pressure sensor (Baratron 226A, MKS Instruments) as it is the case for the reboiler. The sensor is connected at one side to the old gaseous extraction port and on the other side to the re-machined outlet for the liquid xenon at the bottom, as indicated in figure 3.9. The calibration of the liquid level using the new sensor is visualized in figure 3.10, where the pre-separator was filled in two steps. First, liquid xenon is accumulating in the liquid-out tube at the bottom of the condenser as well as in the funnel-shaped bottom of the vessel once the pipe is filled. This causes a first increase in the differential pressure due to the hydrostatic pressure, indicated by the steep rising. During the filling, the temperature was $T = -92\,°\mathrm{C}$ and the pressure was $P = 2.5\,\mathrm{bar}$, yielding a liquid xenon density of $\rho_{\mathrm{Xe}} = 2832\,\mathrm{kg/m^3}$ [30]. With the heights $h_{\mathrm{pipe}} = 67\,\mathrm{mm}$ and $h_{\mathrm{funnel}} = 8.4\,\mathrm{mm}$ of the respective parts, and with the gravitational acceleration constant $g = 9.81\,\mathrm{N/kg}$ the expected pressure increase can be calculated to be

$$\Delta p_{\mathrm{pipe}} = \rho_{\mathrm{Xe}} \cdot g \cdot h_{\mathrm{pipe}} = 18.6\,\mathrm{mbar}, \tag{3.20}$$

$$\Delta p_{\mathrm{funnel}} = \rho_{\mathrm{Xe}} \cdot g \cdot h_{\mathrm{funnel}} = 2.3\,\mathrm{mbar}. \tag{3.21}$$

This has to be taken into account, before calculating the actual liquid level.

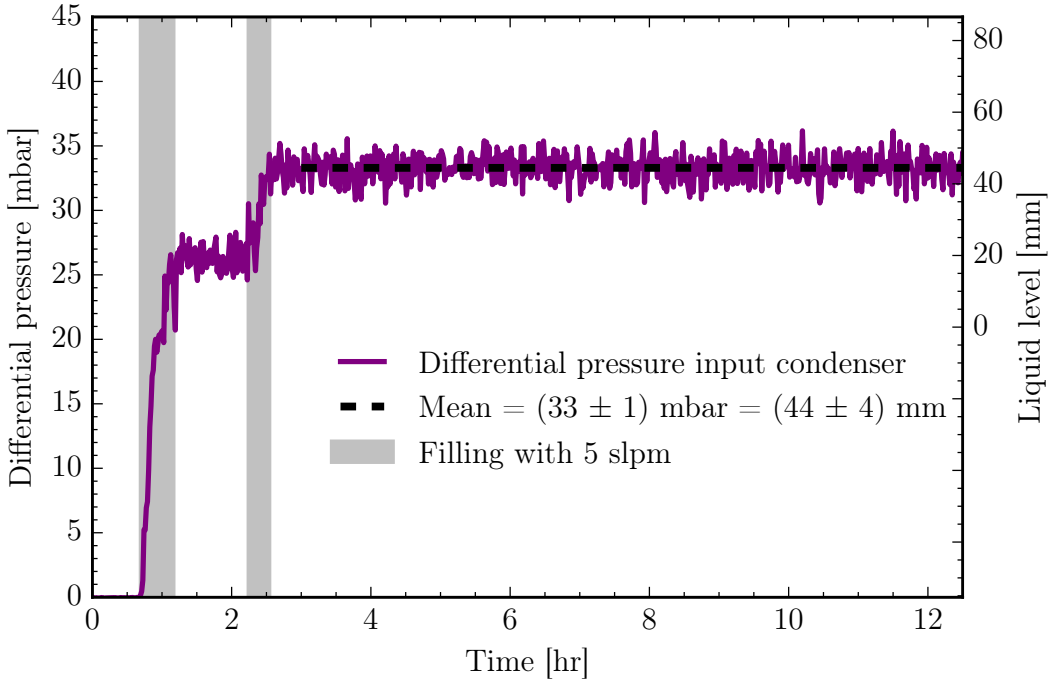


Figure 3.10: **Calibration of liquid level inside the input condenser:** Left axis: Measured differential pressure in mbar. Right axis: Corresponding liquid level in mm. Note that the first measured 21 mbar are a result of filling up the pipe below the condenser and the funnel-part of the vessel.

Once the liquid reached the cylindrical part, the increase of the pressure at the same filling speed of 5 slpm is less steep. After filling, the level was constant over several hours. Using the mean value of $\Delta p_{\text{measure}} = (33 \pm 1)$ mbar during this period, the corresponding height and thus the liquid level $h_{\text{pre-separator}}$ can be determined with

$$h_{\text{pre-separator}} = \frac{(\Delta p_{\text{measure}} - \Delta p_{\text{pipe}} - \Delta p_{\text{funnel}})}{\rho_{\text{Xe}} \cdot g} = (44 \pm 4)\,\text{mm}. \tag{3.22}$$

These values were measured at fixed temperature and pressure in a steady state system. The operation conditions can differ between distillation runs, leading to differences in the liquid xenon density and therefore to different absolute liquid level measurements, which have to be taken into account. When changing from steady state into distillation operation, a liquid xenon flow is established through the bottom pipe to one of the feed valves, causing the differential pressure measurements to drop to 0 mbar in some cases, but not always. All in all, it is possible to monitor the level behavior during operation with a combination of the three PT1000 at the outside of the vessel and the differential pressure method.

## Slow control in Münster: LabVIEW

For the monitoring and controlling during the commissioning of the Phase-2 system in Münster, an extended version of the existing LabVIEW based slow

control was utilized as sketched in figure 3.11.

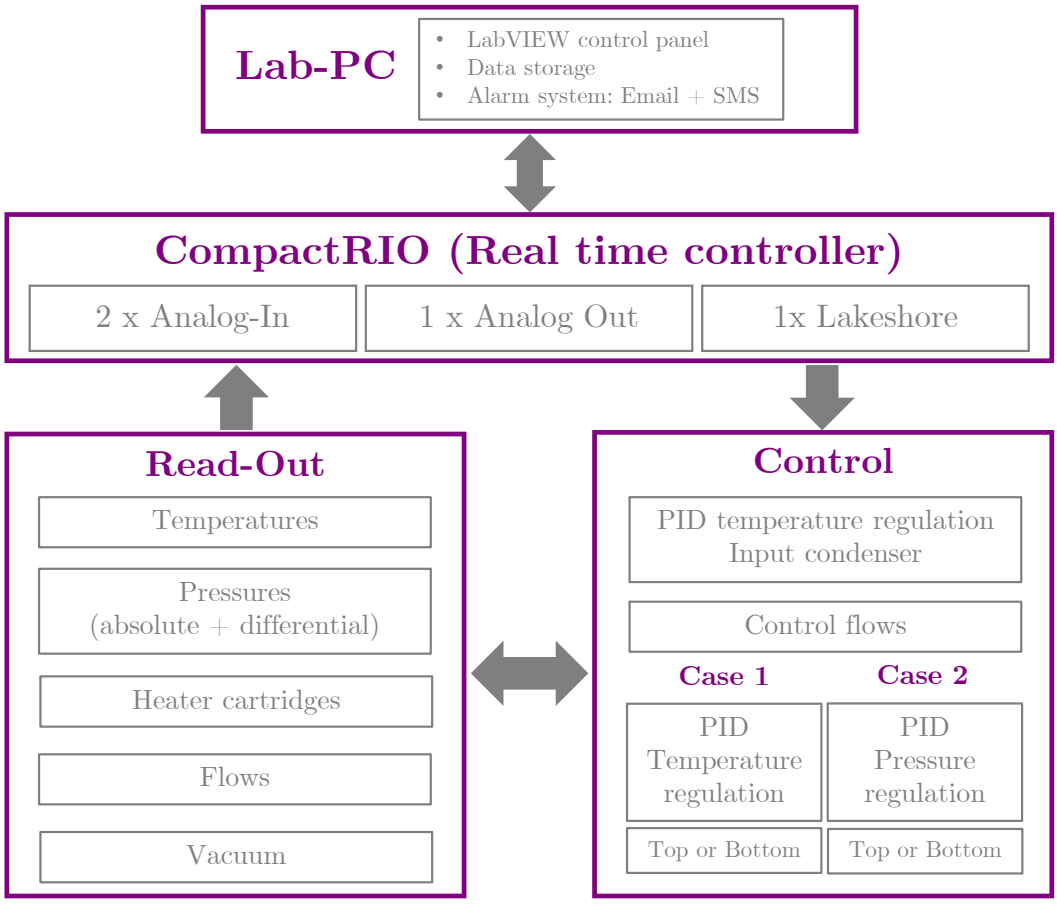


Figure 3.11: **Scheme of the LabVIEW based slow control in Münster:** The slow control system consists of a Lab-PC, a CompactRIO real time controller with analog input and output modules and a temperature controller (Lakeshore). This allows to monitor and control the process variables such as temperatures, heaters, pressures and flows during operation.

The real time controller CompactRIO (NI 9074, National Instruments) is equipped with two analog-in modules (NI 9205, National Instruments). This allows to measure the absolute and differential pressures, the flows, the insulation vacuum and the temperatures with PT1000 sensors. Here, the temperature is determined by the voltage drop over the resistance of the PT1000 sensor connected to a constant current source. An analog-out module (NI 9263, National Instruments) is used to regulate the flows of the four flow controllers in the system. In addition, a temperature controller (Lakeshore 336, Cryophysics) is connected via an Ethernet interface to the CompactRIO, which measures the temperatures of the three silicon diodes, installed at input condenser, top condenser and reboiler.

In order to keep the temperature in the input condenser constant, the power output of the cartridge and its control is regulated by a proportional–integral–derivative (PID) controller circuit within the Lakeshore 336 in all use cases. For the filling of the column, the temperature at the top condenser is kept constant

by heating with the heater located at the top, in order to guarantee a stable liquefaction of the xenon and cooling the system from top to bottom (Case 1, PID Temperature control, Top). During a standard distillation, a stable operation is achieved when controlling on the pressure inside the package tube, while cooling at the top and heating with the heater cartridges at the bottom of the system (Case 2, PID Pressure regulation, Bottom). For the respective regulations, each case features its own software based PID circuit implemented within the LabVIEW code. The software controls two external power supplies, one for top heater cartridges and one for bottom heater cartridges.

The stand-alone system is connected via Ethernet to a Lab-PC. This gives the possibility to access the control panel of LabVIEW to change setpoints and monitor the system online via live-plots. An additional program running on the Lab-PC stores the acquired data sent via network-streams and is able to send Email and SMS messages in case of emergency. All details about the development of this slow control system can be found in [60, 64].

## 3.3 Integration as a XENON1T subsystem

After the successful commissioning of the Phase-2 column in Münster, it was rebuilt to the smaller Phase-1 version for transportation to Italy. Before re-assembly as final setup in XENON1T, the smaller version was used at XENON100 in a reverse mode in order to test the feasibility of cryogenic distillation for radon removal. This is presented in chapter 7. In this section, the final Phase-2 distillation plant as a XENON1T subsystem along with different operation modes is presented. While the bottom and middle part of the distillation column are installed in the ground floor of the XENON1T service building as visualized in figure 3.12, the top of the system towers into the first floor with its total height of about 5.5 m. A gas bottle rack (Bottles), the system for Recovering and Storage of XENON1T ReStoX (RSX) as well as the water purification loop (WLP) for the water tank, are located in the ground floor. On the first floor are the Data Acquisition System (DAQ) and an operation room for shifters. The purification (PUR) and cryogenic (CRY) systems are installed on the second floor. The water tank with a diameter and height of about 10 m stands next to the service building, containing the outer and inner cryostat, where the TPC is installed. The relevant subsystems, involved in distillation operations, are briefly presented in the following. All details about the subsystems can be found in [41].

### Gas bottle rack

The gas bottle rack features four bottle connections, all equipped with weight measurements, allowing to fill raw xenon to the system. Different extraction ports give the possibility to measure the gas purity with a commercial gas chromatograph before filling [68]. In addition, a liquid nitrogen bath can be utilized to cool down two aluminum bottles to recover xenon from other systems, such as ReStoX or directly from the detector.

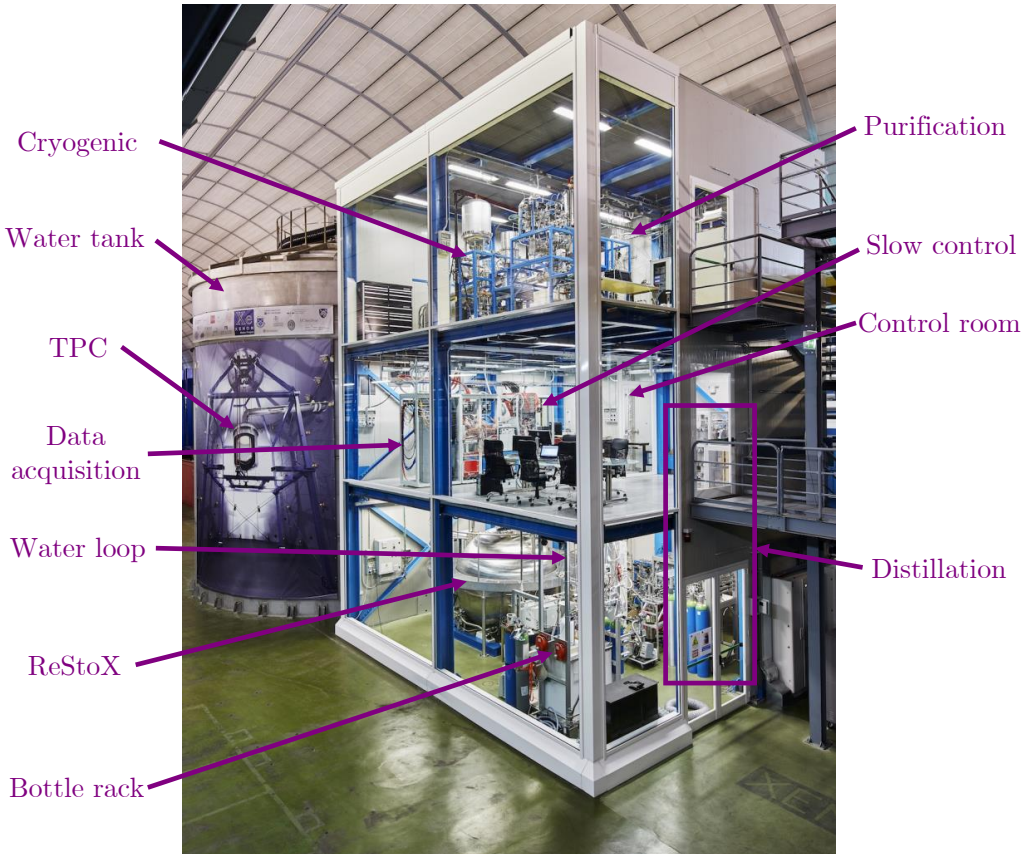


Figure 3.12: **The XENON1T experiment:** The picture shows the installed XENON1T system with the different subsystems. Photo by Enrico Sacchetti.

## ReStoX: Recovering and Storage of XENON1T

The ReStoX system is a double-walled stainless steel sphere, where the inner sphere (diameter = 210 cm) is cooled down with liquid nitrogen to liquid xenon temperatures and below, while an insulation vacuum is established between the inner and outer sphere to avoid heat losses. The system is rated for high pressures up to 70 bar and can store up to 7.6 tonnes of xenon either in gas, liquid or solid phase, preserving the high purity of the xenon. In case of emergency, the xenon from the detector can be recovered safely and controlled in liquid phase within a few hours. After maintenance of the TPC, the detector can be filled again from ReStoX.

## Purification

In the standard detector operation, the purification system recirculates xenon from the inner-most of the detector to remove electronegative impurities. In order to reach a concentration of 1 ppb oxygen equivalent, the system is made of two parallel circuits. Initially, each side was equipped with one high-purity pump (QDrive, Chart) allowing for a total flow of up to 45 slpm. In order to reduce the stress and to increase the lifespan of the pumps, one arm was upgraded with an additional QDrive in series. A fourth pump was in repair and no spare

was available for the second arm. With that, flows up to 50 slpm were achieved. After science run 1, another upgrade yielded flows up to 90 slpm. Here, the inlet pipes to the purification system were changed from 1/2-inch to 1-inch diameter. Furthermore, a new magnetically-coupled piston pump developed in Münster replaced the existing pumps [70, 71]. Each arm features a flow controller to measure and control the flow. Two hot metal getters (PS4-MT50-R, SAES) after the pump(s) trap electronegative impurities, while xenon as noble gas can pass unaffected. In addition, the purification system can act as xenon gas distributor, when the detector circulation is stopped, since all other subsystems that handle xenon have at least one in-going and one out-going connection with this system. The prototype of the gas purification system was developed in [60].

## Cryogenic

The cryogenic system liquefies the in-coming xenon during the filling of the detector and, once filled, keeps the xenon temperature during data taking constant. This is achieved by two redundant pulse tube refrigerators (PTRs), where one is used as active cooling tower and one is used as backup in case of a failure of the first PTR. In addition, a liquid nitrogen cooling tower is installed in case of emergency, which can be activated to ensure a constant liquid xenon temperature even without electrical power.

The cryogenic system is connected to the cryostat, which houses the TPC, inside the water tank, via a double wall vacuum insulated umbilical tube. The evaporating xenon steam from the inner cryostat is guided through this pipe to the cooling towers of the cryogenic system, where it re-condensates. The liquefied xenon is fed back via a tube within the umbilical tube. The tubes are inclined downwards with respect to the cryogenic system, in order to use gravity to establish a down-going liquid flow. It is possible to extract a fraction of the evaporating xenon at three different locations of the cryogenic system before condensation. This extracted gas can either be fed to the main purification loop or can be fed to the distillation system in order to remove krypton and radon, while the detector is filled (See online distillation below).

An additional internal pipe is connected to a heat exchanger at the cryogenic system, where liquid xenon from the detector is extracted, evaporated and guided to the purification system to continuously remove the electronegative impurities as mentioned above. The purified gaseous xenon from the purification system is connected to the other side of this heat exchanger to liquefy the xenon again and feed it back into the detector.

In the following, different possible operation modes between the distillation column and other subsystems are presented. A simplified scheme in figure 3.13 highlights all possible connections, using only a minimal set of the valves involved.

### 3.3.1 Standard distillation operations

The standard operations are indicated by the solid purple lines in figure 3.13, where a certain amount of raw xenon is filled from one subsystem to another subsystem through the distillation column to remove krypton. These are referred to as offline distillation. As one example, the raw xenon transfer from fresh bottles to ReStoX is explained in the following: In the standard mode, the purification system acts as gas distributor and no standard detector circulation can be performed. After connecting the bottles at the gas bottle rack, the raw gas is guided via FV202 to one of the two parallel circuits of the purification system. This allows to pump xenon via FV226 into the distillation system with flows up to 18 slpm. Using either the over-pressure from the bottles or the pump, a high pressure of about 2.8 bar can be created in the input condenser in order to push liquid xenon into the package tube. In this location, the column is operated at 2.0 bar. The liquid feed valve LF5 with an injection height of 212 cm with respect to the reboiler is preferable for a stable operation and a good separation performance. While 1 % of the feed flow is extracted as krypton-enriched xenon at the top of the column and is stored into the off-gas bottle via HV409, the purified xenon is extracted and pumped back to the second arm of the purification via HV402. From here, the gas is filled into ReStoX (1 bar) via FV208.

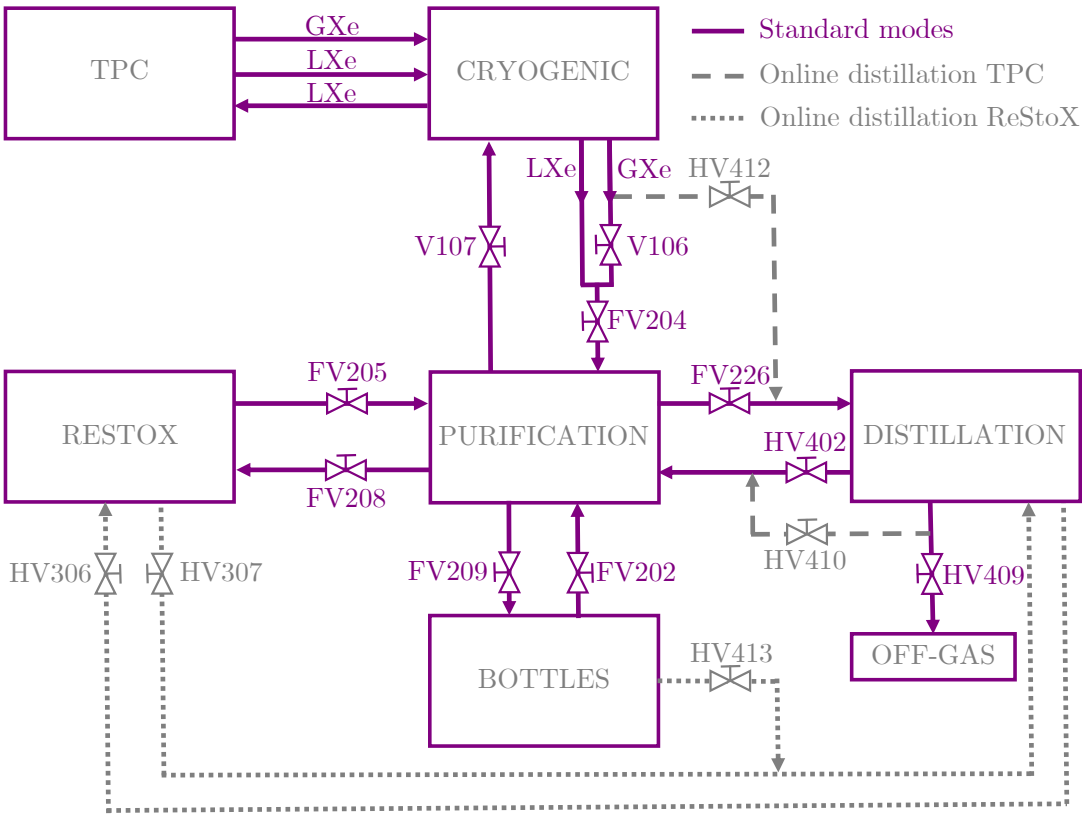


Figure 3.13: **Different operation modes for distillation:** The simplified scheme shows the connections between the distillation system and other subsystems involved, using only a minimal set of valves.

With an upgrade of the pipes, it is possible to fill directly from the bottles to the distillation system via HV413, indicated by the grey dotted line in figure 3.13. Instead of sending back the purified xenon to the purification system, it can be filled directly into ReStoX via HV306. In this case, the flow between the systems is created by pressure differences between them and no additional pump is required. As consequence, the detector purification loop can continue without interruption. This gives the possibility to add new xenon to the storage system without disturbing the detector operation.

The standard pipes also allow to pass the xenon from ReStoX once through the distillation column via the purification system, while filling the TPC via the cryogenic system. With a total of 3200 kg and a design process speed of 3 kg/h (8.3 slpm) of the distillation column, the XENON1T inventory would be depleted in krypton within 45 days. During this time period, no other detector operations for commissioning are possible. For this reason, a removal operation was investigated, where krypton is removed while the detector is filled already. As consequence, the desired krypton in xenon concentration can be reached in parallel to a fully operational TPC. This online krypton removal mode is briefly introduced in the following, while the results can be found in chapter 6.

### 3.3.2 Online TPC distillation

The inner cryostat, which houses the TPC, is filled with liquid xenon and has a gaseous phase above at a pressure of about 1.9 bar. In terms of krypton removal, this system can be described as a single distillation stage, where the gaseous xenon has a higher krypton concentration compared to the liquid xenon due to the relative volatility as described in section 3.1. By continuously cleaning the 20 kg of xenon in the gas phase from krypton, the equilibrium of krypton particles between liquid and gas phase is disturbed. As consequence, the krypton from the liquid phase and thus from the inner-most of the detector should migrate into the gaseous phase, where it is removed again. Thus, the krypton in xenon concentration inside the fiducial volume should be lowered as well, allowing to start the dark matter search as soon as reaching the desired purity. More details are given in chapter 6.

Technically, the gaseous xenon can be extracted at three ports of the cryogenic system with a maximum flow rate of 3.75 slpm, limited by the installed flow controllers in this part. From here, it can be fed via HV412 through a new pipe directly into the distillation system in parallel to the main circulation loop, as indicated by the grey dashed line in figure 3.13. The xenon gas is solely driven by the pressure difference between the cryogenic system (1.95 bar) and the input condenser of the distillation system (1.7 bar) such that no additional pump is required. As consequence, the main column pressure has to be lowered from the standard operation pressure of 2.0 bar to around 1.55 bar, such that liquid xenon from the input condenser can be pushed into the column package. For stable operation, the liquid feed valve LF2 is preferable, which has a height of 62.3 cm with respect to the reboiler. From here, off-gas from the top of the column is stored at a flow rate of 1 % of the feed flow in a bottle, cooled with liquid nitrogen, as in the standard mode. The purified xenon is fed back with a flow of 99 % of the feed flow via HV402 to the purification system and thus back into

the main circulation loop. In order to have a gas flow between the two systems, the outlet column pressure has to be sufficiently high (1.55 bar) compared to the purification system inlet pressure of 1.45 bar. With the pump(s) in the purification system, the xenon is filled back to the inner-most of the detector. In summary, an adjustment with a successive pressure decrease between all involved systems is required in order to achieve a stable distillation operation. In addition, it is of importance to overfill the detector with additional xenon in advance to compensate for the krypton-enriched off-gas losses.

The same three extraction ports can be used to continuously remove radon from the cryogenic system before entering the detector, using the column in inverse mode. Since radon is accumulated at the bottom of the system due to its lower volatility compared to xenon, the valve HV402 is closed and the radon is trapped until disintegration in the liquid reservoir in the reboiler. The gas from the top of the column is extracted as radon-depleted xenon and is fed back to the purification system via HV410 through an additional new pipe. The valve HV409 is closed in this mode, since there are no xenon losses due to the absence of any off-gas. Since radon is continuously emanating from detector materials, the online radon removal has to be also operated continuously. The process speed is the same as in krypton mode, limited to 3.75 slpm by the flow controllers at the cryogenic system. The pressure differences between the subsystems need to be adjusted the same way as explained above. More details on the radon removal results are presented in section 7.2. The same idea of online krypton removal can be applied to ReStoX and is introduced in the next section.

### 3.3.3 Online ReStoX distillation

Same as the detector, ReStoX can be seen as a single distillation stage, made of a liquid reservoir, containing most of the mass, with a gaseous phase above, where the more volatile contaminants in xenon like krypton, but also argon and helium, are enriched. Using the standard operation lines, indicated as solid purple lines in figure 3.13, and the pump(s), the gas phase of ReStoX can be continuously cleaned via the two independent arms of the purification system and the valves FV205, FV226, HV402 and FV208. Again, about 1 % of the process flow is stored as krypton-enriched off-gas. With this mode, high concentrations of helium were removed before the first time of detector filling as presented in chapter 5.

An online distillation of ReStoX without interruption of the main detector purification loop can be achieved via HV306 and HV307, indicated by the grey dotted lines in figure 3.13. For this mode, an additional circulation pump in front of the distillation system has to be installed, in order to extract xenon gas from ReStoX and compress it to the required high pressure of 2.7 bar at the input condenser. Due to the higher pressure of 2.0 bar of the column outlet compared to the ReStoX pressure of 1 bar, a gaseous flow can be established without any additional pump by pressure difference.

### 3.3.4 Slow control in XENON1T

Each subsystem in XENON1T is controlled by a Programmable Automation Controller (PAC, RX3i family, General Electric), equipped with several input and output modules. For the distillation system, the CompactRIO controller and its modules were exchanged by such a PAC. One analog output module (IC693ALG392-CF) controls the four flow controllers as well as the heater cartridges at the reboiler and the top condenser. One digital output module (IC694MDL754-CD) and one digital input module (IC694MDL660-BC) regulate the automatic liquid nitrogen filling of the off-gas bottle dewar. One analog input module (IC695ALG616-FB) features the read-out of the absolute and differential pressure sensors and the voltage drop of the potentiometers of the feed valves connected to a constant current source. Two universal analog input modules (IC695ALG600-DD) allow the direct measurement of the temperatures obtained with PT1000 sensors, while one serial communication module (IC695ETM001-EP) reads and controls the Lakeshore 336 temperature controller.

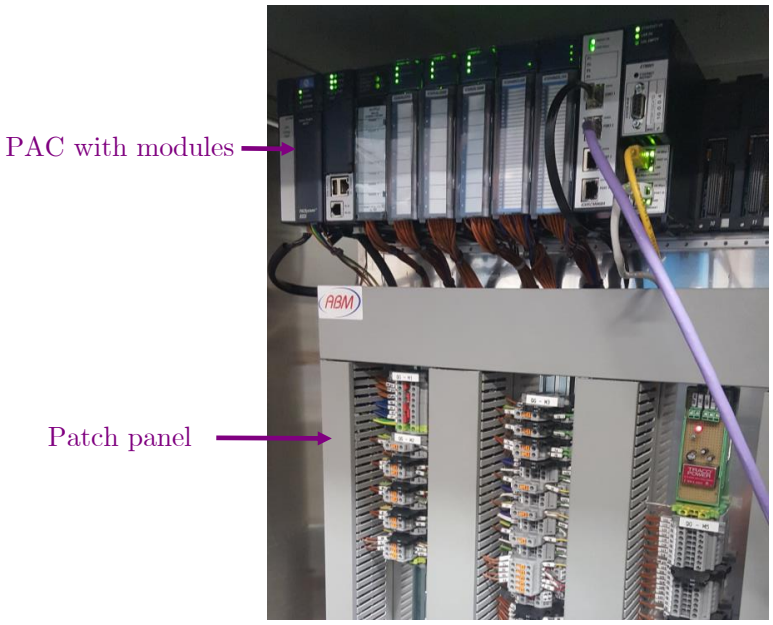


Figure 3.14: **PAC and patch panel of the distillation system:** The patch panel in the bottom is the interface between the sensors and the PAC modules at the top, housing a fuse for each cable to meet the LNGS safety requirements.

The LabVIEW based programmed code for the slow control was translated into the PAC logic with the help of Sergej Schneider, keeping the same PID controlling structures as before. This allows for a temperature or pressure regulation via top or bottom heating.

The variables of the distillation subsystem were allocated with the pre-fix number 4, such as PI424 describing the absolute pressure inside the column, in order to quickly differentiate between the subsystems for example in case of emergency. In addition, a patch panel was installed by the company ABM, where each sensor cable has its own fuse, to meet the LNGS underground safety

requirements. The PAC with its modules along with the installed cables on the patch panel are pictured in figure 3.14.

All PACs are network-connected with two redundant Supervisory Control And Data Acquisition (SCADA) servers, running in active-passive fail-over mode at the first floor of the service building. The obtained data with a polling rate of 1 Hz is stored in a database called Historian. In case of a system failure or connection loss, alarms are triggered and distributed via Email, SMS and pre-recorded voice-mails to a list of experts. Instead of a Lab-PC as in Münster, the system is monitored and controlled via a touch panel directly underground or remotely via the so-called Webspace service, running on the SCADA servers. This allows remote access from all over the world for shifters and experts via a browser application. In order to be able to change the operation settings within the distillation process, the user account requires to belong to the expert list of the distillation system. This avoids misuse by untrained personal. A picture of the main distillation controlling page along with all relevant sensors and regulation modes is visualized in figure 3.15. While the Webspace is restricted by the amount of users logged in at the same time and in order to avoid accidental change of control parameters, the Xe1TViewer was created by the slow control group [72] for fast and passive monitoring of the overall system with no restriction in number of users and independent from the operation system of the client.

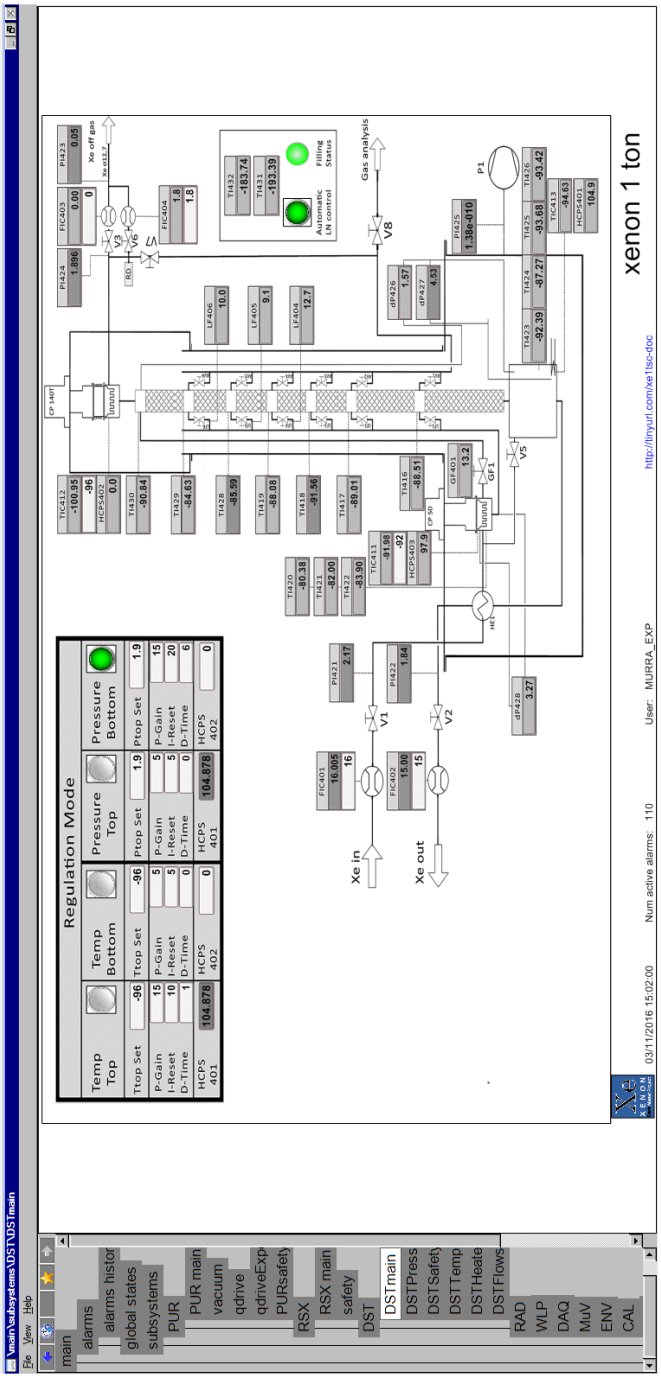


Figure 3.15: **Webspace browser application of XENON1T:** The picture shows the main control panel of the distillation system along with all relevant sensors and regulation modes during a distillation operation.

# Characterization 4

The performance of the Phase-2 distillation system such as stable operation and separation efficiency during commissioning at WWU Münster as well as at XENON1T was investigated in several distillation tests. In this chapter, the characterization of the system is presented. First, the thermodynamic stability is explained based on one standard offline distillation at design parameters followed by one online krypton removal campaign at XENON1T over the span of 46 days of continuous distillation. Second, the determination of the separation factor for krypton removal is explained along with the achieved purity of xenon.

Parts of this chapter are published in [61] by the XENON collaboration, where Stephan Rosendahl and the author of this thesis are corresponding authors.

## 4.1 Thermodynamic stability

The thermodynamic stability during the distillation process ensures the optimal mass exchange along the package material between liquid and gas streams such that an optimal separation is guaranteed. During commissioning in Münster and at XENON1T, several distillation runs were performed at different flows, pressures and feed heights. In a first example, a standard offline distillation over the course of about three days under the design parameters is discussed, in order to verify the functionality of the final Phase-2 system after installation at LNGS. As a second example, the longest continuous distillation operation so far of about 46 days, namely the online krypton removal campaign as described in chapter 6, was chosen to be presented in detail as well. Due to the detector conditions, the distillation process parameters were different from the design values. Therefore, it is discussed, if these differences still meet the requirements for an optimal separation process.

### Standard offline distillation

For an offline distillation campaign, four bottles were connected to the gas bottle rack with a total amount of 212 kg of xenon. This xenon required to be purified and filled into ReStoX. The involved subsystems along with a minimal set of valves used is presented in section 3.3.1. The raw gas was pushed to the distillation column via the purification system by an over-pressure of around 3 bar from the gas bottles, allowing to create a flow rate of 8.5 slpm (3.1 kg/h), controlled with the inlet flow controller FIC401 of the distillation system. Inside

the input condenser, the incoming xenon was liquefied and injected at a feed height of 212 cm via LF5. In this operation, the gas feed valve GF1 was kept close and all incoming xenon was fed in pure liquid feed. While the krypton-enriched off-gas was stored in a bottle with an extraction flow of 0.085 slpm, the purified xenon was sent back to the purification system and from there into ReStox. In other offline distillation runs, stable operations of up to 18.5 slpm (6.7 kg/h) were achieved, but are not explicitly presented here. This is more than a factor of two higher with respect to the initial design value of 3 kg/h.

In figure 4.1, a set of the most important system parameters is displayed, namely the absolute column pressure (PI424), the differential pressure along the package tube (DP426), the in-gas flow (FIC401), the purified liquid-out flow (FIC402) and the reboiler liquid level (DP427). The operation lasted from 22 Sep 2015 until 24 Sep 2015. During the first day, the reboiler liquid level DP427 (figure 4.1, panel 5) was disturbed after starting the process and was slowly decreasing, indicating that the mass balance of the system was not optimal due to a slightly too high extraction flow FIC402 (figure 4.1, panel 4). By adjusting the extraction flow accordingly, a constant liquid level and thus mass balance in the system was achieved. The period of adjustment is shaded grey in figure 4.1, while starting from 23 Sep 2015, the operation is considered as stable.

The stability of the system can be divided into the thermodynamic part such as pressures and temperatures and the mass balance part due to adjustment of the in-going and outgoing flows. In order to provide a stable liquid xenon feed, the PID controller kept the temperature of the input condenser constant at a value of TIC411 $= (-92.48 \pm 0.01)\,°\mathrm{C}$ (not shown) utilizing an average heating power of HCPS403 $= (81.7 \pm 0.3)\,\mathrm{W}$ (not shown). This resulted in a constant pressure in the input condenser of PI421 $= (2.64 \pm 0.01)\,\mathrm{bar}$ (not shown).

In contrast to the input condenser, the PID controller for the stability in the package tube is regulated on the main pressure PI424. In order to create the desired pressure, the corresponding amount of xenon particles has to be evaporated by heating from the bottom. For a high reflux ratio, the maximum cooling power is applied at the top condenser for the liquefaction. The setpoint of PI424 $= 1.87\,\mathrm{bar}$ was kept constant at all times during the operation with a standard deviation of $\sigma_{\mathrm{PI424}} = 0.009\,\mathrm{bar}$ as presented in the first panel in figure 4.1. The average heating power from the bottom was determined to be HCPS401 $= (120.0 \pm 0.9)\,\mathrm{W}$ (not shown), while the temperature at the top condenser was TIC412 $= (-97.71 \pm 0.02)\,°\mathrm{C}$ (not shown).

The amount and velocity of the evaporated xenon particles from the bottom influence also the differential pressure DP426 along the package tube (figure 4.1, panel 2), measured between the reboiler and the top condenser. If the vapor stream is so strong that the down-rinsing liquid stream is pulled up again before reaching the reboiler, the differential pressure along the tube will dramatically increase and the distillation process becomes unstable. This phenomenon is called flooding. According to the company Sulzer, a good reference point for a stable operation is a pressure drop of 1 mbar/m of package material [66]. The measured value of DP426 $= (2.34 \pm 0.16)\,\mathrm{mbar}$ with the package height of 2.7 m yields a drop of about 0.9 mbar/m. This is about 10 % below the advised value from Sulzer, but also well below the flooding point. In order to increase and

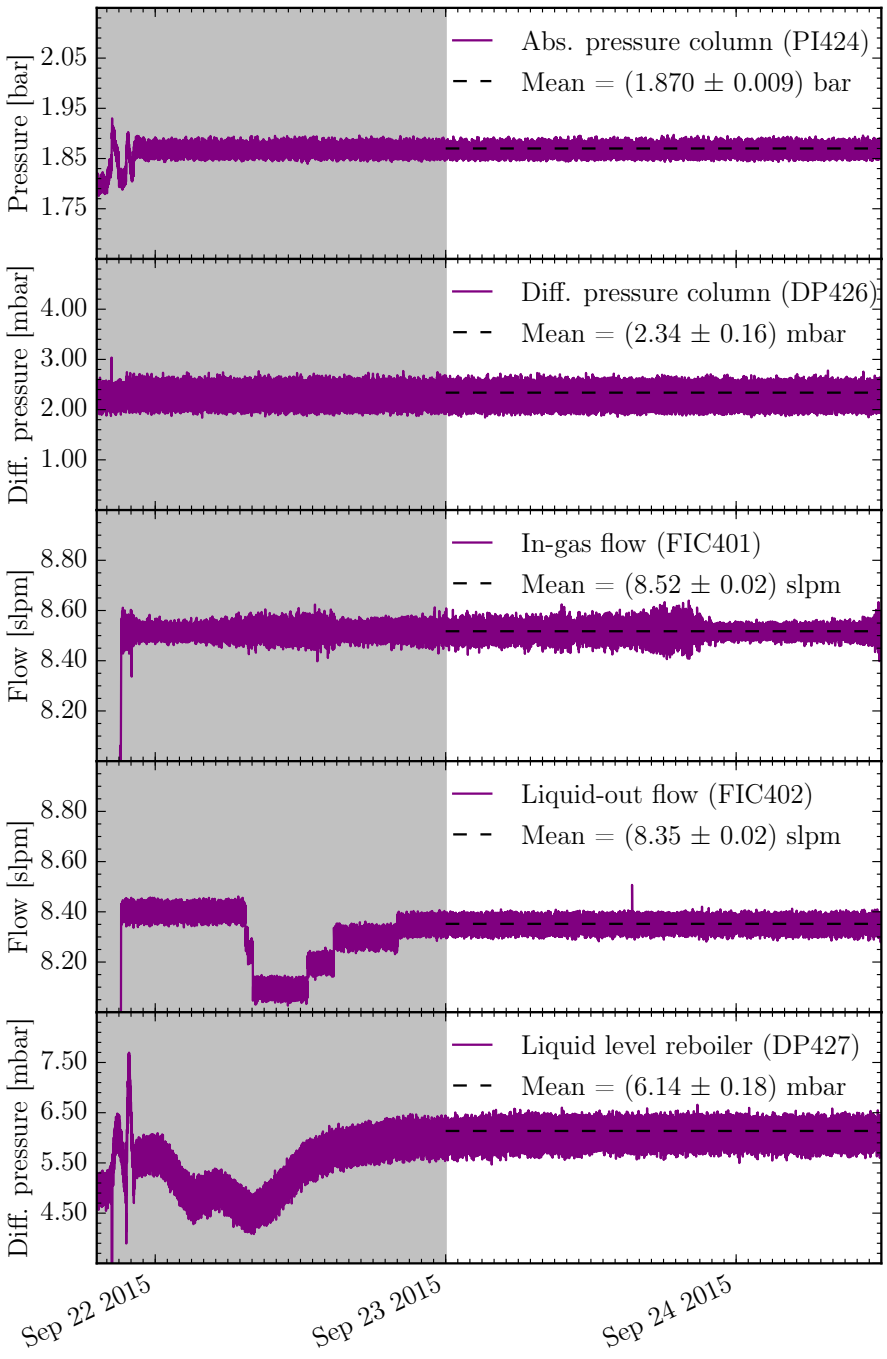


Figure 4.1: **Thermodynamic stability under design parameters for an offline distillation.**

optimize the pressure drop, the main pressure PI424 in the column can be raised further, resulting into a higher drop, tested during other distillation operations in Münster. Another possibility to increase the differential pressure DP426 would be to increase the cooling power at the top of the column. This would result into a higher heating from the bottom in order to keep the main pressure constant. Therefore, the used refrigerator at the top condenser would have to be replaced.

The mass balance in the system can be regulated with the in-gas flow controller FIC401 (figure 4.1, panel 3), the liquid-out flow controller FIC402 (figure 4.1,

panel 4) and the off-gas flow controller FIC403 (not shown). The in-gas flow controller FIC401 during the offline distillation is used as regulating and monitoring device. A mean value of FIC401 $= (8.52 \pm 0.02)$ slpm was measured as displayed in the third panel in figure 4.1. The off-gas was extracted at a fixed flow rate of FIC403 $= (0.0850 \pm 0.0001)$ slpm. Investigations in Münster [67] revealed that the absolute flow measurements can differentiate up to 25 % between the three flow controllers of the distillation system. Therefore, the mass balance is not achieved by setting the flow difference between in-going and outgoing flows accordingly, but by fixing flows FIC401 and FIC403 and by adjusting the liquid-out flow FIC402 such that a constant liquid level in the reboiler DP427 is obtained. When the liquid level, measured by the hydrostatic pressure, is increasing over the course of several days, the flow controller FIC402 requires to be manually increased in order to remove more xenon and vice versa. This regulation can be seen in the grey shaded area in the fourth and fifth panel of figure 4.1. The mean value of the liquid-out flow during the stable operation was determined to be FIC402 $= (8.35 \pm 0.02)$ slpm, while the average liquid level was DP427 $= (6.14 \pm 0.18)$ mbar. This corresponds to a height of about 2.2 cm and a xenon mass of about 3.1 kg in the reboiler.

One of the most important parameters during a distillation operation is a high reflux ratio $R$ ($R_{\text{Design}} = 191$), which represents the fraction of xenon that is fed back as liquid flow ($L$) to the column and of the xenon that is extracted as off-gas ($D$), as explained in section 3.1. The reflux is estimated in the following: Assuming a pure liquid feed ($q = 1$), the evaporated up-streaming flow $V'$ in the rectifying section equals the gaseous stream $V$ in the stripping section as shown in section 3.1. With the enthalpy $\Delta h_{\nu,\text{Xe}} = 92.2\,\text{kJ/kg}$ between liquid and gaseous xenon and the heating power at the reboiler HCPS401 $= (120.0 \pm 0.9)$ W follows

$$V' = V = \frac{\text{HCPS401}}{\Delta h_{\nu,\text{Xe}}} = 4.7\,\text{kg/h}. \tag{4.1}$$

Based on equation (3.8), the reflux ratio can be calculated to be

$$R = \frac{L}{D} = \frac{V - D}{D} = \frac{V' - D}{D} \approx 152. \tag{4.2}$$

The estimated value is about 20 % lower than the design value of 191 and also lower than the reflux ratio of 183 measured with the Phase-1 system under the same flow and similar pressure conditions [60]. Since in Phase-2 a longer package tube is installed, the heat losses are greater than for Phase-1 which had the same cold-head. As consequence, less cooling power is available at the top to liquefy xenon and to feed it back to the package tube. Therefore, the reflux ratio in Phase-2 is lower compared to Phase-1 for similar conditions. However, the value is still much higher than standard industrial reflux ratios on the order of 10 [62] and should be sufficient for a good separation efficiency.

### Online distillation

In the online distillation mode, a fraction of the gaseous phase from the cryogenic system is extracted with a flow rate of about 3.75 slpm (1.35 kg/h) and guided to the input condenser of the distillation system, from where the gas is liquefied and injected at a feed height of 62.3 cm via LF2. In addition, a small gas fraction is guided via the gas feed valve GF1 directly to the top of the column in order to avoid any blanket effect and to utilize the input condenser as first distillation stage. While the krypton-enriched off-gas is stored in a bottle with an extraction flow of 0.04 slpm, the purified xenon is sent back to the main purification loop and is added to the standard circulation flow before it is filled back to the inner-most of the detector. The technical operation along with the involved subsystems and a minimal set of valves is explained in section 3.3.2. The process speed during this operation was not limited by the distillation column performance, but by the flow controllers FCV101, FCV102 and FCV103 at the three extraction ports of the cryogenic system with a maximum flow rate of 1.25 slpm each.

In figure 4.2, the same set of key parameters as in figure 4.1 are visualized. The operation lasted from 28 Oct 2016 until 12 Dec 2016 and was with 46 days the longest continuous distillation run with the Phase-2 column so far. During the first days, the reboiler liquid level DP427 (figure 4.2, panel 5) was increasing, indicating that the mass balance of the system was not optimal due to a slightly too low extraction flow FIC402 (figure 4.2, panel 4), which was adjusted accordingly. During the last days, this extraction flow was increased step-wise to flush back more xenon to the detector system before emptying and preparing the column for the radon mode (See section 7.2). For this reason, these two areas are shaded grey in figure 4.2 and only the time from 03 Nov 2016 until 06 Dec 2016 is considered as stable operation.

The temperature of the input condenser was constant at a level of TIC411 $= (-93.50 \pm 0.01)\,°\mathrm{C}$ (not shown) utilizing an average heating power of HCPS403 $= (96.7 \pm 0.6)\,\mathrm{W}$ (not shown). This resulted in a constant pressure in the input condenser of PI421 $= (1.70 \pm 0.01)\,\mathrm{bar}$ (not shown).

The PID controller regulated the main pressure on a setpoint of PI424 $= 1.56\,\mathrm{bar}$ at all times during the operation with a standard deviation of $\sigma_{\mathrm{PI424}} = 0.001\,\mathrm{bar}$ as presented in the first panel in figure 4.2. The average heating power from the bottom was determined to be HCPS401 $= (84.3 \pm 2.2)\,\mathrm{W}$ (not shown), while the temperature at the top condenser was TIC412 $= (-101.47 \pm 0.02)\,°\mathrm{C}$ (not shown).

The value of the differential pressure along the package tube (figure 4.2, panel 2) of DP426 $= (1.83 \pm 0.06)\,\mathrm{mbar}$ and the package height of 2.7 m yield a drop of about 0.7 mbar/m during the online distillation mode. This is about 30 % below the advised value from Sulzer as explained in the last section, but also well below the flooding point. In order to increase and optimize the pressure drop, the main pressure PI424 in the column can be raised to the design value of 1.9 bar resulting into a drop of 0.9 mbar/m, as shown in the last section and also in [61]. However, as explained in section 3.3.2, a raise of the main pressure PI424 is not possible in this case, because of the required descending pressures between the involved subsystems to allow a xenon flow without an additional pump.

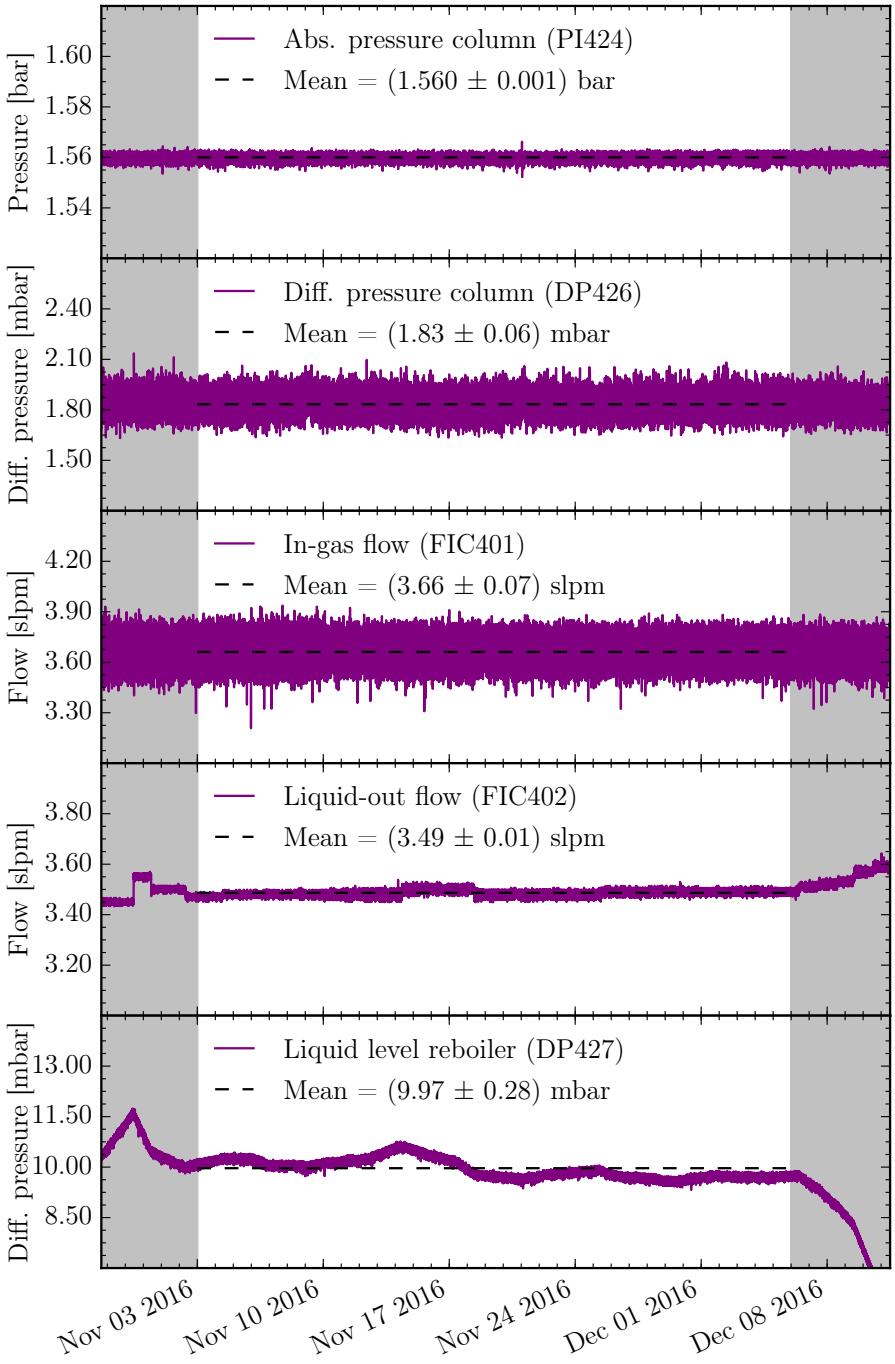


Figure 4.2: **Thermodynamic stability during a 46 days online distillation run.**

In the online distillation operation, the three flow controllers FCV101, FCV102 and FCV103 from the cryogenic system control the incoming xenon. In order to not over-regulate the system, the in-gas flow controller FIC401 of the distillation system is fully opened and is just used as monitoring device. A mean value of FIC401 $= (3.66 \pm 0.07)$ slpm was measured as visualized in the third panel in figure 4.2. The off-gas was extracted at a fixed flow rate of FIC403 $= (0.040\,32 \pm 0.000\,01)$ slpm. Again, the mass balance was achieved by fixing

flows FIC401 and FIC403 and by adjusting the liquid-out flow FIC402 such that a constant liquid level in the reboiler DP427 was obtained. The manual regulation can be seen in the grey shaded areas in the fourth and fifth panel of figure 4.2. The mean value of the liquid-out flow was determined to be FIC402 $=$ $(3.49 \pm 0.01)$ slpm, while the average liquid level was DP427 $=$ $(9.97 \pm 0.28)$ mbar. This corresponds to a height of about 3.5 cm and a xenon mass of about 5 kg in the reboiler. However, the maximum deviation from the mean liquid level was 0.8 mbar. In order to keep the liquid level on a constant value with less deviation, a PID regulation would be preferable over a manual adjustment by the operator.

The reflux ratio as most important parameter is estimated in the following: The feed to the package tube is mainly in liquid phase and a small fraction of the raw xenon is extracted in gaseous form and guided to the top. Since this gas fraction is not measurable, a minimum and maximum reflux ratio can be estimated, assuming a pure liquid and a pure gaseous feed $F$, respectively. The real reflux ratio is in between those two. For a pure liquid feed ($q = 1$) follows with the enthalpy $\Delta h_{\nu,\mathrm{Xe}} = 92.2\,\mathrm{kJ/kg}$ between liquid and gaseous xenon, and the heating power at the reboiler HCPS401 $=$ $(84.3 \pm 2.2)$ W

$$V' = V = \frac{\mathrm{HCPS401}}{\Delta h_{\nu,\mathrm{Xe}}} = 3.3\,\mathrm{kg/h}. \tag{4.3}$$

Based on equation (3.8), the reflux ratio can be calculated to be

$$R = \frac{L}{D} = \frac{V - D}{D} = \frac{V' - D}{D} \approx 226. \tag{4.4}$$

Assuming a pure gaseous feed ($q = 0$), the up-stream in the stripping section is $V = 4.6\,\mathrm{kg/h}$. Thus, the reflux ratio changes to

$$R = \frac{(V' + F) - D}{D} \approx 317. \tag{4.5}$$

In the case of the minimal reflux ratio for a pure liquid feed, the value of 226 is already much higher than the measured reflux ratio of the offline distillation under design parameters with Phase-2 ($R = 151$) as well as with Phase-1 ($R = 183$), and the design value ($R = 191$). The combination of the different parameters with respect to the design values such as the process speed, the off-gas extraction flow, the heating power at the reboiler to keep the lower operation pressure constant, and the amount of xenon that is fed back to the tube, leads to an increase of the reflux ratio. This guarantees a good separation performance.

The first example showed that the distillation column is working stable in terms of thermodynamics and mass balance as initially designed and even beyond. The second example demonstrated the flexibility of the system. It can also be adapted to operate in initially unforeseen operations like the online distillation, limited by the overall detector conditions. In addition, it was proven, that stability was achieved over a long period of time without any interruptions or intervention. This is a key requirement to distill a high amount of xenon either via offline mode or via online mode.

In the next section, the separation capability is presented. The krypton reduction during the online removal campaign is discussed in chapter 6.

## 4.2 Krypton reduction

Despite the thermodynamic stability during the distillation process, the reduction capability and the achieved purified output concentration of krypton in xenon are the most important characteristics of the distillation plant. The reduction factor $F_{\mathrm{red}}$ is given by the ratio of the natural krypton in xenon concentration $c_F$ in the gas feed and the concentration $c_B$ in the purified liquid-out xenon

$$F_{\mathrm{red}} = \frac{^{\mathrm{nat}}\mathrm{Kr/Xe}_{(\mathrm{in-gas})}}{^{\mathrm{nat}}\mathrm{Kr/Xe}_{(\mathrm{liquid-out})}} \equiv \frac{c_F}{c_B} \qquad [60, 61]. \tag{4.6}$$

A concentration of $c_B < 200\,\mathrm{ppq}$ is necessary to meet the background requirements for a 2 tonne × yr exposure with XENON1T, as presented in section 2.5.1. Starting with a gas feed concentration in the order of ppb, the distillation system for XENON1T requires to feature reduction factors of $F_{\mathrm{red}} \sim 10^4 - 10^5$, in order to achieve the desired purity. The lowest ever measured krypton in xenon concentration was $c_B < 26\,\mathrm{ppq}$ (90 % C.L.), achieved with the Phase-1 distillation plant. However, the reduction factor was determined to be only $F_{\mathrm{red}} > 5.6 \times 10^3$ (90 % C.L.), due to a low input concentration of $c_F = (136 \pm 22)\,\mathrm{ppt}$ during commissioning of Phase-1 [60, 61]. From above numbers, an HETP value of 15 cm or less was calculated for Phase-1 by applying the McCabe-Thiele diagram, as evaluated in section 3.1.

In the following, the krypton reduction factor of the Phase-2 system is calculated from measurements during the commissioning in Münster as well from measurements after installation as subsystem at XENON1T. In addition, the achieved output concentrations are presented and the HETP values are derived using the McCabe-Thiele method to compare with Phase-1.

### Münster

During commissioning in Münster, the duration of the distillation runs was limited by the amount of available xenon to about 11 h at the design flow rate of 8.5 slpm. Here, a bottle to bottle distillation was performed. Using the over-pressure from the raw xenon bottle, the gas was pushed via a prototype gas system through a hot metal getter into the distillation plant. From here, off-gas was extracted at the top of the column, while the purified xenon was sucked into a liquid nitrogen cooled bottle, which acted as cryogenic pump. All details of the infrastructure for the distillation system in Münster including the prototype gas system can be found in [60].

By measuring the krypton content within the feed gas and within the purified liquid-out gas, the reduction factor of the Phase-2 system can be estimated following equation (4.6). For the measurement of the absolute concentration of natural krypton in xenon a residual gas analyzer (RGA) behind a $LN_2$-cooled coldtrap was designed, installed and calibrated in Münster [60, 73, 74]. This system was based on the design in [75]. The basic scheme of the setup is sketched in figure 4.3.

A xenon gas sample ($\approx$ 90 ml) is introduced via a differential pumping section into a spiral gas routing pipe, cooled to 77 K by submerging it in liquid nitrogen. At this temperature, most of the xenon is frozen in the coldtrap, reaching a

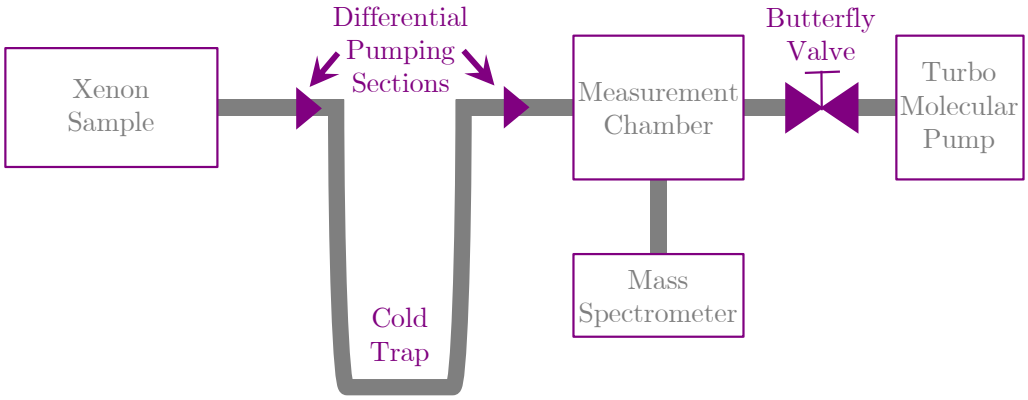


Figure 4.3: **Scheme of the coldtrap-enhanced Residual Gas Analyzer:** The system consists of the sample container, two differential pumping sections to reduce the pressure, the $LN_2$ coldtrap to freeze xenon while krypton can pass unaffected, the measurement chamber, the butterfly valve in front of the turbo molecular pump to control the effective pumping speed and a residual gas analyzer based on a quadropule mass spectrometer to measure the krypton content. Scheme based on [74].

vapor pressure of $3 \times 10^{-3}$ mbar, whereas the krypton remains mostly gaseous due to its higher vapour pressure of 2 mbar and low partial pressure within the sample. As consequence, the krypton concentration is artificially enhanced. From the coldtrap, the prepared sample is injected via a second differential pumping section into the measurement chamber, equipped with a commercial quadrupol mass-filter (Inficon, Transpector 2 H200M) and an oil-free turbo-molecular pumping system. The effective pumping speed inside the chamber can be controlled with the help of a custom-made butterfly valve, mounted before the pump, in order to increase the dynamic range and thus, to achieve a higher sensitivity. The absolute calibration of the setup is done by measuring samples with known concentrations of krypton in xenon by mixing pure krypton into a pure xenon sample, extracted from the distillation outlet. From such a series of calibration measurements, a sensitivity limit of $(206 \pm 36)$ ppt was obtained. Details on the setup, calibration and analysis of the data are summarized in [74].

Since the expected concentration of the distilled xenon is at the ppq level, the raw xenon was doped artificially with pure krypton to probe high separation factors. During a bottle to bottle distillation at a flow rate of 8 slpm, the concentration of natural krypton in the purified xenon was found to be below the sensitivity limit of the RGA system. In order to not spoil the pipes with high amount of krypton, the inlet krypton concentration was measured after the purified outlet and was found to be $(20.2 \pm 5.4)$ ppm. In order to compute a lower limit for the reduction factor, a monte carlo simulation calculated $10^8$ times the reduction factor as following: In each step, the inlet concentration was created by a random generator following a normal distribution with $\mu = 20.2$ ppm and $\sigma = 5.4$ ppm. Since the krypton in xenon content in the outlet was expected to be in the ppq level, the outlet concentration was conservatively assumed to follow

a uniform distribution between 0 ppt and $(206 \pm 36)$ ppt. The right boundary was smeared out by a normal distribution with $\mu = 206$ ppt and $\sigma = 36$ ppt. The resulting distribution of the $10^8$ computed entries is visualized in figure 4.4. By calculating the 10 % quantile, the lower limit of the reduction factor is

$$F_{\text{red}} > 0.94 \cdot 10^5 \quad (90\,\%\,\text{C.L.}), \tag{4.7}$$

proving the design value of $10^4$ - $10^5$. Since this is only a lower limit, a meaningful HETP value cannot be calculated from this value. This is done in the next section during a distillation run at LNGS after installation of the system at XENON1T.

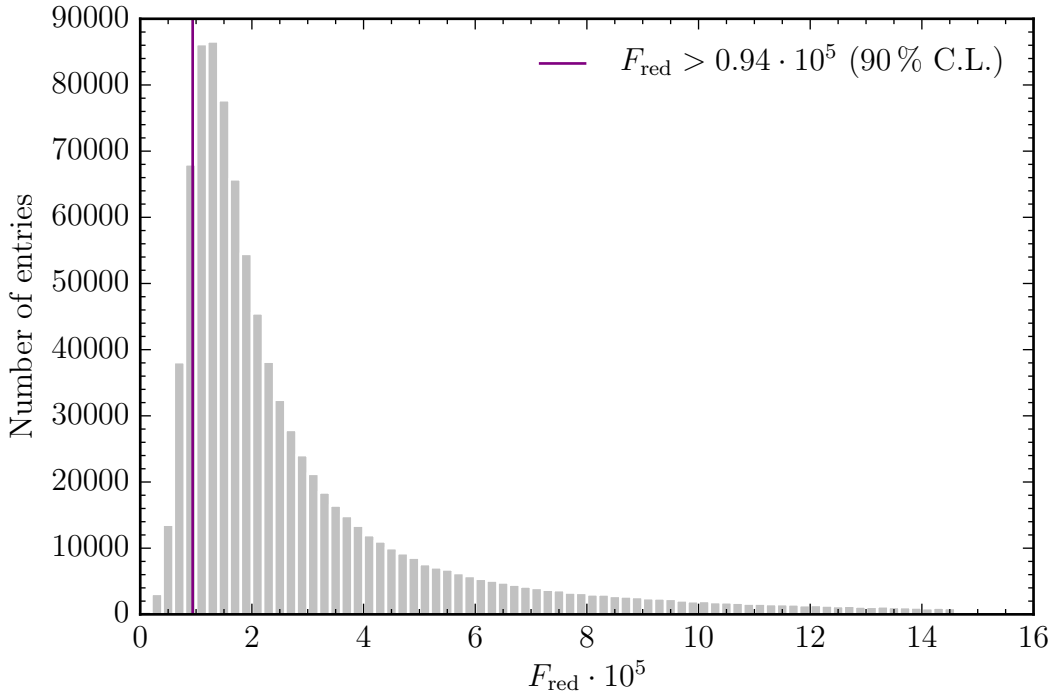


Figure 4.4: **Reduction factor during commissioning in Münster:** In a monte carlo simulation $10^8$ reduction factors were computed using the given inlet and outlet concentrations. A lower limit for the reduction factor with a 90 % confidence limit was calculated from the obtained distribution.

## LNGS

Before filling the full inventory of the acquired xenon for XENON1T from bottles into the ReStoX system, each bottle was screened for impurities, such as krypton, argon, nitrogen or oxygen, with a commercial gas chromatograph (GC) (Trace GC Ultra, Thermo Fischer) which was installed next to the gas bottle rack [68,69]. For the commissioning run of the Phase-2 column after installation at XENON1T, which was presented already in figure 4.1 in terms of thermodynamic stability, four bottles with the highest krypton content were selected to be purified from

krypton before filling into ReStoX in order to not further spoil the rest of the inventory.

The mixture of three bottles with an amount of $(164.2 \pm 3.0)$ kg was measured to contain a krypton in xenon concentration of $(453 \pm 53)$ ppb. The fourth bottle with $(48.2 \pm 1.0)$ kg of xenon was certified by the company with a concentration of krypton below 1000 ppb, but was not measured explicitly with the GC [68, 69]. In order to specify the reduction capability after the transport and installation at LNGS, the purified xenon from the distillation system was not measured with the RGA setup, but with an off-site system developed and located at the Max-Planck-Institut für Kernphysik in Heidelberg with much higher sensitivity. This is reviewed briefly in the following:

The rare gas mass spectrometer (RGMS) detects trace amounts of natural krypton in xenon down to the ppq level. The projected detection limit was determined to be $^{\mathrm{nat}}\mathrm{Kr/Xe} = 8$ ppq [50]. Similar to the RGA system, a separation of the bulk of xenon from the krypton component has to be done before the sample is injected into the analyzer. This separation is realized by gas-chromatography, where the sample is guided with a helium carrier gas through separation columns, which are filled with a special adsorbent, cooled with liquid ethanol to $-80\,^{\circ}\mathrm{C}$. Different travel times due to different interaction strength of krypton compared to xenon with the adsorbent lead to a separation of the components. More details on the system as well as on its sensitivity are given in [50].

The xenon sample from the column outlet was not extracted directly at the distillation system, but at a dedicated port at the purification system. A careful preparation of the sample container, namely baking at temperatures of about $100\,^{\circ}\mathrm{C}$ and pumping to pressures of $1 \times 10^{-7}$ mbar for several hours or days, is of crucial importance to avoid any contamination of the sample during extraction. For cleanliness, the container is made of four metal sealed 1/2-inch valves, welded together in series to enclose three volumes of a total of about $10\,\mathrm{cm}^3$, where the two adjacent volumes shield the inner volume against any kind of leaks through the outer valves. After extraction of the sample, the container was removed and shipped to Heidelberg. During the commissioning run a krypton in xenon concentration of $(730 \pm 140)$ ppq was measured.

From the measurements of the inlet and the outlet the reduction factor can be obtained using again the monte carlo simulation: In each step, an inlet concentration from the three measured bottles is randomly created following a normal distribution with $\mu = 453$ ppb and $\sigma = 53$ ppb. Since the concentration of the forth bottle was unknown, a concentration between 0 ppb and 1000 ppb was created following a uniform distribution. The inlet concentration $c_F$ is then calculated by weighting the two generated concentrations with the mass of the bottles. The purified xenon concentration $c_B$ is randomly computed following a normal distribution with $\mu = 730$ ppq and $\sigma = 140$ ppq. In a last step, the reduction factor can be calculated following equation (4.6).

The resulting distribution is displayed in figure 4.5. By calculating the 50 % quantile with a one sigma confidence interval yields the reduction factor of

$$\mathrm{F_{red}} = (6.4^{+1.9}_{-1.4}) \cdot 10^5. \tag{4.8}$$

This value confirms the measured reduction during commissioning in Münster and outperforms the required design value of $1 \times 10^5$ for XENON1T. Together

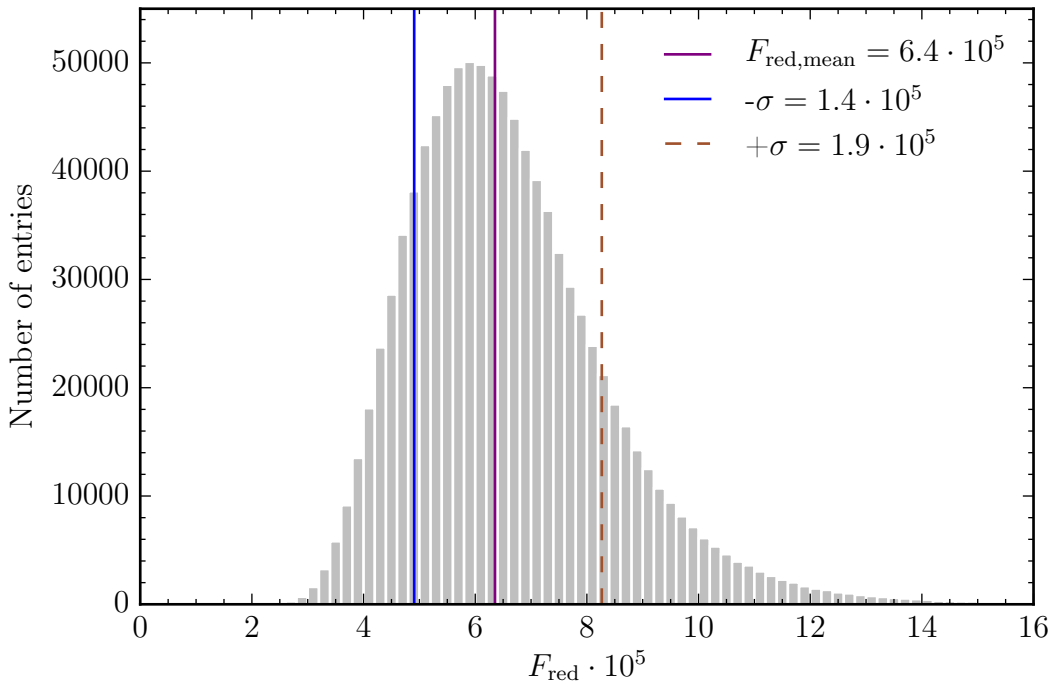


Figure 4.5: **Reduction factor during commissioning at LNGS:** In a monte carlo simulation $10^8$ reduction factors were computed using the given inlet and outlet concentrations. The reduction factor is given by the mean of the obtained distribution within a one sigma confidence interval.

with the flows, feed height, the measured inlet and outlet concentration, and the calculated reduction factor, an HETP value is estimated using the McCabe-Thiele method. From the McCabe-Thiele diagram in figure 4.6 the total number of theoretical plates $n_{TP}$ was determined to be 9, where 7 stages are in the stripping section below the feed point with a height of $h_{feed} = 192\,\text{cm}$. Due to a fully saturated liquid feed during this distillation run, the input condenser did not act as a first separation stage and can be neglected for the diagram.

With this, the HETP value is calculated to be

$$\text{HETP} = \frac{h_{feed}}{n_{TP,stripping}} \approx 27\,\text{cm}, \tag{4.9}$$

which is significantly higher compared to the value of 15 cm stated by the Phase-1 column. One explanation could be that the description by the McCabe-Thiele method might reached its limit to be applicable for ultra-low concentrations. Since the sample was not directly extracted from the column outlet, but at a port of the purification system, another possibility is, that leaks or internally contaminated pipes between the two subsystems affected the sample collection. Additionally, the transport and preparation could have potentially contaminated the liquid-out sample. For this reason, the absolute concentration in the liquid-out line during the distillation process may have been lower, and thus, the reduction factor might be even higher. This would lead to a lower HETP value.

However, the impurity of $(730 \pm 140)$ ppq is too high for the XENON1T design

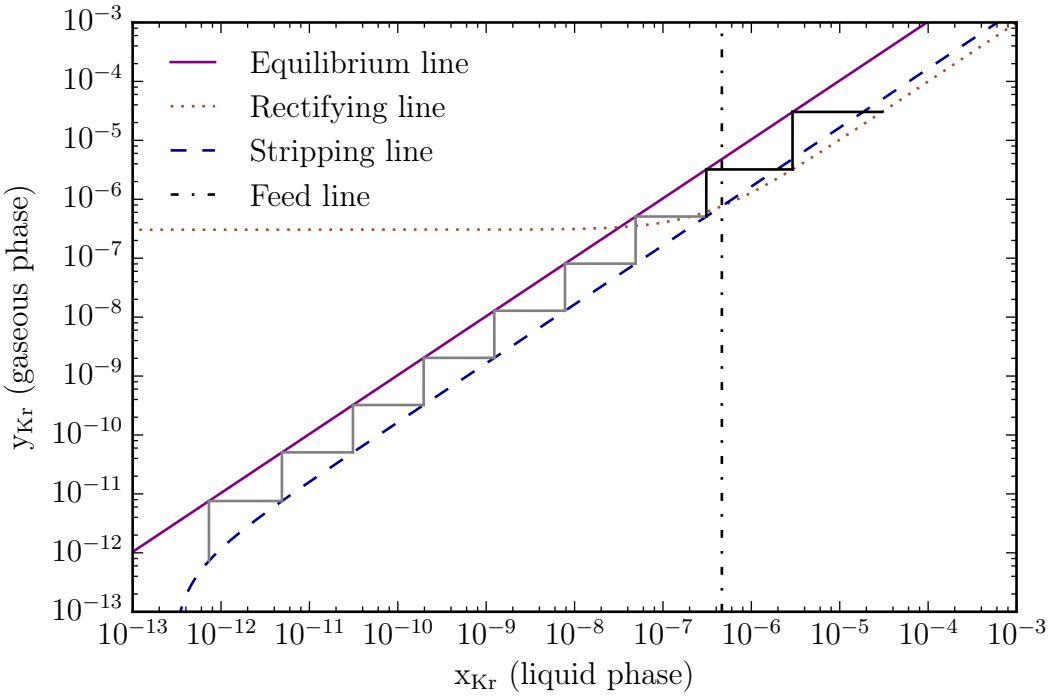


Figure 4.6: **McCabe-Thiele diagram for Phase-2 system:** The McCabe-Thiele method is applied following the conditions during the commissioning run at LNGS. In the stripping section below the feed height of 192 cm, 7 theoretical distillation stages can be drawn, indicated in solid grey. From this, a HETP value of about 27 cm was estimated.

goal of 200 ppq. Therefore, another sample for an RGMS measurement was extracted directly from the column outlet during a later distillation process to avoid any contamination as described above. During the cleaning of raw xenon with an input concentration of about 50 ppb, the purified xenon was found with a krypton in xenon concentration of

$$c_B < 48\,\text{ppq} \quad (90\,\%\,\text{C.L.}), \tag{4.10}$$

only limited by the sensitivity of the RGMS during the measurements. The obtained value is comparable to the lowest ever measured concentration of less than 26 ppq from Phase-1 and is a about a factor four better than required for XENON1T. The achieved natural krypton in xenon concentrations of different dark matter experiments are summarized in table 4.1 for comparison. It can be seen that new standards were set with the two phases of the distillation plant for XENON1T.

Table 4.1: **Results on the krypton concentration measurements of different experiments [61].**

| Experiment | Technique | $^{nat}$Kr/Xe [ppq] | |
|---|---|---|---|
| XENON100 | Distillation | 950 | [50] |
| PandaX | Distillation | 1000 | [76] |
| XMASS | Distillation | 2700 | [77] |
| LUX | Chromatography | $< 200$ | [78] |
| XENON1T Phase-1 | Distillation | $< 26$ | [60, 61] |
| XENON1T final | Distillation | $< 48$ | [61] |

# Online ReStoX distillation 5

The commercially acquired xenon gas was transferred into ReStoX from bottles before the initial filling of the detector. During this procedure, each bottle was screened with a gas-chromatographic system (GC) for impurities such as hydrogen, argon and krypton as well as nitrogen and oxygen. Bottles with a krypton in xenon concentration greater 50 ppb were not filled to ReStoX, but were collected for a distillation campaign in order to prevent a contamination of the overall xenon inventory inside the storage system. Some of these bottles were used to determine the separation factor of the Phase-2 distillation plant after commissioning at XENON1T, as presented in section 4.2. The final composition of the 3.5 tonnes of mixed xenon inside the ReStoX was measured and compared to the result of the single bottle measurements. The extracted samples from the gaseous phase of ReStoX are summarized in table 5.1. Since the GC system was not sensitive to helium, the concentration was measured with a mass spectrometer setup in Heidelberg. The filling procedure and impurity measurements are summarized in [68, 69].

The concentration for each impurity in the gaseous phase of ReStoX is larger compared to the estimation from the bottle screening. This can be explained from the fact, that ReStoX itself is a static single-stage distillation system, where the lighter contaminants with respect to xenon are enriched in the gas phase above the liquid due to their higher relative volatility $\alpha$, as described in section 3.1. This phenomenon is also true for helium as the lightest noble gas.

If the helium-enriched xenon gas with a measured concentration of

Table 5.1: Comparison of the estimation from bottle screening and ReStoX gas phase measurements. Note that oxygen and argon cannot be separated by the GC system. The helium concentration was measured with a mass spectrometer system in Heidelberg. Results taken from [69].

| **Impurity** | **Bottle estimate [ppm]** | **ReStoX gas phase [ppm]** |
|---|---|---|
| $H_2$ | 0.06 - 0.1 | $0.50 \pm 0.05$ |
| He | - | $66.0 \pm 2.0$ |
| $O_2$ + Ar | 0.25 - 0.55 | $4.3 \pm 0.4$ |
| $N_2$ | 0.99 - 1.65 | $3.1 \pm 0.4$ |
| Kr | 0.003 - 0.025 | $0.050 \pm 0.005$ |

$c_{\mathrm{He,GXe}} = (66 \pm 2)$ ppm was filled to the detector first, the helium might harm the PMTs by migrating into the evacuated housing. As consequence, the charge avalanche between the dynodes within the PMT ionizes the trapped helium atoms. This creates afterpulses [56] and thus, potentially destroys the functionality or decreases the lifetime of the photo sensors. Therefore, the gas phase of ReStoX ($\mathcal{O}(38\,\mathrm{kg})$ of xenon) was continuously looped through the distillation column in order to decrease the helium content. The procedure of this online distillation mode along with the involved subsystems is described in section 3.3.3. In total, the distillation system processed 225 kg of xenon at a flow of 8.9 slpm (3.2 kg/h) between 06 Mar 2016 and 09 Mar 2016. During the purification, several samples were extracted and measured for the respective helium and krypton content to monitor the evolution of these impurities.

At the beginning of this chapter, a kinetic gas model is developed to describe the migration of particles between a liquid and gaseous xenon interface. Based on this, a model for an ideal online distillation operation is derived in the second section and different scenarios are simulated. The third section summarizes the different phases of the distillation operation along with details about the sample extraction. Then, an analysis of the samples in terms of the krypton in xenon amount is performed and the online distillation model is applied to the evolution. In the last part, the helium removal is discussed and the relative volatility of helium is determined.

## 5.1 Kinetic gas model

In order to understand the particle migration from liquid into gas in a liquid-gas interface, a probabilistic particle model based on kinematic gas theory is developed. In a first step, the liquid-gas interface of a single gas species, e.g. xenon, is investigated. Figure 5.1 visualizes such an interface. The closed volume is filled with liquid L up to the height $h_{\mathrm{L}}$.

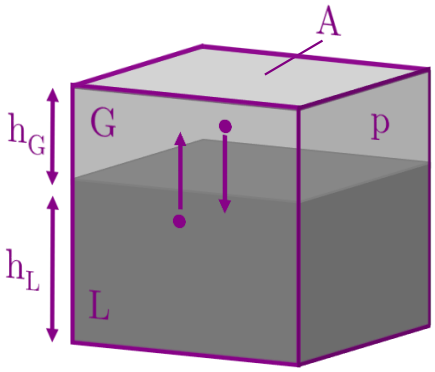


Figure 5.1: **Scheme of a liquid-gas interface:** The closed volume is filled with liquid L up to a height $h_{\mathrm{L}}$. In equilibrium, a gaseous phase G forms with a height $h_{\mathrm{G}}$ and the partial pressure p. The interface surface is denoted with A. Particles can change from liquid to gas and vice versa for a given temperature.

In equilibrium, a gaseous phase G forms above the liquid with a height $h_\mathrm{G}$ and partial pressure p. This pressure is independent from the heights $h_\mathrm{L}$ and $h_\mathrm{G}$ as well as the interface surface A. For a given temperature and a certain velocity and direction, atoms can overcome the binding of the liquid phase and change into the gas. The rate of vaporizing atoms can be expressed as

$$\dot{N}_{\mathrm{L}\to\mathrm{G}} = \sigma \cdot A \cdot f \cdot \chi_{\mathrm{L}\to\mathrm{G}}. \tag{5.1}$$

Here, $\sigma$ denotes the atom density at the surface, given by the number of atoms near the surface $N_\mathrm{surf}$ over the surface A. Furthermore, $f$ is the trial frequency of a particle to change from liquid into gas, while $\chi_{\mathrm{L}\to\mathrm{G}}$ is the vaporize probability.

On the other hand, a counterflux of atoms migrating from the gas into the liquid exists. The rate of liquefying atoms can be expressed as

$$\dot{N}_{\mathrm{G}\to\mathrm{L}} = n_\mathrm{G} \cdot \frac{\bar{v}}{4} \cdot A \cdot \chi_{\mathrm{G}\to\mathrm{L}}. \tag{5.2}$$

The atom density in the gas is given by $n_\mathrm{G}$, while the mean velocity of the atoms is $\bar{v}$. In combination, the expression $n_\mathrm{G} \cdot \frac{\bar{v}}{4}$ denotes the atom flux towards the liquid-gas interface[1]. The liquefying probability is $\chi_{\mathrm{G}\to\mathrm{L}}$, which depends on the velocity and the direction of the atom. With the ideal gas law

$$pV = \nu RT \quad \text{and} \quad R = k_B \cdot N_A \tag{5.3}$$

the gas density $n_\mathrm{G}$ can be rewritten as

$$n_\mathrm{G} = \frac{N}{V} = \frac{\nu N_A}{V} = \frac{pN_A}{RT} = \frac{p}{k_B T}. \tag{5.4}$$

Here, $N$ denotes the number of atoms in a volume $V$. Furthermore, $\nu$ is the amount of substance in the gas, $N_A$ is the Avogadro constant ($6.022 \times 10^{23}\,1/\mathrm{mol}$) and $R$ is the gas constant ($8.314\,\mathrm{J}/(\mathrm{mol}\cdot\mathrm{K})$). It can be seen that the atom density can be expressed as the pressure $p$ in the system over the Boltzmann constant $k_B$ ($1.38 \times 10^{-23}\,\mathrm{J/K}$) and the temperature $T$.

In equilibrium between the liquid and the gas phase, both fluxes are the same ($\dot{N}^\mathrm{e}_{\mathrm{L}\to\mathrm{G}} = \dot{N}^\mathrm{e}_{\mathrm{G}\to\mathrm{L}}$) and the pressure in the system is $p_\mathrm{e}$. It follows

$$\sigma \cdot A \cdot f \cdot \chi_{\mathrm{L}\to\mathrm{G}} = \frac{p_\mathrm{e}}{k_B T} \cdot \frac{\bar{v}}{4} \cdot A \cdot \chi_{\mathrm{G}\to\mathrm{L}} \tag{5.5}$$

$$p_\mathrm{e} = \frac{4 \cdot \sigma \cdot f \cdot \chi_{\mathrm{L}\to\mathrm{G}} \cdot k_B T}{\bar{v} \cdot \chi_{\mathrm{G}\to\mathrm{L}}}. \tag{5.6}$$

The pressure is defined only by quantities that depend on the gas species as well as on temperature.

In a next step, these equations can be used to investigate the behavior of the liquid-gas interface out of equilibrium for $p \neq p_\mathrm{e}$. In this case, the vaporizing rate does not change, i.e. $\dot{N}_{\mathrm{L}\to\mathrm{G}} = \dot{N}^\mathrm{e}_{\mathrm{L}\to\mathrm{G}}$, but the liquefying rate $\dot{N}_{\mathrm{G}\to\mathrm{L}}$ is different to the equilibrium rate $\dot{N}^\mathrm{e}_{\mathrm{G}\to\mathrm{L}}$:

$$\dot{N}_{\mathrm{G}\to\mathrm{L}} = \frac{p}{k_B T} \cdot \frac{\bar{v}}{4} \cdot A \cdot \chi_{\mathrm{G}\to\mathrm{L}} = \frac{p}{p_\mathrm{e}} \dot{N}^\mathrm{e}_{\mathrm{G}\to\mathrm{L}} = \frac{p}{p_\mathrm{e}} \dot{N}^\mathrm{e}_{\mathrm{L}\to\mathrm{G}} = \frac{p}{p_\mathrm{e}} \dot{N}_{\mathrm{L}\to\mathrm{G}}. \tag{5.7}$$

[1] This flux is equivalent to a particle flux through an aperture.

The net particle flux from the liquid into the gaseous phase for $p < p_\mathrm{e}$ (or vice versa for $p > p_\mathrm{e}$) is then

$$\Delta\dot{N} = \dot{N}_{\mathrm{L}\to\mathrm{G}} - \dot{N}_{\mathrm{G}\to\mathrm{L}} = \frac{p_\mathrm{e} - p}{p_\mathrm{e}}\dot{N}_{\mathrm{L}\to\mathrm{G}} = \frac{\Delta p}{p_\mathrm{e}}\dot{N}_{\mathrm{L}\to\mathrm{G}}. \tag{5.8}$$

Since the system reacts on a pressure difference $\Delta p$ with a net particle flux $\Delta\dot{N} \sim \Delta p$, it returns exponentially in time with a time constant $\tau$ to the equilibrium pressure $p_\mathrm{e}$:

$$p(t) = p_\mathrm{e} + (p(t=0) - p_\mathrm{e})e^{-\frac{t}{\tau}}. \tag{5.9}$$

This is equivalent to

$$\Delta p(t) = \Delta p(t=0)e^{-\frac{t}{\tau}}. \tag{5.10}$$

The time constant $\tau$ is derived in the following. Based on equations (5.1) and (5.8), the net particle flux can be rewritten as

$$\Delta\dot{N} = \frac{\Delta p}{p_\mathrm{e}} \cdot A \cdot \frac{\dot{N}_{\mathrm{L}\to\mathrm{G}}}{A} = \frac{\Delta p}{p_\mathrm{e}} \cdot A \cdot \sigma \cdot f \cdot \chi_{\mathrm{L}\to\mathrm{G}} = \frac{\Delta p}{p_\mathrm{e}} \cdot A \cdot K(a,T) \tag{5.11}$$

$$\text{with} \quad K(a,T) := \sigma \cdot f \cdot \chi_{\mathrm{L}\to\mathrm{G}}. \tag{5.12}$$

The defined $K(a,T)$ depends only on the gas species $a$ and the temperature $T$, while the surface $A$ cancels out[2]. On the other hand, with the ideal gas law (see equation (5.3)) the number of atoms in the gas with $N_\mathrm{G} = N$ can be expressed as

$$N = \nu \cdot N_A = \frac{pV}{k_B T} = p \cdot \frac{h_\mathrm{G} \cdot A}{k_B T}. \tag{5.13}$$

It follows

$$\Delta\dot{N} = \Delta\dot{p} \cdot \frac{h_\mathrm{G} \cdot A}{k_B T}. \tag{5.14}$$

Using equations (5.10), (5.11) and (5.14), the following differential equation for the particle direction from gas to liquid can be set up:

$$\Delta\dot{p} = \frac{K(a,T) \cdot k_B T}{p_\mathrm{e}} \cdot \frac{1}{h_\mathrm{G}} \cdot \Delta p = -\frac{1}{\tau}\Delta p. \tag{5.15}$$

From that, the time constant can be derived as

$$\tau = \tau_0 \cdot h_\mathrm{G} = \frac{p_\mathrm{e}}{K(a,T) \cdot k_B T} \cdot h_\mathrm{G}. \tag{5.16}$$

It depends on the parameters describing the dynamics of the system and thus, the gas species, on the temperature as well as on the geometric height $h_\mathrm{G}$, but not on the surface A.

Finally, the following relation can be derived for the liquid-gas interface based on the ideal gas law:

$$\frac{1}{\tau}\Delta pV = \Delta\dot{p}V = (\dot{p} - \dot{p}_\mathrm{e})\,V = \dot{p}V = \frac{\partial}{\partial t}\left(k_B T \cdot N_\mathrm{G}\right). \tag{5.17}$$

The same arguments and derivations above are valid for an individual atom species in a gas mixture, e.g. krypton in xenon, according to Raoult's law and can be applied to describe the particle flux during an online distillation process. This will be investigated in the next section.

[2]For a gas mixture it depends on the fraction of the given gas species via $\sigma$.

## 5.2 Ideal online distillation model

The idea of an online distillation in an ideal situation is illustrated in figure 5.2. The following derivations are valid for all lighter noble gases with respect to xenon, and will be exemplary shown for krypton.

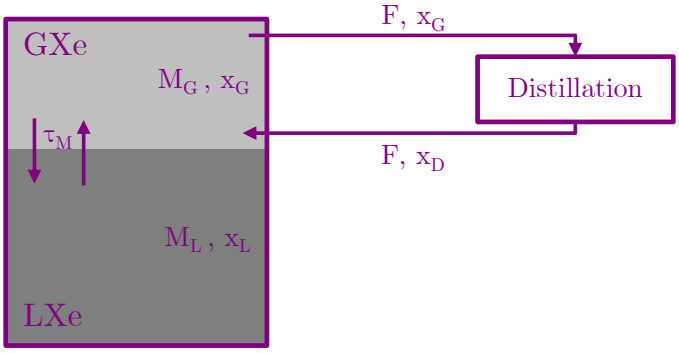


Figure 5.2: **Scheme of an ideal online distillation:** Xenon with a krypton concentration $x_G$ from the gas phase GXe (mass $M_G$) is removed at a flow $F$ and is purified with the distillation column. From here, xenon with a concentration of $x_D$ is fed back at the same flow. The krypton from the liquid phase LXe (mass $M_L$) with a concentration $x_L$ is then migrating into the gas. The exchange time constant between liquid and gas is denoted as $\tau_M$.

The xenon with a krypton fraction of $x_G$ is extracted at a flow $F$ from the gaseous phase (GXe) with the mass $M_G$ and is sent to the distillation plant. From here, xenon with a krypton concentration $x_D$ returns to the GXe at the same flow neglecting off-gas losses. The liquid phase (LXe) possesses a mass of $M_L$ and a krypton fraction $x_L$. The exchange time constant between the two phases is denoted by $\tau_M$.

At equilibrium between the liquid-gas interface, the fraction of krypton in the GXe $x_G$ is related to the fraction in the LXe part $x_L$ via the relative volatility $\alpha$, as introduced in section 3.1. For $x_L << (\alpha - 1)$ follows

$$x_G \approx \alpha x_L. \tag{5.18}$$

Furthermore, it follows for the xenon fractions in gas and liquid $x_{G,Xe} \approx x_{L,Xe} \approx 1$, as the gas mixture is mainly xenon with trace amounts of krypton. Thus, the pressure in the system $p$ is equal to the partial pressure $p_{e,Xe}$ of xenon. With that, the relative volatility in this case is defined by

$$\alpha = \frac{x_G}{x_L} = \frac{p_{e,Kr}}{p} \tag{5.19}$$

with $p_{e,Kr} = x_G^e \cdot p$ being the partial pressure of krypton.

Finally, a differential equation for each of the two phases can be set up that describes the number of krypton particles over time during the online distillation. Based on equation (5.17) and the ideal gas law, the equation for the GXe phase

is

$$\begin{aligned}\frac{\partial}{\partial t}\left(k_B T \cdot N_{\mathrm{G,Kr}}\right) &= \frac{\partial}{\partial t}\left(x_{\mathrm{G}} \cdot pV\right) \\ &= \dot{x}_{\mathrm{G}} \cdot pV \\ &= \frac{1}{\tau_{\mathrm{M,G}}} \Delta pV - \left(x_{\mathrm{G}} - x_{\mathrm{D}}\right) \frac{F}{pV} \cdot pV, \end{aligned} \tag{5.20}$$

with

$$\Delta p = \left(\alpha x_{\mathrm{L}} - x_{\mathrm{G}}\right) \cdot p \quad \text{and} \quad \frac{1}{\tau_{\mathrm{G}}} := \frac{F}{pV}. \tag{5.21}$$

The first term in equation (5.20) $\frac{1}{\tau_{\mathrm{M,G}}} \Delta pV$ indicates the krypton migration from the liquid into the gas when the system is away from equilibrium due to distillation. It depends on the migration time constant $\tau = \tau_{\mathrm{M,G}}$ from equation (5.16) and is proportional to the difference with the equilibrium concentration $(\alpha x_{\mathrm{L}} - x_{\mathrm{G}})$.

The second term represents the krypton extraction $-x_{\mathrm{G}} \cdot F/pV$ from the GXe phase to the distillation column. Additionally, a krypton rate of $+x_{\mathrm{D}} \cdot F/pV$ returns from the column. Both fluxes can be summarized to the term $-\left(x_{\mathrm{G}} - x_{\mathrm{D}}\right)/\tau_{\mathrm{G}}$ with $\tau_{\mathrm{G}}$ being the GXe cycle time through the column.

In this work, usually the krypton concentration in xenon is measured instead of a particle number. Therefore, the equation (5.20) can be written in terms of concentrations as

$$\dot{x}_{\mathrm{G}} = \frac{1}{\tau_{\mathrm{M,G}}} \left(\alpha x_{\mathrm{L}} - x_{\mathrm{G}}\right) - \frac{1}{\tau_{\mathrm{G}}} \left(x_{\mathrm{G}} - x_{\mathrm{D}}\right). \tag{5.22}$$

Analogously, the evolution in the liquid phase can be derived as

$$\begin{aligned}\frac{\partial}{\partial t}\left(k_B T \cdot N_{\mathrm{L,Kr}}\right) &= \frac{\partial}{\partial t}\left(x_{\mathrm{L}} \cdot pV\right) \\ &= \dot{x}_{\mathrm{L}} \cdot pV \\ &= -\frac{1}{\tau_{\mathrm{M,L}}} \Delta pV = -\frac{1}{\tau_{\mathrm{M,L}}} \left(\alpha x_{\mathrm{L}} - x_{\mathrm{G}}\right) pV \end{aligned} \tag{5.23}$$

and thus,

$$\dot{x}_{\mathrm{L}} = -\frac{1}{\tau_{\mathrm{M,L}}} \left(\alpha x_{\mathrm{L}} - x_{\mathrm{G}}\right). \tag{5.24}$$

Here, the krypton can leave the liquid phase only via migration into the gaseous phase. Furthermore, for online distillation close to equilibrium ($\tau_{\mathrm{G}} >> \tau_{\mathrm{M,G}}, \tau_{\mathrm{M,L}}$), the same number of krypton atoms that changes into the GXe reservoir needs to leave the LXe reservoir. Hereby, $\tau_{\mathrm{M,G}}$ denotes the time constant for the gaseous phase, while $\tau_{\mathrm{M,L}}$ denotes the one for the liquid phase. These constants are not the same, but are related via the masses in both phases. This relation is derived in the following. During the online distillation, equations (5.22) and (5.24) are valid. When stopping the distillation ($\rightarrow \left(x_{\mathrm{G}} - x_{\mathrm{D}}\right)/\tau_{\mathrm{G}} = 0$), the system returns exponentially towards equilibrium by particle migration, as derived in equation (5.8). As mentioned before, the krypton amount going into the gas has to be equal to the amount that leaves the liquid. It follows with the respective masses $M_{\mathrm{G}}$ for the gas and $M_{\mathrm{L}}$ for the liquid

$$\frac{\partial(M_{\mathrm{G}} \cdot |x_{\mathrm{G}}|)}{\partial t} = \frac{\partial(M_{\mathrm{L}} \cdot |x_{\mathrm{L}}|)}{\partial t}. \tag{5.25}$$

For no distillation ($F = 0$) and for constant mass reservoirs over time and thus, for a constant filling height in the liquid-gas interface, above equation can be rewritten as

$$M_{\mathrm{G}} \cdot |\dot{x}_{\mathrm{G}}| = M_{\mathrm{L}} \cdot |\dot{x}_{\mathrm{L}}| \tag{5.26}$$

$$\Leftrightarrow \frac{M_{\mathrm{G}}}{\tau_{\mathrm{M,G}}} (\alpha x_{\mathrm{L}} - x_{\mathrm{G}}) = \frac{M_{\mathrm{L}}}{\tau_{\mathrm{M,L}}} (\alpha x_{\mathrm{L}} - x_{\mathrm{G}}) \tag{5.27}$$

$$\Leftrightarrow \tau_{\mathrm{M,L}} = \tau_{\mathrm{M,G}} \frac{M_{\mathrm{L}}}{M_{\mathrm{G}}}. \tag{5.28}$$

This relation holds also for online distillation ($F \neq 0$). Finally, the coupled differential equations to describe the krypton evolution in the gaseous and liquid reservoir in a liquid-gas interface for an ideal online distillation process can be written as

$$\dot{x}_{\mathrm{G}} = \frac{1}{\tau_{\mathrm{M,G}}} (\alpha x_{\mathrm{L}} - x_{\mathrm{G}}) - \frac{1}{\tau_{\mathrm{G}}} (x_{\mathrm{G}} - x_{\mathrm{D}}), \tag{5.29}$$

$$\dot{x}_{\mathrm{L}} = -\frac{1}{\tau_{\mathrm{M,G}}} \frac{M_{\mathrm{G}}}{M_{\mathrm{L}}} (\alpha x_{\mathrm{L}} - x_{\mathrm{G}}). \tag{5.30}$$

In order to solve the equations and to predict the evolution over time, the coupled system is integrated with the function *odeint* from the *scipy* python package for a set of starting conditions. Then, in each time step, the solution from the last step is used for the integration. In this manner, the concentrations $x_{\mathrm{G}}$ and $x_{\mathrm{L}}$ are computed as function of time $t$.

To investigate the behavior of the system, several situations are simulated. These are not necessarily representative for a potential online distillation process in XENON1T, but can give a handle on how the system can react to different given conditions.

Case 1: It is assumed that no krypton is returning from the distillation column ($x_{\mathrm{D}} = 0$) and that the system is in equilibrium before starting the distillation process ($(\alpha x_{\mathrm{L}} - x_{\mathrm{G}}) = 0$). A typical krypton starting concentration in the liquid is $x_{\mathrm{L},0} = 1.0 \times 10^{-9}$ mol/mol. This leads at equilibrium to a krypton fraction in the gas of $x_{\mathrm{G},0} = 1.0 \times 10^{-8}$ mol/mol with $\alpha = 10$. Furthermore, $M_{\mathrm{G}} = 10\,\mathrm{kg}$ and $M_{\mathrm{L}} = 1000\,\mathrm{kg}$ are fixed. The reaction of the system to different time constants starting from partcile equilibrium (case 1), but sharing the same parameters as defined above, are simulated and visualized in figure 5.3. Furthermore, the parameters and values are summarized in table 5.2.

In the top panel (case 1a), a system with values for the time constants typical for XENON1T ($\tau_{\mathrm{G}} = 4\,\mathrm{h} = 0.17\,\mathrm{d}$ and $\tau_{\mathrm{M,G}} = 1\,\mathrm{h} = 0.04\,\mathrm{d} \rightarrow \tau_{\mathrm{M,L}} = 100\,\mathrm{h} = 4.17\,\mathrm{d}$) is presented. It can be seen that both curves start with their respective starting krypton fraction. The $x_{\mathrm{G}}$ (grey solid line) features a decreasing slope during the first hours after starting. Then, both curves decrease in parallel with a ratio $x_{\mathrm{G}}/x_{\mathrm{L}} = 8.12$ and possess the same effective time constant of $\tau_{\mathrm{eff}} = 2.22\,\mathrm{d}$, as indicated by the dashed brown lines.

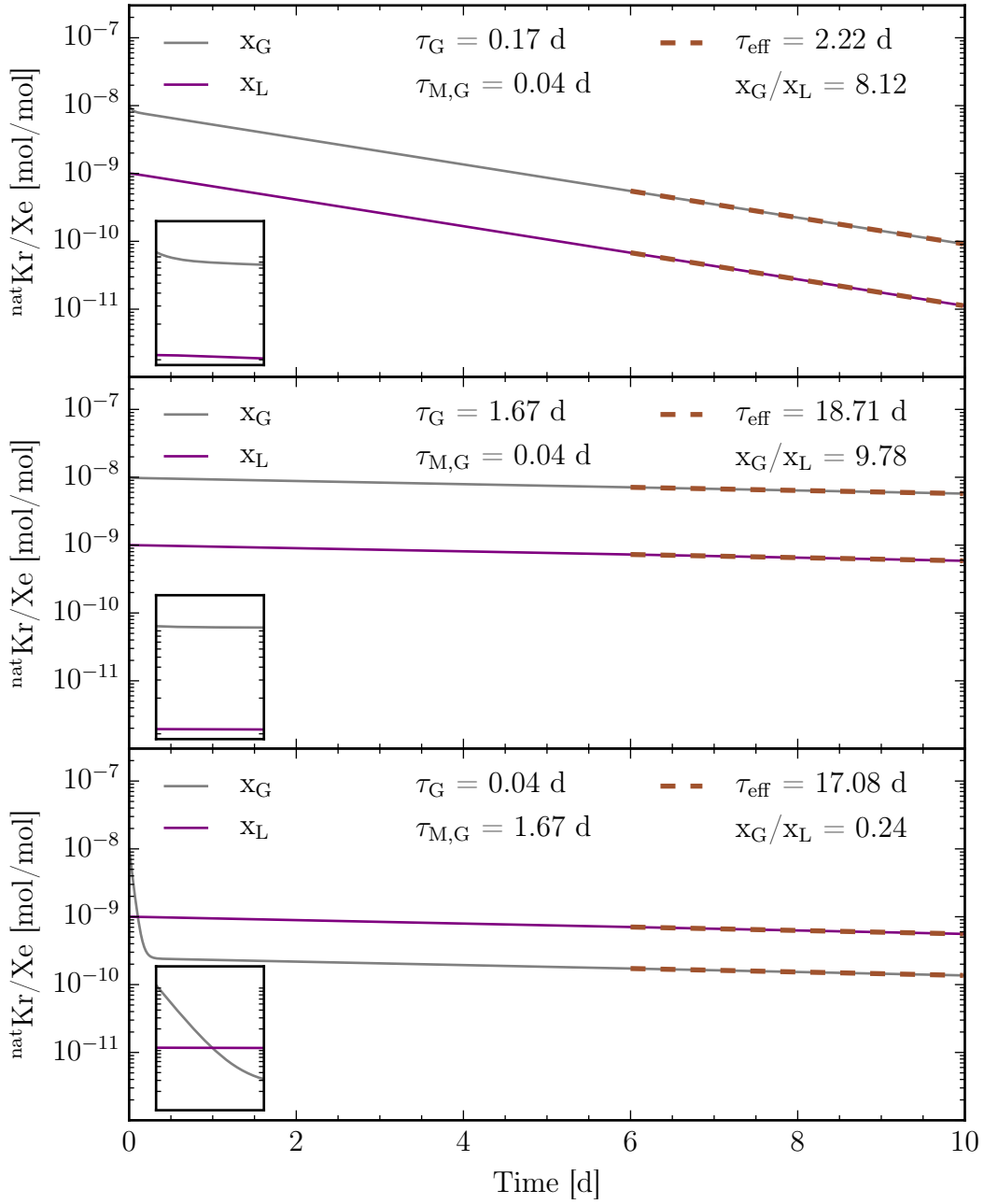


Figure 5.3: **Simulation for case 1:** In all three panels, the grey solid line represents the krypton fraction in the gaseous phase $x_G$, while the fraction in the liquid $x_L$ is visualized in purple. The insets show a zoom in of the evolution for the first 0.2 d. In each case, the same conditions were applied except the time constants, as summarized in table 5.2. The time constants for the GXe cycle time $\tau_G$ and the migration time $\tau_{M,G}$ are stated in the respective panel. In each case, both curves feature the same effective time constant $\tau_{eff}$ in the long term behavior with a constant ratio $x_G/x_L$. The effective time constant and the ratio are different for each case and depend on the given conditions.

Table 5.2: Set of parameters used for the simulation of case 1. In all three cases 1a, 1b and 1c, particle equilibrium was assumed before starting the distillation process.

| Parameter | Case 1a | Case 1b | Case 1c |
|---|---|---|---|
| $\alpha$ | | 10.0 | |
| $x_{\mathrm{L},0}$ | | $1.0 \times 10^{-9}$ mol/mol | |
| $x_{\mathrm{G},0}$ | | $1.0 \times 10^{-8}$ mol/mol | |
| $M_{\mathrm{G}}$ | | 10 kg | |
| $M_{\mathrm{L}}$ | | 1000 kg | |
| $\tau_{\mathrm{G}}$ | 4 h = 0.17 d | 40 h = 1.67 d | 1 h = 0.04 d |
| $\tau_{\mathrm{M,G}}$ | 1 h = 0.04 d | 1 h = 0.04 d | 40 h = 1.67 d |
| $\tau_{\mathrm{M,L}} = \tau_{\mathrm{M,G}} \frac{M_{\mathrm{L}}}{M_{\mathrm{G}}}$ | 100 h = 4.17 d | 100 h = 4.17 d | 4000 h = 166.67 d |

In the middle panel (case 1b), the cycle time of the GXe through the distillation system $\tau_{\mathrm{G}}$ is chosen to be 10 times larger than in the top panel ($\tau_{\mathrm{G}} = 40\,\mathrm{h} = 1.67\,\mathrm{d}$ and $\tau_{\mathrm{M,G}} = 1\,\mathrm{h} = 0.04\,\mathrm{d} \rightarrow \tau_{\mathrm{M,L}} = 100\,\mathrm{h} = 4.17\,\mathrm{d}$) and thus, 40 times larger than the migration time $\tau_{\mathrm{M,G}}$. The $x_{\mathrm{G}}$ evolution (grey solid line) does not feature anymore a steep decrease at the beginning of the operation, as the cycling time is much larger now than the migration time. Therefore, krypton is not removed faster from the GXe reservoir than it is recovered from the LXe reservoir. Again, both curves are parallel for the long term evolution with an effective time constant $\tau_{\mathrm{eff}} = 18.71\,\mathrm{d}$. Furthermore, the ratio of both curves is 9.78, which is almost the equilibrium ratio of 10. Both values hint towards a much less efficient online distillation process compared to before.

In the bottom panel (case 1c), the contrary situation is tested. The migration time $\tau_{\mathrm{M,G}}$ is assumed to be 40 times larger than the cycle time ($\tau_{\mathrm{G}} = 1\,\mathrm{h} = 0.04\,\mathrm{d}$ and $\tau_{\mathrm{M,G}} = 40\,\mathrm{h} = 1.67\,\mathrm{d} \rightarrow \tau_{\mathrm{M,L}} = 4000\,\mathrm{h} = 166.67\,\mathrm{d}$). In contrast to the other two simulations, the $x_{\mathrm{G}}$ (grey solid line) steeply decreases at the beginning with the time constant $\tau_{\mathrm{G}}$ and undershoots the liquid krypton fraction (purple solid line). After 0.2 d, the evolution starts to be dominated by the much larger migration time constant and the curve follows a decrease with the effective time constant $\tau_{\mathrm{eff}} = 17.08\,\mathrm{d}$. It stays below the liquid krypton fraction and both curves decrease in parallel with a constant ratio of 0.24. Thus, for $\tau_{\mathrm{G}} < \tau_{\mathrm{M,G}}, \tau_{\mathrm{M,L}}$, online distillation becomes ineffective, since the krypton from the gaseous phase is removed quickly, but not refilled fast enough from the liquid reservoir.

In all three cases, both curves share the same time constant, which leads to a constant ratio $x_{\mathrm{G}}/x_{\mathrm{L}}$. The effective time constant is a non-trivial combination of the involved time constants $\tau_{\mathrm{G}}$ and $\tau_{\mathrm{M,G}}$, the masses $M_{\mathrm{G}}$ and $M_{\mathrm{L}}$ as well as the relative volatility $\alpha$. Assuming that for large times both curves for $x_{\mathrm{G}}$ and $x_{\mathrm{L}}$ share the same effective time constant $\tau_{\mathrm{eff}}$, their evolution can be described by effective differential equations:

$$\dot{x}_{\mathrm{G}} = -\frac{x_{\mathrm{G}}}{\tau_{\mathrm{eff}}} \quad \text{for} \quad t >> 0\,\mathrm{d}, \tag{5.31}$$

$$\dot{x}_{\mathrm{L}} = -\frac{x_{\mathrm{L}}}{\tau_{\mathrm{eff}}} \quad \text{for} \quad t >> 0\,\mathrm{d}. \tag{5.32}$$

Using equations (5.29) to (5.32), the following relations are valid for large times:

$$-\frac{x_\mathrm{G}}{\tau_\mathrm{eff}} = \frac{1}{\tau_\mathrm{M,G}}\left(\alpha x_\mathrm{L} - x_\mathrm{G}\right) - \frac{x_\mathrm{G}}{\tau_\mathrm{G}} \quad \text{for} \quad x_\mathrm{D} = 0, \tag{5.33}$$

$$-\frac{x_\mathrm{L}}{\tau_\mathrm{eff}} = -\frac{1}{\tau_\mathrm{M,G}}\frac{M_\mathrm{G}}{M_\mathrm{L}}\left(\alpha x_\mathrm{L} - x_\mathrm{G}\right). \tag{5.34}$$

The second equation can be rearranged to obtain the ratio $x_\mathrm{G}/x_\mathrm{L}$:

$$\frac{x_\mathrm{G}}{x_\mathrm{L}} = \alpha - \frac{M_\mathrm{L}}{M_\mathrm{G}}\frac{\tau_\mathrm{M,G}}{\tau_\mathrm{eff}}. \tag{5.35}$$

This can be utilized to eliminate $x_\mathrm{G}$ and $x_\mathrm{L}$ from the first equation. In this manner, the effective time constant can be calculated to

$$\begin{aligned}\tau_\mathrm{eff} = \big[&\sqrt{2\tau_\mathrm{M,G}\tau_\mathrm{G}M_\mathrm{L}\left(M_\mathrm{L} - \alpha M_\mathrm{G}\right) + \tau_\mathrm{G}^2\left(\alpha M_\mathrm{G} + M_\mathrm{L}\right)^2 + \tau_\mathrm{M,G}^2 M_\mathrm{L}^2} \\ &+ \alpha\tau_\mathrm{G}M_\mathrm{G} + \tau_\mathrm{M,G}M_\mathrm{L} + \tau_\mathrm{G}M_\mathrm{L}\big] \\ &\cdot \left[2\alpha M_\mathrm{G}\right]^{-1}.\end{aligned} \tag{5.36}$$

The calculated time constants and ratios are in agreement with the simulated values, allowing for the estimation of the effective time constant for a potential online distillation process, if the migration time $\tau_\mathrm{M,G}$ is known.

Case 2: The simulations were repeated for a system away from equilibrium at the start of the distillation process. In more detail, the initial krypton fractions are set to $x_{\mathrm{L},0} = x_{\mathrm{G},0} = 1.0 \times 10^{-9}\,\mathrm{mol/mol}$, while the rest of the configuration stayed the same. Again, the cases 2a, 2b and 2c for different time constants are analyzed. The resulting curves for case 2 are visualized in figure 5.4 and the set of parameters used is summarized in table 5.3.

Table 5.3: Set of parameters used for the simulation of case 2. In case 2a, 2b, and 2c, the same krypton fractions in the liquid and in the gas were assumed before starting the distillation process.

| Parameter | Case 2a | Case 2b | Case 2c |
|---|---|---|---|
| $\alpha$ | | 10.0 | |
| $x_{\mathrm{L},0}$ | | $1.0 \times 10^{-9}\,\mathrm{mol/mol}$ | |
| $x_{\mathrm{G},0}$ | | $1.0 \times 10^{-9}\,\mathrm{mol/mol}$ | |
| $M_\mathrm{G}$ | | 10 kg | |
| $M_\mathrm{L}$ | | 1000 kg | |
| $\tau_\mathrm{G}$ | 4 h = 0.17 d | 40 h = 1.67 d | 1 h = 0.04 d |
| $\tau_\mathrm{M,G}$ | 1 h = 0.04 d | 1 h = 0.04 d | 40 h = 1.67 d |
| $\tau_\mathrm{M,L} = \tau_\mathrm{M,G}\frac{M_\mathrm{L}}{M_\mathrm{G}}$ | 100 h = 4.17 d | 100 h = 4.17 d | 4000 h = 166.67 d |

In all three cases 2a, 2b and 2c, the same long term behavior as in the cases 1a, 1b and 1c were found. The main difference is the evolution of $x_\mathrm{G}$ at the very beginning of the online distillation process, as visualized by the insets in each panel for the first 0.2 d. In the top panel (case 2a) as well as in the middle panel (case 2b), the krypton gas fraction is steeply rising. This can be explained

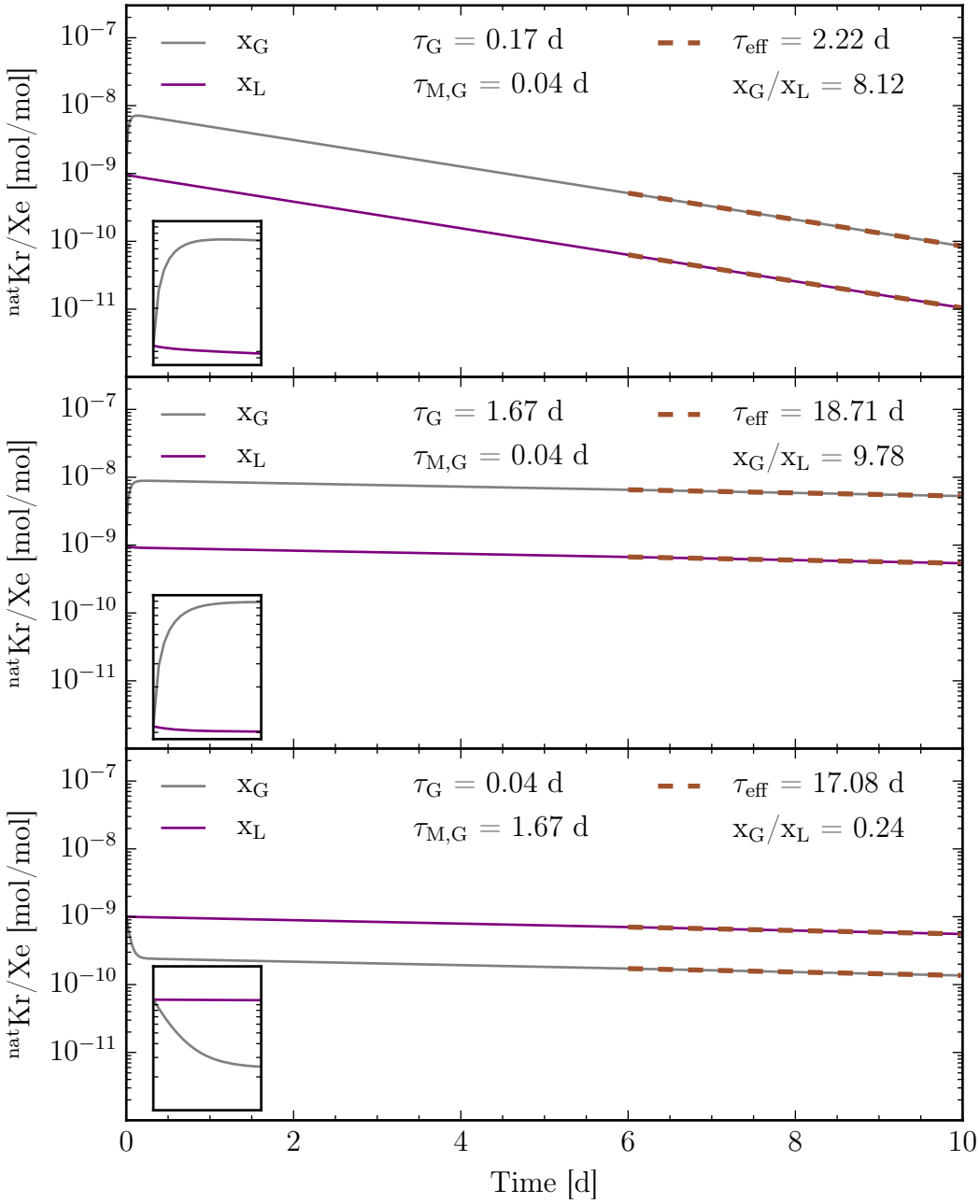


Figure 5.4: **Simulation for case 2:** The starting fractions in the liquid and the gas were assumed to be the same with $x_{L,0} = x_{G,0} = 1.0 \times 10^{-9}$ mol/mol. The insets show a zoom in of the evolution for the first 0.2 d. In all three panels, the grey solid line represents the krypton fraction $x_G$ in the GXe, while the fraction $x_L$ in the LXe is visualized in purple. The set of parameters used is summarized in table 5.3. The different time constants for the GXe cycle time $\tau_G$ and the migration time $\tau_{M,G}$ are stated in the respective panel. The same effective time constants and ratios as in case 1 (figure 5.3) were found. The difference to case 1 is the $x_G$ evolution at the very beginning of the distillation process.

with the first term in equations (5.22) and (5.24), which is driven by the short migration time constant $\tau_{M,G}$. In the bottom panel (case 2c), the GXe cycle time $\tau_G$ is much smaller than $\tau_{M,G}$. Therefore, the krypton from the gas is extracted faster than krypton can migrate from the liquid into the gas and thus, the $x_G$ evolution features a steep decrease at the beginning, comparable to the case 1c.

In summary, the simulations of case 1 and case 2 showed that the longterm removal effect does not depend on the starting krypton concentrations in the two phases, as the same effective time constants and ratios were obtained. These effective constants depend on the cycle time $\tau_G$ and the migration time $\tau_{M,G}$. Therefore, it is preferably to purify the gaseous part as fast as possible, which results into a small value of $\tau_G$ and will push the system further away from equilibrium. Additionally, a fast migration from liquid into gas is required. This migration depends on the gas species, as derived above, and for the removal in the liquid phase on the mass ratio $M_G/M_L$. In ReStoX as well as in XENON1T, the mass ratio is on the order of $10^{-2}$ and cannot be optimized further. Thus, the migration time cannot be further optimized by the operator. If the migration time is much larger than the cycle time, as in the cases 1c and 2c, the distillation process is inefficient and cannot be optimized further. A first investigation for the migration time was performed with an online distillation of ReStoX and is presented in the next sections. Based on these results, the same concept was adopted for XENON1T, as discussed in chapter 6.

## 5.3 Operation and sample extraction

During the performed ReStoX distillation operation, xenon is extracted from the GXe ReStoX phase at a process flow $F$, is then purified by the distillation column and is fed back into the GXe part. This corresponds to the process visualized in figure 5.2 and can be described by the developed online distillation model.

Here, the storage vessel ReStoX is assumed to be a static single liquid-gas interface. The different xenon masses $M_G$ and $M_L$ in the two phases can be estimated from the total xenon amount, measured to be WI301 = $(3499 \pm 5)$ kg with the ReStoX scale. The 1 bar operating pressure and saturation temperature of 164.82 K yield a liquid xenon density of 2.943 kg/L [30], corresponding to a liquid xenon volume of 1189 L. In combination with the total volume of the inner ReStoX sphere of 5005 L[3] and the gaseous density 0.01 kg/L, the mass within the GXe is calculated to be $M_G = (38 \pm 1)$ kg. Consequently, the LXe mass is $M_L = (3461 \pm 6)$ kg. The uncertainty of the GXe value was conservatively estimated to be 1 kg, allowing a 100 L uncertainty in the calculated GXe volume and taking into account that the liquid xenon volume was determined with the total xenon mass initially.

Several samples were extracted before, during and after the process in order to monitor the helium and krypton concentrations over time. In the case of helium, only the RGA system next to the distillation column was used. For krypton, a combination of GC, RGA as well as RGMS measurements is available. The

[3]The volume of heater and heat exchanger inside the inner sphere were subtracted.

sample extraction is briefly summarized here, while the analysis of the RGA samples is presented later in this section. The xenon gas from ReStoX was guided to the distillation system via one branch of the purification system, as described in section 3.3.3. Therefore, the samples were taken at a port at the purification system. Before extraction, the pipette was evacuated to a pressure of about $1.0 \times 10^{-4}$ mbar and was flushed once with xenon to clean it from potential contamination. After filling, the closed container was disconnected from the purification system and was attached to the evacuated measurement volume of the RGA system, while pipettes for the RGMS measurement were sent to MPIK Heidelberg. After opening the pipette, the measurement volume of the RGA system was filled with xenon at a pressure of 0.3 bar. The pipette was closed off again in order to achieve reproducible sample sizes. A standard krypton in xenon measurement was performed, as described in [74], where the gas is guided through the coldtrap, immersed in liquid nitrogen. Following that, a measurement of the mass-over-charge ratio $^{m}/_{z}$[4] from 1 - 41 was performed to estimate the helium ($^{m}/_{z} = 4$) content later on. The analysis of the krypton concentration is presented in section 5.4, while helium is explained in section 5.5. After the measurement, the pipette was installed again at the purification system in order to prepare the next sample extraction.

The samples give direct inside in the impurity concentrations $x_G$ in the GXe ReStoX part, as they are extracted from the purification system, while no measurement of the concentrations $x_L$ in LXe reservoir is available.

The complete investigated time span in the following lasts from 04 Mar 2016 00:00 until 16 Mar 2016 00:00 and is divided in six different operation phases:

I ReStoX in equilibrium (04 Mar 2016 00:00 - 04 Mar 2016 15:20): The GXe and LXe reservoirs are assumed to be in equilibrium. After ReStoX filling and a few weeks before the distillation, the impurity concentrations in the GXe were determined with the GC system and an additional MPIK-RGA system in Heidelberg [68, 69]. In order to make use of this knowledge, it is assumed that these concentrations did not change until distillation. No xenon was extracted from the GXe phase, and thus it is assumed that the concentration of lighter noble gases with respect to xenon in the liquid-gas interface can be related to the relative volatility $\alpha$.

II Cooling + filling DST (04 Mar 2016 15:20 - 06 Mar 2016 14:40): The distillation system was filled with gaseous xenon from ReStoX and the cooling process was initiated. For the filling, additional xenon from the GXe ReStoX phase was stepwise filled to the column. Due to the extraction, the equilibrium in ReStoX started to be disturbed, as also helium and krypton were removed in the filling process. In this period, one sample was extracted and measured with the on-site Münster RGA system.

III Online DST (06 Mar 2016 14:40 - 08 Mar 2016 08:40): Immediately after, the online distillation process was initiated. After stabilizing, the process flow was 3.2 kg/h. Xenon was extracted from the ReStoX GXe reservoir and

[4] The mass-over-charge ratio $^{m}/_{z}$ is dimensionless, as the mass is defined here as the atomic mass number A over the nuclear charge number Z.

purified with the distillation column. From here, 1 % of the feed flow was stored as off-gas in a bottle and 99 % were sent back to the GXe part of ReStoX. In total, three RGA samples were extracted during this operation phase.

IV Interruption (08 Mar 2016 08:40 - 08 Mar 2016 09:53): The chiller of the distillation plant providing cooling water for the compressors was forced to be moved to another position. Therefore, the distillation process was stopped for about 70 min.

V Online DST (08 Mar 2016 09:53 - 09 Mar 2016 16:25): Afterwards, the distillation process was re-started at the same process flow. One RGA sample and one pipette for RGMS measurement were taken during this period.

VI ReStoX to equilibrium (09 Mar 2016 16:25 - 16 Mar 2016 00:00): After the distillation flow was stopped, it is assumed that the impurities in the liquid-gas interface converge towards particle equilibrium again. To investigate this effect, an additional RGA sample was extracted two days after distillation. In parallel, the same xenon sample was stored into a pipette for RGMS and MPIK-RGA measurements for cross calibration purposes.

A more detailed overview of the different distillation flows and the relevant coupled differential equations in each period to apply the online distillation model are given in section 5.4. For a better overview, table 5.4 contains a summary of the extracted samples. The determination of the absolute concentrations is explained in section 5.4 and section 5.5.

Table 5.4: Extracted samples before, during and after the online ReStoX distillation. Samples were measured either by the on-site Münster RGA (RGA), the RMGS system or with an additional RGA system (MPIK-RGA). The last two devices are located off-site at MPIK Heidelberg. The determination of the absolute concentrations is presented in section 5.4 and section 5.5. Note that the first sample was measured a few weeks before the online distillation. Assuming equilibrium in ReStoX, as no xenon was extracted in between, the results were assumed to be still valid on 04 Mar 2016 12:00.

| Time | Phase | Methode | He/Xe [ppm] | Kr/Xe [ppb] |
|---|---|---|---|---|
| 04 Mar 2016 12:00 | I | MPIK-RGA/GC | $66.0 \pm 2.0$ | $50.0 \pm 5.0$ |
| 04 Mar 2016 17:30 | II | RGA | $66.0 \pm 5.1$ | - |
| 06 Mar 2016 12:20 | II | RGA | $43.8 \pm 3.4$ | $40.0 \pm 2.6$ |
| 06 Mar 2016 20:48 | III | RGA | $28.9 \pm 2.2$ | $24.4 \pm 1.7$ |
| 07 Mar 2016 14:30 | III | RGA | $8.9 \pm 0.7$ | $15.9 \pm 2.0$ |
| 08 Mar 2016 08:15 | III | RGA | $2.5 \pm 0.2$ | $15.7 \pm 1.3$ |
| 09 Mar 2016 11:00 | V | RGA | $0.46 \pm 0.04$ | $10.9 \pm 0.7$ |
| 09 Mar 2016 15:50 | V | RGMS | - | $12.7 \pm 2.0$ |
| 12 Mar 2016 11:19 | VI | RGA | $0.43 \pm 0.03$ | $23.1 \pm 1.8$ |
| 12 Mar 2016 11:19 | VI | MPIK-RGA/RGMS | $<4.0$ | $23.1 \pm 0.6$ |

## 5.4 Krypton removal

The primary goal of the online ReStoX distillation was the overall reduction of helium to protect the photo sensors in the TPC during the first filling of the cryostat. However, the krypton evolution can be investigated as well. As parts of the results of the krypton evolution are used for the fitting of the helium samples, krypton is discussed first. The RGMS samples were measured and analyzed off-site in Heidelberg yielding an absolute value for the krypton in xenon level. The analysis of the Münster RGA samples is explained in the following before the online distillation model can be applied.

### Sample analysis

The RGA system at LNGS was not calibrated absolutely anymore for the krypton in xenon measurement after changing of a differential pumping section in Münster just before shipment. However, the two parallel samples from 12 Mar 2016 11:19 (see table 5.4), one for the RGA and one for RGMS, allow for a cross calibration of the RGA system, as explained later on.

Since each pipette was extracted at the same port at the same pressure conditions at the purification system, all samples featured the same pressure in the measurement volume of the RGA system. Therefore, the same flow behavior during sample introduction can be expected. Thus, different measurements can be compared directly and no flow correction is applied [74]. Without the necessity of the flow correction, the krypton evolution was obtained in a different way compared to the standard procedure. The krypton determination of the first krypton pipette is exemplary presented in the following.

The pipette was connected to the RGA system and opened, such that the xenon probe was released into the sample volume. Then the pipette was closed off again to guarantee the same conditions for each sample. The respective pressure was measured to be 0.3 bar and was the same for each pipette. A mass-over-charge range from 76 to 88 was chosen with 5 PPAmu[5] and a DWELL[6] of 64, meaning that the RGA measures in steps of 0.2, where each step is measured over the time span of 64 ms. The raw measurement for the first sample is visualized in figure 5.5, showing $^{m}/_{z} = 83$ (grey, corresponding to $^{83}$Kr), $^{m}/_{z} = 84$ (purple, corresponding to $^{84}$Kr), $^{m}/_{z} = 85$ (blue, corresponding to background[7]), $^{m}/_{z} = 86$ (brown, corresponding to $^{86}$Kr) and $^{m}/_{z} = 87$ (green, corresponding to background), respectively.

In each scan, the measured current of the respective $^{m}/_{z}$-ratio is the sum from two mass steps left until two mass steps right with respect to the highest bin. As example, $^{84}$Kr is obtained from summing up 83.6 up to 84.4. This gives more statistics against the single highest bin [74]. The background within the main chamber is measured between (150–200) s, before introducing the sample to the coldtrap. The average respective background is subtracted from the spectra.

[5] PPAmu = Parts per arbitrary mass unit. The setting indicates how many steps are measured between neighboring mass-over-charge points.

[6] DWELL time is the measurement time for each step.

[7] The isotope $^{85}$Kr is not abundant enough to be measured with the RGA. Therefore, $^{m}/_{z} = 85$ is considered as background.

A steep rise in $^{83}$Kr, $^{84}$Kr and $^{86}$Kr as the most abundant isotopes occurred after opening the sample, followed by a shoulder-like structure, originating from not fully understood freezing effects within the coldtrap. However, after reaching a maximum, these isotopes are slowly decreasing. The $^{m}/_{z}$ ratios 85 and 87 are utilized to monitor the background in the chamber, whereas the mass 87 falls below the minimal signal size to be recorded. In order to obtain a value that can

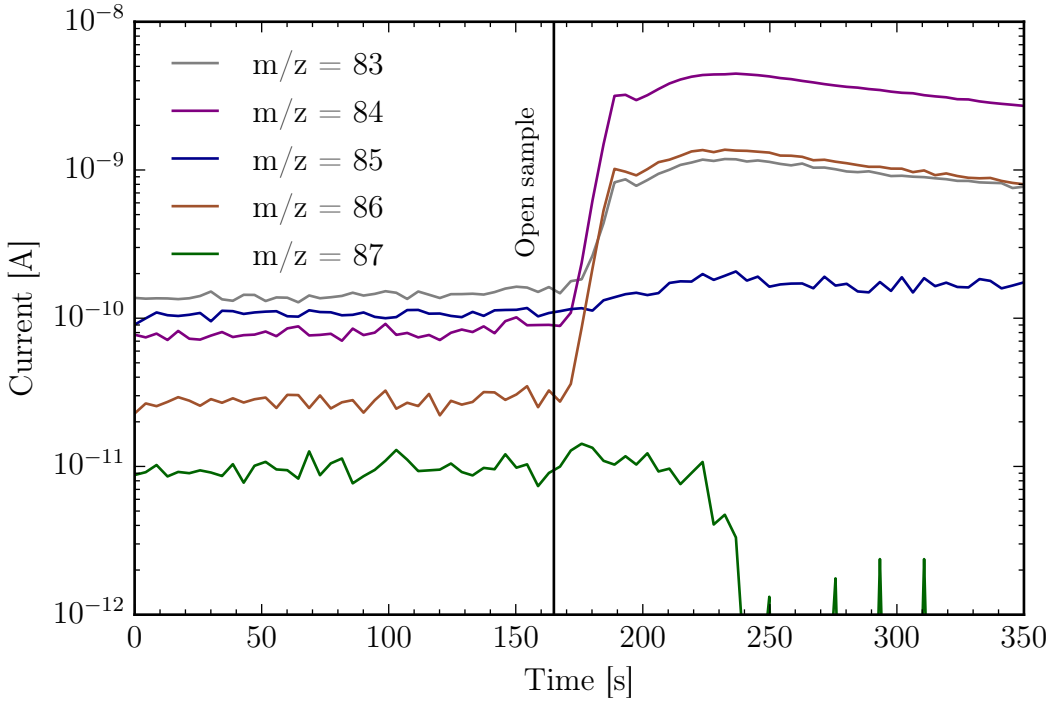


Figure 5.5: **Raw krypton in xenon RGA measurement of the first pipette.** The measured current for several krypton isotopes versus time is visualized. During the first 165 s, the respective background in the main chamber was monitored. It is averaged and used later on for the subtraction from the respective isotope. After opening to the sample volume (black vertical line), the most abundant isotopes $^{83}$Kr (grey), $^{84}$Kr (purple) and $^{86}$Kr (brown) increased, while the $^{m}/_{z}$-ratios 85 (blue) and 87 (green) followed the background in the chamber. $^{m}/_{z} = 87$ even falls below the minimal signal size to be recorded after 240 s probably because of saturation effects of the RGA system. The measurement was taken with a mass-over-charge range from 76 to 88 at a resolution of 5 PPAmu and a DWELL of 64 ms.

be compared relatively to other pipettes, the maximum of $^{83}$Kr, $^{84}$Kr and $^{86}$Kr is determined and the spectra are normalized to the respective maximum. Since all three isotopes describe the same process, the resulting normalized spectra should be comparable. This is confirmed and visualized in figure 5.6. In order to increase statistics, the integral over 60 s after the maximum is calculated for each isotope. The integration window is indicated by the green shaded area. At last, the mean of the three integrals along with the standard deviation is computed and used for the comparison to other pipettes. Like that, the three most abundant krypton

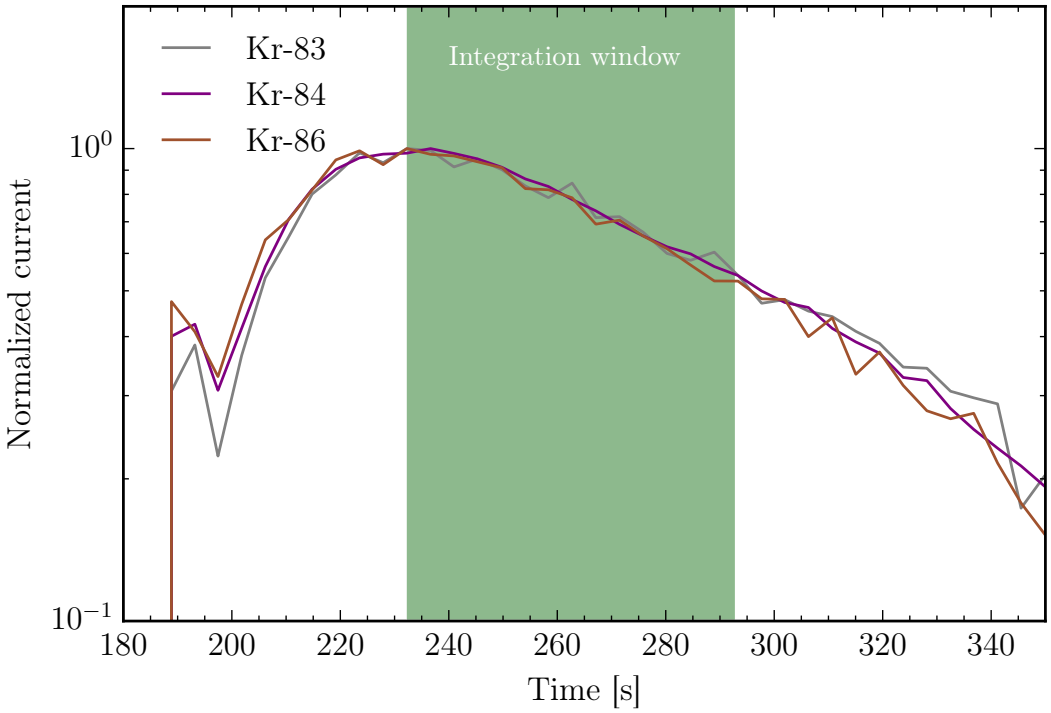


Figure 5.6: **Normalized krypton in xenon RGA measurement of the first pipette:** After determination of the maximum of $^{83}$Kr (grey), $^{84}$Kr (purple) and $^{86}$Kr (brown), the respective spectrum was normalized to the maximum. All three normalized isotope spectra follow the same behavior as expected. For better statistics, each spectrum was integrated over a 60 s window (green shaded area) and the mean and standard deviation of the three integrals was computed to allow the comparison to other pipettes.

isotopes can be utilized, yielding a more robust result compared to the usage of only $^{84}$Kr. For the analysis of the other pipettes, the respective maxima of $^{83}$Kr, $^{84}$Kr and $^{86}$Kr were found, but the spectra were normalized to the maxima of the first pipette, allowing for the relative comparison of the different samples by the normalization factor.

An additional sanity check is the calculation of the ratios between the background corrected maximum currents for the three isotopes in each sample. This is visualized in figure 5.7. The expected ratios from the natural krypton abundance are $(^{84}\mathrm{Kr}/^{83}\mathrm{Kr})_{\mathrm{nat.}} = 5.0$ (blue line) and $(^{84}\mathrm{Kr}/^{86}\mathrm{Kr})_{\mathrm{nat.}} = 3.3$ (brown line). The measured ratios $(^{84}\mathrm{Kr}/^{83}\mathrm{Kr})_{\mathrm{i,meas.}}$ (purple points) and $(^{84}\mathrm{Kr}/^{86}\mathrm{Kr})_{\mathrm{i,meas.}}$ (grey points) yield a mean of $4.2 \pm 0.1$ (purple dashed line) and $3.1 \pm 0.2$ (grey dashed line), respectively. This hints towards a different krypton isotope composition in ReStoX compared to the natural abundance[8]. However, as the ratios are consistent within the samples, the pipettes can be used to monitor the evolution.

Finally, the parallel RGMS gas sample from 12 Mar 2016 11:19 during phase VI with an absolute krypton in xenon concentration of $c_{\mathrm{VI,RGMS}} = (23.1 \pm 0.6)$ ppb

[8] A possible explanation is that one or more of the initial bottles featured a different krypton isotope composition.

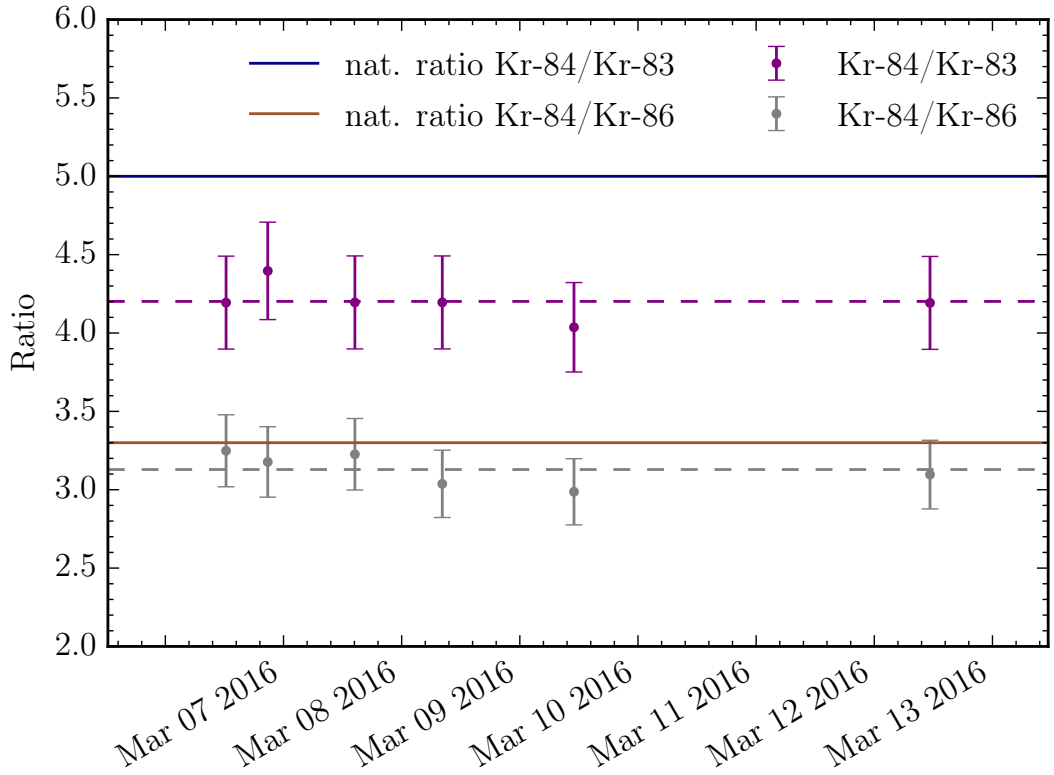


Figure 5.7: **Krypton isotope ratios:** The expected ratios from the natural krypton abundance are $({}^{84}\mathrm{Kr}/{}^{83}\mathrm{Kr})_{\mathrm{nat.}} = 5.0$ (blue line) and $({}^{84}\mathrm{Kr}/{}^{86}\mathrm{Kr})_{\mathrm{nat.}} = 3.3$ (brown line). The measured ratios $({}^{84}\mathrm{Kr}/{}^{83}\mathrm{Kr})_{\mathrm{i,meas.}}$ (purple points) and $({}^{84}\mathrm{Kr}/{}^{86}\mathrm{Kr})_{\mathrm{i,meas.}}$ (grey points) yield a mean of $4.2 \pm 0.1$ (purple dashed line) and $3.1 \pm 0.2$ (grey dashed line), respectively.

was used to transform the integrated current from the RGA measurements into an absolute scale. For pipette $i$ with an normalized integrated current $c_{\mathrm{i,RGA}}$ follows an absolute krypton in xenon concentration $c_{\mathrm{i,abs}}$ of

$$c_{\mathrm{i,abs}} = c_{\mathrm{i,RGA}} \cdot \frac{c_{\mathrm{VI,RGMS}}}{c_{\mathrm{VI,RGA}}}. \tag{5.37}$$

Here, $c_{\mathrm{VI,RGA}}$ corresponds to the normalized integrated current of the parallel RGA sample from 12 Mar 2016 11:19 during phase VI. The uncertainty $\Delta c_{\mathrm{i,abs}}$ was calculated with

$$\Delta c_{\mathrm{i,abs}} = c_{\mathrm{i,abs}} \cdot \sqrt{\left(\frac{\Delta c_{\mathrm{i,RGA}}}{c_{\mathrm{i,RGA}}}\right)^2 + \left(\frac{\Delta c_{\mathrm{VI,RGMS}}}{c_{\mathrm{VI,RGMS}}}\right)^2 + \left(\frac{\Delta c_{\mathrm{VI,RGA}}}{c_{\mathrm{VI,RGA}}}\right)^2}, \tag{5.38}$$

where the respective uncertainty is indicated by $\Delta$. The resulting absolute values are listed in table 5.4 of the previous section.

## Evolution

After determining the absolute krypton concentration $x_{\mathrm{G}}$ in all samples, the ideal online distillation model can be applied to describe the data. The equations (5.29)

and (5.30), describing the change $\dot{x}_\mathrm{G}$ over time in the GXe as well as the change $\dot{x}_\mathrm{L}$ in the LXe are repeated here:

$$\dot{x}_\mathrm{G} = \frac{1}{\tau_\mathrm{M,G}} (\alpha x_\mathrm{L} - x_\mathrm{G}) - \frac{1}{\tau_\mathrm{G}} (x_\mathrm{G} - x_\mathrm{D}) ,$$
$$\dot{x}_\mathrm{L} = -\frac{1}{\tau_\mathrm{M,G}} \frac{M_\mathrm{G}}{M_\mathrm{L}} (\alpha x_\mathrm{L} - x_\mathrm{G}) .$$

As discussed in section 4.2, the krypton reduction factor of the distillation column was determined to $\mathrm{F_{red}} = (6.4^{+1.9}_{-1.4}) \cdot 10^5$. Thus, starting at the ppb level, the output krypton concentration is comparably small and is assumed to be $x_\mathrm{D} = 0\,\mathrm{ppb}$ for the following analysis. Furthermore, the cycle time $\tau_\mathrm{G}$ is not constant, but time dependent, and is given by the ratio of the GXe mass $M_\mathrm{G}$ and the time dependent purification flow $F(t)$:

$$\tau_\mathrm{G}(t) = \frac{M_\mathrm{G}}{F(t)}. \tag{5.39}$$

The total off-gas losses were estimated to be 3 kg, which is about 0.1 % of the total ReStoX inventory. Therefore, the two mass reservoirs $M_\mathrm{G}$ and $M_\mathrm{L}$ are assumed to be constant in time. From the initial estimation, both masses are used as constrained fit parameters later on. The flow values were taken from the slow control data. Here, one averaged value each 10 s was queried to take also flow periods on the minute scale into account. Finally, the data points were linearly interpolated to reproduce the flow at any given time $t$. The flow during all operation phases is visualized in the top panel of figure 5.8. With the two remarks, the coupled differential equations can be rewritten as

$$\dot{x}_\mathrm{G} = \frac{1}{\tau_\mathrm{M,G}} (\alpha x_\mathrm{L} - x_\mathrm{G}) - \frac{F(t)}{M_\mathrm{G}} \cdot x_\mathrm{G}, \tag{5.40}$$
$$\dot{x}_\mathrm{L} = -\frac{1}{\tau_\mathrm{M,G}} \frac{M_\mathrm{G}}{M_\mathrm{L}} (\alpha x_\mathrm{L} - x_\mathrm{G}) . \tag{5.41}$$

These two equations describe the change during the ongoing distillation process and are valid for $F(t) > 0$. This is partially the case during the operation phase II, when xenon is extracted from ReStoX to further cool and fill the column. Furthermore, this is fully the case during phases III and V, the main distillation processes.

Before any extraction ($F(t) = 0$), ReStoX was assumed to be in equilibrium (phase I), and thus, $(\alpha x_\mathrm{L} - x_\mathrm{G}) = 0$. With that follows

$$\dot{x}_\mathrm{G} = 0, \tag{5.42}$$
$$\dot{x}_\mathrm{L} = 0. \tag{5.43}$$

By extracting xenon from ReStoX ($F(t) > 0$) either due to filling of the column or due to the distillation process, the system is pushed away from equilibrium. When the extraction flow is stopped again ($F(t) = 0$) and the system is out of equilibrium ($(\alpha x_\mathrm{L} - x_\mathrm{G}) \neq 0$), it converges back by particle migration between

the liquid-gas interface. The coupled differential equations change to

$$\dot{x}_{\mathrm{G}} = \frac{1}{\tau_{\mathrm{M,G}}} \left(\alpha x_{\mathrm{L}} - x_{\mathrm{G}}\right), \tag{5.44}$$

$$\dot{x}_{\mathrm{L}} = -\frac{1}{\tau_{\mathrm{M,G}}} \frac{M_{\mathrm{G}}}{M_{\mathrm{L}}} \left(\alpha x_{\mathrm{L}} - x_{\mathrm{G}}\right). \tag{5.45}$$

These equations are partially valid during phase II, and fully valid during phase IV, where the distillation process was interrupted for about 70 min, and during phase VI, after the distillation process was stopped and ReStoX was going back to equilibrium.

In order to model the measured evolution, a fitting routine was programmed in python based on a $\chi^2$-minimization with iMinuit. In each time step, the routine selects the corresponding differential equation system depending on the operation phase and the flow, as explained above. Then, as described in section 5.2, the coupled system is integrated with the function *odeint* from the *scipy* python package. In each time step, the solution from the last step is used as starting condition for the integration. In this manner, the concentrations $x_{\mathrm{G}}$ and $x_{\mathrm{L}}$ are computed for a given time $t$. At last, the resulting curve for $x_{\mathrm{G}}$ is compared to the data points and the best set of fit parameter is determined by the $\chi^2$-minimization. For a constrained fit, a quadratic penalty term is added to the $\chi^2$ value for each constrained parameter. It applies

$$\chi^2_{\mathrm{tot}} = \chi^2 + \frac{\left(p - p_0\right)^2}{\sigma^2_{p_0}} \tag{5.46}$$

with $p$ being a fit parameter, $p_0$ its constraint and $\sigma_{p_0}$ the uncertainty of the constraint.

One fit parameter is the initial krypton concentration $x_{\mathrm{G},0}$ in the GXe reservoir. As ReStoX is assumed to be in equilibrium in operation phase I and no sample from the LXe reservoir is available, the initial krypton concentration $x_{\mathrm{L},0}$ in the liquid is not a free parameter, but is set to

$$x_{\mathrm{L},0} = \frac{x_{\mathrm{G},0}}{\alpha_{\mathrm{Kr}}}. \tag{5.47}$$

The relative volatility $\alpha_{\mathrm{Kr}}$ is another fitting parameter. For the given ReStoX pressure of 1 bar and saturation temperature of 164.82 K, the expected volatility is $\alpha_{\mathrm{theo}} = 12.68$. The two masses in the liquid-gas interface are assumed to be constant over time due to a negligible off-gas flow and are estimated to be $M_{\mathrm{G}} = (38 \pm 1)\,\mathrm{kg}$ and $M_{\mathrm{L}} = (3461 \pm 6)\,\mathrm{kg}$. They were used as constrained fit parameters. Since the two masses are constant, also the filling height in the vessel is assumed to be constant. Thus, the migration time $\tau_{\mathrm{M,G}}$ is time independent and is another free parameter.

All fit parameters along with selected constraints and fitting results are summarized in table 5.5, while the best fit curves are highlighted in figure 5.8. The top panel visualizes the flow (purple) during the different operation phases I-VI (shaded areas). The middle panel contains the data points (blue for GC, purple for RGA and green for RGMS) and the fitted gaseous krypton concentration $x_{\mathrm{G}}$ (grey) and the coupled liquid krypton concentration $x_{\mathrm{L}}$ (brown). Furthermore,

Table 5.5: Best fit parameters along with their respective constraint to describe the online ReStoX distillation krypton data.

| Parameter | Constraint | Result |
|---|---|---|
| $x_{\mathrm{G},0}$ | - | $(43.4 \pm 2.0) \times 10^{-9}\,\mathrm{mol/mol}$ |
| $\alpha_{\mathrm{Kr}}$ | - | $23.2 \pm 2.8$ |
| $M_{\mathrm{G}}$ | $(38 \pm 5)\,\mathrm{kg}$ | $(37.5 \pm 1.8)\,\mathrm{kg}$ |
| $M_{\mathrm{L}}$ | $(3461 \pm 10)\,\mathrm{kg}$ | $(3461.0 \pm 3.5)\,\mathrm{kg}$ |
| $\tau_{\mathrm{M,G}}$ | - | $(0.66 \pm 0.10)\,\mathrm{d}$ |
| $\chi^2$ / NDF | - | 6.5 / 5.0 |

the inset zooms in to the first 2.5 d to show the influence of the xenon extraction in phase II. The bottom panel indicates the respective normalized residuals (blue for GC, purple for RGA and green for RGMS).

During phase I, the grey curve is constant, as expected during equilibrium of ReStoX. The fitted initial gaseous krypton concentration is $x_{\mathrm{G},0} = (43.4 \pm 2.0) \times 10^{-9}\,\mathrm{mol/mol}$ such that the grey line undershoots the measured GC data point ($(50 \pm 5) \times 10^{-9}\,\mathrm{mol/mol}$). However, both values agree within their uncertainties.

During phase II, two times a small amount of xenon was extracted to prefill and cool the column, as visible in the flow panel. The effect on the GXe concentration change is visualized in the inset of figure 5.8. The grey curve is two times decreasing and then converging back to the new equilibrium. At the end of phase II, the column was filled, such that a first steeper decrease can be observed.

Immediately after, the continuous distillation process was initiated in phase III. The stable purification flow was measured to be around $F = 3.2\,\mathrm{kg/h}$ and the grey curve depends on equations (5.40) and (5.41).

Due to the chiller movement in phase IV, the distillation process was stopped ($F(t) = 0$) and ReStoX starts to converge to equilibrium according to equations (5.44) and (5.45). This is indicated by the steep increase of the grey curve during this period. Note that the neighboring RGA sample was extracted at 08 Mar 2016 08:15, just before stopping of the process at 08 Mar 2016 08:40.

After the interruption, the online distillation was restarted (phase V) at a flow of $F = 3.2\,\mathrm{kg/h}$ and the grey curve follows again equations (5.40) and (5.41). Just before stopping of the process, a RGMS sample (green) was taken.

In phase VI, ReStoX converges to equilibrium and the grey curve follows equations (5.44) and (5.45) as soon as the distillation was stopped. This expected behavior is heavily supported by the last sample from 12 Mar 2016 11:19, measured with RGMS (green) and RGA (purple) in parallel. For the fitting, only the RGA data point was used, while the RGMS point is shown for a complete overview. Different important aspects can be derived from the last sample. First, the same sample extraction allowed to use the absolute RGMS value as a cross calibration for the RGA system. Second, it allows for a more robust determination of the migration time $\tau_{\mathrm{M,G}}$, as this variable dominates the particle migration when reaching equilibrium. Third, although the distillation

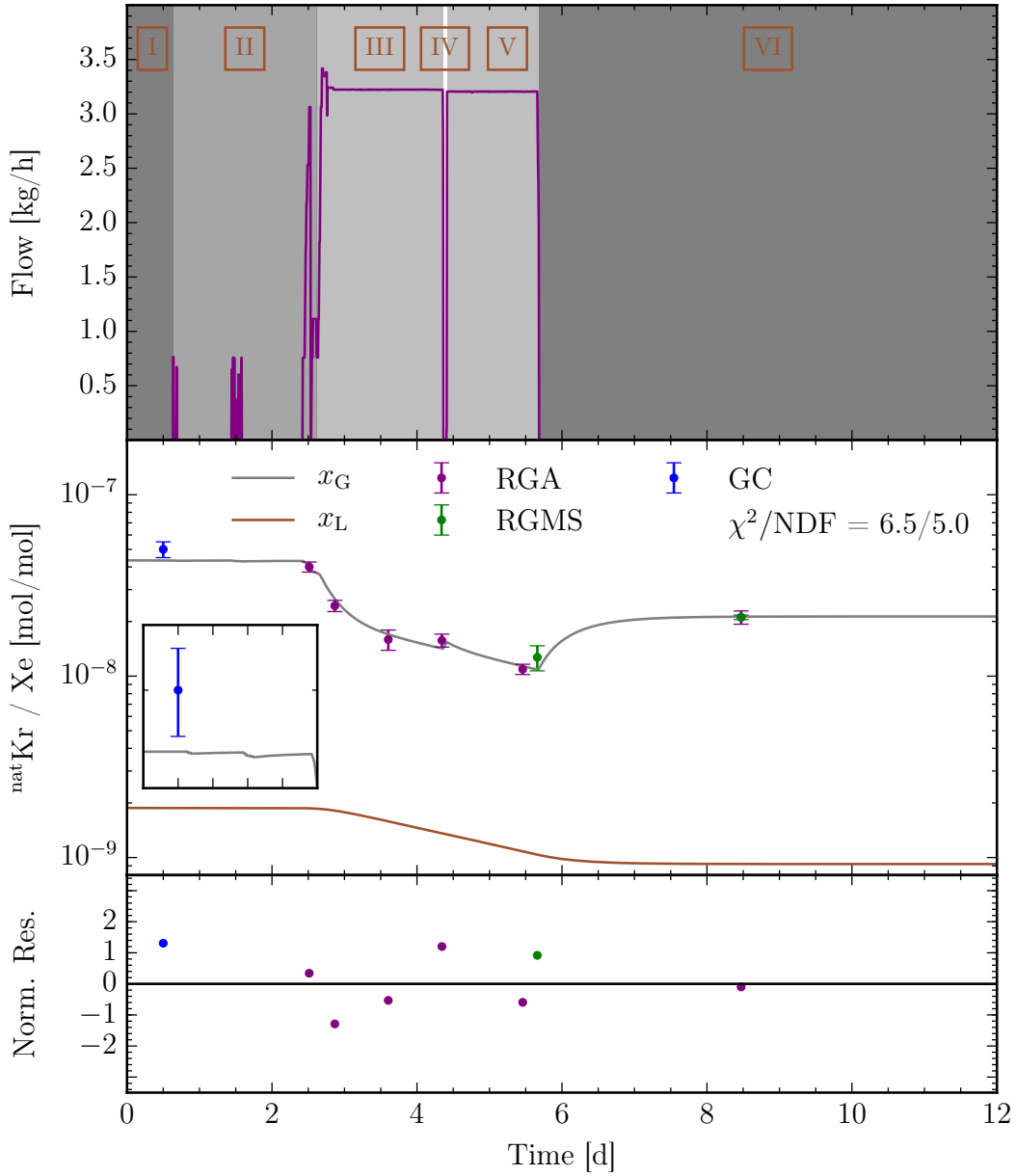


Figure 5.8: **Fit online ReStoX distillation model to krypton data:** The top panel visualizes the flow (purple) during the different operation phases I-VI (shaded areas). The middle panel contains the data points (blue for GC, purple for RGA and green for RGMS) and the fitted gaseous krypton concentration $x_G$ (grey) and the coupled liquid krypton concentration $x_L$ (brown). Furthermore, the inset zooms in to the first 2.5 d to show the influence of the xenon extraction in phase II. The bottom panel indicates the respective normalized residuals (blue for GC, purple for RGA and green for RGMS).

was stopped, particles in the liquid reservoir keep on changing into the GXe part until equilibrium. Thus, the brown curve, corresponding to the concentration $x_L$, further decreases. This self-distilling effect is of particular interest for the application at XENON1T.

In contrast to the grey gaseous concentration curve, the brown liquid concentration curve does not show any spikes during the different periods and is much more smooth. This behavior is expected, as the change in the liquid is in any scenario driven by the migration time $\tau_{\mathrm{M,G}}$ and $\alpha_{\mathrm{Kr}}$, as soon as the global system is pushed away from equilibrium.

The results for the masses are $M_{\mathrm{G}} = (37.5 \pm 1.8)\,\mathrm{kg}$ and $M_{\mathrm{L}} = (3461.0 \pm 3.5)\,\mathrm{kg}$, as expected from the constraints. The migration rate is determined to be $\tau_{\mathrm{M,G}} = (0.66 \pm 0.10)\,\mathrm{d}$, such that two days after the distillation ReStoX was again in equilibrium. As $\tau_{\mathrm{M,G}}$ depends also on the filling height, a direct application to XENON1T is difficult.

The fit yields a relative volatility of $\alpha_{\mathrm{Kr}} = 23.2 \pm 2.8$, which is a factor 1.8 larger compared to the theoretical value of $\alpha_{\mathrm{theo}} = 12.68$. A possible explanation is that a continuous liquefaction and vaporization along the copper heat exchanger in the gaseous part of ReStoX creates another distillation effect. Consequently, the krypton concentration in the GXe reservoir is further enhanced and $\alpha_{\mathrm{Kr}}$ appears to be larger than the theoretical value. The reduced $\chi^2_{\mathrm{red}}$ of the fit was calculated to be 1.3.

Several other fitting attempts were performed. When constraining no parameter, the fit yields $\chi^2_{\mathrm{red}} = 0.55$, but the parameters do not make physically sense. When constraining all parameters except the migration time $\tau_{\mathrm{M,G}}$, phases I-V can be well described. However, with $\alpha_{\mathrm{Kr}}$ constrained to $\alpha_{\mathrm{theo}}$, the grey curve largely overshoots the last data point during phase VI.

All in all, the best description of the data points is given by the fit results in table 5.5. Samples from the LXe reservoir of ReStoX would give further insight on the evolution of $x_{\mathrm{L}}$ and on the ratio $x_{\mathrm{G}}/x_{\mathrm{L}}$. This would further constrain the size of $\alpha_{\mathrm{Kr}}$ and could reject or confirm the additional distillation effect in ReStoX. However, during the online ReStoX distillation, the liquid sample extraction was not possible and therefore, no data is available.

The fit results can be utilized to estimate the combined krypton level $c_{\mathrm{GXe+LXe}}$ of the GXe and the LXe reservoir. According to figure 5.8, ReStoX was already in equilibrium during the last RGMS pipette extraction on 12 Mar 2016 11:19. It follows

$$c_{\mathrm{GXe+LXe}} = \frac{c_{\mathrm{VI,RGMS}} \cdot M_{\mathrm{G}} + \frac{c_{\mathrm{VI,RGMS}}}{\alpha_{\mathrm{Kr}}} \cdot M_{\mathrm{L}}}{M_{\mathrm{G}} + M_{\mathrm{L}}} = (1.2 \pm 0.1)\,\mathrm{ppb}. \tag{5.48}$$

Here, the concentration in the LXe reservoir was calculated from the GXe concentration and the relative volatility $\alpha_{\mathrm{Kr}} = 23.2 \pm 2.8$, assuming equilibrium. Again, the mean value along with uncertainties were computed with the self-programmed monte carlo simulation tool, assuming Gaussian uncertainties for the input parameters. This combined value can be compared to the one within the detector after the initial filling. This is discussed in chapter 6.

Based on the results, the XENON1T detector itself should represent a single distillation stage as well. By applying the above technique of online distillation, the fiducial volume within the TPC should be cleaned from krypton by continuously purifying only the much smaller gas phase. This online krypton removal is the topic of chapter 6. In the next section, the helium removal is discussed.

## 5.5 Helium removal

In this section, the online helium removal is investigated analogously to krypton. Firstly, the determination of the helium content is explained in detail with the help of one exemplary sample. Secondly, the column performance is determined comparing an in-gas sample to a sample from the lowest analysis port AV1 above the reboiler. From this, the reduction capability of the column can be estimated. Thirdly, the helium evolution over time is investigated with the developed online distillation model in order to estimate the relative volatility $\alpha_{\mathrm{He}}$ of helium in xenon. Furthermore, the overall helium reduction is computed.

### Sample analysis

The same samples as in the last section were utilized to determine the helium content. As in the case of krypton, the Münster system is not calibrated for the absolute helium in xenon measurement, but a cross calibration can be performed from the initially measured helium concentration in ReStoX.

During the measurement of the helium content, the electron multiplier (EM) in the RGA operated at its limit. This allowed to record only one scan per each pipette in this regime. Therefore, the scans for the different samples were taken at comparable pressure levels within the main RGA chamber on the order of $8 \times 10^{-6}$ mbar[9]. The corresponding RGA spectrum for the sample from 07 Mar 2016 14:30 during operation phase III is presented in figure 5.9, where the peaks of several prominent atomic or molecular species are highlighted. The measured current was corrected for the pressure within the main chamber. In this example it was $8.7 \times 10^{-6}$ mbar.

In order to compare the helium concentration between different pipettes, the area of the helium peak around 4 was calculated. In detail, the highest bin, the two bins left and the two bins right were summed up. The integral is more robust compared to the single bin [74]. Here, the step size during measurements was 0.2 (5 PPAmu) at a measurement time of 64 ms (DWELL) for each step, such that the integral was computed from 3.6 up to 4.4. A single scan did not allow for the determination of a statistical uncertainty for each individual pipette. However, during the measurement of two pipettes, it was possible to take 8 scans. From these, the uncertainty for the integral could be conservatively estimated to be less than 5 %. Assuming a linear behavior throughout the RGA measurement range, this relative uncertainty was applied to all measured samples.

### Column performance

To validate the column performance, the RGA spectrum in figure 5.9 is compared with a measurement from the enriched xenon off-gas from the top of the column as well as with the cleaner xenon from the lowest analysis port AV1, which is 30.4 cm above the reboiler. This will provide a lower limit on the removal power. The sequence of the three measurements was of crucial importance to not spoil the RGA measurement volumes. This was found during krypton in

[9] The RGA system measures the pressure in torr, which was converted into mbar in this work.

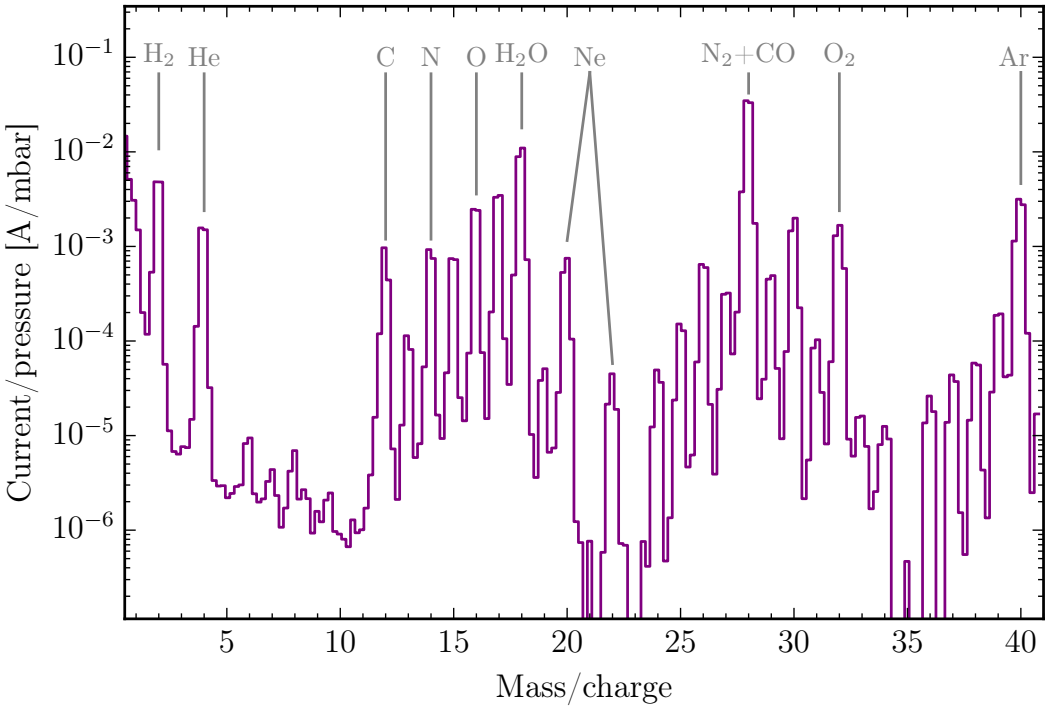


Figure 5.9: **Measured RGA spectrum for sample 07 Mar 2016 14:30:** Shown is the mass-over-charge range 1 - 41. The measured current was corrected for the pressure of $8.7 \times 10^{-6}$ mbar within the main chamber. Several prominent components within the xenon are indicated at their respective mass.

xenon measurements in [60, 74]: First, the AV1 as the cleanest sample has to be measured, followed by the in-gas pipette (07 Mar 2016 14:30). At the end, the most dirty sample from the off-gas can be processed. The comparison of the three obtained spectra is shown in figure 5.10 for $^{m}/_{z}$ of 1 - 8 for a better overview. Again, the measured current was corrected with the respective pressure during the scan. Here, $^{m}/_{z} = 4$ corresponds to helium. As expected, the off-gas sample with the helium-enriched xenon from the top of the distillation system features the highest peak with an integrated pressure corrected current of $(1.7 \pm 0.1) \times 10^{-1}$ A/mbar. While the in-gas sample is in the middle with an integral of $(3.3 \pm 0.2) \times 10^{-3}$ A/mbar, the most clean xenon is found within the AV1 sample, where only a vague peak for helium can be observed with $(2.5 \pm 0.1) \times 10^{-5}$ A/mbar.

The reduction factor $F_{\mathrm{red,He}}$ of the distillation system can be estimated by comparing the in-gas and the purified outlet, as presented for krypton in section 4.2. Since no sample from the reboiler outlet is available, the obtained value for the AV1 sample is exploited as an upper limit of the helium in xenon amount. From this, a lower limit for the reduction capability can be computed with the help of the self-programmed monte carlo simulation tool. Here, the reduction factor is calculated $10^8$ times as in the following (see also section 4.2): In each step, the measured in-gas concentration was created by a random generator following a normal distribution with $\mu = 3.3 \times 10^{-3}$ A/mbar

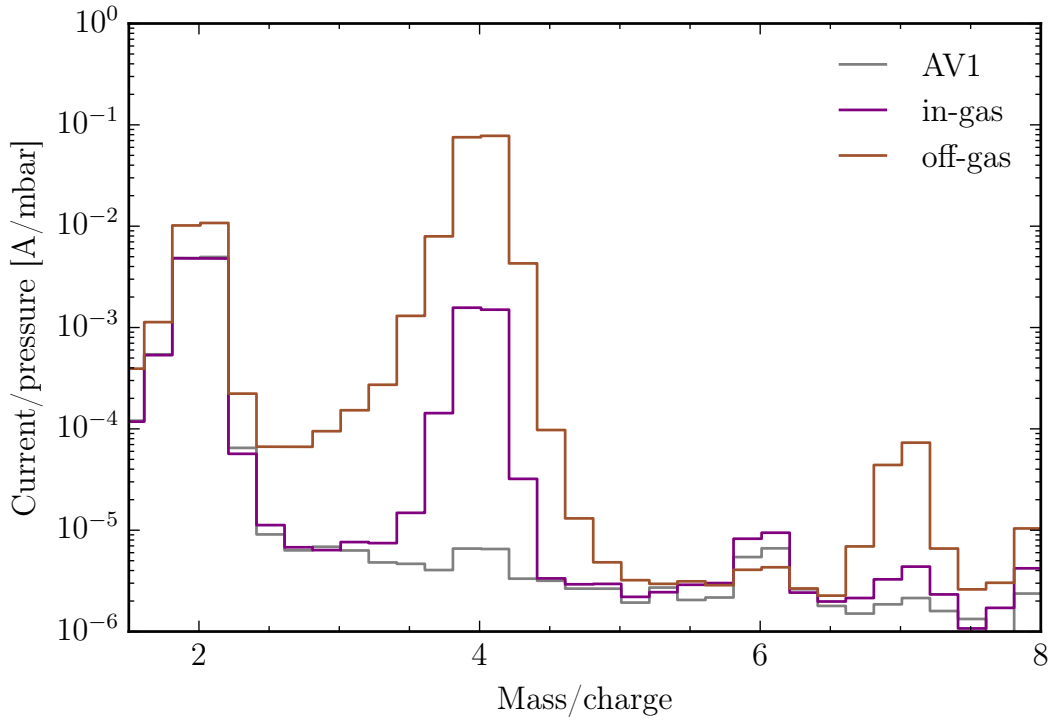


Figure 5.10: **Comparison of the helium content in samples from AV1, in-gas and off-gas.** Shown is $^{m}/_{z}$ of 1 - 8, where 4 corresponds to helium.

and $\sigma = 0.2 \times 10^{-3}$ A/mbar. Since the helium in xenon content in the outlet was expected to be much lower than the AV1 sample, the outlet was assumed to follow a uniform distribution between 0 A/mbar and the measured value of AV1 with $(2.5 \pm 0.1) \times 10^{-5}$ A/mbar, where the right boundary was smeared out by a normal distribution with $\mu = 2.5 \times 10^{-5}$ A/mbar and $\sigma = 0.1 \times 10^{-5}$ A/mbar. This resulted in

$$\mathrm{F}_{\mathrm{red,He}} > 144 \quad (90\,\%\,\mathrm{C.L.}). \tag{5.49}$$

Due to the non-negligible background visible in the AV1 spectrum, the obtained reduction factor reflects a conservative value and is limited by the sensitivity of the RGA, while it is expected to be much higher.

## Evolution

The samples to monitor the helium concentration in the GXe reservoir are summarized in table 5.4. A sample on 12 Mar 2016 11:19 was taken for the cross calibration with the MPIK-RGA in Heidelberg. However, as the helium level was below the MPIK-RGA sensitivity limit of 4 ppm, no absolute calibration from this sample was possible. However, the sample on 04 Mar 2016 17:30 for the Münster RGA was directly extracted from the GXe ReStoX phase while the warm column was filled from ReStoX. Therefore, the determined helium concentration of $c_{\mathrm{I,MPIK-RGA}} = (66.0 \pm 2.0)$ ppm after the ReStoX filling can be exploited as cross calibration point. For pipette $i$ with a normalized integrated

Table 5.6: Best fit parameters along with their respective constraint to describe the online ReStoX distillation helium data.

| Parameter | Constraint | Result |
|---|---|---|
| $x_{\mathrm{G},0}$ | - | $(52.4 \pm 2.2) \times 10^{-6}\,\mathrm{mol/mol}$ |
| $\alpha_{\mathrm{He}}$ | - | $440 \pm 34$ |
| $M_{\mathrm{G}}$ | $(38 \pm 1)\,\mathrm{kg}$ | $(37.9 \pm 0.4)\,\mathrm{kg}$ |
| $M_{\mathrm{L}}$ | $(3461 \pm 50)\,\mathrm{kg}$ | $(3461 \pm 19)\,\mathrm{kg}$ |
| $\tau_{\mathrm{M,G}}$ | $[0, 0.66]\,\mathrm{d}$ | $(0.66 \pm 0.41)\,\mathrm{d}$ |
| $\chi^2$ / NDF | - | 15.0 / 4.0 |

current $c_{\mathrm{i,RGA}}$ follows an absolute helium in xenon concentration $c_{\mathrm{i,abs}}$ of

$$c_{\mathrm{i,abs}} = c_{\mathrm{i,RGA}} \cdot \frac{c_{\mathrm{I,MPIK-RGA}}}{c_{\mathrm{II,RGA}}}. \tag{5.50}$$

Here, $c_{\mathrm{II,RGA}}$ corresponds to the normalized integrated current of the ReStoX sample from 04 Mar 2016 17:30 during phase II, measured with the Münster RGA. The uncertainty $\Delta c_{\mathrm{i,abs}}$ was calculated with

$$\Delta c_{\mathrm{i,abs}} = c_{\mathrm{i,abs}} \cdot \sqrt{\left(\frac{\Delta c_{\mathrm{i,RGA}}}{c_{\mathrm{i,RGA}}}\right)^2 + \left(\frac{\Delta c_{\mathrm{I,MPIK-RGA}}}{c_{\mathrm{I,MPIK-RGA}}}\right)^2 + \left(\frac{\Delta c_{\mathrm{II,RGA}}}{c_{\mathrm{II,RGA}}}\right)^2}, \tag{5.51}$$

where the respective uncertainty is indicated by $\Delta$. The resulting absolute values are listed in table 5.4.

As indicated by the AV1 measurement in the last part, the outlet concentration of the column can be assumed to be essentially helium-free and thus, $x_{\mathrm{D}} = 0\,\mathrm{A/mbar}$. With that, analogously to krypton, equations (5.40) to (5.45) are applied to fit the evolution.

Again, the initial gaseous concentration $x_{\mathrm{G},0}$ is a free parameter, while the initial liquid concentration $x_{\mathrm{L},0}$ is determined by the relative volatility $\alpha_{\mathrm{He}}$. The expected helium volatility in this pressure and temperature regime is unknown and $\alpha_{\mathrm{He}}$ is another fit parameter.

The different xenon masses $M_{\mathrm{G}}$ and $M_{\mathrm{L}}$ in the two phases are used again as constrained fit parameters. Here, different constraints were applied to make the fit converge.

The migration time $\tau_{\mathrm{M,G}}$ is expected to be smaller than in the krypton case, as helium as lighter noble gas should change faster from liquid to gas. Thus, for the fitting, the allowed fit range $\tau_{\mathrm{M,G}}$ is limited upwards to the krypton migration time of 0.66 d.

The same fit routine with a $\chi^2$-minimization based on iMinuit is used. The fit results along with the applied constraints are summarized in table 5.6. The evolution along with the fitted model is visualized in figure 5.11.

The top panel visualizes the flow (purple) during the different operation phases I-VI (shaded areas). The middle panel contains the data points (purple for RGA) and the fitted gaseous helium concentration $x_{\mathrm{G}}$ (grey) and the coupled liquid helium concentration $x_{\mathrm{L}}$ (brown). Furthermore, the inset zooms in to the time

range (4.1–4.7) d to show the influence of the distillation interruption during phase IV. The bottom panel indicates the respective normalized residuals (purple for RGA).

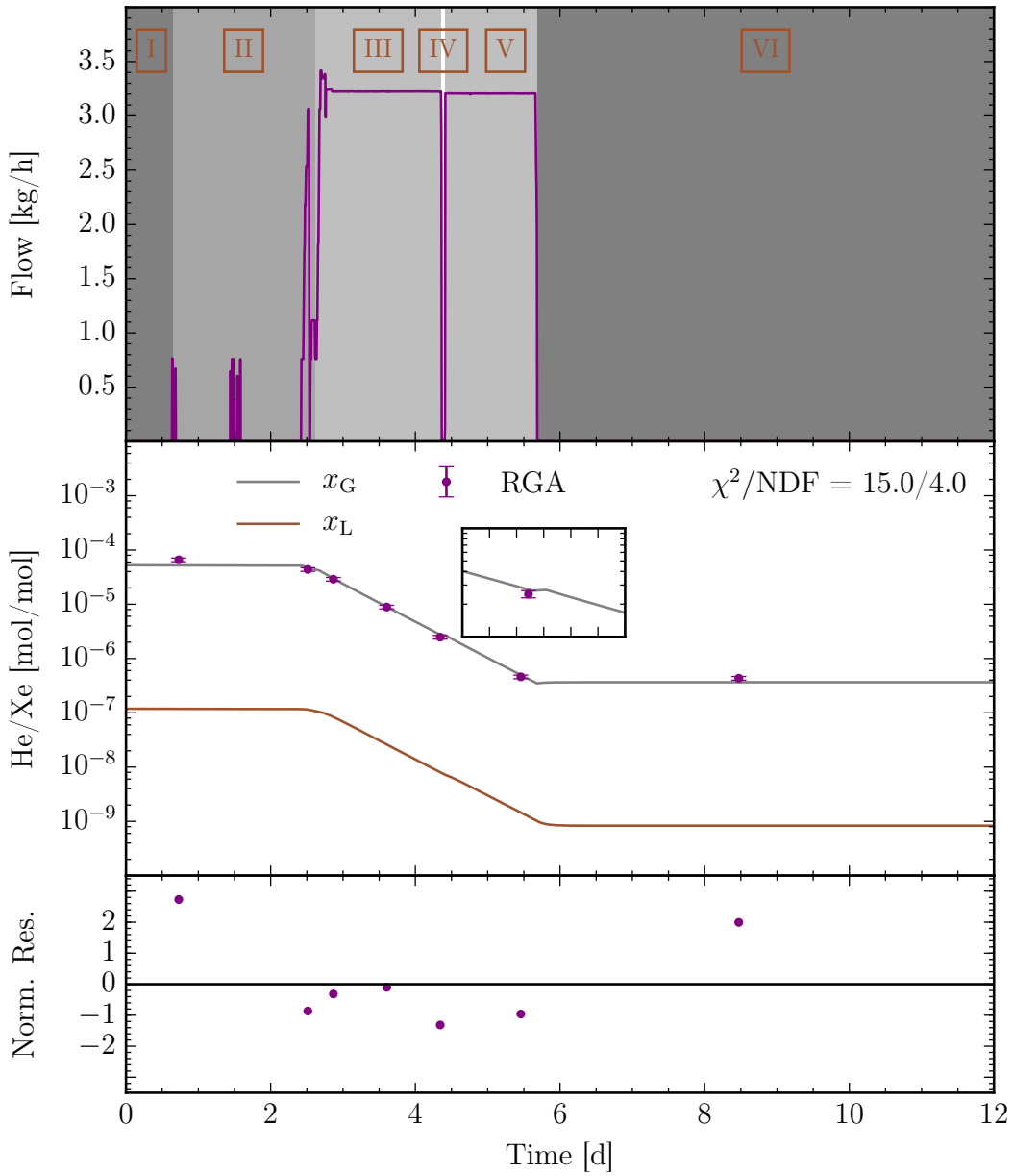


Figure 5.11: **Fit online ReStoX distillation model to helium data:** The top panel visualizes the flow (purple) during the different operation phases I-VI (shaded areas). The middle panel contains the data points (purple for RGA) and the fitted gaseous helium concentration $x_G$ (grey) and the coupled liquid helium concentration $x_L$ (brown). Furthermore, the inset zooms in to the time range (4.1–4.7) d to show the influence of the distillation interruption during phase IV. The bottom panel indicates the respective normalized residuals (purple for RGA).

During phase I, the grey curve is constant, as expected during equilibrium of ReStoX. The fitted initial gaseous helium concentration is $(52.4 \pm 2.2) \times 10^{-6}$ mol/mol such that the grey line undershoots the initially measured concentration of $(66.0 \pm 2.0)$ ppm.

During phase II, two times a small amount of xenon was extracted to pre-fill and cool the column, as visible in the flow panel. The effect on the GXe concentration change is negligible in this case. At the end of phase II, the column was filled, such that a first steeper decrease can be observed. Immediately after, the continuous distillation process was initiated in phase III and the grey curve follows equations (5.40) and (5.41). Due to the chiller movement in phase IV, the distillation process was stopped ($F(t) = 0$) and ReStoX starts to converge to equilibrium according to equations (5.44) and (5.45). In contrast to krypton, the grey curve does not feature a steep rising, but follows a small increasing slope. This effect is highlighted in the inset of figure 5.11. After the interruption, the online distillation was restarted (phase V) at a flow of $F = 3.2\,\mathrm{kg/h}$ and the grey curve follows again equations (5.40) and (5.41). In phase VI, ReStoX converges to equilibrium and the grey curve follows equations (5.44) and (5.45) as soon as the distillation was stopped. Again, only a small increase in $x_\mathrm{G}$ can be observed, which is supported by the last data point.

This can be an indication for two possible scenarios: In the first scenario, the relative volatility is such high, that all helium particles are already gathered in the GXe reservoir from the beginning and only a negligible amount is located in the LXe. In this way, a negligible number of particles are migrating from the LXe into the GXe after stopping the distillation and therefore, the grey curve stays almost constant. In the second scenario, the migration time is large, such that the increase in the gaseous helium concentration cannot be observed on the few day scale. During the fitting it was found that both variables are correlated if left completely free and the two scenarios cannot be distinguished. This was another reason to limit the migration time to be below the krypton migration time.

The brown liquid concentration curve does not show any spikes during the different periods and is smooth. This behavior is expected, as the change in the liquid is in any scenario driven by the migration time $\tau_\mathrm{M,G}$ and $\alpha_\mathrm{He}$, as soon as the global system is pushed away from equilibrium.

The results for the masses are $M_\mathrm{G} = (37.9 \pm 0.4)\,\mathrm{kg}$ and $M_\mathrm{L} = (3461 \pm 19)\,\mathrm{kg}$, as expected from the constraints and in agreement with the krypton fit results. The migration rate is determined to be $\tau_\mathrm{M,G} = (0.66 \pm 0.41)\,\mathrm{d}$, which is the limit from the krypton fit, but with large uncertainties.

The fit yields a relative volatility of $\alpha_\mathrm{He} = 440 \pm 34$. As no expectation value from theory is available and a potential self-distillation effect cannot be excluded, as it was observed for krypton, the result is conservatively re-phrased that an helium enrichment in the GXe reservoir compared to the LXe phase of $440 \pm 34$ was determined. In order to get a more robust result, additional information about the liquid concentration is required, which is not available.

The overall helium reduction $r_\mathrm{He}$ within the GXe of ReStoX after the distillation campaign can be obtained with the help of the fitted starting concentration of $(52.4 \pm 2.2)$ ppm and the last sample from 12 Mar 2016 11:19 with a value

of$(0.43 \pm 0.03)$ ppm. It follows

$$r_{\mathrm{He}} = 120.9^{+11.5}_{-10.0}. \tag{5.52}$$

The same sample for the last data point was measured off-site in Heidelberg with the MPIK-RGA. The helium concentration was below the sensitivity limit of 4 ppm, yielding a reduction of $\mathrm{r_{He}} > 18.3\,(90\,\%\,\mathrm{C.L.})$. This is in agreement with the result above. The sensitivity of the off-site Heidelberg RGA was a limiting factor to proof a higher reduction.

In summary, the helium reduction was successful and allowed for the filling of the detector without potential damage of the photo sensors. Furthermore, the developed online distillation model was applied to the data and an estimation of the helium enrichment in the gaseous phase was presented, yielding reasonable results.

# Online krypton removal at XENON1T 6

The natural krypton in xenon concentration needs to be reduced from a level of a few ppb to the level of 200 ppq in order to avoid leakage events in the region of interest for the dark matter search. These events originate from the decay of the radioactive isotope $^{85}$Kr. This reduction can be achieved with the Phase-2 distillation system, as presented in chapter 4.

In theory, the xenon inventory of about 3200 kg inside the cryostat has to be purified once before starting a science run. In this offline distillation mode, xenon is transferred from ReStoX via the distillation system into the cryostat at a process speed of up to 6 kg/h, as explained in section 3.3.1. This allows the purification of the complete inventory within 23 days. However, the collaboration decided to fill the detector in April 2016 without initial krypton removal in order to investigate the functionality of the TPC along with the overall system. After its successful commissioning, the next step was to reduce the krypton induced background. In order to be able to perform the offline distillation, the xenon has to be recovered first from the filled cryostat into ReStoX. Then, the cryostat warms up, is evacuated and pumped for several days. In the optimal case, the systems are flushed with krypton-free xenon from the distillation system followed by a second evacuation and pumping procedure. After that, the detector can be re-filled again through the distillation column. In order to reach a sufficient electron lifetime and thus, to be able to drift electrons in the liquid xenon, the purification system needs to continuously remove electronegative impurities over the course of about 8 weeks. All in all, at least 90 days were estimated to fulfill all the required steps, while the rest of the detector is not operational.

Therefore, a new online krypton removal technique was developed within this thesis that allows the reduction of krypton, while the detector system is left filled and the TPC is fully operational. The first section of this chapter will introduce the basic concept of the new technique as well as the different operation processes during the development. Furthermore, a model is derived that can describe the evolution of the krypton concentration in the liquid and gas volumes over the span of 540 d, including the commissioning phase, science run 0 and science run 1 of XENON1T. The krypton evolution was monitored via the extraction and measurement of gas samples with the RGA and RGMS systems. Additionally, the electronic recoil background rate within the TPC gives a direct insight to the amount of krypton in liquid xenon. The sample analysis and results for all three methods are presented in the second section. In the third section, the online

krypton removal model is fitted to the obtained data points. The fit reveals how the different distillation modes work and how they can be optimized for the future.

## 6.1 Operation modes and model

The detector system is assumed to be a distillation stage with a liquid-gas interface, where the gaseous phase is enriched in krypton due to its volatility, similar to the storage vessel ReStoX (see chapter 5). This is sketched in figure 6.1, where krypton particles are indicated as brown dots. The cryostat houses the TPC and is filled with liquid xenon (LXe). The liquid level in the TPC is regulated with a diving bell system and is lower compared to the level in the cryostat. The cryogenic pipe connects the detector with the cryogenic system and is filled with gaseous xenon (GXe). Here, xenon is liquefied with a pulse tube refrigerator (PTR) in order to keep the system cold and to counter an evaporated xenon flow due to external heat inputs. The porcupine contains the PMT cable feed-throughs and is connected to the gaseous reservoir as well. The purification system extracts xenon from outside the TPC with the pumps, removes electronegative impurities with the getters and pumps back the clean xenon into the TPC.

The basic concept of the online krypton removal is to continuously purify the gaseous phase of the detector with the help of the distillation column. This can be done by extracting krypton-enriched xenon gas via ports at the porcupine, the cryogenic pipe as well as the cryogenic system. Krypton-free xenon is then guided back to the purification system and from here, back into the detector. As the krypton particle balance between the liquid and gas phase is disturbed due to the removal of krypton from the gas, krypton particles from the liquid migrate into the gas. From here, they are removed again and a continuous migration from liquid to gas is established. Consequently, the total xenon inventory of about 3200 kg can be purified by processing the mere amount of about 20 kg of gaseous xenon.

When there is no distillation, the detector can be operated in different circulation modes, namely *standard circulation*, *liquid only circulation* or *no circulation*, in order to remove electronegative impurities, extract xenon samples from the liquid reservoir, or to maintain the purification system. In between, five distillation campaigns for krypton removal and two for online radon removal were performed. In a first operation (referred to as *liquid + gas*), the online distillation was tested without any hardware modification of the global system. Here, a liquid-gas mixture was extracted from the purification system and processed by the distillation column. For the second test, the main purification loop was stopped and only xenon from the gaseous detector phase was purified with the column (referred to as *gas only*). Since both methods showed promising results, it was decided to modify the global system in such a way that the xenon from the gas part could be processed directly by the distillation column in parallel to the main purification loop (referred to as *upgraded gas only*), as explained in figure 6.1. Two short operations of the upgraded mode were tested, where the GXe phase was purified for only one day each, followed by a long term online

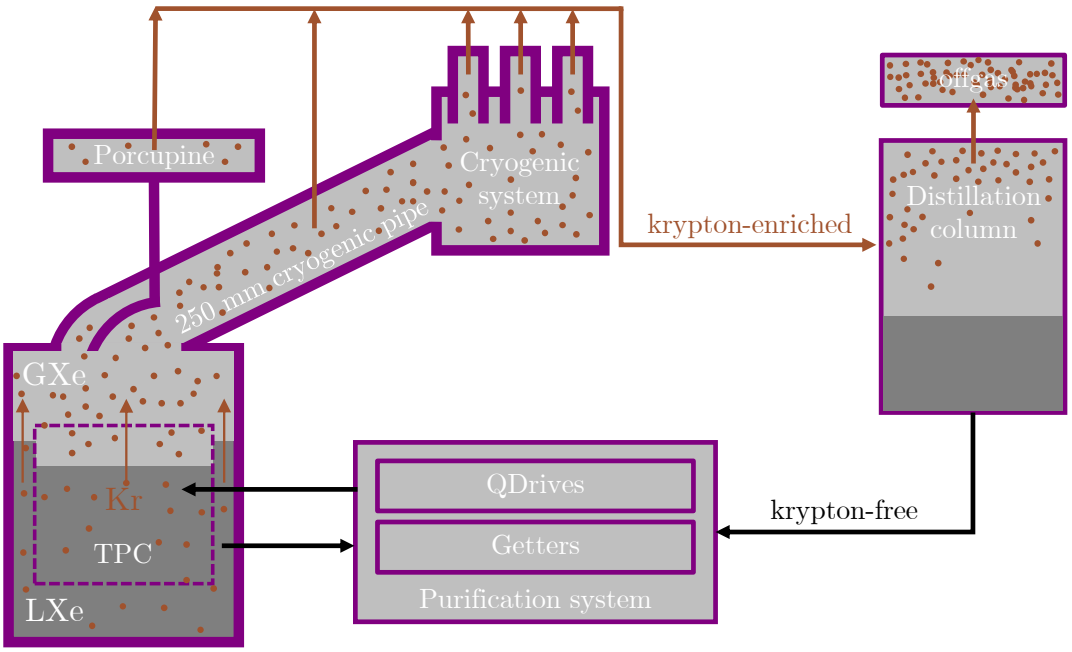


Figure 6.1: **Basic concept of online krypton removal:** The cryostat is housing the TPC and is filled with liquid xenon (LXe) and a gaseous phase above (GXe). The liquid level in the TPC is regulated with a diving bell system and is lower compared to the level in the cryostat. The detector is assumed to be a single distillation stage, where krypton (brown dots) is enriched in the gaseous xenon. The distillation column is illustrated on the right, where 1 % of the process flow is extracted as krypton-enriched off-gas into a storage bottle. When the gas phase of the detector is continuously purified with the help of the distillation column by extracting krypton-enriched xenon and re-feeding krypton-free xenon via the purification system, the krypton particle balance is disturbed. Thus, krypton within the LXe migrates into the GXe reservoir to counter the imbalance. Like that, the total xenon inventory of 3200 kg can be purified by continuously cycling the mere amount of about 20 kg xenon in the gas.

distillation with the final configuration. Additionally, the upgraded system allowed for online radon removal as well. This is discussed in chapter 7. The different operations performed are visualized in figure 6.2 for a time span from 05 Aug 2016 until 28 Jan 2018. The distillation campaigns are highlighted in grey and are summarized in table 6.1.

The krypton concentration evolution over time within the liquid and gaseous xenon of the detector can be modeled with the online distillation model, developed in chapter 5. The coupled differential equations for the ideal case have to be adjusted to each of the seven different operation modes in figure 6.2. This is derived in the following.

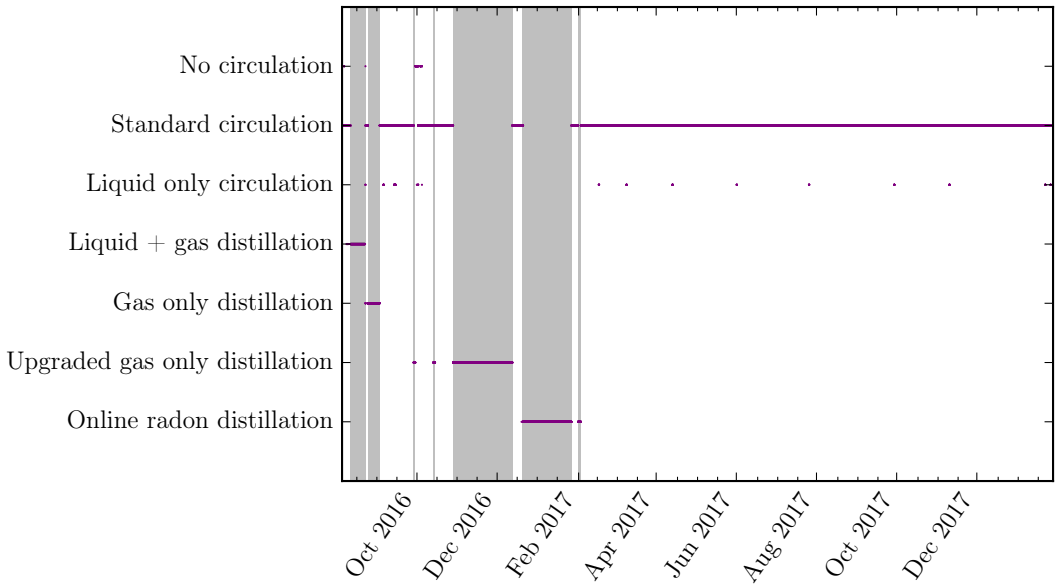


Figure 6.2: **Operation modes from Aug 2016 until Jan 2018:** Distillation periods (Liquid + gas, gas only, upgraded gas only, online radon removal) are highlighted in grey. The different detector operations are standard circulation, liquid only circulation and no circulation. The purple points indicate at which time an operation was performed. The radon removal campaign is presented in chapter 7.

Table 6.1: Different operation modes of the online krypton removal development.

| Period | Mode |
|---|---|
| 11 Aug - 22 Aug 2016 | Liquid + gas |
| 22 Aug 2016 | Gas only (First try) |
| 24 Aug - 02 Sep 2016 | Gas only |
| 28 Sep - 29 Sep 2016 | Upgraded gas only 1 |
| 13 Oct - 14 Oct 2016 | Upgraded gas only 2 |
| 28 Oct - 12 Dec 2016 | Upgraded gas only 3 |
| 19 Dec 2016 - 26 Jan 2017 | Online radon removal |
| 31 Jan - 02 Feb 2017 | Online radon removal |

## No circulation

The most simple operation mode is referred to as *no circulation*, where no xenon leaves or enters the detector system. In the ideal case, the model contains a liquid xenon reservoir (LXe) with mass $M_\mathrm{L}$ and krypton concentration $x_\mathrm{L}$ and a gaseous xenon reservoir (GXe) with mass $M_\mathrm{G}$ and concentration $x_\mathrm{G}$, as visualized in figure 6.3. Krypton can migrate from the liquid into the gas due to a distillation effect. This is modeled with the time constant $\tau_\mathrm{Mig}$ and scales with $(\alpha x_\mathrm{L} - x_\mathrm{G})$, as derived in section 5.2.

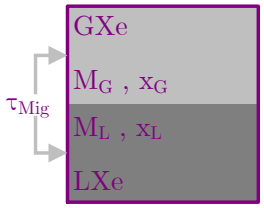


Figure 6.3: **Ideal liquid and gas interface:** The liquid (gaseous) xenon phase LXe (GXe) in the detector contains the mass $M_\mathrm{L}$ ($M_\mathrm{G}$) and a krypton concentration of $x_\mathrm{L}$ ($x_\mathrm{G}$). The exchange between the GXe and LXe can happen via distillation, modeled with the migration time $\tau_\mathrm{Mig}$.

In reality, heat input from outside the cryostat creates an additional evaporation flow $F_\mathrm{vap}$ of xenon. Therefore, the cryogenic system contains a pulse tube refrigerator (PTR) in order to re-condense this xenon at a flow $F_\mathrm{con}$, as shown in figure 6.4.

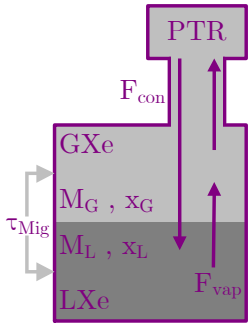


Figure 6.4: **Krypton concentrations and xenon mass flows for the no circulation mode:** The liquid (gaseous) xenon phase LXe (GXe) in the detector contains the mass $M_\mathrm{L}$ ($M_\mathrm{G}$) and a krypton concentration of $x_\mathrm{L}$ ($x_\mathrm{G}$). The exchange between the GXe and LXe can happen either due to distillation, modeled with the migration time $\tau_\mathrm{Mig}$ or by vaporization ($F_\mathrm{vap}$) and condensation ($F_\mathrm{con}$). No xenon leaves or enters the detector in this mode.

Here, the evaporated and condensed xenon flows have to be equal ($F_\mathrm{vap} = F_\mathrm{con}$) in order to keep the liquid level in the detector stable. As these flows allow krypton to migrate between the two phases, they need to be taken into account as well: The evaporated krypton particle flux going from the LXe into the GXe

part is $\alpha \cdot F_{\text{vap}} \cdot x_{\text{L}}$, while the condensed krypton particle flux, going back from the GXe into LXe, is given by $\frac{F_{\text{con}}}{\alpha} \cdot x_{\text{G}}$. Thus, krypton can not only change from liquid into gas, but also vice versa. Taking all together, the evolution of krypton in xenon in both phases can be expressed via a coupled differential equation system:

$$\frac{dx_{\text{G}}}{dt} = \overbrace{+\frac{1}{\tau_{\text{Mig}}}\left[\alpha x_{\text{L}} - x_{\text{G}}\right]}^{\text{distillation}} \overbrace{-\frac{F_{\text{con}}}{\alpha \cdot M_{\text{G}}} \cdot x_{\text{G}}}^{\text{condensation}} \overbrace{+\frac{\alpha \cdot F_{\text{vap}}}{M_{\text{G}}} \cdot x_{\text{L}}}^{\text{evaporation}}, \tag{6.1}$$

$$\frac{dx_{\text{L}}}{dt} = \overbrace{-\frac{1}{\tau_{\text{Mig}}} \cdot \frac{M_{\text{G}}}{M_{\text{L}}}\left[\alpha x_{\text{L}} - x_{\text{G}}\right]}^{\text{distillation}} \overbrace{+\frac{F_{\text{con}}}{\alpha \cdot M_{\text{L}}} \cdot x_{\text{G}}}^{\text{condensation}} \overbrace{-\frac{\alpha \cdot F_{\text{vap}}}{M_{\text{L}}} \cdot x_{\text{L}}}^{\text{evaporation}}. \tag{6.2}$$

In both equations, the first term corresponds to the distillation effect, the second term to the condensation and the third to the evaporation. In the case of the condensation and evaporation terms, the krypton particle flux is divided by the respective mass of the phase in order to model a change in the concentration rather than in the number of particles. Furthermore, the sign of each term indicates if krypton is leaving $(-)$ or entering $(+)$ the respective phase.

In equilibrium ($\frac{dx_{\text{G}}}{dt} = 0$), equation (6.1) for the GXe phase can be re-written as

$$x_{\text{G}}\left(\frac{1}{\tau_{\text{Mig}}} + \frac{F_{\text{con}}}{\alpha \cdot M_{\text{G}}}\right) = \alpha x_{\text{L}}\left(\frac{1}{\tau_{\text{Mig}}} + \frac{F_{\text{vap}}}{M_{\text{G}}}\right). \tag{6.3}$$

With $F_{\text{con}} = F_{\text{vap}}$ follows

$$x_{\text{G}} = \alpha \cdot \frac{\left(\frac{1}{\tau_{\text{Mig}}} + \frac{F_{\text{con}}}{M_{\text{G}}}\right)}{\left(\frac{1}{\tau_{\text{Mig}}} + \frac{F_{\text{con}}}{\alpha \cdot M_{\text{G}}}\right)} \cdot x_{\text{L}}. \tag{6.4}$$

While $F_{\text{con}}$, $M_{\text{G}}$ and $\alpha$ are fixed, the only unknown parameter is the migration time $\tau_{\text{Mig}}$. Therefore, the two extreme cases for a fast and a slow migration time can be investigated. It follows

$$x_{\text{G}} = \alpha x_{\text{L}} \quad \text{for} \quad \frac{1}{\tau_{\text{Mig}}} >> \frac{F_{\text{con}}}{M_{\text{G}}}, \tag{6.5}$$

$$x_{\text{G}} = \alpha^2 x_{\text{L}} \quad \text{for} \quad \frac{1}{\tau_{\text{Mig}}} << \frac{F_{\text{con}}}{M_{\text{G}}}. \tag{6.6}$$

This shows that the detector system, by design, features a krypton concentration in the GXe larger than the relative volatility. This makes the online krypton distillation even more attractive and efficient. A first estimate with typical values of $\alpha = 10.5$, $F_{\text{con}} = 10\,\text{slpm}$ ($84\,\text{kg/d}$), $M_{\text{G}} = 21.5\,\text{kg}$ and $\tau_{\text{Mig}} = 0.67\,\text{d}$, assuming the same migration time as in ReStoX, leads to

$$x_{\text{G}} \approx 30 \cdot x_{\text{L}}, \tag{6.7}$$

about a factor three larger than $\alpha$. With this information, the krypton distribution between the gas and liquid phase in equilibrium can be calculated for the no circulation mode with

$$x_{\text{tot}} \cdot (M_{\text{G}} + M_{\text{L}}) = x_{\text{G}} \cdot M_{\text{G}} + x_{\text{L}} \cdot M_{\text{L}} \tag{6.8}$$

Above equation can be solved using equation (6.7) and $M_L = 3190\,\text{kg}$ and leads to

$$x_G = 0.17 \cdot x_{tot} \quad \text{and} \quad x_L = 0.83 \cdot x_{tot}. \tag{6.9}$$

Already 17 % of the total krypton amount are inside the GXe reservoir. This krypton bulk can be removed fast and efficient when starting an online distillation process. However, usually, the detector is operated in the standard circulation mode, where xenon is continuously pumped through the purification cycle. This affects also the krypton evolution in the two reservoirs. The respective differential equations are derived in the following.

## Standard circulation

During normal detector operation, e.g. dark matter search or calibration, the purification system is running in the standard circulation. The goal is to continuously remove electronegative impurities from the liquid as well as the gaseous part of the detector system. This also affects the krypton distribution within the system. Therefore, the detector model in figure 6.4 is expanded with the circulation through the purification system, as sketched in figure 6.5.

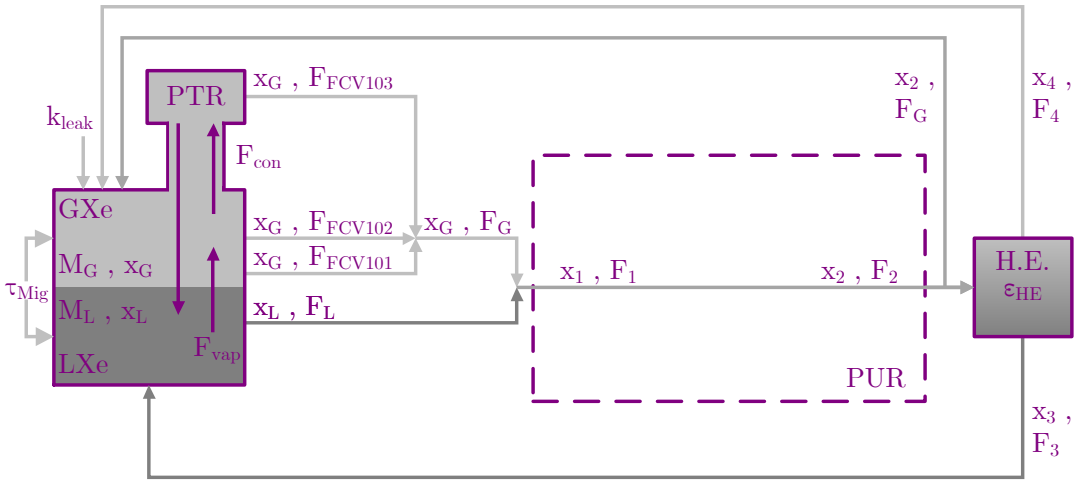


Figure 6.5: **Krypton concentrations and xenon mass flows for the standard circulation mode:** The liquid (gaseous) xenon phase LXe (GXe) in the detector contains the mass $M_L$ ($M_G$) and a krypton concentration of $x_L$ ($x_G$). The exchange between the GXe and LXe can happen either due to distillation, modeled with the migration time $\tau_{Mig}$ or by vaporization ($F_{vap}$) and condensation ($F_{con}$). Different concentrations in different locations are denoted as $x_i$ with their respective flow $F_i$. The heat exchanger (H.E.) liquefies the returning gas with an efficiency $\epsilon_{HE}<1$. Thus, the H.E. features an additional distillation effect.

Xenon with a krypton concentration $x_G$ is extracted from the GXe reservoir via three ports with the flows $F_{FCV101}$ (porcupine), $F_{FCV102}$ (cryopipe) and $F_{FCV103}$ (condenser stations), yielding the summed flow $F_G$, containing the concentration $x_G$ as well. This flow is typically on the order of 3.8 slpm.

A krypton concentration of $x_{\mathrm{L}}$ is extracted from the LXe part at a flow $F_{\mathrm{L}}$ through a heat exchanger, typically around (40–45) slpm. Note that in XENON1T the liquid xenon is extracted from outside the TPC. However, it is presumed that the krypton concentration in the LXe reservoir is homogeneously distributed at all times. Furthermore, the assumption is made that the krypton fraction, vaporized via the heat exchanger, remains the same, as this is a pressure-driven flow. The flows from the gas and liquid are mixed together and guided to the purification system. Then, the combined krypton particle flux $x_1 \cdot F_1$ at the purification inlet is given by

$$x_1 \cdot F_1 = x_{\mathrm{G}} \cdot F_{\mathrm{G}} + x_{\mathrm{L}} \cdot F_{\mathrm{L}} \tag{6.10}$$

With above equation, the concentration $x_1$ in the summed flow $F_1 = F_{\mathrm{G}} + F_{\mathrm{L}}$ can be derived as

$$x_1 = \frac{F_{\mathrm{G}}}{F_1} \cdot x_{\mathrm{G}} + \frac{F_{\mathrm{L}}}{F_1} \cdot x_{\mathrm{L}}. \tag{6.11}$$

Inside the purification system, two heated getters remove the electronegative impurities. The noble gas krypton can pass these getters unaffected. Thus, the outlet flow from the purification system $F_2$ equals $F_1$ and both contain the same krypton concentration: $x_2 = x_1$. From the outlet, a krypton particle flux $x_2 \cdot F_{\mathrm{G}}$ is going back into the GXe reservoir. A part of this flow is guided directly into the bell in order to keep the TPC level stable. In this model, the gaseous bell volume is not separated from the rest of the GXe reservoir, as both volumes are assumed to be in good contact with a fast gas exchange.

The remaining krypton flux $x_2 \cdot F_{\mathrm{L}}$ is going into the heat exchanger for liquefaction. Due to its efficiency of $\epsilon_{\mathrm{HE}}<1$, the in-going flow is split into a krypton particle flux $x_3 \cdot F_3$ guided into the liquid and a krypton particle flux $x_4 \cdot F_4$ added to the gaseous phase. It applies

$$x_2 \cdot F_{\mathrm{L}} = x_3 \cdot F_3 + x_4 \cdot F_4. \tag{6.12}$$

As krypton prefers to stay in the gaseous phase, the concentration $x_4$ should contain a higher krypton concentration with respect to $x_3$, scaling with $\alpha$: $x_4 = \alpha x_3$. Furthermore, the flows can be calculated to be $F_3 = \epsilon_{\mathrm{HE}} \cdot F_{\mathrm{L}}$ and $F_4 = (1 - \epsilon_{\mathrm{HE}}) \cdot F_{\mathrm{L}}$. With that, the two krypton particle fluxes to liquid and gas can be calculated as

$$x_3 \cdot F_3 = \frac{x_2}{\epsilon_{\mathrm{HE}} + \alpha \cdot (1 - \epsilon_{\mathrm{HE}})} \cdot \epsilon_{\mathrm{HE}} \cdot F_{\mathrm{L}}, \tag{6.13}$$

$$x_4 \cdot F_4 = \frac{\alpha \cdot x_2}{\epsilon_{\mathrm{HE}} + \alpha\,(1 - \epsilon_{\mathrm{HE}})} \cdot (1 - \epsilon_{\mathrm{HE}}) \cdot F_{\mathrm{L}}. \tag{6.14}$$

In order to get a handle on the size of the effective krypton fluxes after the exchanger in contrast to the xenon flow, typical XENON1T values can be used to calculate equations (6.13) and (6.14). With $\alpha = 10.5, \epsilon_{\mathrm{HE}} = 0.95$ and $F_{\mathrm{L}} = 40\,\mathrm{slpm}$ (340 kg/d) follows

$$x_3 \cdot F_3 = 0.64 \cdot x_2 \cdot F_{\mathrm{L}} \quad \text{and} \quad x_4 \cdot F_4 = 0.36 \cdot x_2 \cdot F_{\mathrm{L}}. \tag{6.15}$$

About one third of the in-going krypton flux $x_2 \cdot F_{\mathrm{L}}$ is guided into the GXe reservoir. For an efficiency of $\epsilon_{\mathrm{HE}} = 0.91$, the flux would be split evenly between

the reservoirs. It can be seen that a less efficient heat exchanger would be beneficial for the online distillation, as more krypton would return to the gas volume.

Due to the heat exchanger inefficiency, more gas returns to the GXe volume than extracted. Thus, the condensation flow $F_{\mathrm{con}}$ in this mode is larger than the evaporated flow $F_{\mathrm{vap}}$. It applies

$$F_{\mathrm{con}} = F_{\mathrm{vap}} + (1 - \epsilon_{\mathrm{HE}}) \cdot F_{\mathrm{L}}. \tag{6.16}$$

In addition, the RGMS data set, presented in the next section 6.2, reveals a krypton increase over the time after the last online distillation campaign. This indicates that krypton is entering the closed system either due to micro leaks or outgassing. Since both cannot be differentiated, a single leak parameter can be introduced into the model to combine the effects. As the increase found is slow compared to the other exchange times in the system, the position of the leak is negligible and thus, it was added as a krypton particle flux $k_{\mathrm{leak}}$ into the GXe.

With the additional fluxes, the differential equations (6.1) and (6.2) of the no circulation mode can be expanded for the standard circulation mode to

$$\begin{aligned}\frac{dx_{\mathrm{G}}}{dt} =& \overbrace{+\frac{1}{\tau_{\mathrm{Mig}}}\left[\alpha x_{\mathrm{L}} - x_{\mathrm{G}}\right]}^{\text{distillation}} \overbrace{-\frac{F_{\mathrm{con}}}{\alpha \cdot M_{\mathrm{G}}} \cdot x_{\mathrm{G}}}^{\text{condensation}} \overbrace{+\frac{\alpha \cdot F_{\mathrm{vap}}}{M_{\mathrm{G}}} \cdot x_{\mathrm{L}}}^{\text{evaporation}} \\ & \overbrace{-\frac{F_{\mathrm{G}}}{M_{\mathrm{G}}} \cdot x_{\mathrm{G}}}^{\text{extraction}} \overbrace{+\frac{F_{\mathrm{G}}}{M_{\mathrm{G}}} \cdot x_1}^{\text{return}} \overbrace{+\frac{F_4}{M_{\mathrm{G}}} \cdot x_4}^{\text{return H.E.}} \overbrace{+\frac{k_{\mathrm{leak}}}{M_{\mathrm{G}}}}^{\text{leak}},\end{aligned} \tag{6.17}$$

$$\begin{aligned}\frac{dx_{\mathrm{L}}}{dt} =& \overbrace{-\frac{1}{\tau_{\mathrm{Mig}}} \cdot \frac{M_{\mathrm{G}}}{M_{\mathrm{L}}}\left[\alpha x_{\mathrm{L}} - x_{\mathrm{G}}\right]}^{\text{distillation}} \overbrace{+\frac{F_{\mathrm{con}}}{\alpha \cdot M_{\mathrm{L}}} \cdot x_{\mathrm{G}}}^{\text{condensation}} \overbrace{-\frac{\alpha \cdot F_{\mathrm{vap}}}{M_{\mathrm{L}}} \cdot x_{\mathrm{L}}}^{\text{evaporation}} \\ & \overbrace{-\frac{F_{\mathrm{L}}}{M_{\mathrm{L}}} \cdot x_{\mathrm{L}}}^{\text{extraction}} \overbrace{+\frac{F_3}{M_{\mathrm{L}}} \cdot x_3}^{\text{return H.E.}}.\end{aligned} \tag{6.18}$$

In both equations, the different terms model the in-going (+) and out-going (−) krypton fluxes in the respective reservoir. The distillation, condensation and evaporation are the same terms as in the no circulation mode. In addition, equation (6.17) contains the gas extraction, the returning gas, the additional gas from the heat exchanger (H.E.) and the constant leak rate. In contrast, equation (6.18) includes only the extraction and the liquid returning from the heat exchanger (H.E.). Again, the different krypton fluxes are divided by the respective mass in order to model the concentration change.

For the equilibrium ($\frac{dx_{\mathrm{G}}}{dt} = 0$) and neglecting the leak rate, the relation between $x_{\mathrm{G}}$ and $x_{\mathrm{L}}$ can be investigated by solving equation (6.17) for $x_{\mathrm{G}}$ and applying typical XENON1T parameters, e.g. $\alpha = 10.5$, $F_{\mathrm{vap}} = 10\,\mathrm{slpm}$ (84 kg/d), $F_{\mathrm{G}} = 3.8\,\mathrm{slpm}$ (32 kg/d), $F_{\mathrm{L}} = 40\,\mathrm{slpm}$ (340 kg/d), $M_{\mathrm{G}} = 21.5\,\mathrm{kg}$, $\epsilon_{\mathrm{HE}} = 0.95$ and $\tau_{\mathrm{Mig}} = 0.67\,\mathrm{d}$, assuming the same migration time as in ReStoX:

$$x_{\mathrm{G}} \approx 22 \cdot x_{\mathrm{L}}. \tag{6.19}$$

This value is lower compared to the no circulation mode of 30. Naively, one could expect a higher enhancement than in the no circulation mode due to the

additional distillation effect by the heat exchanger. However, the investigation reveals that mixing the krypton-enriched xenon from the gas with the liquid xenon leads to a higher krypton flux back into the LXe volume via the heat exchanger. However, the enhancement in the standard circulation is still a factor two larger than the relative volatility $\alpha$. Thus, the online distillation is also promising in this mode. Beside the standard circulation, the detector can be operated in a liquid only circulation mode. This mode is briefly reviewed in the next section.

## Liquid only circulation

The liquid only circulation allows for the extraction of xenon samples at the purification system that contain the krypton concentration $x_\mathrm{L}$. This gives direct insight to the krypton inside the liquid reservoir and thus, the TPC. The main

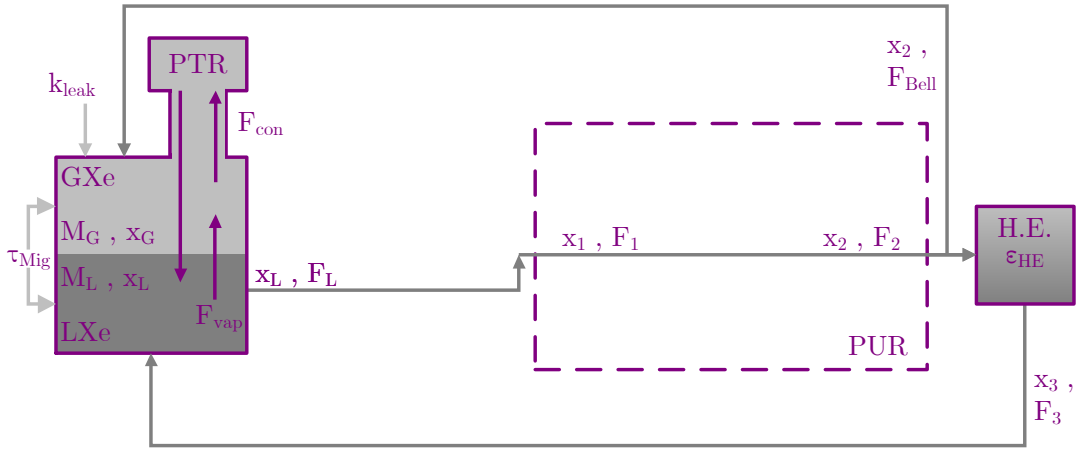


Figure 6.6: **Krypton concentrations and xenon mass flows for the liquid only circulation mode:** The liquid (gaseous) xenon phase LXe (GXe) in the detector contains the mass $M_\mathrm{L}$ ($M_\mathrm{G}$) and a krypton concentration of $x_\mathrm{L}$ ($x_\mathrm{G}$). The exchange between the GXe and LXe can happen either due to distillation, modeled with the migration time $\tau_\mathrm{Mig}$ or by vaporization ($F_\mathrm{vap}$) and condensation ($F_\mathrm{con}$). Different concentrations in different locations are denoted as $x_\mathrm{i}$ with their respective flow $F_\mathrm{i}$. This mode allows for the extraction of xenon samples at the purification system that contain the krypton concentration in the TPC.

difference to the standard circulation is that xenon is solely extracted from the LXe reservoir with a concentration $x_\mathrm{L}$ at a flow $F_\mathrm{L}$, as visualized in figure 6.6. As before, the same flow enters and leaves the purification system:

$$F_2 = F_1 = F_\mathrm{L}. \tag{6.20}$$

It contains the same krypton concentration

$$x_2 = x_1 = x_\mathrm{L}. \tag{6.21}$$

The RGMS samples are extracted at the inlet of the purification system, where the xenon contains the concentration $x_1$. While in the standard circulation, $x_1$ represents the mixture from liquid and gas, in the liquid only circulation, it corresponds to the liquid krypton concentration, as stated above. Furthermore, it allows for an absolute calibration of the event rate measured with the TPC. This is discussed in section 6.2.

From the outlet of the purification system, a flow $F_{\mathrm{Bell}}$ carries xenon with a concentration $x_2 = x_{\mathrm{L}}$ into the bell. Thus, a flow of $(F_{\mathrm{L}} - F_{\mathrm{Bell}})$ is entering the heat exchanger. As a flow $F_{\mathrm{L}}$ is extracted through the exchanger from the liquid reservoir, it can liquefy a returning xenon flow of $\epsilon_{\mathrm{HE}} \cdot F_{\mathrm{L}}$. In the case of XENON1T, it applies

$$(F_{\mathrm{L}} - F_{\mathrm{Bell}}) \lesssim \epsilon_{\mathrm{HE}} \cdot F_{\mathrm{L}}. \tag{6.22}$$

Thus, it is assumed that the full flow is liquefied and returns into the LXe volume:

$$x_3 \cdot F_3 = x_{\mathrm{L}} \cdot (F_{\mathrm{L}} - F_{\mathrm{Bell}}), \tag{6.23}$$

$$x_4 \cdot F_4 = 0. \tag{6.24}$$

With that, the condensation flow in the cryogenic system is

$$F_{\mathrm{con}} = F_{\mathrm{vap}} + F_{\mathrm{Bell}}. \tag{6.25}$$

The coupled differential equations for the liquid only circulation are given by

$$\begin{aligned}\frac{dx_{\mathrm{G}}}{dt} = &\overbrace{+\frac{1}{\tau_{\mathrm{Mig}}}\left[\alpha x_{\mathrm{L}} - x_{\mathrm{G}}\right]}^{\text{distillation}} \overbrace{-\frac{F_{\mathrm{con}}}{\alpha \cdot M_{\mathrm{G}}} \cdot x_{\mathrm{G}}}^{\text{condensation}} \overbrace{+\frac{\alpha \cdot F_{\mathrm{vap}}}{M_{\mathrm{G}}} \cdot x_{\mathrm{L}}}^{\text{evaporation}} \\ &\overbrace{+\frac{F_{\mathrm{Bell}}}{M_{\mathrm{G}}} \cdot x_{\mathrm{L}}}^{\text{return}} \overbrace{+\frac{k_{\mathrm{leak}}}{M_{\mathrm{G}}}}^{\text{leak}},\end{aligned} \tag{6.26}$$

$$\begin{aligned}\frac{dx_{\mathrm{L}}}{dt} = &\overbrace{-\frac{1}{\tau_{\mathrm{Mig}}} \cdot \frac{M_{\mathrm{G}}}{M_{\mathrm{L}}}\left[\alpha x_{\mathrm{L}} - x_{\mathrm{G}}\right]}^{\text{distillation}} \overbrace{+\frac{F_{\mathrm{con}}}{\alpha \cdot M_{\mathrm{L}}} \cdot x_{\mathrm{G}}}^{\text{condensation}} \overbrace{-\frac{\alpha \cdot F_{\mathrm{vap}}}{M_{\mathrm{L}}} \cdot x_{\mathrm{L}}}^{\text{evaporation}} \\ &\overbrace{-\frac{F_{\mathrm{L}}}{M_{\mathrm{L}}} \cdot x_{\mathrm{L}}}^{\text{extraction}} \overbrace{+\frac{(F_{\mathrm{L}} - F_{\mathrm{Bell}})}{M_{\mathrm{L}}} \cdot x_{\mathrm{L}}}^{\text{return H.E.}}.\end{aligned} \tag{6.27}$$

Here, equation (6.26) does not contain a GXe extraction and H.E. return term. However, a krypton flux is carried from the liquid into the gaseous reservoir due to the bell flow. Again, its equilibrium relation can be analyzed with $\alpha = 10.5$, $F_{\mathrm{vap}} = 10\,\mathrm{slpm}$ ($84\,\mathrm{kg/d}$), $F_{\mathrm{Bell}} = 1.5\,\mathrm{slpm}$ ($13\,\mathrm{kg/d}$), $M_{\mathrm{G}} = 21.5\,\mathrm{kg}$, and $\tau_{\mathrm{Mig}} = 0.67\,\mathrm{d}$, assuming the same migration time as in ReStoX:

$$x_{\mathrm{G}} \approx 29 \cdot x_{\mathrm{L}}. \tag{6.28}$$

This value is comparable to the enhancement factor of 30 in the no circulation mode. It is larger than the standard circulation mode ($x_{\mathrm{G}} \approx 22 \cdot x_{\mathrm{L}}$), as no krypton-enriched xenon is extracted from the GXe volume and mixed with the xenon from the LXe reservoir. Thus, no additional krypton can be carried

into the LXe via the heat exchanger. The investigation reveals that the xenon extracted from the GXe should be guided directly into the distillation system without mixing for an optimized online distillation operation. In the following, the three different distillation modes are explained.

## Liquid+gas distillation

A first test for the proof of principle of the new online distillation method was performed without any hardware modifications of the global system and is referred to as *liquid+gas* distillation. The campaign lasted from 11 Aug - 22 Aug 2016. In principle, the purification system was operated in standard circulation mode to further remove electronegative impurities and thus, to further increase the electron lifetime. Additionally, no interference with other subsystems occurred allowing for the continuation of the commissioning of the TPC, as planned. The main difference to the standard mode was the extraction of a liquid-gas xenon mixture from the purification system, guided to the inlet of the distillation column. The scheme in figure 6.5 for the standard circulation was updated including the distillation process, as visualized in figure 6.7.

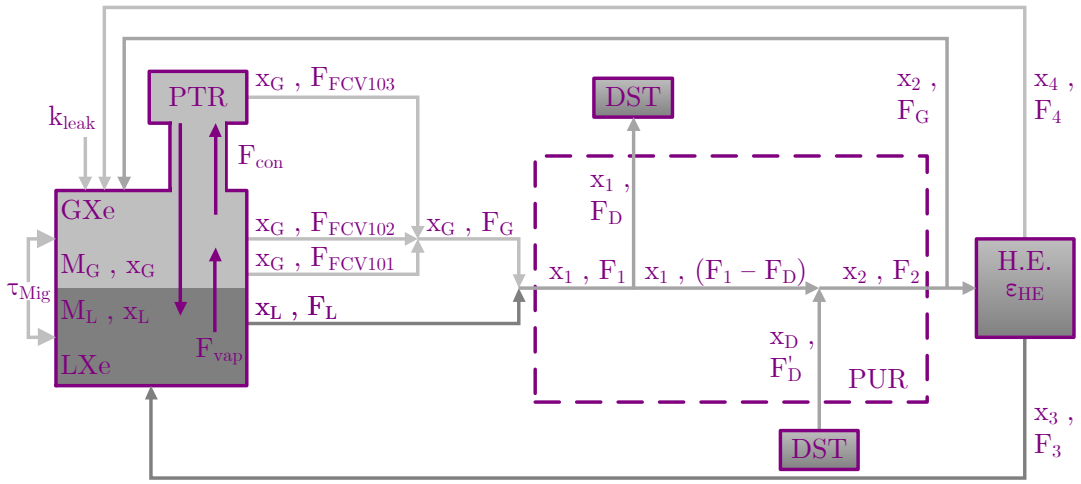


Figure 6.7: **Krypton concentrations and xenon mass flows for the liquid+gas distillation mode:** The liquid (gaseous) xenon phase LXe (GXe) in the detector contains the mass $M_L$ ($M_G$) and a krypton concentration of $x_L$ ($x_G$). The exchange between the GXe and LXe can happen either due to distillation, modeled with the migration time $\tau_{Mig}$ or by vaporization ($F_{vap}$) and condensation ($F_{con}$). Different concentrations in different locations are denoted as $x_i$ with their respective flow $F_i$. The heat exchanger (H.E.) liquefies the returning gas with an efficiency $\epsilon_{HE}<1$. Thus, the H.E. features a distillation effect. In this mode, a liquid-gas xenon mixture was purified by the distillation column.

As in the standard mode, krypton-enriched xenon is extracted from the GXe at a flow $F_G$ with a concentration $x_G$ and is mixed with a xenon flow $F_L$ from the

LXe volume with concentration $x_{\mathrm{L}}$. As reminder, the summed flow $F_1 = F_{\mathrm{G}} + F_{\mathrm{L}}$ contains the concentration

$$x_1 = \frac{F_{\mathrm{G}}}{F_1} \cdot x_{\mathrm{G}} + \frac{F_{\mathrm{L}}}{F_1} \cdot x_{\mathrm{L}}. \tag{6.29}$$

From this location, several pipettes were extracted during the liquid+gas distillation to monitor the krypton in xenon evolution. These samples were measured directly on-site with the RGA system next to the distillation column. The sample analysis is presented in section 6.2.

The mass flow $F_{\mathrm{D}} \approx 7.5\,\mathrm{slpm}$ with concentration $x_1$ is guided to the distillation column, where krypton is removed within the off-gas. The purified xenon from the distillation outlet is denoted as $x_{\mathrm{D}}$ and returns at the flow $F'_{\mathrm{D}} \approx 7.4\,\mathrm{slpm}$ to the purification system. The krypton particle flux $x_2 \cdot F_2$ at the purification system outlet is

$$x_2 \cdot F_2 = x_1 \cdot (F_1 - F_{\mathrm{D}}) + x_{\mathrm{D}} \cdot F'_{\mathrm{D}} \tag{6.30}$$

From that, $x_2$ can be calculated:

$$x_2 = \left(\frac{F_1 - F_{\mathrm{D}}}{F_2}\right) \cdot x_1 + \frac{F'_{\mathrm{D}}}{F_2} \cdot x_{\mathrm{D}} \tag{6.31}$$

In order to simplify the equation above, some assumptions are made: The off-gas mass flow $F_{\mathrm{D}} - F'_{\mathrm{D}}$ can be neglected such that $F_{\mathrm{D}} = F'_{\mathrm{D}}$ is valid. With that, it applies also $F_2 = F_1$. Using equation (6.29), leads to

$$x_2 = \left(1 - \frac{F_{\mathrm{D}}}{F_1}\right) \cdot \left(\frac{F_{\mathrm{G}}}{F_1} \cdot x_{\mathrm{G}} + \frac{F_{\mathrm{L}}}{F_1} \cdot x_{\mathrm{L}}\right) + \frac{F_{\mathrm{D}}}{F_1} \cdot x_{\mathrm{D}}. \tag{6.32}$$

At the purification outlet, a krypton flux $x_2 \cdot F_{\mathrm{G}}$ returns directly into the GXe volume, while a krypton flux of $x_2 \cdot F_{\mathrm{L}}$ is partially liquefied in the heat exchanger. As derived in the standard circulation mode, the liquid ($x_3 \cdot F_3$) and gas ($x_4 \cdot F_4$) fluxes are given by

$$x_3 \cdot F_3 = \frac{x_2}{\epsilon_{\mathrm{HE}} + \alpha \cdot (1 - \epsilon_{\mathrm{HE}})} \cdot \epsilon_{\mathrm{HE}} \cdot F_{\mathrm{L}}, \tag{6.33}$$

$$x_4 \cdot F_4 = \frac{\alpha \cdot x_2}{\epsilon_{\mathrm{HE}} + \alpha\,(1 - \epsilon_{\mathrm{HE}})} \cdot (1 - \epsilon_{\mathrm{HE}}) \cdot F_{\mathrm{L}}. \tag{6.34}$$

Also here, the condensation flow $F_{\mathrm{con}}$ is larger than the evaporated flow $F_{\mathrm{vap}}$ due to the heat exchanger inefficiency. It applies

$$F_{\mathrm{con}} = F_{\mathrm{vap}} + (1 - \epsilon_{\mathrm{HE}}) \cdot F_{\mathrm{L}}. \tag{6.35}$$

Taking all in-going and out-going krypton fluxes into account, the coupled

differential equation system can be derived:

$$\begin{aligned}\frac{dx_{\mathrm{G}}}{dt} =& \overbrace{+\frac{1}{\tau_{\mathrm{Mig}}}\left[\alpha x_{\mathrm{L}} - x_{\mathrm{G}}\right]}^{\text{distillation}} \overbrace{-\frac{F_{\mathrm{con}}}{\alpha \cdot M_{\mathrm{G}}} \cdot x_{\mathrm{G}}}^{\text{condensation}} \overbrace{+\frac{\alpha \cdot F_{\mathrm{vap}}}{M_{\mathrm{G}}} \cdot x_{\mathrm{L}}}^{\text{evaporation}} \\ & \overbrace{-\frac{F_{\mathrm{G}}}{M_{\mathrm{G}}} \cdot x_{\mathrm{G}}}^{\text{extraction}} \overbrace{+\frac{F_{\mathrm{G}}}{M_{\mathrm{G}}} \cdot x_2}^{\text{return}} \overbrace{+\frac{F_4}{M_{\mathrm{G}}} \cdot x_4}^{\text{return H.E.}} \overbrace{+\frac{k_{\mathrm{leak}}}{M_{\mathrm{G}}}}^{\text{leak}}, \end{aligned} \tag{6.36}$$

$$\begin{aligned}\frac{dx_{\mathrm{L}}}{dt} =& \overbrace{-\frac{1}{\tau_{\mathrm{Mig}}} \cdot \frac{M_{\mathrm{G}}}{M_{\mathrm{L}}}\left[\alpha x_{\mathrm{L}} - x_{\mathrm{G}}\right]}^{\text{distillation}} \overbrace{+\frac{F_{\mathrm{con}}}{\alpha \cdot M_{\mathrm{L}}} \cdot x_{\mathrm{G}}}^{\text{condensation}} \overbrace{-\frac{\alpha \cdot F_{\mathrm{vap}}}{M_{\mathrm{L}}} \cdot x_{\mathrm{L}}}^{\text{evaporation}} \\ & \overbrace{-\frac{F_{\mathrm{L}}}{M_{\mathrm{L}}} \cdot x_{\mathrm{L}}}^{\text{extraction}} \overbrace{+\frac{F_3}{M_{\mathrm{L}}} \cdot x_3}^{\text{return H.E.}}. \end{aligned} \tag{6.37}$$

In principle, both equations include the same terms as in the standard circulation mode. The difference is, that the purification outlet flux $F_2$ contains a reduced krypton concentration $x_2$. Thus, the returning fluxes $x_2 \cdot F_{\mathrm{G}}$, $x_3 \cdot F_3$ and $x_4 \cdot F_4$ posses a lower krypton concentration as well. As this operation mode was not optimized, a gas only distillation mode was tested, where only the GXe reservoir was circulated. This is reviewed next.

## Gas only distillation

In the second distillation mode, the circulation of the purification system was changed such that only the gaseous part of the detector was purified. This allowed for the testing of the krypton removal for an increased exchange time of the gas phase without any hardware modification. Additionally, the electronegative impurities might accumulate inside the gas phase as well, slowing down the electron lifetime increase drastically. They would also be removed efficiently along with krypton. A first starting attempt was performed on 22 Aug 2016, but after a few hours a QDrive pump broke. Thus, the test was postponed a few days in order to exchange the pump. Finally, the main campaign of this mode was operated from 24 Aug - 02 Sep 2016. A scheme in figure 6.8 illustrates the process including all relevant flows and concentrations in the different locations of the global system.

In this mode, gaseous xenon with a krypton concentration $x_{\mathrm{G}}$ is extracted from the condenser stations at a flow of $F_{\mathrm{FCV103}}$ ($\approx 1.2\,\mathrm{slpm}$) as well as via the heat exchanger at a flow $F_{\mathrm{g}}$ ($\approx 20\,\mathrm{slpm}$). As no xenon is extracted from the liquid reservoir ($F_{\mathrm{L}} = 0\,\mathrm{slpm}$), the heat exchanger is not operational. The summed flow $F_1 = F_{\mathrm{FCV103}} + F_{\mathrm{g}}$, entering the purification system, contains the concentration $x_1 = x_{\mathrm{G}}$. Consequently, $x_1$ is different to the liquid+gas mode, and thus, the RGA samples taken from this location give direct access to $x_{\mathrm{G}}$. From here, again, the flow to (from) the distillation column is $F_{\mathrm{D}} \approx 7\,\mathrm{slpm}$ ($F'_{\mathrm{D}} \approx 6.9\,\mathrm{slpm}$) and the outlet concentration is $x_{\mathrm{D}}$. Then, the concentration leaving the purification system is

$$x_2 = \frac{F_1 - F_{\mathrm{D}}}{F_2} \cdot x_1 + \frac{F'_{\mathrm{D}}}{F_2} \cdot x_{\mathrm{D}}. \tag{6.38}$$

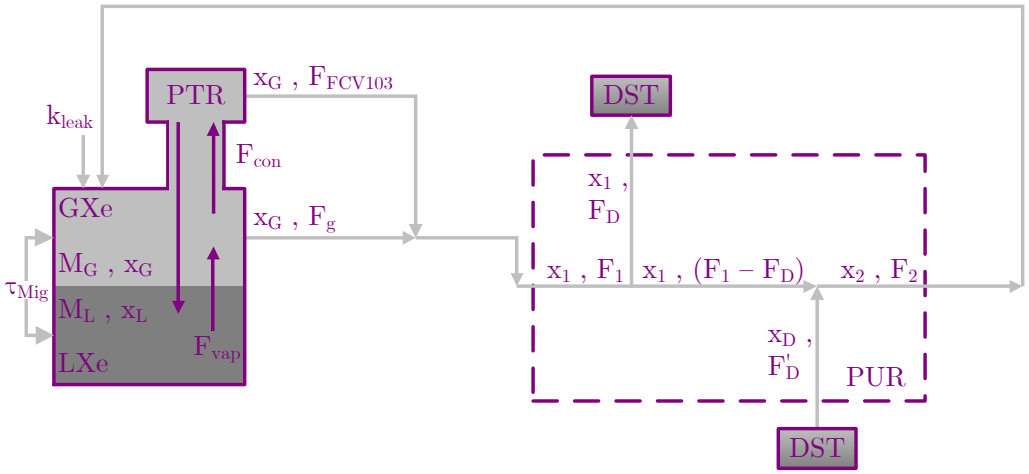


Figure 6.8: **Krypton concentrations and xenon mass flows for the gas only mode:** The liquid (gaseous) xenon phase LXe (GXe) in the detector contains the mass $M_L$ ($M_G$) and a krypton concentration of $x_L$ ($x_G$). The exchange between the GXe and LXe can happen either due to distillation, modeled with the migration time $\tau_{Mig}$ or by vaporization ($F_{vap}$) and condensation ($F_{con}$). Different concentrations in different locations are denoted as $x_i$ with their respective flow $F_i$. The heat exchanger (H.E.) is not operational in this mode and thus, omitted.

The off-gas flow ($F_D - F'_D$) can be neglected, which leads to $F_D = F'_D$. Thus, it applies $F_2 = F_1$. With that, equation (6.38) simplifies to

$$x_2 = \left(1 - \frac{F_D}{F_1}\right) \cdot x_G + \frac{F_D}{F_1} \cdot x_D \tag{6.39}$$

In the gas only circulation mode, the full flux $x_2 \cdot F_2$ returns to the GXe volume, as the heat exchanger is not operational. Thus, the same xenon amount leaves and enters this reservoir and therefore, the condensation flow $F_{con}$ is equal to the evaporated flow $F_{vap}$.

Finally, the two equations, describing the change in the krypton concentration in the GXe and LXe phases are given by

$$\begin{aligned}\frac{dx_G}{dt} = &\overbrace{+\frac{1}{\tau_{Mig}}\left[\alpha x_L - x_G\right]}^{\text{distillation}} \overbrace{-\frac{F_{con}}{\alpha \cdot M_G} \cdot x_G}^{\text{condensation}} \overbrace{+\frac{\alpha \cdot F_{vap}}{M_G} \cdot x_L}^{\text{evaporation}} \\ &\overbrace{-\frac{F_1}{M_G} \cdot x_G}^{\text{extraction}} \overbrace{+\frac{F_2}{M_G} \cdot x_2}^{\text{return}} \overbrace{+\frac{k_{leak}}{M_G}}^{\text{leak}},\end{aligned} \tag{6.40}$$

$$\frac{dx_L}{dt} = \overbrace{-\frac{1}{\tau_{Mig}} \cdot \frac{M_G}{M_L}\left[\alpha x_L - x_G\right]}^{\text{distillation}} \overbrace{+\frac{F_{con}}{\alpha \cdot M_L} \cdot x_G}^{\text{condensation}} \overbrace{-\frac{\alpha \cdot F_{vap}}{M_L} \cdot x_L}^{\text{evaporation}}. \tag{6.41}$$

Here, the krypton exchange in the liquid reservoir depends solely on the distillation, condensation and evaporation terms. Furthermore, both equations are

independent from the heat exchanger efficiency. This is different from the other modes and makes the gas only distillation more sensitive to $\tau_{\mathrm{Mig}}$, $F_{\mathrm{con}}$ and $F_{\mathrm{vap}}$. After the first two distillation campaigns, the flow path for the xenon extraction was optimized. This is presented in the following.

## Upgraded gas only distillation

The final configuration for the online krypton removal required hardware modifications such that a direct connection between the gas phase of the detector and the inlet of the distillation column was possible. The investigation of the liquid only circulation equations for the equilibrium revealed that the direct extraction from the GXe reservoir into the column is beneficial for the online removal, because it creates a faster krypton migration from the liquid into the gas. Furthermore, it allows for the full flow of the main purification loop in parallel to the distillation process.

Two short distillation tests were performed from 28 Sep - 29 Sep 2016 and 13 Oct - 14 Oct 2016 as a first verification of the final configuration. After that, an upgrade of the purification system was done. Initially, only two QDrive pumps were installed. After the installation of a third QDrive in series to one of the existing pumps, a higher total purification flow could be achieved ($\approx 50\,\mathrm{slpm}$). The main purpose was to reduce the stress on the existing pumps and by that to increase their lifespan. A fourth pump for the second branch of the system was planned, but it broke and was in repair during the measurement period.

Finally, a long-term online distillation in the upgraded gas only mode was performed from 28 Oct - 12 Dec 2016. The thermodynamic stability during this process is presented in section 4.1. During the operation, the total xenon inventory of the detector system was reduced by about 6 kg per week due to the off-gas flow of 0.1 slpm. This resulted into a liquid level decrease in the TPC of 0.1 mm per week. Thus, the level was manually adjusted once per week in order to keep this impact negligible for the TPC operation. No further negative influences on the detector operation could be observed.

The distillation process is visualized in figure 6.9 for the involved concentrations and flows in the different system locations.

In this operation, the xenon from the GXe phase, containing the concentration $x_{\mathrm{G}}$, is directly guided into the distillation column at the summed flow $F_{\mathrm{D}} = F_{\mathrm{G}} = F_{\mathrm{FCV101}} + F_{\mathrm{FCV102}} + F_{\mathrm{FCV103}}$.

The xenon from the liquid reservoir is vaporized in the heat exchanger and is guided to the inlet of the purification system with a krypton level of $x_1 = x_{\mathrm{L}}$ at a flow $F_1 = F_{\mathrm{L}}$. The purified xenon from the distillation system is fed back to the purification system with a krypton fraction $x_{\mathrm{D}}$ and a flow $F'_{\mathrm{D}}$. For the negligible off-gas flow $(F_{\mathrm{D}} - F'_{\mathrm{D}})$ applies $F'_{\mathrm{D}} = F_{\mathrm{D}} = F_{\mathrm{G}}$. Consequently, the flow at the purification outlet is $F_2 = F_{\mathrm{G}} + F_{\mathrm{L}}$. The concentration in this location can be calculated to be

$$x_2 = \frac{F_{\mathrm{L}}}{F_2} \cdot x_{\mathrm{L}} + \frac{F_{\mathrm{G}}}{F_2} \cdot x_{\mathrm{D}}. \tag{6.42}$$

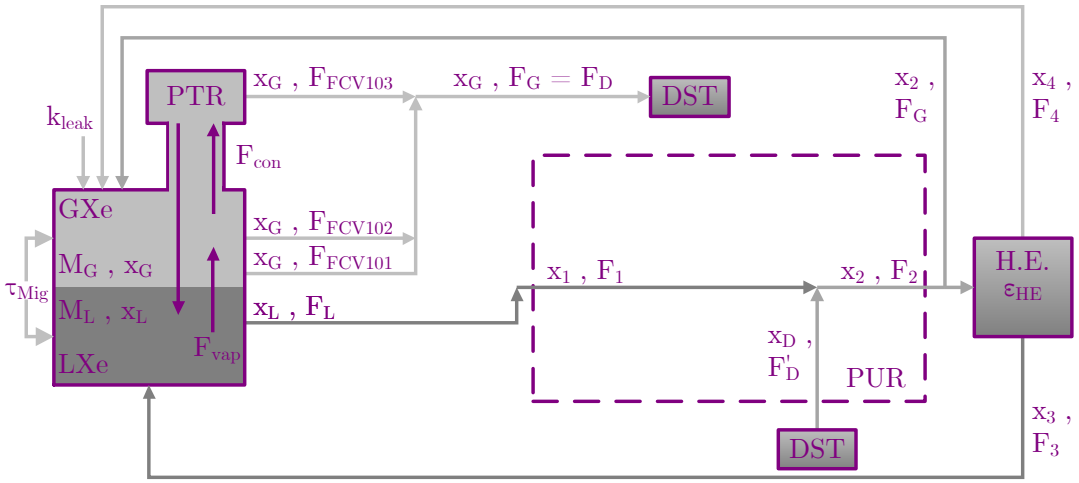


Figure 6.9: **Krypton concentrations and xenon mass flows for the upgraded gas only mode:** The liquid (gaseous) xenon phase LXe (GXe) in the detector contains the mass $M_L$ ($M_G$) and a krypton concentration of $x_L$ ($x_G$). The exchange between the GXe and LXe can happen either due to distillation, modeled with the migration time $\tau_{Mig}$ or by vaporization ($F_{vap}$) and condensation ($F_{con}$). Different concentrations in different locations are denoted as $x_i$ with their respective flow $F_i$. The heat exchanger (H.E.) liquefies the returning gas with an efficiency $\epsilon_{HE}<1$. Thus, the H.E. features a distillation effect. In this mode, xenon is extracted from the GXe reservoir and is directly purified by the distillation system.

Analogous to the liquid+gas distillation and the standard circulation, xenon with a concentration $x_2$ at a mass flow rate $F_G$ resturns into the GXe phase. The rest is partially liquefied in the heat exchanger and thus, split into two fluxes:

$$x_3 \cdot F_3 = \frac{x_2}{\epsilon_{HE} + \alpha \cdot (1 - \epsilon_{HE})} \cdot \epsilon_{HE} \cdot F_L, \tag{6.43}$$

$$x_4 \cdot F_4 = \frac{\alpha \cdot x_2}{\epsilon_{HE} + \alpha\,(1 - \epsilon_{HE})} \cdot (1 - \epsilon_{HE}) \cdot F_L. \tag{6.44}$$

Also here, the condensation flow $F_{con}$ is larger than the evaporated flow $F_{vap}$ due to the heat exchanger inefficiency. It applies

$$F_{con} = F_{vap} + (1 - \epsilon_{HE}) \cdot F_L. \tag{6.45}$$

The coupled differential equation system is

$$\begin{aligned}\frac{dx_\mathrm{G}}{dt} =& \overbrace{+\frac{1}{\tau_\mathrm{Mig}}\left[\alpha x_\mathrm{L} - x_\mathrm{G}\right]}^{\text{distillation}} \overbrace{-\frac{F_\mathrm{con}}{\alpha \cdot M_\mathrm{G}} \cdot x_\mathrm{G}}^{\text{condensation}} \overbrace{+\frac{\alpha \cdot F_\mathrm{vap}}{M_\mathrm{G}} \cdot x_\mathrm{L}}^{\text{evaporation}} \\ & \overbrace{-\frac{F_\mathrm{G}}{M_\mathrm{G}} \cdot x_\mathrm{G}}^{\text{extraction}} \overbrace{+\frac{F_\mathrm{G}}{M_\mathrm{G}} \cdot x_2}^{\text{return}} \overbrace{+\frac{F_4}{M_\mathrm{G}} \cdot x_4}^{\text{return H.E.}} \overbrace{+\frac{k_\mathrm{leak}}{M_\mathrm{G}}}^{\text{leak}}, \end{aligned} \tag{6.46}$$

$$\begin{aligned}\frac{dx_\mathrm{L}}{dt} =& \overbrace{-\frac{1}{\tau_\mathrm{Mig}} \cdot \frac{M_\mathrm{G}}{M_\mathrm{L}}\left[\alpha x_\mathrm{L} - x_\mathrm{G}\right]}^{\text{distillation}} \overbrace{+\frac{F_\mathrm{con}}{\alpha \cdot M_\mathrm{L}} \cdot x_\mathrm{G}}^{\text{condensation}} \overbrace{-\frac{\alpha \cdot F_\mathrm{vap}}{M_\mathrm{L}} \cdot x_\mathrm{L}}^{\text{evaporation}} \\ & \overbrace{-\frac{F_\mathrm{L}}{M_\mathrm{L}} \cdot x_\mathrm{L}}^{\text{extraction}} \overbrace{+\frac{F_3}{M_\mathrm{L}} \cdot x_3}^{\text{return H.E.}}. \end{aligned} \tag{6.47}$$

Again, in both equations, the different terms model the in-going and out-going krypton fluxes in the respective reservoir. The difference to the liquid+gas and standard circulation is the composition of the concentration $x_2$ at the purification outlet. The same flow path was used to verify online radon removal at XENON1T. This mode is briefly reviewed next.

### Online radon distillation

Two online radon removal campaigns from 19 Dec 2016 - 26 Jan 2017 and from 31 Jan - 02 Feb 2017 were performed. This operation mode features the same flow paths as visualized in figure 6.9 for the upgraded gas only distillation. Therefore, the same differential equations (6.46) and (6.47) can be applied with small modifications: In this process, radon as less volatile component is enriched in the reboiler at the bottom of the column until disintegration. Thus, no off-gas is extracted. The radon-depleted xenon leaves the column at the top and is flowing back to the purification system. Here, it is added to the xenon extracted from the LXe detector part. As krypton is not influenced by the radon removal process, the column outlet flow contains the krypton concentration $x_\mathrm{G}$. Thus, it applies

$$x_2 = \frac{F_\mathrm{L}}{F_2} \cdot x_\mathrm{L} + \frac{F_\mathrm{G}}{F_2} \cdot x_\mathrm{G}. \tag{6.48}$$

With that, the rest can be modeled as in the upgraded gas only operation mode.

## 6.2 Sample analysis

The krypton in xenon evolution over time was monitored in order to quantify the online removal quality for the different operation modes. This was done in three ways: the on-site residual gas analyzer system (RGA), the off-site rare gas mass spectrometer (RGMS), and the electronic recoil event rate inside the TPC itself. In the following, the sample analysis for the three cases is presented.

### 6.2.1 RGA

The on-site RGA behind a $LN_2$-cooled coldtrap was especially useful for the first two online removal tests, liquid+gas and gas only, as it provided a fast and direct feedback for the krypton in xenon concentrations. During the upgraded gas only operations, the krypton concentrations reached a level below the RGA sensitivity. Thus, no pipettes were extracted for the measurement with the on-site RGA system in this mode. All details about the RGA system can be found in [74].

Similar to section 5.4, all extracted pipettes within one operation mode featured the same pressure. Thus, the same flow behavior during the measurement can be expected and no flow correction is applied in a first step. Consequently, the samples can be directly compared. For each pipette, the mass-over-charge range 83 - 87 with a resolution of 5 PPAmu and a DWELL of 64 ms was measured during each scan. The background for each $^{m}/_{z}$-value was monitored before the sample introduction. It was averaged and subtracted from the respective spectrum.

In figure 6.10, the isotope ratios $^{84}Kr/^{83}Kr$ and $^{84}Kr/^{86}Kr$ for each pipette during the liquid+gas and gas only distillation are visualized. In both distillation modes, the ratios are consistent throughout the samples. The ratios for the natural abundance of $^{84}Kr/^{83}Kr = 5.0$ ($^{84}Kr/^{86}Kr = 3.3$) is indicated in blue (brown). While the average ratios of $^{84}Kr/^{86}Kr = 3.4 \pm 0.1$ for both modes agree with the natural one, the average ratios $^{84}Kr/^{83}Kr = 6.9 \pm 0.3$ for liquid+gas and $^{84}Kr/^{83}Kr = 7.1 \pm 0.3$ for gas only are a factor 1.4 too high. Due to the usage of $^{83m}Kr$ as a calibration source in XENON1T, it is expected that the $^{83}Kr$ amount is increased. This would lead to a lower ratio with respect to the natural one. Most likely, another background component with mass-over-charge of 83 is contributing as well. This can result into a false decreasing evolution over time, when comparing different samples to each other. Therefore, $^{83}Kr$ is rejected for the further analysis.

As in section 5.4, but without $^{83}Kr$, the spectra of the isotopes $^{84}Kr$ as well as $^{86}Kr$ were normalized with the respective maximum current of the first pipette. Then, the two spectra were integrated for a fixed window of 100 s and the mean of the two integrals along with the standard deviations are computed and used for the comparison to other pipettes within the same operation mode. Like that, the two most abundant krypton isotopes, matching the ratio from natural abundance, can be utilized, yielding a more robust result compared to the usage of only $^{84}Kr$.

In order to allow for the fitting of the evolution model, an absolute krypton in xenon concentration is required. As presented in section 5.4, two parallel samples were extracted on 12 Mar 2016 11:19 during the online ReStoX distillation, one for the RGA and one for RGMS, allowing for an absolute calibration of the RGA data. So far, a flow correction was not required, when comparing samples within one operation mode as they featured the same pressure in the measurement volume and thus, the same flow behaviour. However, by applying this correction, samples of other batches with varying pressures and flows can be compared [74]. Under the assumption that the RGA performance does not change over time, a flow correction of the first pipette of the liquid+gas as well as the gas only operation allows for an absolute calibration of all other pipettes. The correction

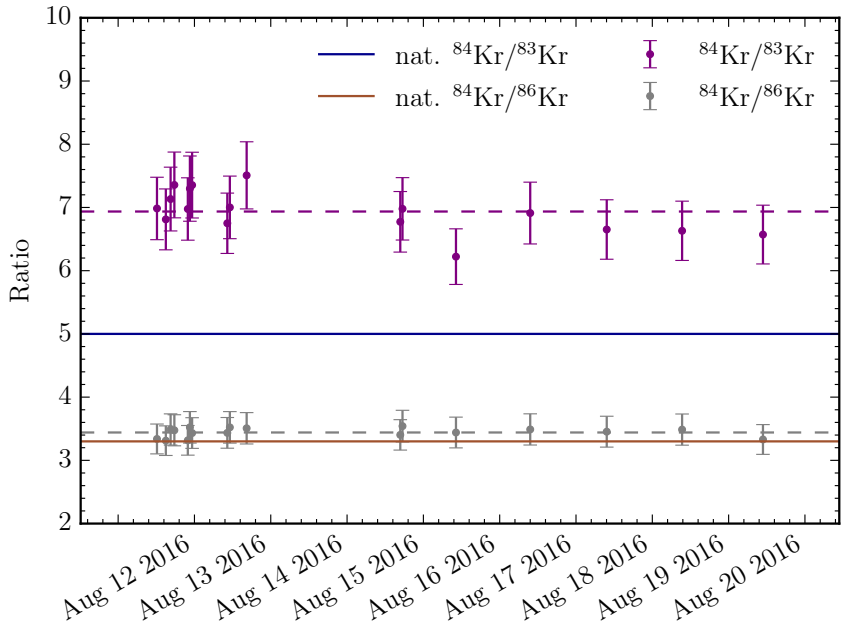


(a) Liquid + gas distillation mode

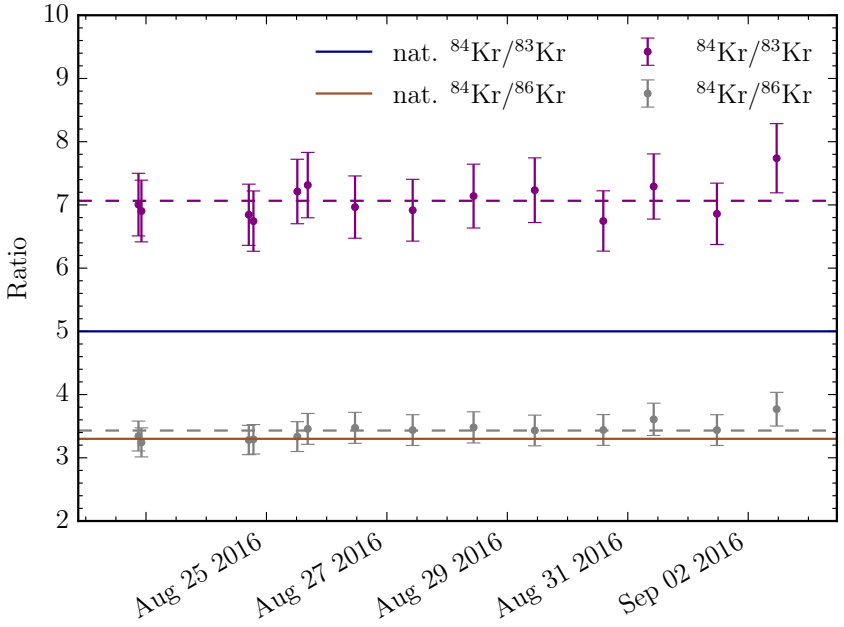


(b) Gas only distillation mode

Figure 6.10: **Krypton isotope ratios during the liquid+gas and gas only distillation operations.**

for the ReStoX sample is exemplary shown in the following whereas the procedure is the same for the other two samples:

The raw currents $I_{\text{raw}}$ for $\frac{m}{z} = 84$ (purple) and $\frac{m}{z} = 86$ (grey) are visualized in the top panel of figure 6.11. The opening of the sample volume to the cold-trap followed by the RGA main chamber is shifted to $t = 0\,\text{s}$. It can be observed, that the gas is trapped inside the cold-trap for about 50 s. Then, a signal in both masses can be seen. After a maximum around 100 s, both signals start to

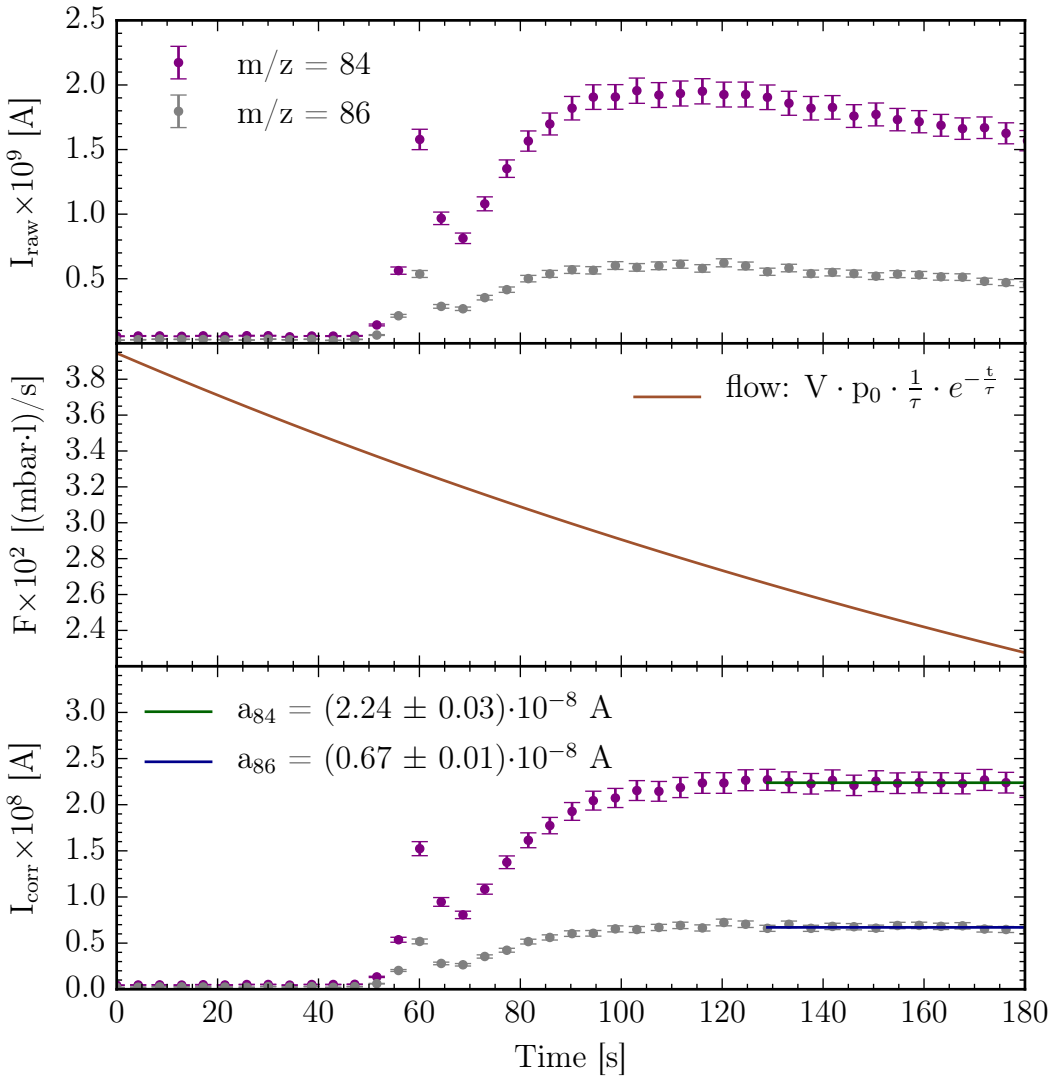


Figure 6.11: **RGA ReStoX sample analysis with flow correction:** Top: The raw currents $I_{raw}$ for $\frac{m}{z} = 84$ (purple) and $\frac{m}{z} = 86$ (grey) increase 50 s after opening the sample volume. After a maximum around 100 sec, both signals start to decrease again. Middle: The flow into the cold-trap can be derived from the measured pressure drop in the measurement volume. It can be applied to the raw data in order to flatten the decreasing signals. Bottom: The corrected currents are flattened for large times. A constant to each plateau is fitted in order to compare the signal to other pipettes.

decrease again. This decrease can be flattened by a flow correction allowing for the comparison of samples with different pressures.

In a first step for the flow correction, the pressure drop during the measurement inside the sample volume $V$ is fitted with an exponential function

$$p(t) = p_0 \cdot e^{-\frac{t}{\tau}}, \tag{6.49}$$

with $p_0$ being the initial pressure in the sample volume and $\tau$ being the time

Table 6.2: Fitted RGA signals $a_{84}$ and $a_{86}$ along with their ratio for a ReStoX, a liquid+gas and a gas only sample after flow correction. With that, the samples can be compared directly.

| Sample | $a_{84}$ [A] | $a_{86}$ [A] | Ratio |
|---|---|---|---|
| ReStoX | $(2.24 \pm 0.03) \times 10^{-8}$ | $(0.67 \pm 0.01) \times 10^{-8}$ | 3.34 |
| Liquid+gas | $(1.64 \pm 0.01) \times 10^{-8}$ | $(0.47 \pm 0.01) \times 10^{-8}$ | 3.50 |
| Gas only | $(3.36 \pm 0.02) \times 10^{-8}$ | $(1.00 \pm 0.01) \times 10^{-8}$ | 3.36 |

constant of the decrease. From this, the flow $F$ can be derived as

$$F(t) = -V \cdot \frac{dp(t)}{dt} = V \cdot p_0 \cdot \frac{1}{\tau} \cdot e^{-\frac{t}{\tau}}. \tag{6.50}$$

The resulting flow is presented in the middle panel of figure 6.11 for $V = 40\,\text{ml}$, $p_0 = 320\,\text{mbar}$ and $\tau = 327\,\text{s}$. The corrected current $I_{\text{corr}}$ can be calculated with

$$I_{\text{corr}}(t) = I_{\text{raw}}(t) \cdot \frac{F_{\text{norm}}}{F(t)}. \tag{6.51}$$

Here, $F_{\text{norm}} = 0.317\,(\text{mbar} \cdot \text{l})/\text{s}$ denotes a normalization factor taken from [74]. This factor as well as the sample volume $V$ are the same for all pipettes. The corrected currents are shown in the bottom panel in figure 6.11 along with two fits with a constant in the flattened region between 130 s and 180 s. In more detail, a constant plateau of $a_{84} = (2.24 \pm 0.03) \times 10^{-8}\,\text{A}$ for $^{84}$Kr and a constant of $a_{86} = (0.67 \pm 0.01) \times 10^{-8}\,\text{A}$ for $^{86}$Kr were obtained. The ratio $^{84}\text{Kr}/^{86}\text{Kr}$ yields 3.3, in agreement with the expected ratio from the natural abundance. The determined currents correspond to an absolute krypton in xenon concentration of $(23.1 \pm 0.6)\,\text{ppb}$, measured with the RGMS from an identical sample. Above correction is applied to the first sample during the liquid+gas distillation as well as the first pipette during the gas only distillation. The fitted constants are summarized in table 6.2.

Finally, the normalized integrated currents $I_{\text{i,LG}}$ (Liquid+gas) and $I_{\text{i,GO}}$ (Gas only) from the RGA measurements during the two operation modes can be transformed into absolute concentrations $c_{\text{i,abs,LG}}$ and $c_{\text{i,abs,GO}}$ with the help of $c_{\text{RSX,RGMS}} = (23.1 \pm 0.6)\,\text{ppb}$, $a_{84,\text{RSX}}$ and $a_{86,\text{RSX}}$:

$$c_{\text{i,abs,LG}} = \underbrace{\frac{\frac{c_{\text{RSX,RGMS}}}{a_{84,\text{RSX}}} \cdot a_{84,\text{LG}}}{2} \cdot \frac{I_{\text{i,LG}}}{I_{1,\text{LG}}}}_{f_1} + \underbrace{\frac{\frac{c_{\text{RSX,RGMS}}}{a_{86,\text{RSX}}} \cdot a_{86,\text{LG}}}{2} \cdot \frac{I_{\text{i,LG}}}{I_{1,\text{LG}}}}_{f_2}. \tag{6.52}$$

The uncertainty $\Delta c_{\text{i,abs,LG}}$ is given by

$$\Delta c_{\text{i,abs,LG}} = \sqrt{\Delta f_1^2 + \Delta f_2^2}, \tag{6.53}$$

with

$$\Delta f_1 = f_1 \cdot \sqrt{\left(\frac{\Delta c_{\mathrm{RSX,RGMS}}}{c_{\mathrm{RSX,RGMS}}}\right)^2 + \left(\frac{\Delta a_{84,\mathrm{RSX}}}{a_{84,\mathrm{RSX}}}\right)^2 + \left(\frac{\Delta a_{84,\mathrm{LG}}}{a_{84,\mathrm{LG}}}\right)^2 + \left(\frac{\Delta I_{\mathrm{i,LG}}}{I_{\mathrm{i,LG}}}\right)^2 + \left(\frac{\Delta I_{1,\mathrm{LG}}}{I_{1,\mathrm{LG}}}\right)^2}, \tag{6.54}$$

$$\Delta f_2 = f_2 \cdot \sqrt{\left(\frac{\Delta c_{\mathrm{RSX,RGMS}}}{c_{\mathrm{RSX,RGMS}}}\right)^2 + \left(\frac{\Delta a_{86,\mathrm{RSX}}}{a_{86,\mathrm{RSX}}}\right)^2 + \left(\frac{\Delta a_{86,\mathrm{LG}}}{a_{86,\mathrm{LG}}}\right)^2 + \left(\frac{\Delta I_{\mathrm{i,LG}}}{I_{\mathrm{i,LG}}}\right)^2 + \left(\frac{\Delta I_{1,\mathrm{LG}}}{I_{1,\mathrm{LG}}}\right)^2} \tag{6.55}$$

The calculation for the gas only pipettes is done analogously. The absolute values during both periods are highlighted in figure 6.12.

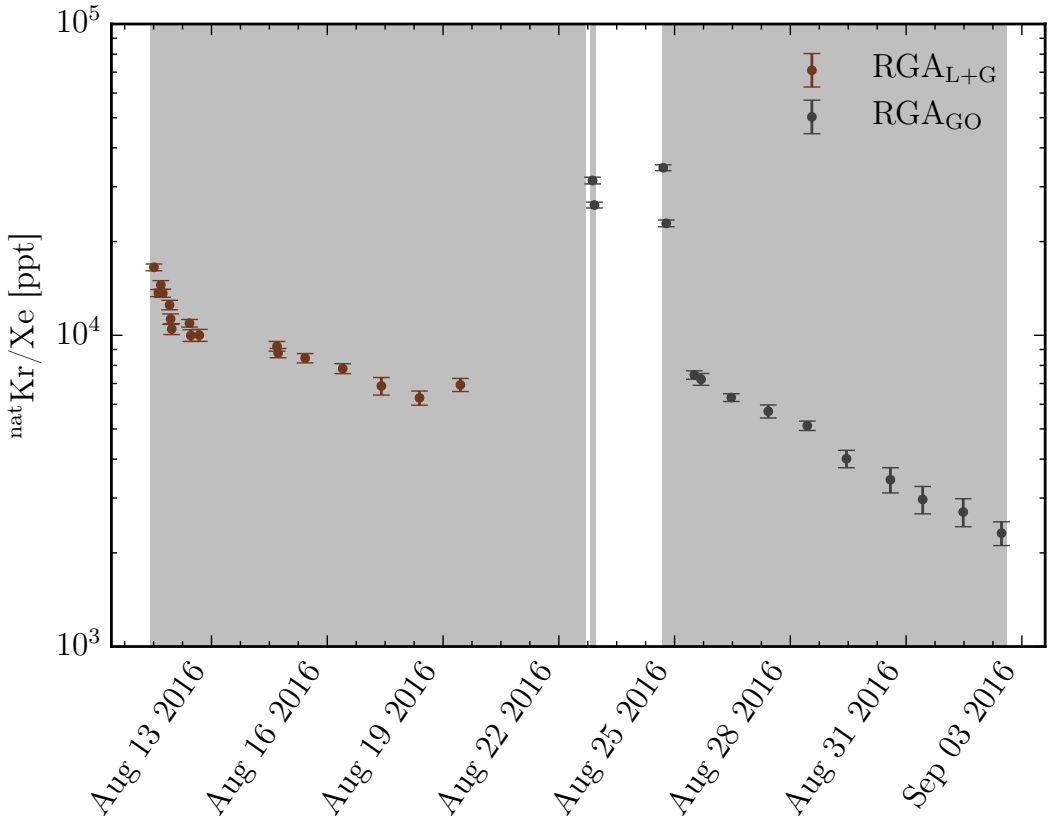


Figure 6.12: **Krypton concentrations from RGA data:** The brown data points represent the samples during liquid+gas distillation, while the darkgrey points correspond to the gas only mode. The distillation periods are shaded in grey. During the first gas only distillation attempt (thin shaded area) a QDrive pump broke, such that the operation was postponed by a few days. When starting a distillation process, the krypton level is decreasing steeply during the first hours of operation. Then, the slope changes and a slower removal can be observed.

In both cases, the krypton level is decreasing steeply during the first hours of operation, as expected from the online distillation model. This corresponds to a fast cleaning of the GXe reservoir and thus, a bulk removal of krypton at

the beginning of each operation. Then, the slope changes and a slower removal can be observed, as the combined time constant is dominated by the slower migration processes between the GXe and LXe phases. Note that during the first test of the gas only distillation, a QDrive pump broke such that the process was stopped and restarted a few days later.

### 6.2.2 RGMS

The rare gas mass spectrometer detects trace amounts of natural krypton in xenon down to the ppq level [50]. Therefore, it was used to monitor the absolute krypton in xenon concentration within the fiducial volume during the removal campaign. This was achieved by operating the detector in the liquid only circulation mode, such that the extracted samples at the purification system $x_1$ contained solely xenon from the LXe volume. In total, 16 samples were extracted and measured off-site in Heidelberg during the distillation campaigns, the science run 0 (SR0) and science run 1 (SR1). The results are summarized in table 6.3. The first sample was taken on 22 Aug 2016 and contained a concentration of

Table 6.3: Absolute krypton in xenon concentrations extracted from the LXe in the fiducial volume of XENON1T measured by RGMS in Heidelberg during the online krypton removal campaign, science run 0 (SR0) and science run 1 (SR1). The lowest krypton level in a running xenon based dark matter detector was achieved.

| Date | $^{nat}$Kr/Xe [ppt] | Comments |
|---|---|---|
| 22 Aug 2016 | 1000 ± 200 | After liquid+gas |
| 05 Sep 2016 | 330 ± 50 | After gas only |
| 14 Oct 2016 | 190 ± 30 | During upgraded gas only 2 |
| 08 Nov 2016 | 31 ± 6 | During upgraded gas only 3, SR0 |
| 21 Nov 2016 | 2.6 ± 0.5 | During upgraded gas only 3, SR0 |
| 01 Dec 2016 | 1.3 ± 0.3 | During upgraded gas only 3, SR0 |
| 21 Dec 2016 | 0.62 ± 0.13 | During SR0 |
| 16 Feb 2017 | 0.36 ± 0.06 | During SR1 |
| 09 Mar 2017 | <0.62 | During SR1 |
| 13 Apr 2017 | 0.47 ± 0.07 | During SR1 |
| 25 May 2017 | 1.99 ± 0.31 | Liquid+gas mixture, during SR1 |
| 01 Jun 2017 | 0.57 ± 0.09 | During SR1 |
| 26 Jul 2017 | 0.68 ± 0.11 | During SR1 |
| 29 Sep 2017 | 0.63 ± 0.10 | During SR1 |
| 10 Nov 2017 | 1.09 ± 0.20 | During SR1 |
| 26 Jan 2018 | 0.87 ± 0.16 | During SR1 |

$(1.0 \pm 0.2)$ ppb. With each of the following samples, the concentration decreased. The online krypton removal was stopped on the 12 Dec 2016. The extracted sample from 21 Dec 2016 yielded a concentration of $(620 \pm 130)$ ppq. The pipette from 16 Feb 2017 contained $(360 \pm 60)$ ppq of krypton. This is the lowest krypton level ever achieved in a xenon based detector and is only a factor 1.8 larger

than the initial requirement of 200 ppq for XENON1T. This value was sufficient enough since radon dominated the background. However, the online distillation could just be switched on again, if lower levels would be desired.

An increase of the concentrations can be observed throughout the science run 1 between Feb 2017 and Jan 2018. This is an indication that krypton is entering the liquid xenon phase via outgassing from dead volumes or due to micro leaks and needs to be taken into account for the krypton evolution model.

One sample, on 25 May 2017, was extracted during the standard circulation mode of the detector. Thus, it contained a liquid and gas mixture from the GXe and LXe reservoir. This gives an additional piece of information if the model can describe the global system well also during the standard circulation.

### 6.2.3 ER event rate

Krypton creates low energy[1] signals within the fiducial volume, as explained in section 2.3. The produced krypton decay event rate in the detector is proportional to the number of krypton particles. Thus, at the beginning of the distillation tests, krypton should be the dominant background source as the initial concentration was on the (ppt-ppb)-level. Therefore, by monitoring the overall detector event rate in the low energy region, the krypton evolution can be monitored. Thus, this method gives direct access to the krypton inside the liquid volume LXe. In order to obtain the event rate in the detector from the particle interactions in the TPC, several selection criteria (referred to as cuts) as well as signal corrections have to be applied. This is briefly reviewed.

The data processing and analysis is done with the Processor for Analyzing XENON (PAX) [79] and the Handy Analysis tools for XENON (HAX) [80]. Both were designed for XENON1T with open source software. The structure of PAX is highly customizable by the usage of plugins along the processing, allowing to handle also data from other TPCs. The PMTs record signals from an interaction in the form of pulses within the respective PMT waveform. A pulse is referred to as hit, if a dynamical two-fold threshold condition is fulfilled. In detail, the rising flank must surpass a $1\sigma$ as well as a $5\sigma$ excess with respect to the baseline. The samples within the hit are summed up until the falling flank crosses the $1\sigma$ threshold. This sum can be converted into a number of detected photoelectrons (pe) by applying the experimentally determined PMT gain. Specialized algorithms cluster coincidental PMT hits within a defined time range into peaks. PAX calculates and provides several properties of each peak such as the area in pe as well as the width in ns. These are utilized to classify peaks as S1, S2 or unknown. In each event, the largest S1 as well as the largest S2 are paired to a so called interaction. For each interaction, the radial position as well the interaction depth are computed. Position dependent corrections are applied such as the light collection efficiency for the S1 or an electron lifetime correction for S2 [41]. The corrected signals are referred to as cS1 and cS2 in the following.

In the context of monitoring the low energy event rate, background data was loaded with pre-selections in HAX, as stated in table 6.4. The following custom

[1] In the context of this analysis, low energy corresponds to an energy interval of (0–200) keV.

defined cuts were applied in order to extract the event rate in the detector. The analysis, based on [81], was performed before fixed cuts were defined for the dark matter search.

Table 6.4: Pre-selection for loading of background data with HAX.

| Variable | Selection |
|---|---|
| cS1 | $0\,\text{pe} < \text{cS1} < 2000\,\text{pe}$ |
| cS2 | $\text{cS2} > 150\,\text{pe}$ |
| z | $-96.6\,\text{cm} \leq \text{z} \leq 0\,\text{cm}$ |

### Fiducial volume

A simple cylinder in the center of the TPC was chosen as a fiducial volume with the dimensions $z_{min} = -81.6\,\text{cm}$, $z_{max} = -20.0\,\text{cm}$ with respect to the gate (zero line), and r= 35.36 cm. The assumption of a liquid xenon density of $3\,\text{g/cm}^3$ results into a xenon mass of 726 kg. The top and bottom part as well as the borders of the TPC were removed to avoid events occurring in the gas phase, events on the electrodes as well as surface contamination events. Like that, also external sources, such as radiogenic backgrounds from the detector material, can be reduced. Consequently, only signals produced from intrinsic background sources are selected. The histogram in figure 6.13 visualizes the spatial distribution in the detector for 402 data sets between 21 Oct 2016 and 11 Nov 2016. The grey box highlights the selected fiducial volume. Everything outside this box is removed for further analysis. The exposure for the loaded data sets with a total live time of 390 h for the given fiducial volume was about 11.8 (tonne × day).

### S2 area fraction top

In order to further reject nonphysical events such as coincidentally paired S1 and S2 signals, the reconstructed events can be checked for some standard properties. One way is to investigate the S2 area fraction top (AFT) parameter that resembles the fraction of the S2 peak area seen by the top PMTs. Figure 6.14 illustrates the event distribution for the drift time (depth z) against the S2 AFT. Interactions within the gas gap create events with higher top fraction compared to liquid events. As the bulk of events populates a constant band around a fraction of 0.65, an ad hoc cut was introduced, as indicated by the grey lines. The upper bound was set to 0.75 and the lower bound to 0.5. The data within those bounds was kept, while the outside data was rejected. Note that the depth interval between 0 cm to −20 cm as well as the interval between −81.6 cm to −96.9 cm are removed by the fiducial volume cut. Therefore, also the population at the liquid-gas interface around the zero line is cut away as well as the events at the bottom of the TPC. Thus, the constant cut lines are sufficient to remove events that do not feature the desired fraction recorded by the top PMTs.

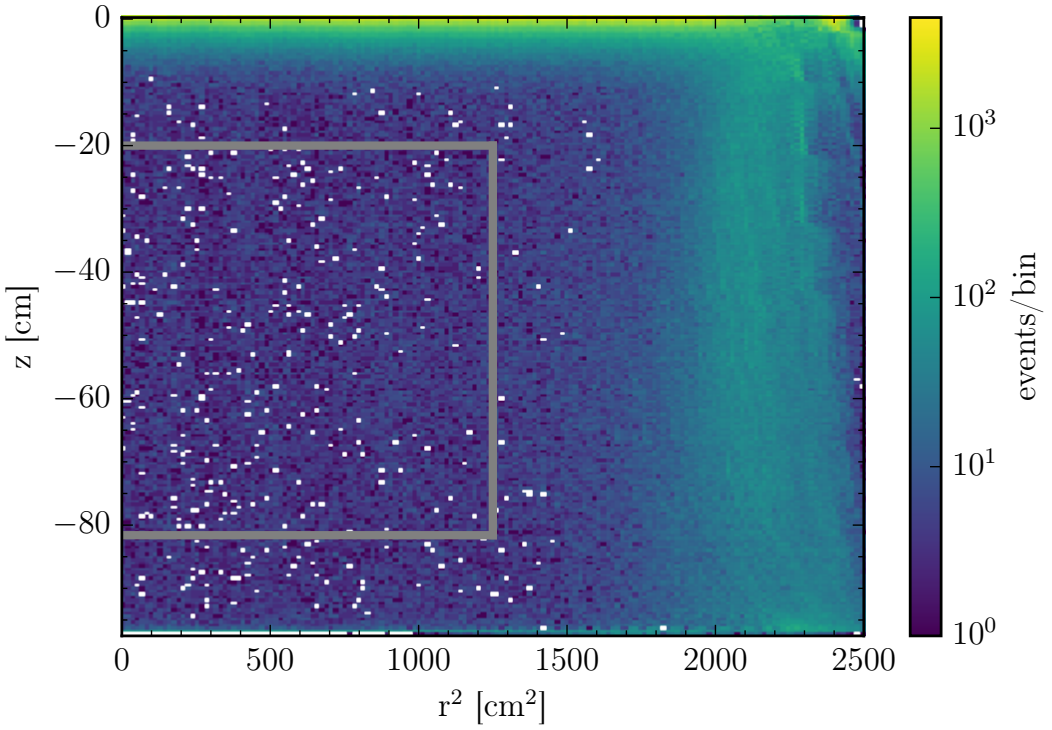


Figure 6.13: **Fiducial volume cut:** The events/bin for radial position $r^2$ versus depth z are illustrated. The histogram represents the full TPC. The grey box highlights the defined fiducial volume to remove external backgrounds as well as events occurring at the liquid-gas interface, at the electrodes and at the walls. The volume corresponds to 726 kg.

### S2 width

Another sanity check is performed on the S2 signal width. The width increases for longer drift times due to the diffusive broadening of the drifting electron cloud. In other words, the deeper an interaction in the TPC occurred, the broader is the measured S2 signal. The standard deviation width $\sigma$ for a Gaussian shaped S2 signal depends on the longitudinal diffusive constant $D$, on the drift time $t$ and on the drift velocity $v$:

$$\sigma(t) = \frac{\sqrt{2 \cdot D \cdot t}}{v} \qquad [82]. \tag{6.56}$$

The finite thickness of the gas gap in the TPC leads to an additional broadening $\sigma_0$. It follows

$$\sigma(t) = \sqrt{\frac{2 \cdot D \cdot t}{v^2} + \sigma_0^2}. \tag{6.57}$$

PAX conventionally calculates the range at the 50 % area corresponding to a width of $1.349 \cdot \sigma$. Therefore, equation (6.57) is scaled to

$$r_{50}(t) = \sqrt{\frac{3.6 \cdot D \cdot t}{v^2} + \omega_0^2}, \tag{6.58}$$

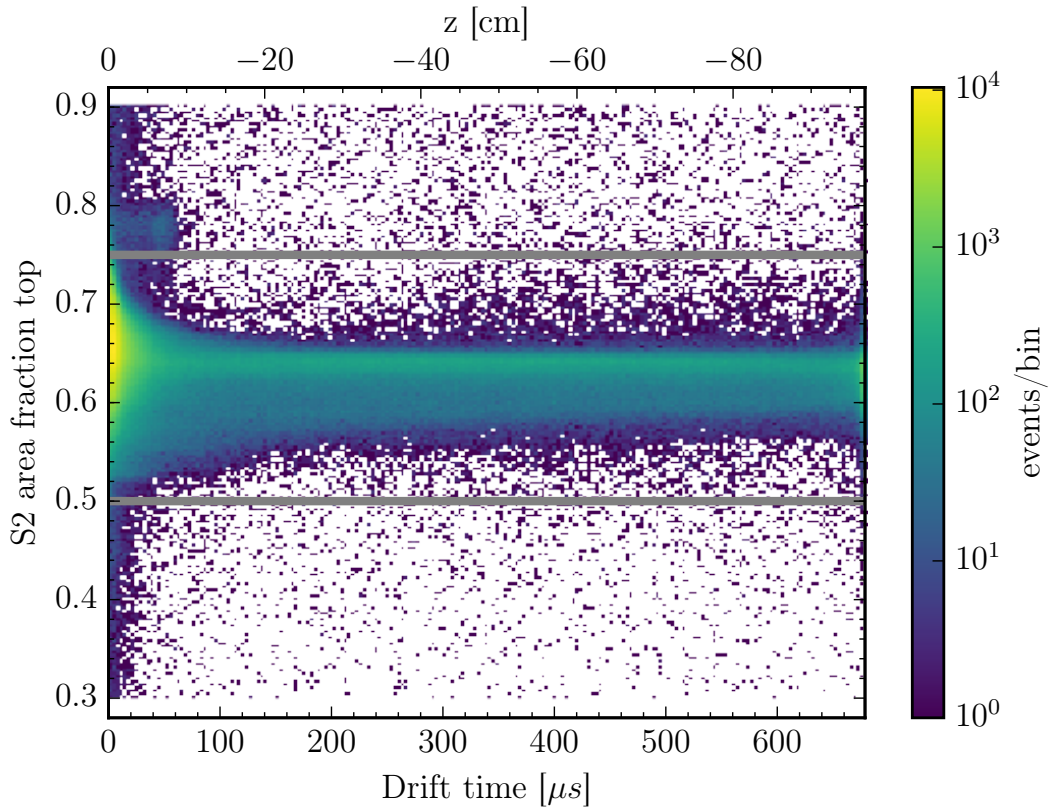


Figure 6.14: **S2 area fraction top cut:** The events/bin for the drift time and depth z versus S2 area fraction top are illustrated. The main purpose is to remove gas events that feature a larger fraction of the S2 peak area recorded by the top PMTs. The bulk of events is located around 0.65. The population around 0 cm and −96.9 cm is removed by the fiducial volume cut. Therefore, a simple cut based on a lower limit of 0.5 and an upper limit of 0.75 was applied as visualized by the grey solid lines.

with $\omega_0 = 1.349 \cdot \sigma_0$ [83]. The relation of the S2 width at the 50 % area versus drift time as well as depth z is visualized in figure 6.15. For drift times below 2 µs, $\omega_0$ can be estimated to 0.29 µs. For a slice in drift time of 600 µs follows a width of $r_{50} = 1.71$ µs. The drift velocity is calculated to be 0.14 cm/µs for the maximum drift length of 96.9 cm and maximum drift time of 675 µs for a given cathode voltage of −12 kV. Taking all information into account, the diffusion constant $D$ can be approximated to be $2.67 \times 10^{-5}$ cm$^2$/µs. With that, equation (6.57) results into the purple dashed curve in figure 6.15 agreeing to the signal relation of S2 width and drift time. In order to remove events not fulfilling this relation, upper and lower rejection curves were defined as the following:

$$r_{50,\mathrm{up}}(t) = 0.3 + 0.4 \cdot t + \sqrt{\frac{3.6 \cdot D \cdot t}{v^2} + \omega_0^2}, \tag{6.59}$$

$$r_{50,\mathrm{low}}(t) = -0.3 - 0.4 \cdot t + \sqrt{\frac{3.6 \cdot D \cdot t}{v^2} + \omega_0^2}. \tag{6.60}$$

Here, a constant term as well as an additional linear term were added ad hoc to

allow a further broadening of the band for higher drift times (deeper depths). Like that, the same S2 width cut could be applied to all the data sets throughout the months of data taking. It takes different detector conditions into account such as drift field or liquid level changes.

As in the case of the S2 AFT cut, the top and bottom part of the TPC are rejected by the fiducial volume cut. Consequently, the populations around 0 cm as well as −96.9 cm are removed and do not need further investigations in the scope of this analysis.

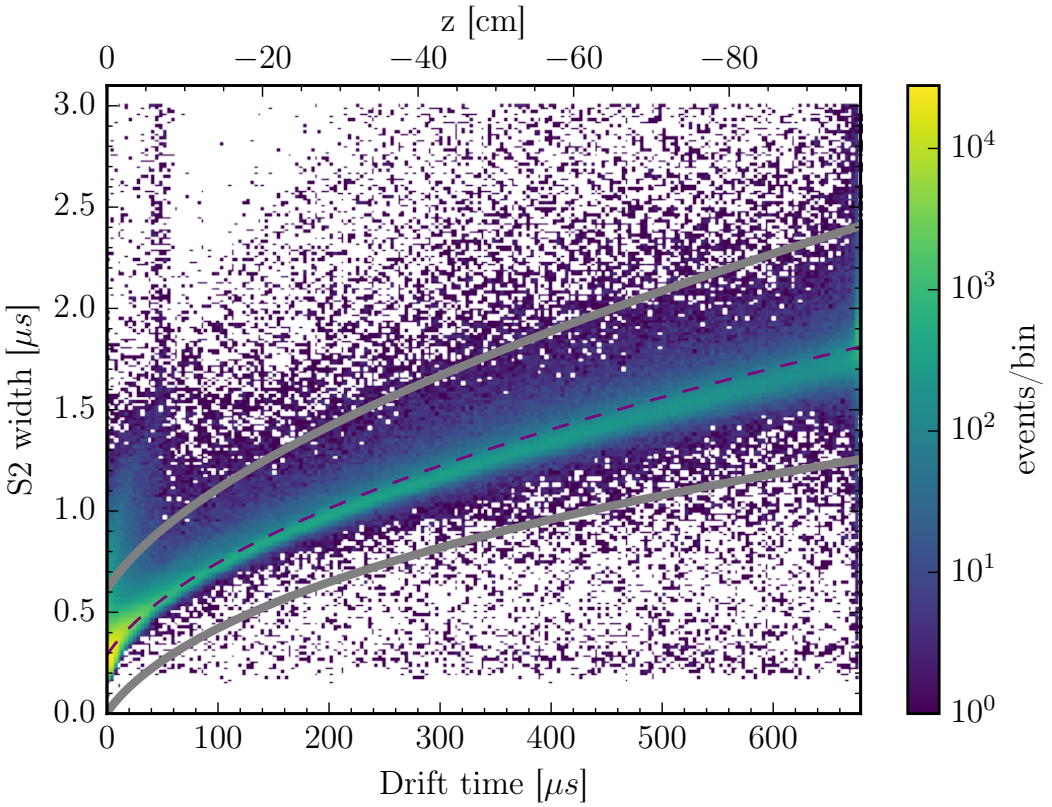


Figure 6.15: **S2 width cut:** The events/bin for the drift time and depth z versus S2 width are illustrated. The S2 width is calculated by PAX as the range at the 50 % area. The deeper an event occured, the broader is the measured S2 signal. This relation follows an diffusion model indicated by the dashed purple line. Upper and lower rejection curves were defined that are visualized as grey. The population around 0 cm and −96.9 cm is removed by the fiducial volume cut and requires therefore no further investigation for this analysis.

### S1 single scatter

A simple S1 single scatter cut was defined. It allowed to remove events where the largest other S1 of an event featured an area larger than 50 pe. This cut was especially helpful during internal calibrations with $^{83m}$Kr as it removed a large fraction of the subsequent krypton decays. Otherwise, the vast amount of calibration events with a total released energy around 41 keV would swarm the

energy range of interest for this analysis. During background and NR calibration with an AmBe source, this cut was less important.

### AmBe cut

The nuclear recoil band was calibrated with an AmBe source from 21 Oct 2016 until 11 Nov 2016, introducing neutrons and high energy gammas to the TPC. This affected also the determined event rate within this analysis. Therefore, an additional spatial cut was required in order to clean the data sample. The source was placed at middle height ($z_{AmBe} = -50\,cm$) next to the TPC ($x_{AmBe} = 56\,cm$, $y_{AmBe} = 44\,cm$) with the help of the calibration belt system within the water tank [41]. It was scrutinized that cutting the fiducial volume in half with respect to the source position was sufficient. The events/bin for the radial distribution is visualized in figure 6.16. On the top right, an increased number of events can be observed as a result of the AmBe source. Events left below the grey solid line were kept for the analysis, while events right above were rejected. Of course, the halved fiducial volume and thus, the halved exposure was taken into account when calculating the event rate. This cut was only applied during AmBe calibration to allow higher statistics during normal operation. Additionally, after the calibration, the xenon activation of the different isotopes does not harm the studied region of interest of this analysis anymore.

### Energy conversion and rate calculation

After applying all selection criteria presented above, the cS1 and cS2 signals within the remaining events can be utilized to compute an energy spectrum:

$$E = W \cdot \left( \frac{cS1}{g_1} + \frac{cS2_b}{g_2} \right). \tag{6.61}$$

Here, the mean effective energy $W$ to generate either a photon or electron within liquid xenon is assumed to be 13.7 eV [84]. Furthermore, $cS1$ corresponds to the area of the corrected S1 signal in pe and $cS2_b$ corresponds to the area of the corrected S2 signal seen by the bottom PMTs[2]. The parameters $g_1$ and $g_2$ denote the photon detection efficiency and the charge amplification factor, respectively. By taking the exposure into account, the event rate as events/(kg · d · keV) for a given energy in the region of interest can be calculated. For this analysis, ad hoc values of $g_1 = 0.1048\,pe/ph$ and $g_2 = 14.14\,pe/e^-$ were introduced. As the processed data before SR0 was not available anymore, the analysis was not redone with the official SR0 values $g_1 = 0.1442\,pe/ph$ and $g_2 = 11.52\,pe/e^-$ for the dark matter search [54]. However, it was found that different $g_1, g_2$ shift the energy scale, but do not change the obtained rate as long as the same values were used for all data sets. Two energy spectra are illustrated in figure 6.17 up to 200 keV for the official SR0 values [54]. Here, these values were chosen for better explanation of the method. The purple spectrum in figure 6.17 visualizes the event rate during August 2016, while the brown spectrum results from the presented AmBe calibration period in November 2016.

[2]The bottom signal is used to avoid any saturation effects of the top array PMTs

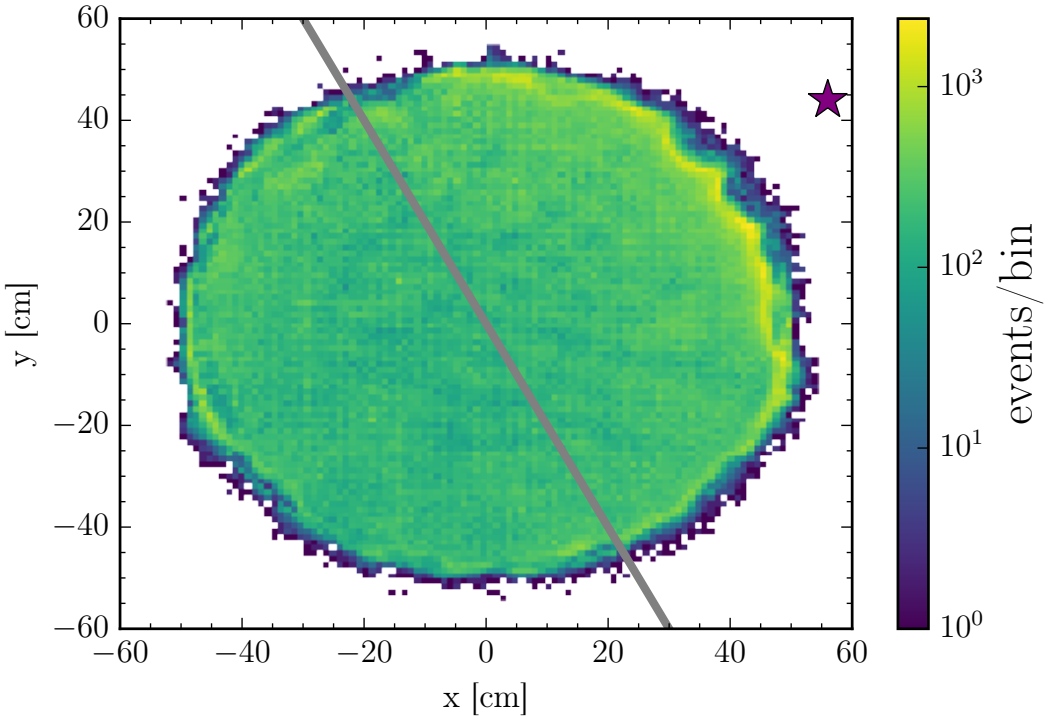


Figure 6.16: **Spatial cut during AmBe calibration:** Events/bin for the radial distribution in x and y. The nuclear recoil band calibration with an AmBe source introduced neutrons and high energy gamma affecting the event rate. Therefore, the defined fiducial volume was cut in half with respect to the source position ($x_{AmBe} = 56\,cm$, $y_{AmBe} = 44\,cm$, $z_{AmBe} = -50\,cm$, purple star) as visualized by the grey solid line. Events right above this line were rejected for further analysis. The halved volume and thus, the halved exposure were used for the event rate calculations. This cut was only applied during the AmBe calibration.

The $^{85}$Kr beta decay with an endpoint energy of 687 keV generates a flat energy spectrum in the detector in the energy region up to 200 keV. In August 2016, no calibration sources were introduced to the TPC except a short test with $^{83m}$Kr beforehand. Consequently, no activated xenon lines are visible. The spectrum is flat and dominated by the $^{85}$Kr beta decay, allowing to select a large energy range of $E_{low} = 70\,keV$ up to $E_{up} = 190\,keV$ for the final rate calculation. In November 2016, the rate per energy bin was about a factor 8 lower due to the online krypton removal campaigns. In contrast, the energy spectrum reveals three features resulting from the AmBe calibration. The introduced neutrons in the TPC activated several xenon isotopes. These deposited their full deexcitation energy via $\gamma$-decay in the selected fiducial volume and thus, created additional peaks in the spectrum.

The peak with the smallest energy of 39.6 keV originates from inelastic scattering of neutrons with the isotope $^{129}$Xe featuring a half-life of 0.97 ns. While the middle peak of 80.2 keV results from the inelastic neutron scattering with $^{131}$Xe (half-life of 0.48 ns), the peak with the highest energy of 163.9 keV is

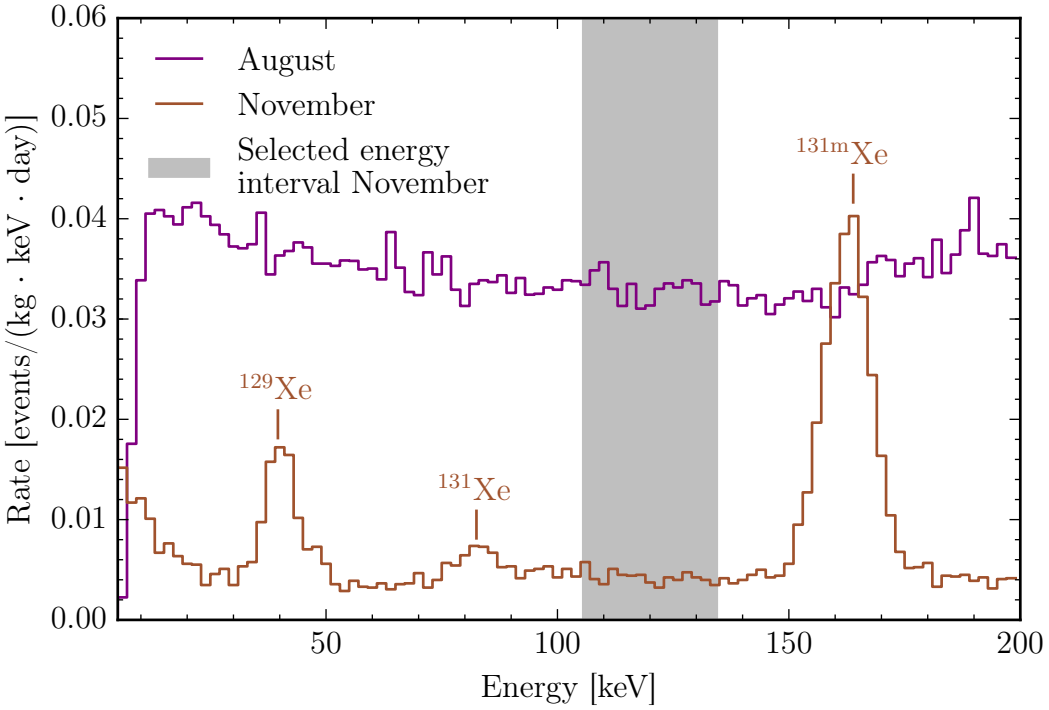


Figure 6.17: **Energy spectrum during August and November 2016:** During August 2016 (purple), no calibration sources were used, except one test with $^{83m}$Kr. The spectrum is flat and is assumed to correspond to the continuous $^{85}$Kr beta decay energy spectrum with an endpoint of 687 keV. This allows to select a large energy range of $E_{low} = 70$ keV up to $E_{up} = 190$ keV. In November 2016 (brown), an AmBe source was applied for neutron calibration. The energy spectrum reveals three features, generated by neutron activation of xenon. Therefore, a smaller energy range can be selected (grey shaded area). Due to the online removal campaign, the rate during November is about a factor 8 lower compared to August.

generated via the decay of the meta stable $^{131m}$Xe with a half-life of 11.9 d. As these decays occur inside the fiducial volume, the full energy is deposited within the liquid xenon on the mm-scale. Therefore, a negligible contribution from Compton scattering is expected for the generated spectrum. The energy range from $E_{low} = 105$ keV to $E_{up} = 140$ keV was found to be flat and was assumed to correspond to the krypton contribution. Consequently, the number of events within the selected range is reduced and leads to larger statistical uncertainties. Additionally, $^{133}$Xe was produced as well, which features a beta decay with an endpoint energy of 427.4 keV at a half-life of 5.2 d, but was not considered for this analysis. The decay values above were taken from [44].

In order to monitor the event rate over time, the explained cuts were applied and the event rate in events/(kg · d · keV) was computed using the selected energy interval and given exposure. The uncertainty was computed via $\sqrt{N}$ with $N$ being the number of remaining events after applying the selection cuts and after the selection of the energy interval. Then, it was scaled with the exposure

and the length of the energy interval. Table 6.5 summarizes the different detector modes as well as selected energy ranges including all periods during the online krypton removal campaigns between August 2016 and January 2017.

Table 6.5: Different detector operations between August 2016 and January 2017. The online krypton removal campaign was monitored with the event rate in the TPC. The selected energy interval between $E_{low}$ and $E_{up}$ for the rate calculation is shown for each period.

| Period | Detector mode | $E_{low}$ [keV] | $E_{up}$ [keV] |
|---|---|---|---|
| 09 Aug - 11 Aug 2016 | $^{83m}$Kr | 70 | 190 |
| 11 Aug - 09 Sep 2016 | background | 70 | 190 |
| 09 Sep - 14 Sep 2016 | hotspot/gimped | 70 | 190 |
| 14 Sep - 10 Oct 2016 | background | 70 | 190 |
| 10 Oct - 19 Oct 2016 | $^{220}$Rn | - | - |
| 19 Oct - 21 Oct 2016 | background | 70 | 190 |
| 21 Oct - 11 Nov 2016 | AmBe | 105 | 135 |
| 11 Nov - 14 Nov 2016 | background | 105 | 135 |
| 14 Nov - 18 Nov 2016 | $^{83m}$Kr | 105 | 135 |
| 18 Nov - 19 Dec 2016 | dark matter | 70 | 135 |
| 19 Dec 2016 - 03 Jan 2017 | $^{220}$Rn | - | - |
| 03 Jan - 18 Jan 2017 | dark matter | 70 | 135 |

At the beginning of August 2016, the detector was calibrated with $^{83m}$Kr for the first time. Afterwards, the first two distillation campaigns liquid+gas and gas only were performed. The detector was operated in the standard background mode during this periods. In middle September 2016, a hotspot was detected originating from the cathode. The emission of single electrons from the electrode created a high DAQ rate. As a result, the data taking was switched into a gimped mode, saving only 1 out of 9 recorded events. This required a live time correction of around a factor 9 for the calculated rates. The uncertainties were scaled up as well. Next, the detector was operated again in stable background mode from 14 Sep 2916 on followed by a first ER band calibration with $^{220}$Rn between 10 Oct and 19 Oct 2016. It is generated from a $^{228}$Th source in the calibration box, housed in the purification system, and is flushed into the TPC via the standard purification loop. The beta radiation within the $^{220}$Rn decay chain created a large fraction of events in the energy region of interest for this analysis. Consequently, the event rate cannot be monitored during this mode. Shortly after the ER calibration, the AmBe source was placed next to the TPC in order to obtain a NR band calibration from 21 Oct until 11 Nov 2016. As explained before, this required to select a smaller energy interval due to xenon activation lines as well as to cut the fiducial volume in half with respect to the source position. The NR calibration was followed by a three days period of background data taking, until a second $^{83m}$Kr was initiated. This lasted for another 4 days. From 18 Nov until 19 Dec 2016, a dark matter search was conducted. The difference between the background mode and dark matter search was that the lowest energy region up to 70 pe in NR discrimination space and cS1 region was blinded. This did not affect this analysis. From here, a second $^{220}$Rn

calibration was performed between 19 Dec 2016 and 3 Jan 2017. Afterwards, the dark matter search continued until it was interrupted and naturally ended by an earthquake on 18 Jan 2017.

The calculated event rate for the time periods presented is visualized in figure 6.18 in blue. Additionally, the absolute krypton in xenon concentration measured with RGMS is illustrated in red. As krypton was the dominant ER background source in August, the first pipette result was scaled to the event rate in order to directly compare the event rate to the measured absolute concentration. The grey shaded areas indicate the period of the online distillation campaigns. In addition to krypton, an online radon removal was tested. This is discussed in section 7.2. The achieved ER event rates of other liquid xenon based dark matter experiments such as XENON100 [47] (grey), LUX [85] (brown) and PandaX-II [86] (purple) are highlighted for comparison. XENON1T clearly reached the lowest background so far with the help of online krypton removal.

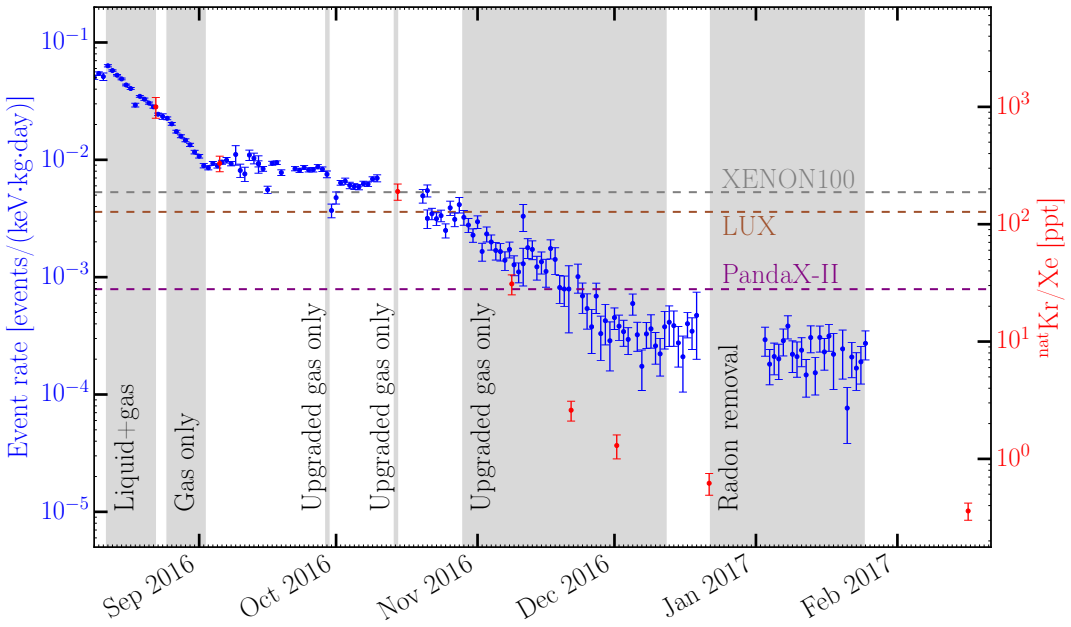


Figure 6.18: **ER event rate during online distillation campaigns:** The ER event rate (blue) between August 2016 and January 2017 was reduced by online distillation campaigns (grey shaded area). Absolute krypton in xenon measurements with RGMS are illustrated in red. At the beginning, the event rate was dominated by the beta decay of $^{85}$Kr. Starting from December 2016, the event rate levels off, while the krypton level continued to decrease. This is an indication that radon is now the dominant background source. The achieved backgrounds of XENON100 [47] (grey), LUX [85] (brown) and PandaX-II [86] (purple) are visualized for comparison. XENON1T clearly reached the lowest background so far due to online distillation.

The krypton induced background in the liquid xenon within the TPC was clearly reduced by online krypton removal with each campaign. The liquid+gas and gas only distillations over the course of several days efficiently reduced the

krypton and thus, the event rate. The two short tests of one day each of the upgraded gas only mode did not yield large reductions. It can be seen that up to here, the measured krypton concentrations within the RGMS samples matched the event rate. The following long term online removal in the upgraded gas only mode, reduced the absolute krypton concentration further, as indicated by the rate evolution as well as the RGMS measurements. However, the event rate levels off, starting from December 2016, while the absolute concentration measurements revealed a further krypton decrease. This is a clear indication that krypton is no longer the dominant ER background source, but radon is.

An absolute ER background rate of $(2.3 \pm 0.2) \times 10^{-4}\,\mathrm{events/(keV \cdot kg \cdot day)}$ was achieved within the inner volume of 726 kg during the radon removal campaign (see section 7.2). This analysis was performed with the early stage PAX version 6.1.1, which did not allow to take all corrections into account, e.g. the deadtime from the DAQ system. This would lead to a higher ER rate, but the effect is expected to be on the percent level. Additionally, ad hoc defined cuts were applied without optimized effieciencies. Analyses with the PAX version 6.4.2 and finalized cuts for energies up to 200 keV used for the dark matter search yielded an ER background rate of $(1.93 \pm 0.25) \times 10^{-4}\,\mathrm{events/(keV \cdot kg \cdot day)}$ in SR0 [54] in a 1 tonne fiducial volume, comparable to the one stated here. However, the presented analysis in this thesis is sufficient to monitor the krypton evolution over time.

An absolute calibration of the ER data points $r_{\mathrm{i,ER}}$ in order to fit the developed model can be achieved with the help of the RGMS pipette from 22 Aug 2016 with a concentration of $c_{1,\mathrm{RGMS}} = (1000 \pm 200)\,\mathrm{ppt}$:

$$c_{\mathrm{i,abs,ER}} = \frac{c_{1,\mathrm{RGMS}}}{r_{14,\mathrm{ER}}} \cdot r_{\mathrm{i,ER}}, \tag{6.62}$$

with $r_{14,\mathrm{ER}} = (2.8 \pm 0.1) \times 10^{-2}\,\mathrm{events/(keV \cdot kg \cdot day)}$ being the ER event rate on 22 Aug 2016. The uncertainties are given by

$$\Delta c_{\mathrm{i,abs,ER}} = c_{\mathrm{i,abs,ER}} \cdot \sqrt{\left(\frac{\Delta c_{1,\mathrm{RGMS}}}{c_{1,\mathrm{RGMS}}}\right)^2 + \left(\frac{\Delta r_{14,\mathrm{ER}}}{r_{14,\mathrm{ER}}}\right)^2 + \left(\frac{\Delta r_{\mathrm{i,ER}}}{r_{\mathrm{i,ER}}}\right)^2}. \tag{6.63}$$

All absolute krypton in xenon concentrations from the various measurement techniques during the full time range are summarized in figure 6.19 for a better overview. The distillation campaigns are shaded in grey. For fitting the model to the data, it was decided to exclude all ER points with less than 10 hr of data to reduce the number of outliers due to low statistics. Furthermore, the period with hotspot and gimped DAQ mode, during Sep 2016 was neglected. As the ER event rate is dominated by radon after the long term upgraded gas only distillation during SR0, it cannot be further applied as a krypton monitoring tool during SR1. Thus, only RGMS samples can be used to investigate the evolution starting from Feb 2017. The RGMS sample on 21 Dec 2016 was taken in parallel with a pipette for an atom trap trace analysis (ATTA) [87]. As this procedure could potentially contaminate the RGMS sample, it was excluded as well.

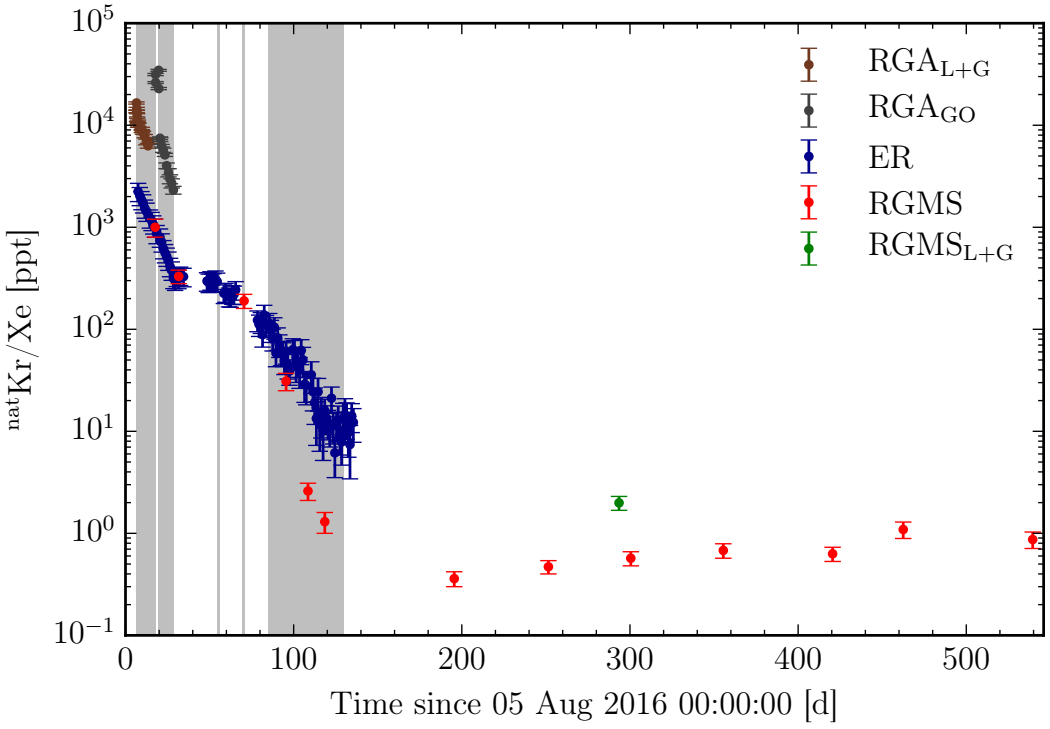


Figure 6.19: **Absolute krypton concentrations in XENON1T for model fitting:** The online distillation periods are shaded in grey. The brown points (RGA$_{L+G}$) represent the residual gas analyzer measurements during the liquid+gas distillation, while the darkgrey points (RGA$_{GO}$) correspond to the RGA samples during the gas only distillation. The blue data points (ER) were obtained from the electronic recoil event rate and the red points (RGMS) from measurements with the rare gas mass spectrometer. One liquid and gas mixture (RGMS$_{L+G}$) was measured with the RGMS, indicated in green.

## 6.3 Fit of model to data

In this section, the model described in section 6.1 is fitted to the absolute krypton in xenon concentrations derived in section 6.2. In a first step, several slow control parameters are queried from the Historian data base for the time period investigated: From the cryogenic system, the flows $F_{\mathrm{FCV101}}$ (extraction from porcupine), $F_{\mathrm{FCV102}}$ (extraction from cryopipe), $F_{\mathrm{FCV103}}$ (extraction from condenser stations) and $F_{\mathrm{FCV104}}$ (flow to the bell) are required. Additionally, the heater power $P_{\mathrm{R121}}$ at the PTR102 is loaded. From the purification system, the flows $F_{\mathrm{FC201}}$ and $F_{\mathrm{FC202}}$ from the two branches are summed to the total purification flow $F_{\mathrm{PUR,tot}}$. From the distillation system, the flows $F_{\mathrm{FIC401}}$ (ingoing distillation flow) and $F_{\mathrm{FIC403}}$ (off-gas flow) are loaded. The parameters are interpolated linearly to provide a continuous function for the fit routine.

The combination of the different flows allows for the calculation of the gaseous extraction flow $F_{\mathrm{G}}$ and and the liquid extraction flow $F_{\mathrm{L}}$ depending on the operation mode. As example, in the standard circulation mode, it applies $F_{\mathrm{G}} = F_{\mathrm{FCV101}} + F_{\mathrm{FCV102}} + F_{\mathrm{FCV103}}$ and $F_{\mathrm{L}} = F_{\mathrm{PUR,tot}} - F_{\mathrm{G}}$. The distillation speed $F_{\mathrm{D}}$ is always directly given by $F_{\mathrm{FIC401}}$. These flows are used as input for the model and are shown in figure 6.20 along with the condensed flow $F_{\mathrm{con}}$ at PTR102. Here, a zoom to the time period up to $t = 132\,\mathrm{d}$ is chosen for a better visualization during the different distillation campaigns (shaded in grey). After that, $F_{\mathrm{G}} \approx 32\,\mathrm{kg/d}\,(3.7\,\mathrm{slpm})$, $F_{\mathrm{L}} \approx 375\,\mathrm{kg/d}\,(44\,\mathrm{slpm})$ as well as $F_{\mathrm{con}} \approx 99\,\mathrm{kg/d}\,(11.6\,\mathrm{slpm})$ are more or less constant.

The condensed flow is calculated with the measured heating power $P_{\mathrm{R121}}$ and the maximum available cooling power $P_{\mathrm{max}}$. The available cooling power was measured to be 240 W at −98 °C without xenon load in October 2015 [88]. A power decrease of 0.1 W/d was found over the course of several months of PTR operation, which needs to be taken into account. With that, a maximum cooling power of 215 W for $t = 0$ can be calculated. Furthermore, $P_{\mathrm{max}}(t)$ as a function of time is given by

$$P_{\mathrm{max}}(t) = -0.1\,\mathrm{W/d} \cdot t + 215\,\mathrm{W}. \tag{6.64}$$

The effective cooling power $P_{\mathrm{cool}}$ used to liquefy the gaseous xenon is calculated with

$$P_{\mathrm{cool}}(t) = P_{\mathrm{max}}(t) - P_{\mathrm{R121}}(t). \tag{6.65}$$

With that, the liquefied xenon flux at the PTR102 can be computed with

$$F_{\mathrm{con}}(t) = \frac{P_{\mathrm{cool}}(t)}{\Delta h_{\nu,\mathrm{Xe}}}, \tag{6.66}$$

with $\Delta h_{\nu,\mathrm{Xe}} = 92.2\,\mathrm{kJ/kg}$ being the difference in the vapor and liquid xenon enthalpy [30]. From the PTR102, the liquid xenon drops into a first funnel and is transported into the collection vessel that connects all three condenser stations. The xenon drops into another vessel and is guided through a tube within the cryogenic pipe of about 15 m until it reaches the cryostat. From here, the xenon is guided in the tube below the TPC. Along the flow path the xenon is in contact with a large surface that is on a higher temperature with respect to the initially liquefied xenon at the PTR. Thus, a certain amount of xenon evaporates before reaching the LXe volume. Therefore, in reality, the calculated values for $F_{\mathrm{con}}$

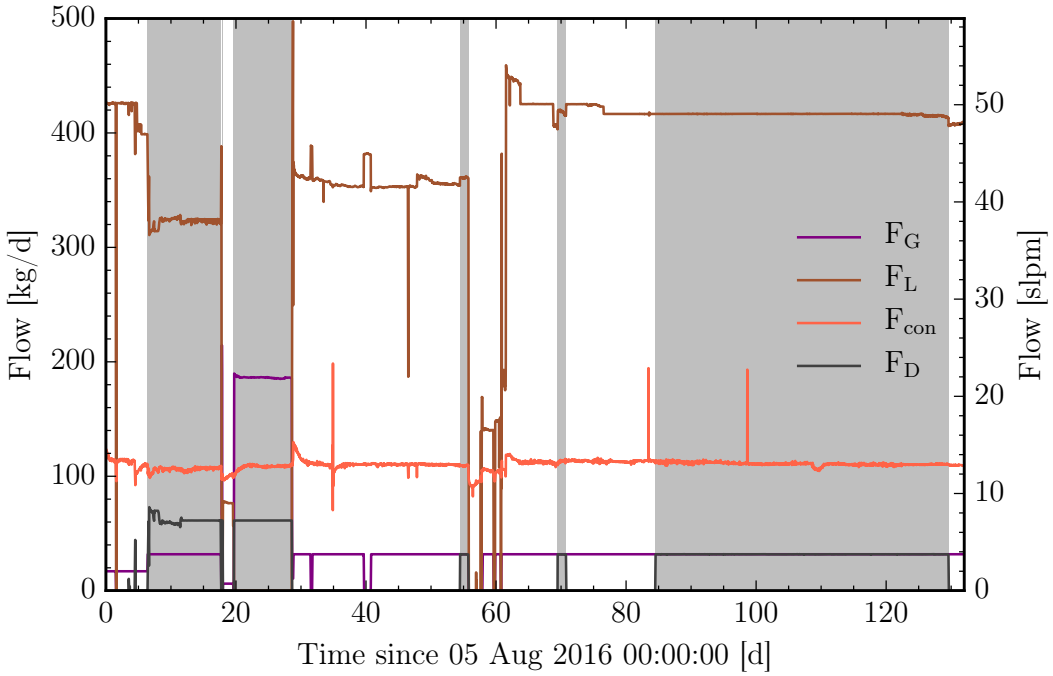


Figure 6.20: **Input flow parameters for model:** Different flow parameters are loaded from the slow control Historian data base allowing for the calculation of the gaseous extraction flow $F_{\mathrm{G}}$ (purple), the liquid extraction flow $F_{\mathrm{L}}$ (brown), the distillation speed $F_{\mathrm{D}}$ (darkgrey) and the condensed flow $F_{\mathrm{con}}$ (red) at the PTR. A time period up to $t = 132\,\mathrm{d}$ is chosen for a better visualization during the different distillation campaigns.

represent only an upper limit of the condensed flow. As the evaporated amount can not be obtained or simulated from the slow control data in the scope of this thesis, a free fit parameter $0 < \epsilon_{\mathrm{con}} \leq 1$ is introduced to the model by multiplying it with $F_{\mathrm{con}}$. This allows to scale down the condensed flow to the required amount of xenon flow $\epsilon_{\mathrm{con}} F_{\mathrm{con}}$ to fit the data. In parallel, this scales down also the evaporation flow $F_{\mathrm{vap}}$ that is calculated either solely from $F_{\mathrm{con}}$ or from a combination of $F_{\mathrm{con}}$ and the heat exchanger efficiency $\epsilon_{\mathrm{HE}}$, as derived in section 6.1.

This efficiency can be calculated with the help of a period with standard detector circulation at $t = 54\,\mathrm{d}$ and without circulation at $t = 56\,\mathrm{d}$. The measured heating powers are $P_{\mathrm{st.circ.}} = P_{\mathrm{R121}}(t = 54\,\mathrm{d}) = 92.5\,\mathrm{W}$ and $P_{\mathrm{no.circ.}} = P_{\mathrm{R121}}(t = 56\,\mathrm{d}) = 111.8\,\mathrm{W}$, respectively. As both values are close in time, the effects of the PTR decrease are negligible. In the standard circulation, additional xenon needs to be liquefied by the PTR due to the gas flow into the bell $F_{\mathrm{FCV104}}$ and the inefficiency of the heat exchanger, creating a larger heat load. Thus, it applies $P_{\mathrm{st.circ.}} < P_{\mathrm{no.circ.}}$. The required power $P_{\mathrm{bell}}$ to cool the flow to the bell

from 18 °C down to −98 °C and liquefy it can be computed with

$$\begin{aligned} P_{\text{bell}} &= F_{\text{FCV104}}(t = 54\,\text{d}) \cdot (c_{\text{p}} \cdot \Delta T + \Delta h_{\nu,\text{Xe}}) \\ &= 0.53\,\text{kg/h} \cdot (0.17\,\text{kJ/(kgK)} \cdot 116\,\text{K} + 92.2\,\text{kJ/kg}) \\ &= 16.5\,\text{W}. \end{aligned} \tag{6.67}$$

Here, $c_{\text{p}} = 0.17\,\text{kJ/(kgK)}$ is the specific heat capacity of xenon and is approximated as constant over the full temperature range [30]. Finally, the heat exchanger efficiency $\epsilon_{\text{HE}}$ is given by

$$\epsilon_{\text{HE}} = \frac{P_{\text{st.circ.}} + P_{\text{bell}}}{P_{\text{no.circ.}}} = 0.975. \tag{6.68}$$

The efficiency was fixed to 0.975 for the fit routine, as no large variations are expected over time.

The relative volatility $\alpha$ is fixed to 10.5 (for a detector pressure of 1.93 bar and saturation temperature of −96 °C) in all parts of the model, except for the heat exchanger. Here, xenon evaporates and liquefies on the large inner surface several times until it finally reaches liquid form. In each evaporation step, krypton can migrate from the liquid into the gas phase. Thus, the assumption is made that the separation effect $\alpha_{\text{HE}}$ due to the heat exchanger is much larger than 10.5. Following equations (6.12) to (6.14), the exchanger divides the in-going krypton flux $x_2 \cdot F_{\text{L}}$ into a gas and liquid flux. A fraction of $x_4 \cdot F_4 = 0.95 \cdot x_2 \cdot F_{\text{L}}$ goes into the GXe phase for $\alpha_{\text{HE}} = 10^3$ (Three evaporation steps) and a fixed $\epsilon_{\text{HE}} = 0.975$, whereas $\alpha_{\text{HE}} = 10^4$ (Four evaporation steps) leads to $x_4 \cdot F_4 = 0.995 \cdot x_2 \cdot F_{\text{L}}$. The model is not sensitive enough to differentiate between the different cases. Consequently, the separation is fixed such that practically all in-going krypton particles return into the GXe volume from the heat exchanger. Therefore, the term $x_4 \cdot F_4$ becomes $x_2 \cdot F_{\text{L}}$, while $x_3 \cdot F_3$ becomes effectively 0.

The masses in both reservoirs were obtained from GEANT4 simulations in [89] and fixed to $M_{\text{G}} = 21.5\,\text{kg}$ and $M_{\text{L}} = 3190\,\text{kg}$, respectively. In the case of the liquid xenon mass, the off-gas losses are calculated from $F_{\text{FIC403}}$ and are subtracted from $M_{\text{L}}$. Thus, $M_{\text{L}}$ decreases over time, whenever an online krypton distillation is performed.

The krypton concentration in the purified outlet of the distillation column is set to $x_{\text{D}} = 0$ to further simplify the model. The separation factor was determined to be $(6.4^{+1.9}_{-1.4}) \cdot 10^5$ with verified outlet concentrations below 48 ppq in section 4.2. Thus, it is assumed that no krypton leaves the distillation system.

An unknown parameter is the time constant $\tau_{\text{Mig}}$ for the migration time of krypton from the liquid into the gas phase. As this time constant is mass dependent and for better consistency, the migration flow $F_{\text{Mig}}$ is introduced as a free fit parameter. It applies

$$\frac{1}{\tau_{\text{Mig}}} = \frac{F_{\text{Mig}}}{M_{\text{G}}}. \tag{6.69}$$

The distillation terms in the differential equations derived in section 6.1 change

to

$$+\frac{1}{\tau_{\mathrm{Mig}}}\left[\alpha x_{\mathrm{L}} - x_{\mathrm{G}}\right] = \frac{F_{\mathrm{Mig}}}{M_{\mathrm{G}}}\left[\alpha x_{\mathrm{L}} - x_{\mathrm{G}}\right] \quad (\mathrm{GXe})\,, \tag{6.70}$$

$$-\frac{1}{\tau_{\mathrm{Mig}}}\cdot\frac{M_{\mathrm{G}}}{M_{\mathrm{L}}}\left[\alpha x_{\mathrm{L}} - x_{\mathrm{G}}\right] = -\frac{F_{\mathrm{Mig}}}{M_{\mathrm{L}}}\left[\alpha x_{\mathrm{L}} - x_{\mathrm{G}}\right] \quad (\mathrm{LXe})\,. \tag{6.71}$$

Another free fit parameter is the krypton leak rate $k_{\mathrm{leak}}$ to the system to describe the krypton increase after the distillation campaigns.

The ER event rate levels off during the long term upgraded gas only distillation due to the radon induced background as derived in the last section. Therefore, a krypton-equivalent radon background constant $c_{\mathrm{Rn}}$ is added as a free parameter to the krypton concentration in the LXe volume to fit the ER data points:

$$x_{\mathrm{L,ER}}(t) = x_{\mathrm{L}}(t) + c_{\mathrm{Rn}}. \tag{6.72}$$

Furthermore, the ER sample analysis is a measure of the $^{85}$Kr particle decay, while the other methods determine the amount of $^{\mathrm{nat}}$Kr. The half-life of $^{85}$Kr is 10.8 yr and thus, much longer than the time period investigated in this thesis. Therefore, a removal term of krypton from the total system due to its decay can be neglected in the differential equations. This is different for radon, as further discussed in chapter 7.

At $t = 0$, the system is operated in standard circulation mode and assumed to be in equilibrium in terms of krypton. Thus, it applies for the krypton change in both reservoirs $dx_{\mathrm{G}}/dt = dx_{\mathrm{L}}/dt = 0$. The starting concentration in the liquid $x_{\mathrm{L},0}$ is a free fit parameter. By solving equation (6.17) of the standard circulation, the corresponding krypton concentration $x_{\mathrm{G},0}$ in the GXe can be calculated with

$$x_{\mathrm{G},0} = \frac{\alpha\left(F_{\mathrm{Mig}} + F_{\mathrm{vap}}\right) + \frac{F_{\mathrm{L}}}{F_{\mathrm{G}}+F_{\mathrm{L}}}\left(F_{\mathrm{G}} + \frac{\alpha_{\mathrm{HE}}(1-\epsilon_{\mathrm{HE}})F_{\mathrm{L}}}{\epsilon_{\mathrm{HE}}+\alpha_{\mathrm{HE}}(1-\epsilon_{\mathrm{HE}})}\right)}{F_{\mathrm{Mig}} + \frac{F_{\mathrm{con}}}{\alpha} + F_{\mathrm{G}}\left(1 - \frac{F_{\mathrm{G}}}{F_{\mathrm{G}}+F_{\mathrm{L}}}\left[1 - \frac{\alpha_{\mathrm{HE}}(1-\epsilon_{\mathrm{HE}})F_{\mathrm{L}}}{\epsilon_{\mathrm{HE}}+\alpha_{\mathrm{HE}}(1-\epsilon_{\mathrm{HE}})}\right]\right)} \cdot x_{\mathrm{L},0}. \tag{6.73}$$

Here, the leak rate $k_{\mathrm{leak}}$ is neglected as it has no influence for the krypton concentrations on the ppb-level at $t = 0$. For a large $\alpha_{\mathrm{HE}}$, above equation further simplifies to

$$x_{\mathrm{G},0} = \frac{\alpha\left(F_{\mathrm{Mig}} + F_{\mathrm{vap}}\right) + F_{\mathrm{L}}}{F_{\mathrm{Mig}} + \frac{F_{\mathrm{con}}}{\alpha} + F_{\mathrm{G}}\left(1 - \frac{F_{\mathrm{G}}}{F_{\mathrm{G}}+F_{\mathrm{L}}}\left[1 - F_{\mathrm{L}}\right]\right)} \cdot x_{\mathrm{L},0} \tag{6.74}$$

For $t > 0$, the fit routine selects the on-going operation mode for a given time $t_{\mathrm{i}}$ based on the computed flows at $t = t_{\mathrm{i}}$ and the time interval. Then, it integrates the corresponding differential equations for the GXe and LXe reservoirs with the function *odeint* from the *scipy* python package to achieve a pair of $x_{\mathrm{G}}(t_{\mathrm{i}})$, $x_{\mathrm{L}}(t_{\mathrm{i}})$. This pair is used for the evaluation of the next step $t_{\mathrm{i}+1}$. Like that, the model is continuous over the full fit range. The step size is chosen to be 30 min = 0.021 d to reach a finer time binning than the extraction times of the RGA samples.

The routine returns the calculated values for $x_{\mathrm{G}}(t)$, $x_{\mathrm{L}}(t)$, $x_1(t)$ and $x_{\mathrm{L,ER}}(t)$ for a given set of model parameters. The results are interpolated for the comparison to the data points. While the $\mathrm{RGA_{L+G}}$ samples during the liquid+gas distillation

Table 6.6: Best parameters to fit the online krypton removal model to data.

| Parameter | Result |
|---|---|
| $x_{\mathrm{L},0}$ | $(2016 \pm 20)$ ppt |
| $F_{\mathrm{Mig}}$ | $(8.9 \pm 0.3)$ kg/d |
| $\epsilon_{\mathrm{con}}$ | $0.31 \pm 0.01$ |
| $c_{\mathrm{Rn}}$ | $(12.2 \pm 0.9)$ ppt |
| $k_{\mathrm{leak}}$ | $(10.4 \pm 0.7) \times 10^{-12}$ kg/d |
| $\chi^2$ / NDF | 605.0 / 133.0 |

are compared to the mixture $x_1$, the $\mathrm{RGA}_{\mathrm{G+O}}$ are checked against $x_{\mathrm{G}}$ giving a direct measure of the krypton inside the GXe volume. The RGMS samples are compared to $x_{\mathrm{L}}$, whereas the single point $\mathrm{RGMS}_{\mathrm{L+G}}$ is compared to $x_1$. The points achieved from the ER event rate are checked against $x_{\mathrm{L,ER}}$. A $\chi^2$-minimization with iMinuit is used to find the best set of parameters for the model to describe the data. The results for the best fit are summarized in table 6.6.

The initial krypton concentration in the liquid phase is determined to be $x_{\mathrm{L},0} = (2016 \pm 20)$ ppt. The corresponding concentration inside the gaseous phase can be computed to be $x_{\mathrm{G},0} = 1.3 \times 10^5$ ppt following equation (6.73). Thus, the enhancement between the two phases can be calculated to be 64, about a factor 6 larger than the relative volatility $\alpha = 10.5$. As discussed in section 6.1, the design of the detector system leads to a lower krypton concentration inside the LXe compared to a single theoretical distillation stage. The total krypton concentration inside the system can be calculated by taking the masses of the two reservoirs into account:

$$x_{\mathrm{tot}} = \frac{x_{\mathrm{G},0} \cdot M_{\mathrm{G}} + x_{\mathrm{L},0} \cdot M_{\mathrm{L}}}{M_{\mathrm{G}} + M_{\mathrm{L}}} = (2.9 \pm 0.3)\,\mathrm{ppb}. \tag{6.75}$$

This concentration is higher compared to the obtained total concentration of $(1.2 \pm 0.1)$ ppb after the online ReStoX distillation, presented in section 5.4. An increased concentration can result from additional bottle filling to ReStoX after the online ReStoX distillation. Furthermore, several steps of filling and recuperation of the global detector system during commissioning can potentially introduce residual krypton.

The migration flow with $F_{\mathrm{Mig}} = (8.9 \pm 0.3)$ kg/d ($(1.05 \pm 0.03)$ slpm) is lower with respect to the other flows within the model. The influence of the different flows and time constants are discussed below in this section.

The scaling factor for the condensed flow is $\epsilon_{\mathrm{con}} = 0.31 \pm 0.01$. With that, the condensed flow $\epsilon_{\mathrm{con}} F_{\mathrm{con}}(t = 0)$ reaching the LXe phase is computed to be 38.1 kg/d (4.5 slpm). About 70 % of the xenon evaporates between the PTR and cryostat. Consequently, the evaporated flow $F_{\mathrm{vap}}(t = 0)$ during the standard circulation mode is calculated to 36.8 kg/d (4.3 slpm), following equation (6.16).

The ER event rate levels off due to the radon-induced background. It is fitted in units of a krypton concentration to $c_{\mathrm{Rn}} = (12.2 \pm 0.9)$ ppt and is a direct measure of the radon contribution in XENON1T. This value can be translated into an ER event rate in a first step with the conversion factor $f_{\mathrm{ppt} \to \mathrm{mdru}} =$

$(0.032 \pm 0.006)$ mdru/ppt, assuming $^{85}\mathrm{Kr}/^{\mathrm{nat}}\mathrm{Kr} = 1.65 \pm 0.30$ [40, 90]. In a next step, this rate can be converted into a radon activity concentration using the factor $f_{\mu\mathrm{Bq/kg}\to\mathrm{mdru}} = 0.029\,\mathrm{mdru}/(\mu\mathrm{Bq/kg})$ [40]. It applies

$$c_{\mathrm{Rn,converted}} = c_{\mathrm{Rn}} \cdot \frac{f_{\mathrm{ppt}\to\mathrm{mdru}}}{f_{\mu\mathrm{Bq/kg}\to\mathrm{mdru}}} = (13.5 \pm 2.6)\,\mu\mathrm{Bq/kg}. \tag{6.76}$$

This is in agreement with the value of $(13.6 \pm 0.9)\,\mu$Bq/kg in XENON1T during December 2016, obtained from in-situ $\alpha-$spectroscopy [91].

The krypton leak rate into the GXe volume is determined to be $k_{\mathrm{leak}} = (10.4 \pm 0.7) \times 10^{-12}\,\mathrm{kg/d}$. This can be translated into a corresponding air leak rate $k_{\mathrm{air}}$ for a better understanding of the leak size:

$$k_{\mathrm{air}} = \frac{k_{\mathrm{leak}} \cdot 16.89}{\rho_{\mathrm{Kr}} \cdot 24 \cdot 60} \cdot \frac{V_{\mathrm{air}}}{V_{\mathrm{Kr}}} = (2.9 \pm 0.2) \times 10^{-5}\,\mathrm{mbar}/(\mathrm{l} \cdot \mathrm{s}), \tag{6.77}$$

with $\rho_{\mathrm{Kr}} = 3.748\,\mathrm{g/sl}$ being the krypton density for standard conditions for temperature and pressure. The volume fraction of krypton in air is $\frac{V_{\mathrm{Kr}}}{V_{\mathrm{air}}} = 1.14 \times 10^{-6}$ vol/vol [92]. The numbers 24, 60 and 16.89 are needed to convert the leak rate from sl/d into mbar/(l · s). The obtained rate is comparable to an independent study yielding a value of $(1.32 \pm 0.04) \times 10^{-5}\,\mathrm{mbar}/(\mathrm{l} \cdot \mathrm{s})$, where only the four RGMS samples from Feb - Jul 2018 were used [93]. In general, air leak rates on the order $(10^{-8}$–$10^{-10})\,\mathrm{mbar}/(\mathrm{l} \cdot \mathrm{s})$ can be achieved for such closed systems. For a further discussion the location of a potential leak needs to be taken into account. Such a leak between getter and detector would result into an electron lifetime between (200–300) $\mu$s, whereas the measured value in the TPC is around 600 $\mu$s [94]. A leak between detector and getter cannot create such an effect in the TPC, as all the electronegative impurities are trapped within the getter. The only consequence is a faster saturation of the getter cartridge. This was not yet observed in XENON1T. One potential location is the calibration source box, where sources are changed from time to time by opening and closing a set of VCR connections. Additional krypton and radon can pass the getter unaffected. However, this will just lead to an increased but constant equilibrium in the case of $^{222}$Rn, as the radon decay with an half-life of 3.8 d is a faster process than the addition of radon through the leak. Therefore, radon is not sensitive to constant leaks on the order of $10^{-5}\,\mathrm{mbar}/(\mathrm{l} \cdot \mathrm{s})$. In the case of $^{85}$Kr, the half-life of 10.8 yr makes krypton the only sensitive detection channel for such leak sizes.

All in all, the leak rate seems to be too high to just originate fully from an external leak, as all connections were leak checked after installation. Another process that might release krypton into the system is outgassing from the PTR surface. At this location, the surface is colder than its surrounding and thus, krypton can freeze-out there. Furthermore, XENON1T was initially filled and cooled down without krypton removal. This could allow for the trapping of a large amount of krypton. This krypton could be released constantly from the PTR. Both effects cannot be distinguished from the model, but only fitted as combined leak.

The fit curves are visualized in figures 6.21 to 6.25 and are discussed in the following. For a better overview, the results are separated into several time periods.

In figure 6.21, the time period from $t = 0$ until $t = 17.7\,\mathrm{d}$ is shown, including the liquid+gas distillation campaign (grey shaded). The blue fit curve $x_{\mathrm{L,ER}}$ fits the blue data points ER well, indicated by the blue normalized residuals in the bottom panel. They stay within $\pm 1\sigma$ deviation between data and fit. The brown curve $x_1$, which is a liquid and gas mixture, is compared to the brown $\mathrm{RGA_{L+G}}$ points. The fit curve cannot fully describe the steep decrease at the beginning of the distillation. Here, the brown residuals in the bottom show a large deviation of up to $9.6\sigma$ for the first RGA point (not shown). Towards the middle of the operation, the curve undershoots the data points with deviations between $0.5\sigma$ and $4\sigma$. In addition to the fitted curves, the corresponding evolution in the GXe phase $x_{\mathrm{G}}$ is drawn in grey. Before the distillation, all three curves are parallel, as predicted from an equilibrium state during the standard circulation. This shows that the construction of the model works as expected. One RGMS data point (red) was taken at the end of the liquid+gas distillation, fitting well to the model shown by the red residual point[3]. The krypton concentration inside the LXe volume was reduced by a factor 1.9 during the liquid+gas distillation.

In figure 6.22, the time period from $t = 17.7\,\mathrm{d}$ until $t = 30.1\,\mathrm{d}$ is visualized. The first thin shaded area denotes the first gas only distillation attempt. Here, two $\mathrm{RGA_{GO}}$ samples (dark grey) were extracted, yielding a direct measure of the krypton concentration in the GXe volume. Both are below the grey fit curve $x_{\mathrm{G}}$ with a deviation of up to $-9.7\sigma$ (not shown). A steep decrease of $x_{\mathrm{G}}$ can be observed, while the concentration in the LXe phase $x_{\mathrm{L,ER}}$ (blue) is not decreasing as fast. This is a verification that at the beginning of the online distillation a bulk of krypton is removed fast from the GXe phase. The wide grey shaded area indicates the stable gas only distillation. Between the two shaded areas, the system drifts back into equilibrium, visible by the increase of $x_{\mathrm{G}}$ and small decrease in $x_{\mathrm{L,ER}}$. The steep decrease in the RGA data points at the beginning of the second gas only distillation attempt can be modeled well with the grey fit curve. Towards the middle, three points show deviations between $1.4\sigma$ and $4.6\sigma$. This could also result from variations in the RGA measurement system. The rest of the points deviate only between $\pm 1\sigma$. The blue fit curve for $x_{\mathrm{L,ER}}$ is slightly higher than the mean of the blue ER data points, but is still within the uncertainties. This is also verified by the blue normalized residuals in the bottom panel. After stopping the distillation process, the krypton concentration in the liquid keeps decreasing when converging to equilibrium. In contrast, the concentration in the gas steeply increases. The krypton concentration inside the LXe volume was reduced by a factor 2.7 during the stable gas only distillation.

In figure 6.23, the time period from $t = 28.6\,\mathrm{d}$ until $t = 139.6\,\mathrm{d}$ is presented. It includes the two short tests with the final upgraded gas only distillation mode (thin grey shaded areas) as well as the long term upgraded gas only distillation (wide grey shaded area). Again, the blue data points (ER) and fit curve ($x_{\mathrm{L,ER}}$) indicate the evolution of the electronic recoil data. For reference, the krypton evolution in the GXe ($x_{\mathrm{G}}$) is shown again in grey. In addition, the figure contains the evolution (red) inside the liquid xenon ($x_{\mathrm{L}}$) fitted to the RGMS data points (red). This curve was omitted so far, as it overlaps with $x_{\mathrm{L,ER}}$ for high krypton

[3]The curves for $x_{\mathrm{L,ER}}$ and $x_{\mathrm{L}}$ overlap for high krypton concentrations at the beginning and therefore, the curve $x_{\mathrm{L}}$ was omitted in this plot.

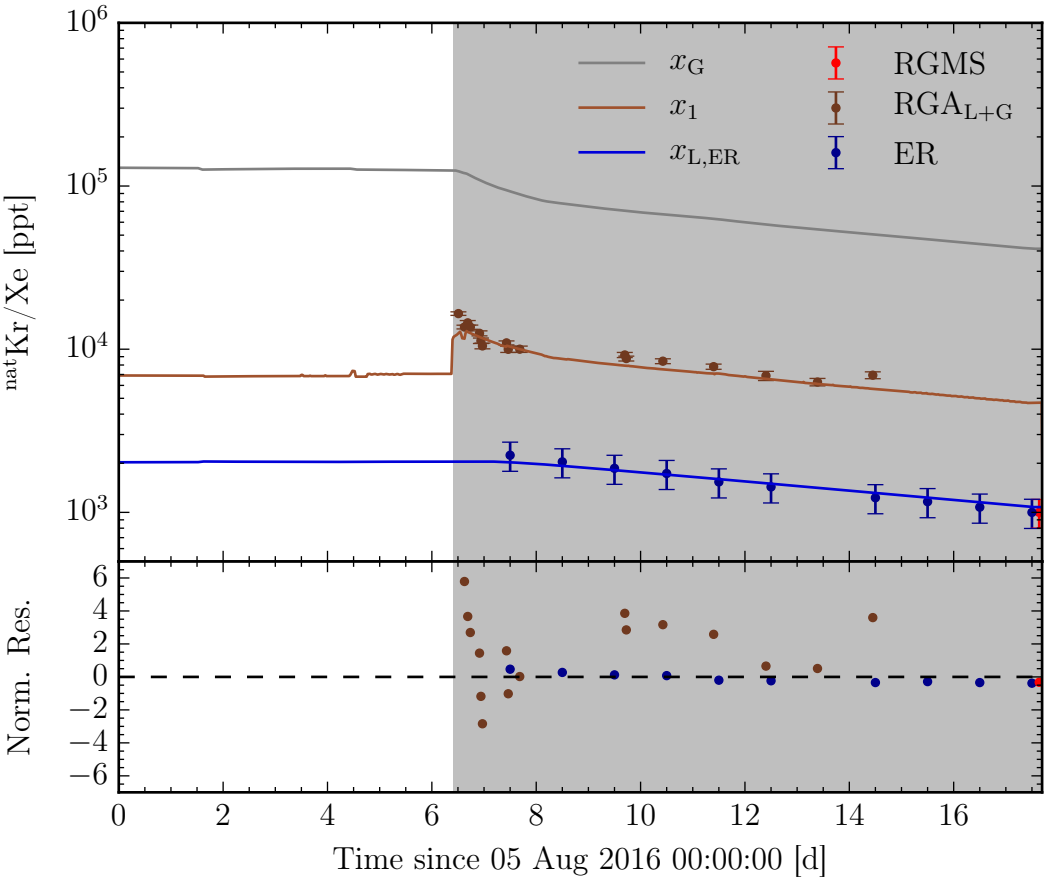


Figure 6.21: **Online krypton removal fit from $t = 0$ until $t = 17.7\,\mathrm{d}$:** The grey shaded area corresponds to the liquid+gas distillation. The blue data points (ER) are fitted well by the blue fit curve ($x_{\mathrm{L,ER}}$). The brown fit curve ($x_1$) undershoots the brown data points ($\mathrm{RGA_{L+G}}$) slightly towards the middle of the campaign. The red data point corresponds to a RGMS sample. In addition, the evolution in the GXe phase ($x_{\mathrm{G}}$) is drawn in grey. The deviation between the curves and data points are shown in the bottom panel in form of normalized residuals in corresponding colors.

concentrations. This can be seen between $t = 28.6\,\mathrm{d}$ until $t = 84.5\,\mathrm{d}$. The ER and RGMS data points feature the same concentrations and are fitted well by their fit curves, as also indicated by the residuals in the bottom panel. They vary between $\pm 2\sigma$. During the two short distillation operations at $t = 54.4\,\mathrm{d}$ and $t = 69.5\,\mathrm{d}$, the curve for the gas evolution $x_{\mathrm{G}}$ is steeply decreasing corresponding to the bulk removal of krypton. The reduction in the liquid is comparably small with 1.14 and 1.15, respectively. Starting from $t = 84.5\,\mathrm{d}$, the long term distillation is started. The blue ER data points level off, as radon takes over as dominant background source in XENON1T. The data is fitted well by the blue curve, except for a bump around $t = 100.0\,\mathrm{d}$, also shown by the blue residuals in the bottom panel. This behavior cannot be explained by the model. Its origin is further discussed below in this section. The red curve reveals how the krypton inside the liquid continues to decrease, while the ER analysis is not sensitive anymore.

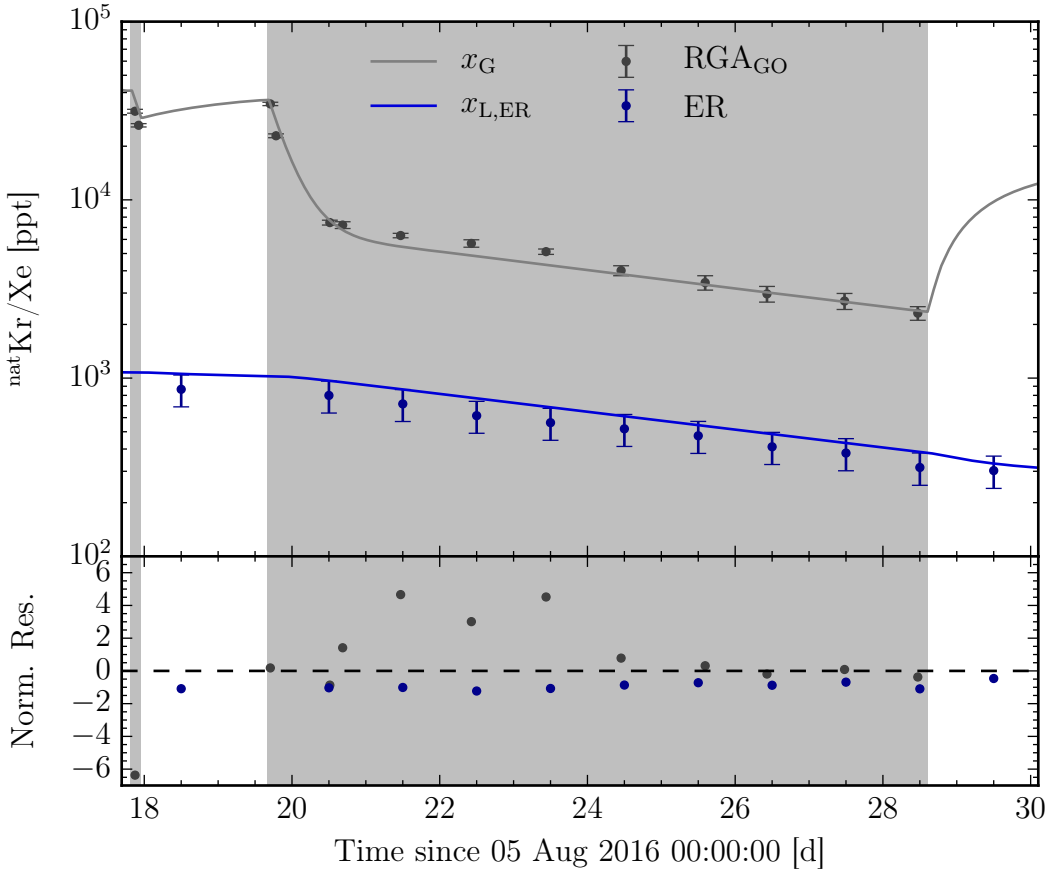


Figure 6.22: **Online krypton removal fit from** $t = 17.7\,\mathrm{d}$ **until** $t = 30.1\,\mathrm{d}$**:** The thin grey shaded area indicates the first gas only distillation attempt, while the wide grey shaded area highlights the stable gas only distillation. The blue data points (ER) are fitted within their uncertainties by the blue curve ($x_{L,ER}$). The dark grey data points ($RGA_{GO}$) are fitted by the krypton concentration in the GXe reservoir ($x_G$). The two first RGA points during the first attempt are below the fit curve. The data points during the stable gas only distillation can be modeled well. The deviation between the curves and data points are shown in the bottom panel in form of normalized residuals in corresponding colors.

It fits the RGMS points well, except for the last RGMS point in this figure, showing a deviation of $2.7\sigma$ from the fit. This might be related to the ER bump. A reduction of $1.71 \times 10^3$ can be calculated by comparing $x_L(t = 84.5\,\mathrm{d})$, the start of the long term distillation, with $x_L(t = 129.6\,\mathrm{d})$, the stop of the operation. After stopping, the system drifts again to equilibrium in the standard circulation mode. The krypton concentration in the GXe reservoir increases steeply. This leads to a further decrease of the concentration in the LXe volume. According to the fitted model, the minimum krypton concentration reached inside the TPC is $x_{L,min} = 0.077\,\mathrm{ppt} = 77\,\mathrm{ppq}$ at $t = 136.6\,\mathrm{d}$. The corresponding concentration in the GXe was calculated to be $x_G(t = 136.6\,\mathrm{d}) = 5.34\,\mathrm{ppt}$, a factor 69 larger, as observed as well during the standard circulation at the beginning of the time

period investigated. Taking the two masses in both reservoirs into account, a total krypton concentration of 0.11 ppt is computed. Due to the leak rate $k_{\text{leak}}$, this unprecedented low concentration cannot be conserved.

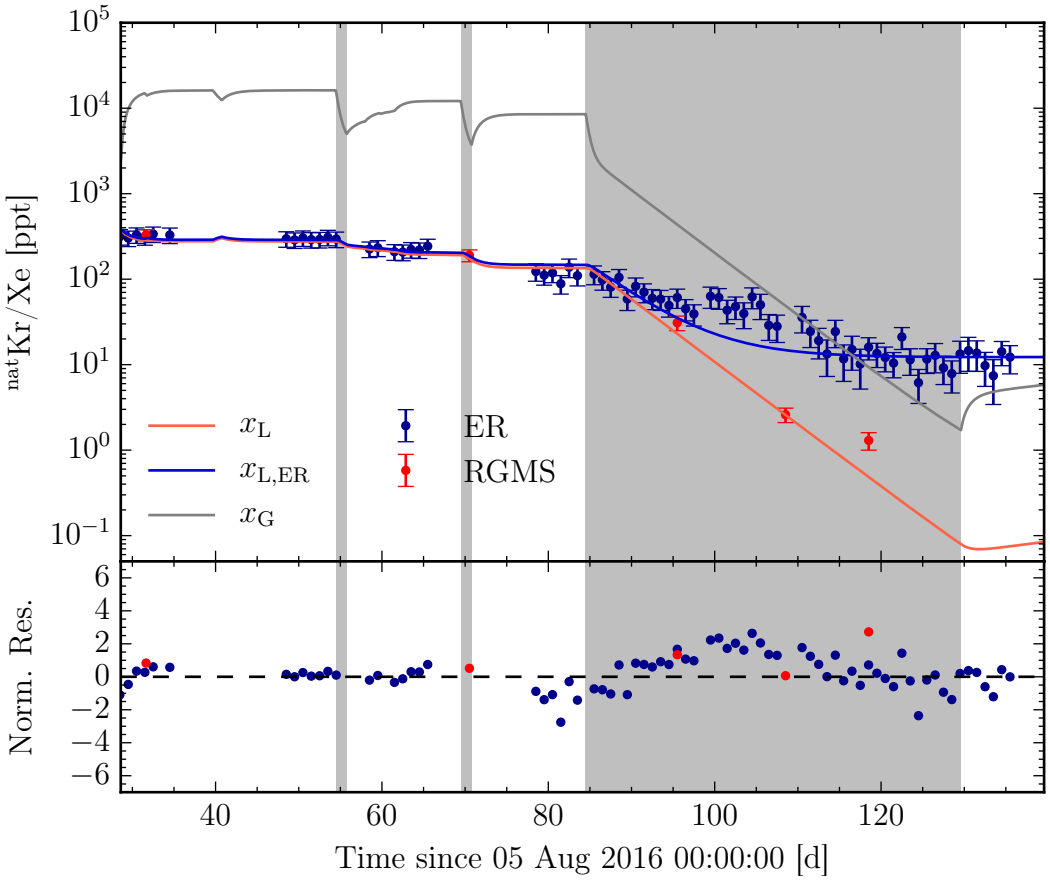


Figure 6.23: **Online krypton removal fit from $t = 28.6$ d until $t = 139.6$ d:** The two thin grey shaded areas indicate two short tests of the final upgraded gas only distillation, while the wide grey shaded area highlights the long term distillation in this mode. The blue data points (ER) are fitted well by the blue curve ($x_{\text{L,ER}}$), except for a bump around $t = 100.0$ d. The ER data levels off, as radon takes over as dominant background source in XENON1T. The red data points (RGMS) are fitted well by the red curve ($x_{\text{L}}$), except for the last point. The evolution in the GXe volume ($x_{\text{G}}$) is visualized in grey. The deviation between the curves and data points are shown in the bottom panel in form of normalized residuals in corresponding colors.

In figure 6.24, the time period from $t = 119.6$ d until $t = 543.0$ d (Jan 30 2018 00:00:00) is illustrated. This time span includes a major part of science run 1 (Jan 18 2017 - Feb 24 2018). The krypton concentration $x_{\text{L}}$ (red) in the LXe part increases over time due to the leak into the system. This is monitored with the RGMS data points (red). The points deviate from the fit within $\pm 2\sigma$. In addition, the liquid and gas mixture point $\text{RGMS}_{\text{L+G}}$ (green) is compared to the mixture $x_1$ (green). It deviates by $-1.7\sigma$ from the fit curve. Note that

only values of $x_1$ during a standard circulation mode are presented, resulting into some gaps where another operation mode is performed. The evolution $x_G$ in the GXe phase is drawn in grey. The krypton concentration inside the liquid increased by a factor 13.5 to $x_L(t = 543.0\,\mathrm{d}) = 1\,\mathrm{ppt}$ with respect to the minimum concentration. However, during the SR1, krypton was sub-dominant compared to radon. Thus, it was not required to re-start the online distillation.

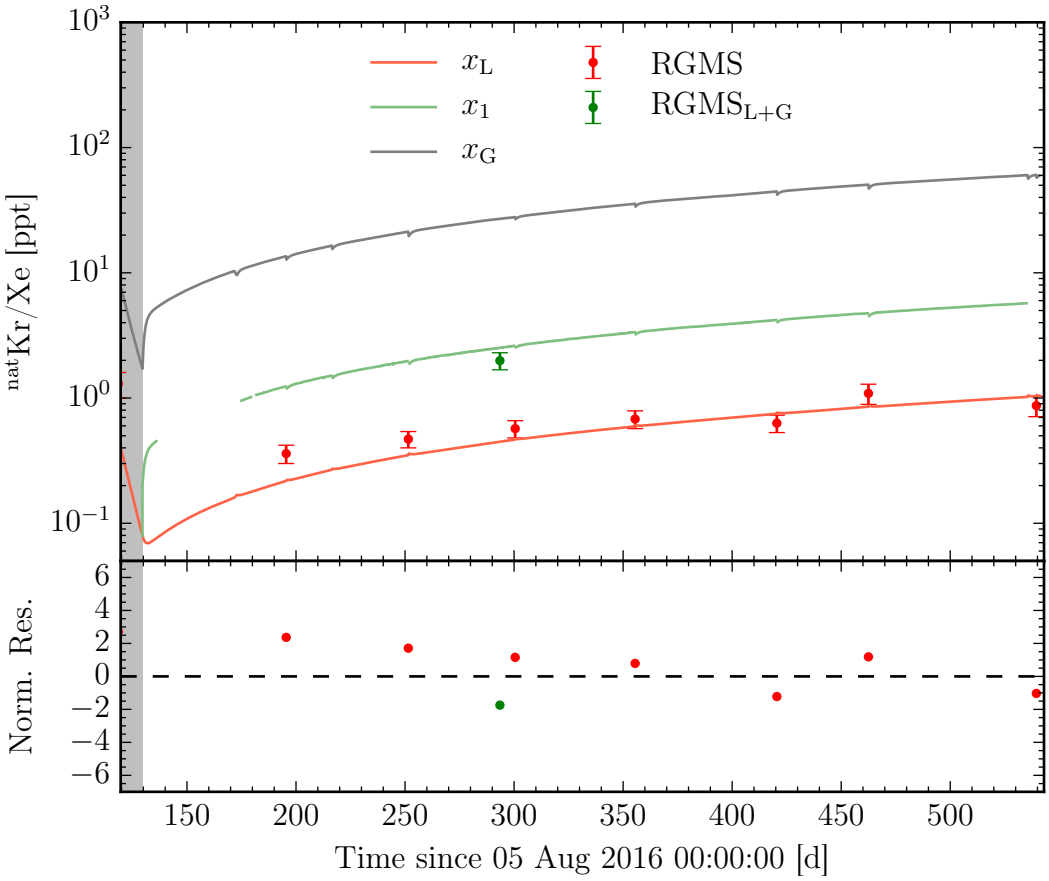


Figure 6.24: **Online krypton removal fit from $t = 119.6\,\mathrm{d}$ until $t = 543.0\,\mathrm{d}$:** The end of the upgraded gas only distillation is grey shaded. After the distillation, the red data points (RGMS) show an increasing krypton concentration in the LXe phase as a result of the leak to the system. The red fit curve ($x_L$) models this increase well. The green data point (RGMS$_{L+G}$ ) is a mixture from liquid and gas extraction during the standard circulation mode. It deviates by $-1.7\sigma$ from the green fit curve ($x_1$). Note that only values of $x_1$ during standard circulation are shown, leading to gaps where another operation is performed. The evolution in the GXe phase ($x_G$) is drawn in grey. The deviation between the curves and data points are shown in the bottom panel in form of normalized residuals in corresponding colors.

The goal of the online krypton removal development is to achieve the lowest possible krypton in xenon concentration inside the LXe volume of the TPC. This can be directly monitored with the extracted RGMS samples. Therefore,

figure 6.25 summarizes the complete set of the RGMS measurements (red) over the total time span of 543 d, including commissioning, science run 0 and science run 1 of XENON1T. The fit curve $x_{\mathrm{L}}$ (red) allows to model and calculate the krypton contribution to the XENON1T background at any given time. This is of importance for different analyses, e.g. annual modulation signals [90]. The evolution $x_{\mathrm{G}}$ (grey) is shown as well.

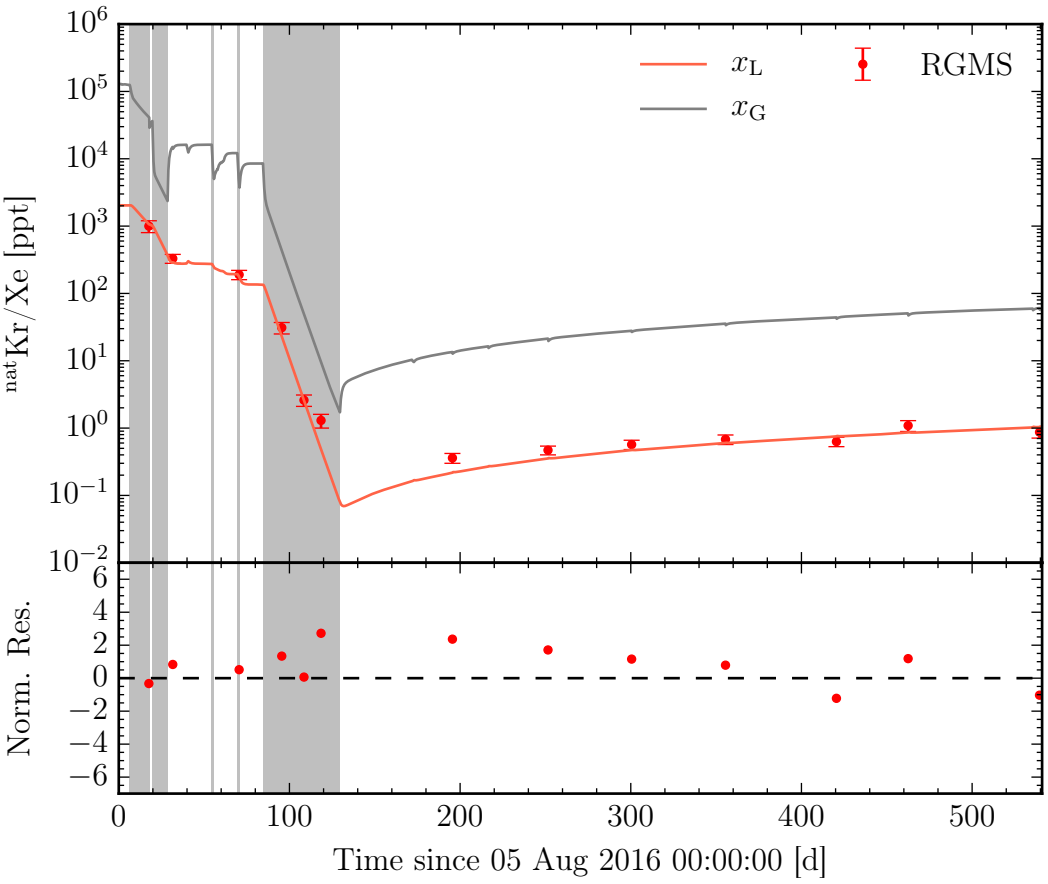


Figure 6.25: **Online krypton removal fit for complete time period:** The complete set of the RGMS measurements (red) over the total time span of 543 d is plotted, including commissioning, science run 0 and science run 1 of XENON1T. The fit curve $x_{\mathrm{L}}$ (red) allows to model and calculate the krypton contribution to the XENON1T background at any given time. This is of importance for different analyses, e.g. annual modulation signals [90]. The evolution $x_{\mathrm{G}}$ (grey) is shown as well.

The reduced $\chi^2_{\mathrm{red}}$ of the fit is 4.55. The deviations of the RGA data points during the liquid+gas and gas only distillation in combination with the bump in the ER data at $t = 100$ d leads to a $\chi^2_{\mathrm{red}}$-value larger 1. Furthermore, the different absolute concentration values are obtained from three different measurement methods. This can lead to unknown systematics that cannot be taken into account for the fit.

As mentioned above, the important part of the model is to understand how the krypton from the liquid is removed in order to reach a low concentration

for the dark matter search. Therefore, the different time constants resulting from the fit in the LXe are investigated in the following to find the main drivers for the krypton migration. The equation for the change $dx_{\mathrm{L}}/dt$ in all seven operation modes discussed in section 6.1 contains a distillation, condensation and evaporation term. For modes with liquid and gas extraction, e.g. standard circulation, liquid+gas distillation, upgraded gas only distillation and online radon removal, an extraction term is introduced to the equation for the krypton change in the LXe phase. Furthermore, a return term from the heat exchanger is required for the model. However, as discussed above, the amount of krypton returning to the LXe phase via the heat exchanger is negligible. Therefore, this term was not taken into account. Following equation (6.18), the time constants for krypton leaving (−) and entering (+) the LXe volume can be defined as

$$\tau_{\mathrm{dst,L\to G}} = -\left[\alpha \cdot \frac{F_{\mathrm{Mig}}}{M_{\mathrm{L}}}\right]^{-1}, \tag{6.78}$$

$$\tau_{\mathrm{vap,L\to G}} = -\left[\alpha \cdot \frac{F_{\mathrm{vap}}}{M_{\mathrm{L}}}\right]^{-1}, \tag{6.79}$$

$$\tau_{\mathrm{extract,L\to G}} = -\left[\frac{F_{\mathrm{L}}}{M_{\mathrm{L}}}\right]^{-1}, \tag{6.80}$$

$$\tau_{\mathrm{dst,G\to L}} = +\left[\frac{F_{\mathrm{Mig}}}{M_{\mathrm{L}}}\right]^{-1}, \tag{6.81}$$

$$\tau_{\mathrm{con,G\to L}} = +\left[\frac{F_{\mathrm{con}}}{\alpha \cdot M_{\mathrm{L}}}\right]^{-1}. \tag{6.82}$$

Here, $\tau_{\mathrm{dst,L\to G}}$ is the time constant for krypton leaving the LXe volume due to the distillation term, $\tau_{\mathrm{vap,L\to G}}$ the one for leaving via the evaporation term and $\tau_{\mathrm{extract,L\to G}}$ the one from the extraction term. In contrast, $\tau_{\mathrm{dst,G\to L}}$ is the time constant for krypton returning into the LXe reservoir due to the distillation term, whereas $\tau_{\mathrm{con,G\to L}}$ is the one from the condensation term.

The time constants are summarized in figure 6.26 for a time span between $t = 0$ and $t = 200\,\mathrm{d}$. For a better visualization, the time constants that enter the LXe are scaled down by a factor 100. It can be seen that the distillation time constant $\tau_{\mathrm{dst,L\to G}}$ (red) with a value of $-34\,\mathrm{d}$ is the slowest process and has the lowest influence on the krypton migration. The main drivers are the evaporation time constant $\tau_{\mathrm{vap,L\to G}} \approx -12.9\,\mathrm{d}$ (purple) and $\tau_{\mathrm{extract,L\to G}} \approx -8.4\,\mathrm{d}$ (blue). During the gas only distillation (second grey shaded area), no liquid is extracted. In this mode, the condensed flow is equal to the evaporation flow and thus, the evaporation time constant is faster with respect to the other periods.

The time constants for the krypton that enters the LXe volume are two orders of magnitude larger. Here, the condensation $\tau_{\mathrm{con,G\to L}} \approx 1010\,\mathrm{d}$ (brown) is the slower process compared to the constant resulting from the distillation term $\tau_{\mathrm{dst,G\to L}} = 357\,\mathrm{d}$ (darkgrey). Note that these terms introduce krypton from the GXe reservoir with a much larger concentration $x_{\mathrm{G}}$. The ratio $x_{\mathrm{G}}/x_{\mathrm{L}}$ is around 65 as derived above. Thus, they do have an influence on the krypton change in the liquid and are not negligible.

Based on above findings, a potential optimization for the krypton online removal process can be discussed. The extraction from the GXe directly into the

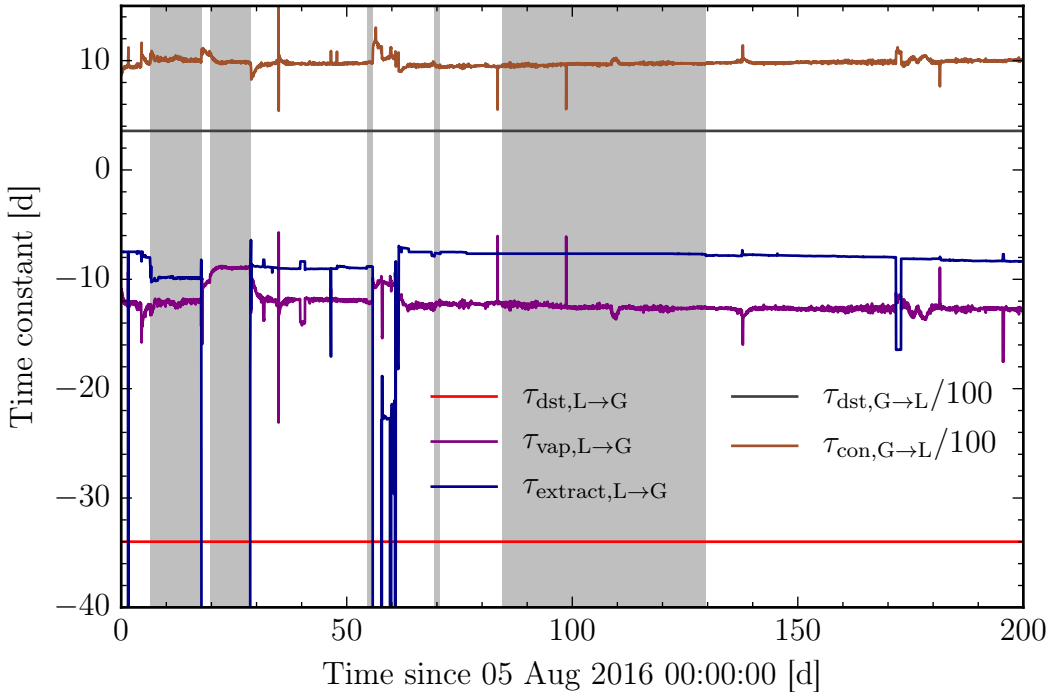


Figure 6.26: **Time constants for krypton change in LXe reservoir:** The distillation time constant $\tau_{\mathrm{dst,L\to G}}$ (red) with a value of $-34\,\mathrm{d}$ is the slowest process and has the lowest influence on the krypton migration. The main drivers are the evaporation time constant $\tau_{\mathrm{vap,L\to G}} \approx -12.9\,\mathrm{d}$ (purple) and $\tau_{\mathrm{extract,L\to G}} \approx -8.4\,\mathrm{d}$ (blue). The condensation $\tau_{\mathrm{con,G\to L}} \approx 1010\,\mathrm{d}$ (brown) is the slower process compared to the constant resulting from the distillation term $\tau_{\mathrm{dst,G\to L}} = 357\,\mathrm{d}$ (darkgrey). Both are scaled down by a factor 100 for a better visualization.

column in the upgraded gas only mode is not the limiting factor of the removal operation. This is indicated by the bulk removal of krypton at the beginning of the distillation. Then, the evolutions in gas and liquid slow down as they are dominated by the migration from liquid into gas. One possibility is to artificially heat from the bottom of the cryostat to further increase the evaporation flow and thus, to make the migration process faster and the time constant $\tau_{\mathrm{vap,L\to G}}$ smaller. However, the heating could create boiling and bubbles in the detector volume that might disturb the TPC data taking. Furthermore, this cannot be applied to the running XENON1T detector, but could be an option for the up-coming experiment XENONnT. A more simple method in XENON1T is to upgrade the purification system with a high-performance pump. Like that, the extraction from the liquid could be increased resulting into a smaller constant $\tau_{\mathrm{extract,L\to G}}$. Such a pump is presented in [70, 95].

In the following, further investigations on the model to data fitting are depicted due to the relatively large $\chi^2_{\mathrm{red}}$ of 4.55. The fit can be re-done as above, but with a free gaseous mass $M_{\mathrm{G}}$. The fit routine yields comparable values as before in table 6.6 and $M_{\mathrm{G}} = 9.4\,\mathrm{kg}$. The corresponding $\chi^2_{\mathrm{red}}$ is 1.79. Exemplary, the time period from $t = 17.7\,\mathrm{d}$ until $t = 30.1\,\mathrm{d}$ during the gas only distillation is

visualized in figure 6.27. The grey fit curve $x_G$ can describe the $RGA_{GO}$ data points much better than before (see figure 6.22), especially the steep decrease at the beginning of the distillation. This is supported by the smaller variation of the normalized residuals.

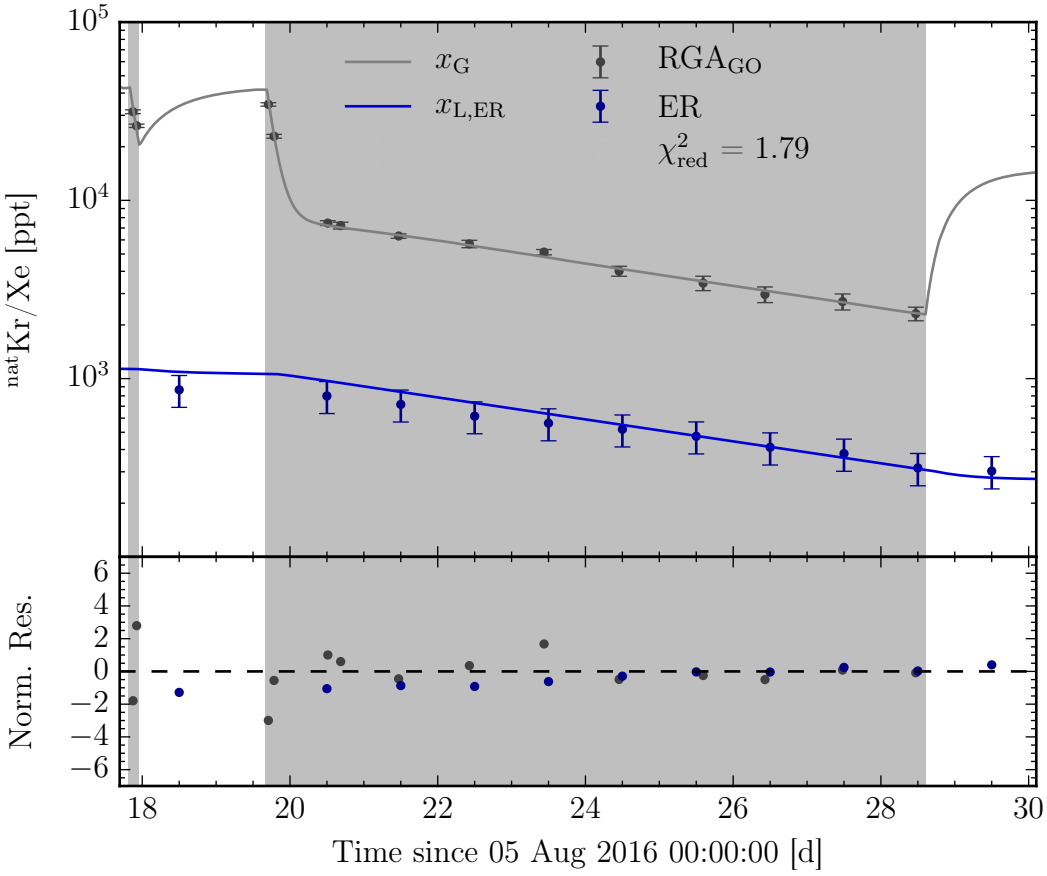


Figure 6.27: **Online krypton removal fit from $t = 17.7$ d until $t = 30.1$ d with free GXe mass:** The grey fit curve $x_G$ can describe the $RGA_{GO}$ data points much better than before (see figure 6.22), especially the steep decrease at the beginning of the distillation. This is supported by the smaller variation of the normalized residuals. The $\chi^2_{red}$ for this fit is 1.79.

Furthermore, the bump in the ER data points around $t = 100$ d is checked. Exactly at the rise of this bump, a power outage at the XENON1T service building forced the compressor of the PTR102 to turn off for several minutes. As consequence, the PTR102 surface inside the condenser station warmed up by about 0.5 °C. This warming up due to the power glitch released a large amount of electronegative impurities that were frozen at the cold surface leading to a decrease in electron lifetime [89]. The assumption is made that also krypton was trapped at this location and is released in form of a delta peak into the GXe volume. The response of the model due to this additional krypton is highlighted in figure 6.28 for the upgraded gas only distillation period from $t = 80.0$ d until $t = 137.6$ d. The bump in the ER data points (blue) can be modeled better than before by the curve $x_{L,ER}$ (blue) (see figure 6.23). Also, the RGMS data points

(red) deviate less than before from the fit curve $x_{\mathrm{L}}$ (red), as indicated by the normalized residuals. The $\chi^2_{\mathrm{red}}$ is further reduced to 1.64[4].

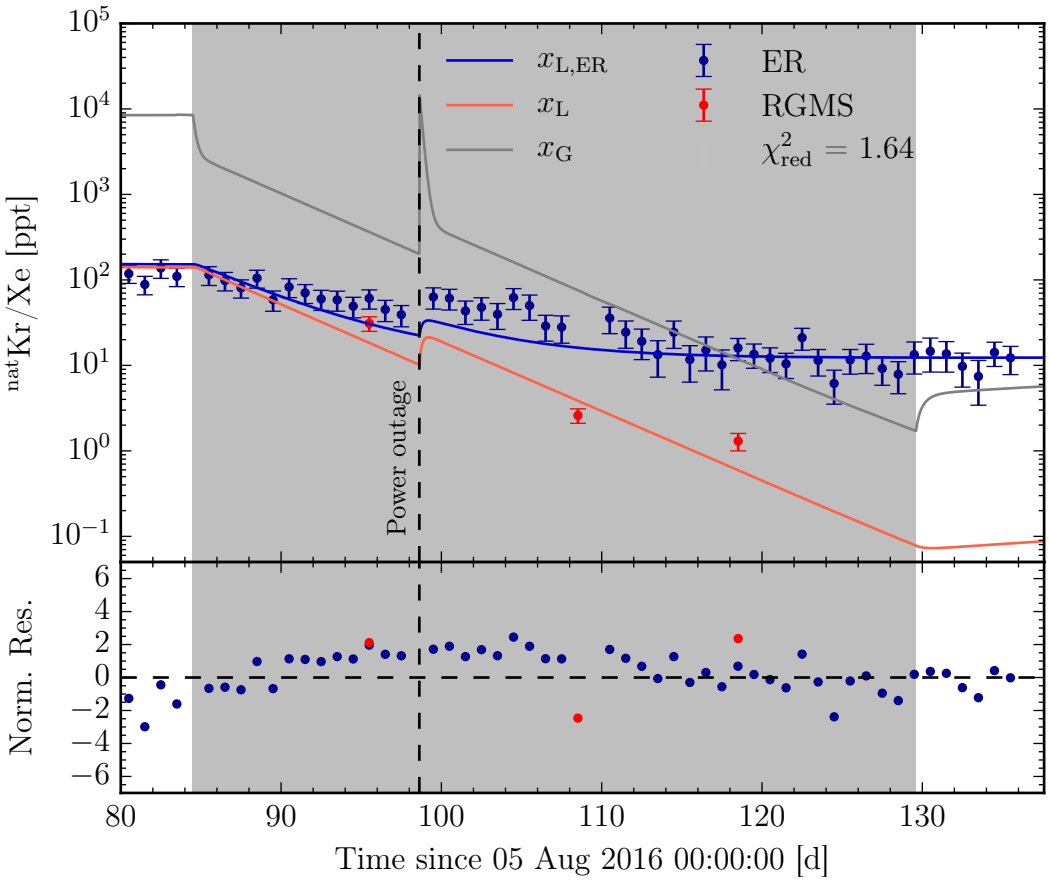


Figure 6.28: **Online krypton removal fit from** $t = 80.0\,\mathrm{d}$ **until** $t = 137.6\,\mathrm{d}$ **with power glitch:** Due to the warming up of the PTR for several minutes after a power outage, krypton was released to the GXe volume. The bump in the blue data points (ER) can be modeled better than before by the blue curve ($x_{\mathrm{L,ER}}$) (see figure 6.23). Also, the red data points (RGMS) deviate less than before from the red fit curve ($x_{\mathrm{L}}$), as indicated by the normalized residuals. The $\chi^2_{\mathrm{red}}$ for this fit is 1.64.

However, an effective mass in the GXe that is about a factor 2 lower than the one calculated cannot be explained. The cryogenic system features several extraction ports at all locations that could be potentially dead volumes. Therefore, the fit results with the free mass are not evaluated in more detail.

All in all, the model presented is able to describe the krypton evolution in the liquid-gas interface for several detector operation modes. This was validated using the three independent measurement methods RGA, RGMS and ER event rate. The concept can also be utilized to predict the migration time, and thus, the duration until a desired krypton concentration in the TPC is reached for different circulation times and for future applications.

[4] Also here, the mass $M_{\mathrm{G}}$ was a free parameter.

In summary, the online krypton removal developed within this thesis efficiently reduced the krypton in xenon concentration to the lowest level ever achieved in a running dark matter detector. The main advantage of the new method is to remove krypton, while the TPC is fully operational, by continuously cycling xenon from the GXe reservoir through the column. In this case, it achieved a confirmed concentration of $(360 \pm 60)$ ppq within 70 days of distillation, starting at around 3 ppb in the combined mixture of the GXe and LXe reservoir. This allowed to start the first XENON1T dark matter run two month earlier with the lowest ER background ever achieved for the WIMP dark matter search.

Additionally, the operation gives the possibility to further reduce the krypton induced background at any given time in XENON1T, if a lower concentration is required without emptying the detector. The same technique and principle can be applied for the next generation experiment XENONnT.

This technique also opens up a complete new set of potential internal calibration sources in large liquid xenon detectors. One example is the isotope $^{37}$Ar. While the lowest calibration energies in XENON1T are 9.4 keV, 32.1 keV and 41.5 keV from the decay of $^{83m}$Kr, $^{37}$Ar allows a calibration down to an energy of 2.8 keV via electron capture [96]. However, its half-life of 35 d is usually too long for the scope of a dark matter search. This problem can be solved by applying the new online removal technique: After the calibration, an online removal campaign could be performed, removing the lighter noble gas argon from xenon. With a relative volatility $\alpha_{\mathrm{Ar}}$ of 50 (see section 3.1), the process is assumed to be even more efficient compared to krypton. With the help of the model developed, the removal time can be estimated in advance. This calibration is planned as last test before the end of the XENON1T lifetime with a gaseous $^{37}$Ar source.

# Online radon removal at XENON100 and XENON1T 7

After the removal of $^{85}$Kr, as described in the previous chapter, the ultimate background for large-scale liquid xenon experiments such as XENON1T and XENONnT is originating from the decay of the noble gas $^{222}$Rn with a half-life of 3.8 days. More precisely, subsequent beta-decays in the decay chain create low energy events. The $^{222}$Rn is continuously emanating from the detector materials due to the decay of trace amounts of $^{226}$Ra within the material. Furthermore, it is homogeneously distributed throughout the sensitive detector volume, making the shielding properties of liquid xenon and fiducialization useless. In order to keep the radon induced background low, all components were screened for their radon emanation before the assembling of XENON1T [97, 98]. To further push down the radon concentration and to further increase the sensitivity for the dark matter search, a radon removal system (RRS) is being developed. In contrast to $^{85}$Kr, the isotope $^{222}$Rn is continuously produced during the dark matter search. Consequently, the RRS requires to operate continuously as well. This can be achieved by the integration of the RRS into an existing purification loop. The basic idea is to trap the radon within the RRS until disintegration, while the purified xenon can be fed back to the detector. One way of trapping was tested with cooled charcoal, where radon gets adsorbed more efficiently than xenon [99]. However, independent studies revealed that the charcoal itself will emanate radon, which results into a limitation in terms of the reduction power of such an RRS [97]. Another way to remove radon from xenon is cryogenic distillation, as described in detail in section 3.1. Due to the difference in vapor pressure of the two noble gases, radon as heavier isotope is enriched in the liquid xenon. This was validated in a xenon boil-off experiment in [45, 65].

In the first part of this chapter, the successful operation of the Münster cryogenic distillation column as a radon removal system at the XENON100 experiment is presented. For this purpose, the distillation system was rebuilt to the smaller Phase-1 version with a total height of about 3 m, featuring a package length of about 1.1 m. Like that, the system could be integrated in the gas purification loop of XENON100. By using the TPC as radon source and monitoring device for the $^{222}$Rn activity concentration at the same time, the capability of cryogenic distillation to reduce radon-induced background was investigated. These measurements were performed in close cooperation with Stefan Bruenner from MPIK Heidelberg and are also presented in [45]. Furthermore, the results were published in [100] by the XENON collaboration,

where Stefan Bruenner and the author of this thesis are the corresponding authors.

The second part of this chapter highlights the successful operation of the final Phase-2 distillation system for the reduction of radon within XENON1T, using the method of online distillation. Here, xenon is extracted from the gaseous phase of the cryogenic system and its connections to the cryostat, in order to remove radon before it migrates into the liquid phase and is flushed into the detector.

## 7.1 XENON100

The XENON100 cryostat houses 161 kg of liquid xenon, from which 62 kg are within the TPC and up to 47 kg can be used as fiducial volume. Therefore, the XENON100 detector is a suitable test-bed for the radon removal investigations. Additionally, the XENON100 system features a gas purification loop made of a gas transfer pump (pump 1), a mass-flow controller (MFC1), and a high-temperature gas purifier (getter) to remove electronegative impurities. The total radon emanation rate was measured in 2012 to be $(11.9 \pm 1.1)$ mBq, whereas $(9.3 \pm 1.0)$ mBq orginate from the cryostat, housing the TPC, and $(2.6 \pm 0.5)$ mBq are generated within the purification loop [97]. For a homogeneous radon distribution throughout the total liquid xenon mass of 161 kg, an activity concentration of about 74 µBq/kg is expected. This is slightly higher compared to the results of $(62.9 \pm 0.8)$ µBq/kg from $\alpha$-event counting using the TPC as radon monitor during that time. The emanation was measured at room temperature and could yield a higher out-gassing rate compared to liquid xenon temperatures, explaining the small discrepancy [97]. Before and between the radon removal campaigns of December 2014 and January/February 2015 the measured radon emanation was in the range of (30–50) µBq/kg, indicating that the out-gassing from the materials is decreasing over the years.

In order to connect the distillation column, the XENON100 purification loop was extended by an interface gas system. The interface also housed an integrated auxiliary $^{222}$Rn emanation source in front of the distillation system with a constant emanation rate of $(91 \pm 6)$ mBq [45]. The source was made of a 2 L stainless steel vessel with VCR connectors, filled with 426 viton O-rings (Novotek). The reduction power $R_C$ of the column was investigated by switching the source on/off via a bypass. This is described in section 7.1.4. Additionally, a pump was installed to extract the purified xenon from the distillation plant. With the help of this second pump, warm xenon gas was circulated through the column and the extended interface gas system via an additional hot metal getter over the course of three days in order to remove potential electronegative impurities before opening to the XENON100 circuit.

The krypton distillation column arrived at LNGS in a shortened version with a package tube length of 1.1 m and a total height of 3 m, similar to Phase-1 [60]. This allowed an installation outside the XENON100 box, whereas the Phase-2 version would have been too tall. In order to use the column as a radon removal system, a few modifications were required: The original inlet of the system stayed the same, but the flow controller FIC401 was removed. During the first

test run, a malfunction caused the controller to close during operation, resulting in a broken membrane of the main circulation pump. This caused a replacement of the pump as well as a delay of the planned operation. While the standard outlet from the bottom of the column was not used and therefore blinded, the off-gas line coming from the top of the column was connected to the interface gas system. The flow controller FIC404 with a maximum flow of 10 slpm in parallel to the original FIC403 with a maximum of only 0.1 slpm allowed for high enough gas extraction flows as well as balancing the liquid level in the reboiler. An emergency recovery system, made of a bottle in a dewar and a pressure regulator, was installed to the inlet of the plant to allow recuperation and re-filling of the column. However, it was only used once to recover the xenon from the distillation and interface system after initial circulation through the getter. Afterwards, the column was pre-cooled and filled always with XENON100 gas only in order to avoid any extra contamination of the XENON100 system. For the controlling and monitoring of the system, the electronic rack of the column as it was built in Münster along with the LabVIEW based slow control [64] was used. A picture of


Figure 7.1: **Experimental setup outside the XENON100 box:** In the left, the modified distillation column for radon removal is installed next to the XENON100 krypton column. In the middle, the interface gas system with the artificial source is shown along with the getter for pre-cleaning of the new systems. On the right, the XENON100 box can be seen, housing the standard gas system and the detector system.

the additional systems outside of the XENON100 box is visualized in figure 7.1, while a basic scheme of the overall setup is sketched in figure 7.2.

During the operation, radon-enriched xenon is pumped via the interface system from the detector towards the distillation column at a flow of about 4.85 slpm, controlled by the MFC1. The incoming gaseous xenon from the detector is pre-cooled to −96 °C inside the input condenser of the distillation plant. From here, the xenon is injected into the middle of the package tube of the column via LF2 with a height of 62.3 cm. A gaseous feed was chosen for a more stable and reliable operation. Some regulation issues with a liquid feed occurred in

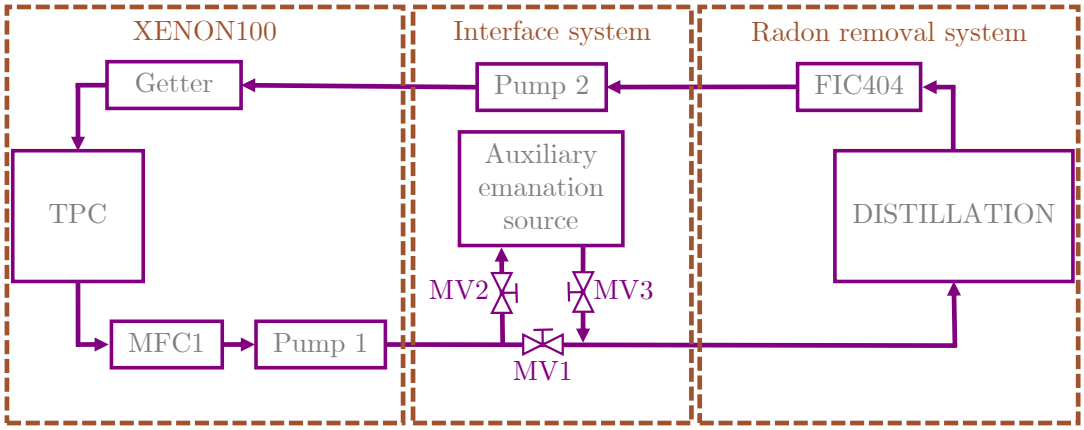


Figure 7.2: **Experimental setup for radon removal at XENON100:** The radon-enriched xenon from the detector is pumped (Pump 1) from the TPC (left) via the interface system (middle) to the distillation column (right), where radon is removed. The purified xenon is pumped back (Pump 2) to the detector via the interface system through the XENON100 getter. The purification flow is controlled via mass flow controllers (MFC1, FIC404) in front of the two gas transfer pumps. A bypass to an auxiliary radon emanation source can be opened (MV2, MV3) to artificially enhance the radon concentration in the detector. Figure and caption based on [100].

the closed loop with the gas system during the initial test. As in the case for krypton distillation, a continuous counter flow between up-streaming xenon gas, evaporated in the reboiler, and down-streaming liquid xenon, liquefied by the top condenser, is established. Due to the lower vapor pressure, the liquid reservoir inside the reboiler becomes radon-enriched, while the gaseous xenon at the top of the column features the lowest radon concentration. From here, the second gas transfer pump (pump 2) extracts the radon-depleted xenon and pushes the gas through the getter back into the detector. The mass balance inside the column is achieved by the off-gas flow controller FIC404 and was measured to be 4.85 slpm. Since the MFC1 seemed to posses an unknown off-set as it was originally calibrated with nitrogen instead of xenon, the flow measured with FIC404 is used in further investigations. In contrast to the standard krypton distillation process, no extraction of highly contaminated xenon from the bottom is required, as radon is trapped inside the reboiler until disintegration, as described in section 3.1. Therefore, the online radon removal is xenon-loss free.

### 7.1.1 Expected radon reduction

In this section, the expected rate evolution of the radon activity concentration inside the TPC is modeled for a given reduction $R_C$ of the column and for the given radon contributors. The radon emanation sources are divided in two types of sources, depending of their position in the overall setup with respect to the radon removal system: Sources, labeled as type 1, are located either inside the

cryostat of XENON100, such as the detector itself, or after the distillaton column within the gas purification loop such as the pump 2 and the getter. Consequently, radon emanated from a type 1 source is flushed into the detector before reaching the removal system. A radon source between the detector and the RRS, such as pump 1 or the auxiliary emanation source, are referred to as type 2. Consequently, radon emanated from a type 2 source is flushed into the removal system before reaching the detector. The different contributors to the final radon activity in XENON100 are depicted in a simplified diagram in figure 7.3.

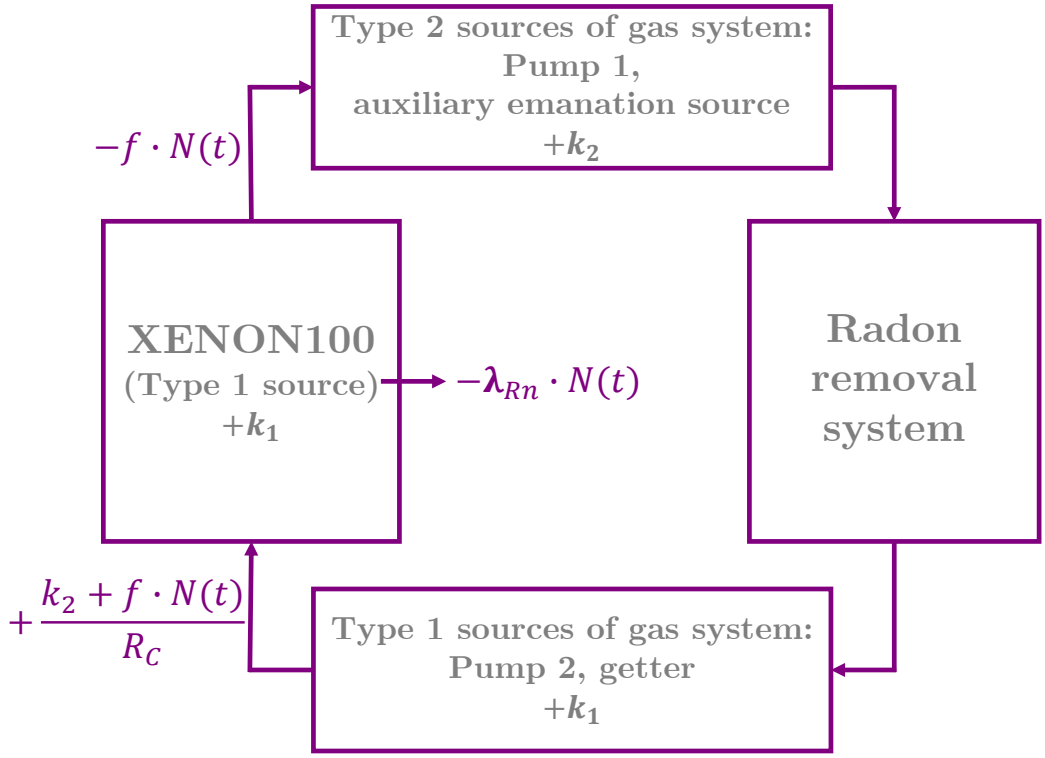


Figure 7.3: **Different radon sources contributing to the radon activity in the XENON100 detector:** The experimental setup can be divided into the XENON100 detector, the radon removal system and the gas system before/behind the radon removal system, respectively. Depending on its position in the system, a radon source is referred to as type 1 or type 2. Figure and caption based on [100].

In order to model the total number of $^{222}$Rn atoms $N(t)$ inside the detector over time, the in-going and out-going radon atoms need to be identified. The number of radon particles is continuously reduced by the radioactive decay ($T_{1/2}$ = 3.8 d) and by the extraction due to the purification flow $F_{Xe}$ in standard liters (sl) per second. In combination with the total amount of the xenon inventory $V_{Xe}$ in sl, an effective circulation rate $f$ can be defined as

$$f = \frac{F_{Xe}}{V_{Xe}}, \tag{7.1}$$

which can be transformed into an effective exchange time $\tau_{exchange} =: 1/f$. Radon atoms can enter the detector directly from the emanation of type 1 sources. This

is assumed to follow a constant $^{222}$Rn production rate $k_1$. The type 2 radon, emanated in the gas system in front of the RRS, is generated at a constant rate $k_2$. However, this type of source together with the radon particles pumped from the detector with a radon particle flux $f \cdot N(t)$ is first reduced within the radon removal system by the reduction factor $R_\mathrm{C}$. Here, $R_\mathrm{C}$ is assumed to be constant and independent on the radon concentration. It is defined, analog to the case of krypton, as the ratio of the radon concentration at the inlet and at the outlet at the top of the column with

$$R_\mathrm{C} \equiv \frac{c_\mathrm{in}}{c_\mathrm{out}}. \tag{7.2}$$

The remaining radon atoms, not removed from the RRS, are pumped back and can re-enter the detector. Summarizing all in-going and out-going atoms, the change in the number of radon atoms inside the detector over time can be expressed by the following differential equation

$$\frac{dN(t)}{dt} = k_1 - \lambda_\mathrm{Rn} \cdot N(t) - f \cdot N(t) + \frac{k_2 + f \cdot N(t)}{R_\mathrm{C}}. \tag{7.3}$$

Here, $\lambda_\mathrm{Rn} \cdot N(t)$ denotes the decay of $^{222}$Rn with its decay constant $\lambda_\mathrm{Rn} = 2.1 \times 10^{-6}\,\mathrm{s}^{-1}$ and $f \cdot N(t)$ denotes the effective radon particle flux, leaving the detector. The number of radon atoms not removed by the distillation column are given by the term $\big(k_2 + f \cdot N(t)\big)/R_\mathrm{C}$. Above differential equation can be solved for the starting condition $N(t=0) = N_0$, where $N_0$ is the number of radon atoms before starting the removal. It follows

$$\begin{aligned} N(t) &= \frac{K}{\Lambda} + \left(N_0 - \frac{K}{\Lambda}\right) \cdot e^{-\Lambda \cdot t}, \\ \text{with} \quad K &= k_1 + \frac{k_2}{R_\mathrm{C}} \quad \text{and} \quad \Lambda = \left(\lambda_\mathrm{Rn} + f \cdot \left(1 - \frac{1}{R_\mathrm{C}}\right)\right). \end{aligned} \tag{7.4}$$

For infinitely large times, the above relation simplifies to the equilibrium relation

$$N_{equi} \overset{t\to\infty}{=} \frac{K}{\Lambda} = \frac{k_1 + \frac{k_2}{R_\mathrm{C}}}{\lambda_\mathrm{Rn} + f \cdot (1 - \frac{1}{R_\mathrm{C}})} \tag{7.5}$$

$$\overset{R_\mathrm{C}\to\infty}{=} \frac{k_1}{\lambda_\mathrm{Rn} + f}, \tag{7.6}$$

where the last step assumes an infinite purification power $R_\mathrm{C}$. Consequently, a perfect radon removal system can fully remove radon, emanated by type 2 sources, as indicated by equation (7.6). However, the exchange time $1/f$ of the xenon within the detector, depending on the total xenon inventory and the purification flow, is limiting the reduction of type 1 sources. Therefore, the different locations of radon sources along with a high re-circulation flow needs be considered, when designing an RRS.

Finally, the overall radon reduction $r$ inside the XENON100 detector itself for a given $R_\mathrm{C}$ of the distillation column can be defined as

$$r \equiv \frac{N_\mathrm{equi}(R_\mathrm{C} = 1)}{N_\mathrm{equi}(R_\mathrm{C})}, \tag{7.7}$$

using equation (7.5). The given purification flow of about 4.85 slpm and the given total xenon inventory of about 158 kg (assuming (3–4) kg filled into column) yield a circulation rate of $f = 3.07 \times 10^{-6}$ 1/s. With that, a reduction $r$ in XENON100 of about 2.46 is expected for an ideal removal system ($R_C = \infty$) and without applying the artificial source, following equation (7.7).

### 7.1.2 Data analysis

In order to monitor the evolution over time before, during and after the distillation, the XENON100 TPC was utilized as a monitoring device. The TPC data analysis to obtain a radon concentration for each day was evaluated in [100] and in more detail in [45]. Therefore, it is only summarized shortly here for completeness.

The light (S1) and charge (S2) signatures of the $\alpha$-decays of $^{222}$Rn (5.5 MeV) and its direct daughter isotope $^{218}$Po (6.0 MeV) can be measured within the XENON100 TPC in order to observe the radon activity concentration over time [51]. For the event selection, a minimum size of the S2 signals is required in order to remove events with incomplete charge collection such as surface events near the detector wall. After correcting the S1 signal for light collection inhomogeneities due to PMT saturation effects [51, 101], the isotopes $^{222}$Rn and $^{218}$Po can be identified via the energy derived from the S1 signal, as presented in [45,100]. By applying an S1 energy cut, 96 % of all $^{222}$Rn events can be selected and used for monitoring the evolution on a daily basis. Additionally, an overlap of 8 % of the neighboring $^{218}$Po peak was determined with a fit using crystal ball functions and was taken into account as well. The signatures of $^{220}$Rn and its direct daughter $^{216}$Po were found to be negligible for further analysis [45, 100].

As a cross check for the $\alpha$-counting, the radon activity concentration can be determined with so-called BiPo events, which are originating from the subsequent decays of $^{214}$Bi and $^{214}$Po within the $^{222}$Rn decay chain. These events can be identified by a time coincidence analysis, where the detection efficiency is about 50 % compared to the $\alpha$-analysis. Details on the analysis method can be found in [51], while the application to the radon removal tests is further explained in [45, 100]. Both methods are in agreement. Therefore, the BiPo cross check will not be presented in the following.

### 7.1.3 Measurements

In total, two distillation runs were performed, mainly differing by the usage of the auxiliary emanation source during the second run. The evolution of the $^{222}$Rn activity concentration in XENON100 is highlighted in figure 7.4.

The complete campaign can be divided into seven different operation phases. These are summarized in the following list as taken from [100]:

I Pre-distillation phase: The XENON100 detector and its purification loop were operated in their standard (background) mode. The averaged $^{222}$Rn activity concentration is $(33.4 \pm 1.3)$ µBq/kg.

II Replacement of pump 1: The gas transfer pump 1 was exchanged at the end of phase II. In this phase, the gas purification was stopped several times.

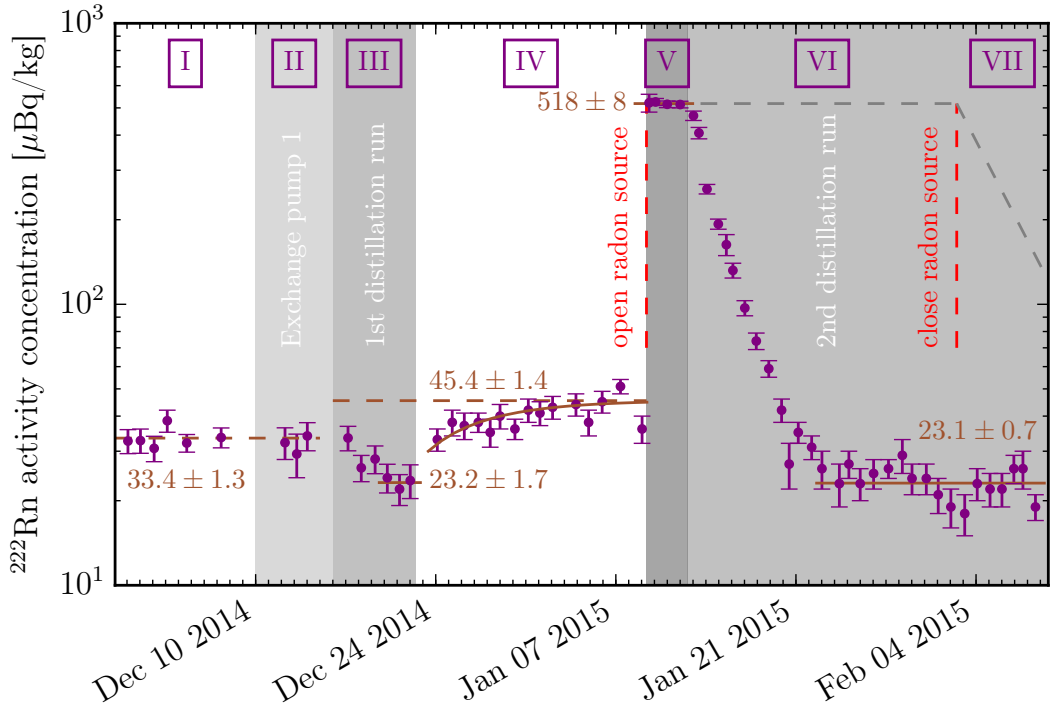


Figure 7.4: **Radon activity concentrations during the radon removal campaign in XENON100:** Different operation modes are indicated by roman numbers. Two distillation runs were performed (Phase III and phase V-VII). During the second run, the auxiliary emanation source was introduced to the system, allowing to probe the reduction capability of the distillation column. The dashed grey line describes the expected evolution without a radon removal system. Figure based on [100].

III First distillation run: Xenon gas was looped through the distillation column, but the auxiliary radon emanation source was bypassed. The observed $^{222}$Rn activity concentration decreased to $(23.2 \pm 1.7)$ µBq/kg.

IV Standard operation: After the first distillation run, most of the radon-enriched LXe reservoir inside the column was transferred into the XENON100 detector (abrupt rise of the activity concentration on Dec 23). Residual, radon-enriched xenon stayed inside the column. The $^{222}$Rn activity concentration in XENON100 increased to the new equilibrium value of $(45.4 \pm 1.4)$ µBq/kg. The increased level with respect to phase I is explained by additional $^{222}$Rn sources after the pump exchange. The detector was operated in its standard (background) mode during this phase.

V Auxiliary radon emanation source opened: Xenon gas was circulated through the auxiliary $^{222}$Rn source, but the distillation column was in bypass. The increased activity concentration was $(518 \pm 8)$ µBq/kg. Since the auxiliary source emanates radon with a constant rate, this level remained constant (emanation equilibrium).

VI Second distillation run: Restart of the online radon removal with the

distillation column. The auxiliary emanation source was kept open during this phase. Due to the radon distillation, the $^{222}$Rn activity concentration decreased to $(23.1 \pm 0.7)$ µBq/kg, below the equilibrium value of phase IV. Without radon removal, we would expect to see a constant level as indicated by the dashed, grey line.

VII Auxiliary radon emanation source closed, radon distillation continued: The activity concentration stayed about constant even though the total amount of radon decreased due to decay (dashed, grey line). As we will discuss in the next section, the constant level is an indication that the distillation column removed close to all radon emanated by the auxiliary emanation source.

From the obtained values during the different phases above, the reduction of the radon activity concentration inside XENON100 for both distillation periods can be calculated.

Due to the fact, that the gas transfer pump 1 of the standard XENON100 gas system was exchanged by the end of phase II, the reached level during the first distillation run in phase III can only be compared to the equilibrium activity concentration of phase IV, since the emanation rate of the new pump is likely to be different. This assumption is supported by the higher concentration in phase IV with respect to phase II. A reduction of $r_{III} = 2.0 \pm 0.2$ is found for the first campaign, using equation (7.7). This is comparable to the expected reduction of 2.46 from the model in section 7.1.1. Note, that during phase IV, the detector was operated in its standard configuration without using the new interface gas system. Therefore, potential emanation sources originating from the interface system are not taken into account and thus, the obtained reduction $r_{III}$ is likely to be higher.

Using the new equilibrium concentration after opening of the auxiliary emanation source in phase V, the reduction during the second distillation run in phase VI is calculated to be $r_{VI} = 22.4 \pm 0.8$. The higher reduction can be explained by a different composition of the radon contributors with respect to the first run. Without the artificial increase in activity, the overall system was dominated by type 1 sources during the first campaign, namely by the emanation from the XENON100 cryostat and its gas system components, as investigated in [97]. As explained by the model, the removal of these sources is strongly suppressed and limited by the purification flow of the system of about $F_{\mathrm{Xe}} = 4.85$ slpm. In contrast to the standard configuration, the system was dominated by type 2 sources during the second campaign, mainly by the auxiliary emanation source as it was installed in front of the radon removal system. As pointed out in the model, the distillation system is highly efficient for type 2 sources. Therefore, the second distillation run can be used to investigate the reduction power $R_{\mathrm{C}}$ in more detail.

### 7.1.4 Column reduction factor

In order to determine the radon reduction factor $R_{\mathrm{C}}$ of the distillation column, the equation model developed in section 7.1.1 can be applied to the second radon

removal campaign with the auxiliary radon source including the phases IV-VII. All possible scenarios for switching on and off the column and the source were measured. Unfortunately, the interface gas system along with its potential emanation sources, such as the pump 2, was not part of the xenon re-circulation cycle during phase IV. Therefore, this phase is neglected for the further investigation and only phases V-VII were analyzed. The reduction capability $R_{\mathrm{C}}$, defined in equation (7.2), of the radon removal system is different from the reduction $r$, defined in equation (7.7), inside the XENON100 detector and can also feature higher values. The model can be used under the assumption of a homogeneous radon distribution throughout the detector for any given time. This was investigated and confirmed by using the acquired data, when the auxiliary source was opened and is further presented in [45, 100]. No concentration gradients were found in the Z-position nor in the radial position.

The type 2 artificial source introduces a new constant emanation rate $k_s$ to the overall system, which can be switched on and off via the bypass in the interface gas system. Therefore, the factor $K$, as defined in equation (7.4), needs to be refined for the cases with and without the contribution of the artificial source:

$$K_s = k_1 + \frac{k_2 + k_s}{R_{\mathrm{C}}}, \text{for auxiliary source open} \tag{7.8}$$

$$K = k_1 + \frac{k_2}{R_{\mathrm{C}}}, \text{for auxiliary source closed.} \tag{7.9}$$

As before, $k_1$ is the constant emanation rate from type 1, while $k_2$ is the contribution from all other type 2 sources within the system, except from the artificial source.

Following equation (7.3) in section 7.1.1, the number of $^{222}$Rn particles for each of the operation phases V-VII can be described with their respective starting condition as

$$N_{\mathrm{V}}(t) = (k_1 + k_2 + k_s) \cdot \lambda_{\mathrm{Rn}}^{-1} = \text{const.}, \tag{7.10}$$

$$N_{\mathrm{VI}}(t) = \frac{K_s}{\Lambda} + \left( N_{\mathrm{V}}(t_{\mathrm{VI}}) - \frac{K_s}{\Lambda} \right) \cdot e^{-\Lambda \cdot (t - t_{\mathrm{VI}})}, \tag{7.11}$$

$$N_{\mathrm{VII}}(t) = \frac{K}{\Lambda} + \left( N_{\mathrm{VI}}(t_{\mathrm{VII}}) - \frac{K}{\Lambda} \right) \cdot e^{-\Lambda \cdot (t - t_{\mathrm{VII}})}. \tag{7.12}$$

Here, $t_{\mathrm{VI}}$ and $t_{\mathrm{VII}}$ are the starting times of phases VI and VII, while $\Lambda$ is the same factor as defined before in equation (7.4).

In order to fit the model to the acquired data, the corresponding $^{222}$Rn activity concentrations $c_1$, $c_2$ and $c_s$ are used instead of the rates $k_1$, $k_2$ and $k_s$ for better comparison to the visualized data in figure 7.4. Equations (7.10) to (7.12) can be applied analogously. A $\chi^2$-minimization fit was performed with the fitting parameters $t_{\mathrm{VI}}$, $t_{\mathrm{VII}}$, $c_1$, $c_2$, $c_s$, $R_{\mathrm{C}}$ and $f$. The time $t_{\mathrm{VII}}$ for closing the auxiliary emanation source was 02 Feb 2015, 10:00 and was therefore fixed for the fit. The distillation process on the 12 Jan 2015 was initiated around 10:30 by slowly guiding 1.5 slpm into the column. The flow was carefully increased up to 4.85 slpm until 19:45. Due to this transition time, $t_{\mathrm{VI}}$ was chosen to be a free parameter. The re-circulation flow $F_{\mathrm{Xe}}$ was measured to be $(4.85 \pm 0.50)$ slpm, corresponding to an effective flow $f$ of $(3.070 \pm 0.331) \times 10^{-6}$ 1/s for a detector

inventory of $(158 \pm 5)$ kg during the second distillation run. This information was used to constrain the $\chi^2$-fit with a penalty term using the effective flow. The uncertainties of the measured flow as well as the inventory were chosen conservatively in order to give the fitting routine more allowed range, when fitting the model. Due to the fact, that the interface gas system and the column were bypassed during operation in phase IV the contribution from type 1 and type 2 sources is different in the following phases. Additionally, the distribution between both types is unknown. Therefore, no further assumption can be made for the fitting for $c1$ and $c2$. Only the rate increase after opening the auxiliary emanation source can be used to require a conservative lower limit of $c_s > 400\,\mu$Bq/kg for the fit. The fit results are summarized in table 7.1.

Table 7.1: Results of the constrained $\chi^2$-minimization fit during radon distillation phases V-VII to determine the reduction capability $R_C$ of the distillation column. Due to its asymmetric uncertainties, a lower limit is determined in figure 7.5.

| Parameter | Fit value |
|---|---|
| $t_{VI}$ | 12 Jan 2015 15:46 $\pm$ 1.5 hr |
| $t_{VII}$ | 02 Feb 2015 10:00 (fixed) |
| $c_1$ | (53 $\pm$ 4) $\mu$Bq/kg |
| $c_2$ | (20 $\pm$ 11) $\mu$Bq/kg |
| $c_s$ | (445 $\pm$ 48) $\mu$Bq/kg |
| $R_C$ | $(124^{+91}_{-64})$ |
| f | $(3.074 \pm 0.053) \cdot 10^{-6}$ 1/s |
| $\chi^2$/NDF | 38.37 / 29.00 |

The transition from source-only operation and the beginning of the distillation process was computed to be 12 Jan 2015 15:46 with an uncertainty of $\pm 1.5$ h. This is in agreement with the expected starting time.

The emanation of the type 1 sources, summarized in $c_1$, was found to be $(53 \pm 4)\,\mu$Bq/kg. This is larger than the total emanation rate of $(45.4 \pm 1.4)\,\mu$Bq/kg during the standard background operation mode in phase IV. This is an indication, that the interface gas system, not included in the circulation loop in phase IV, is indeed generating additional type 1 radon. One possible candidate is the second gas transfer pump (pump 2) behind the distillation plant, which was used to extract the purified xenon.

The type 2 sources were divided into the emanation by the auxiliary source $c_s = (445 \pm 48)\,\mu$Bq/kg and the rest of the type 2 sources, yielding $c_2 = (20 \pm 11)\,\mu$Bq/kg. Both parameters are highly correlated since both denote the same kind of emanation source. The distribution between $c_s$ and $c_2$ seems reasonable, when taking the increase in the activity concentration after opening the source into account.

The constrained effective flow was computed to be $(3.074 \pm 0.053) \times 10^{-6}$ 1/s, resulting into a re-circulation flow of $F_{Xe} = (4.86 \pm 0.18)$ slpm for a given detector mass of $(158 \pm 5)$ kg, in agreement with the measured circulation speed.

The best fit value for the reduction capability $R_C$ of the distillation system was found to be $124^{+91}_{-64}$ with a large asymmetric uncertainties. Therefore, the

$\chi^2$-distribution in dependence of $R_{\mathrm{C}}$ was analyzed around the minimum value $\chi^2_{\mathrm{min}}$, as visualized in figure 7.5, in order to get a better handle on the uncertainty. An asymmetric distribution can be observed, whereas the left side for lower

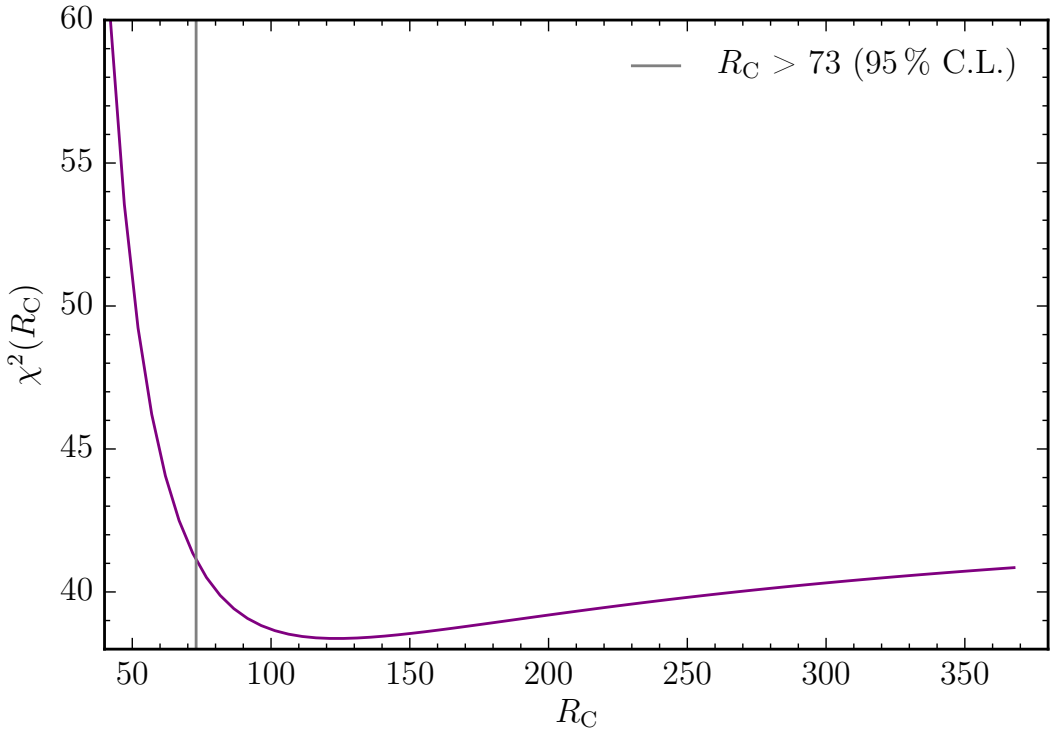


Figure 7.5: **The $\chi^2$ distribution in dependence of the reduction capability $R_{\mathrm{C}}$ around $\chi^2_{min}$:** The found distribution is asymmetric. Therefore, only a lower limit for the reduction is stated to be $> 73$ (95 % C. L.).

values of $R_{\mathrm{C}}$ is steep rising, while for increasing $R_{\mathrm{C}}$-values, the slope is much more flat. The flat slope is an indication that the fitting routine is not sensitive enough to probe higher reduction factors of the column. Therefore, only a lower limit for the reduction capability of

$$R_{\mathrm{C}} > 73 \quad (95\,\%\,\mathrm{C.\ L.}) \tag{7.13}$$

is stated. This limit corresponds to the value of $R_{\mathrm{C}}$ that results into $\chi^2_{\mathrm{min}} + 2.69$ of the $\chi^2$-distribution.

In [45, 100], a limit of $R_{\mathrm{C}} > 27$ (95 % C. L.) was stated, obtained without constraining the effective flow $f$, but only requiring $c_s > 400\,\mu\mathrm{Bq/kg}$. Consequently, a wider range for the flow was available within the fitting routine, allowing to push the flow to higher values, and thus, resulted into a lower reduction factor. In the scope of this thesis, it was decided to constrain in addition the effective flow, since the circulation speed $F_{\mathrm{Xe}}$ was well known from the calibrated flow controller of the distillation system.

The fit was repeated for fixed values of $R_{\mathrm{C}}$ of 10, 27, 73 and is compared to the best fit of 124 in figure 7.6 along with the respective normalized residuals. While the data is poorly described for $R_{\mathrm{C}} = 10$, the differences for $R_{\mathrm{C}} > 73$

are minor, especially visible with the help of the residuals during phase VII after closing the artificial source. Since the radon removal system is highly efficient for

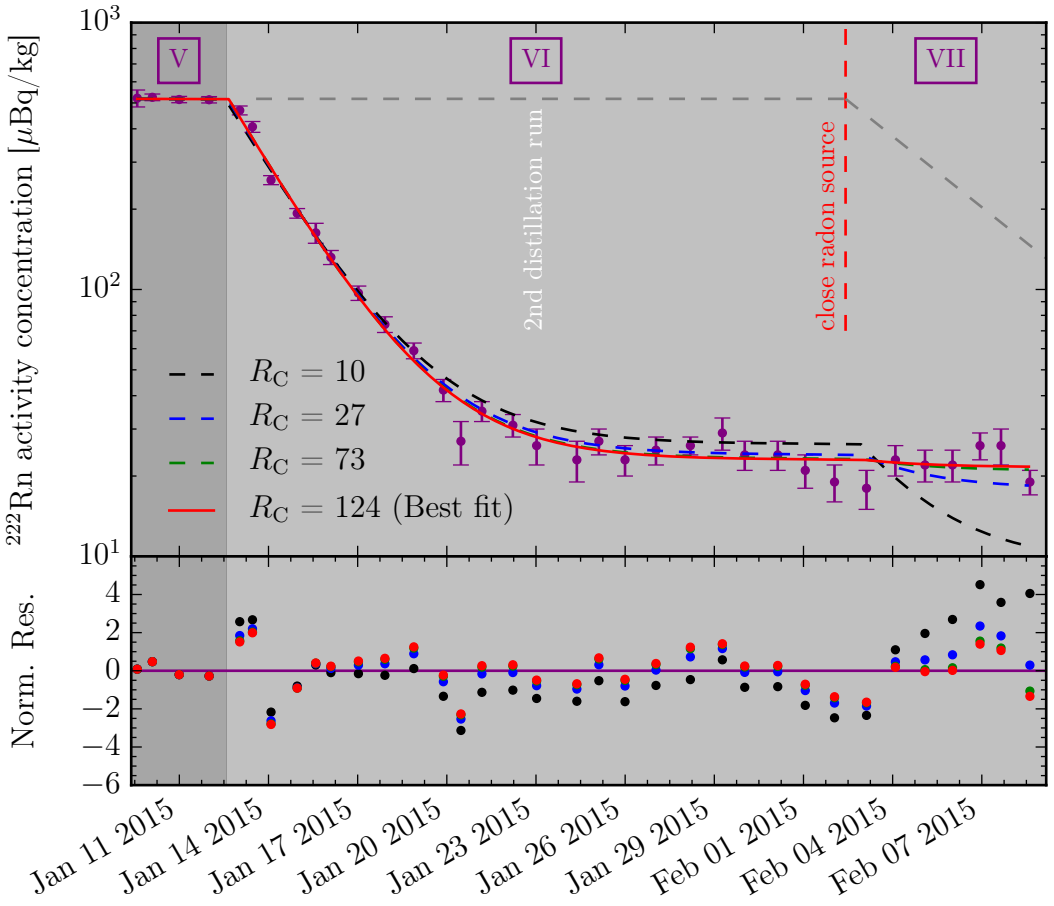


Figure 7.6: **Different fits and residuals for fixed values of $R_C$ during the second distillation run:** The data is poorly described for $R_C = 10$. The differences for $R_C > 73$ are minor, also visible in the residuals in the bottom panel, especially during phase VII after closing the artificial source. The grey dashed line indicates the expected evolution without the presence of a radon removal system.

type 2 sources, a stronger artificial source would be required in order to probe a higher reduction capability of the distillation system.

Another key parameter is the purification flow, as explained in section 7.1.1, the limiting factor for an efficient removal of radon from the innermost of the TPC. In the following, the expected reduction $r$ for the XENON100 experiment is investigated as a function of the purification flow $F_{Xe}$ and the reduction power $R_C$ of the distillation column by using the obtained fit results for $c_1$, $c_2$ and $c_s$. For that, $R_C$ and $F_{Xe}$ are assumed to be independent. The obtained results are visualized in figure 7.7. Furthermore, to compare experiments with different target masses, the purification flow can be transformed into the effective circulation rate $f$ for the given xenon inventory $V_{Xe}$. Following equation (7.6), the distillation is efficient, especially in the case of type 1 dominated systems, if $f$ is large compared to the $^{222}$Rn decay constant $\lambda_{Rn} = 2.1 \times 10^{-6}$ 1/s. Therefore,

the expected reduction $r$ in figure 7.7 is also shown as a function of $f/\lambda_{\mathrm{Rn}}$, indicated by the top axis. The reduction $r$ is calculated following equation (7.7)

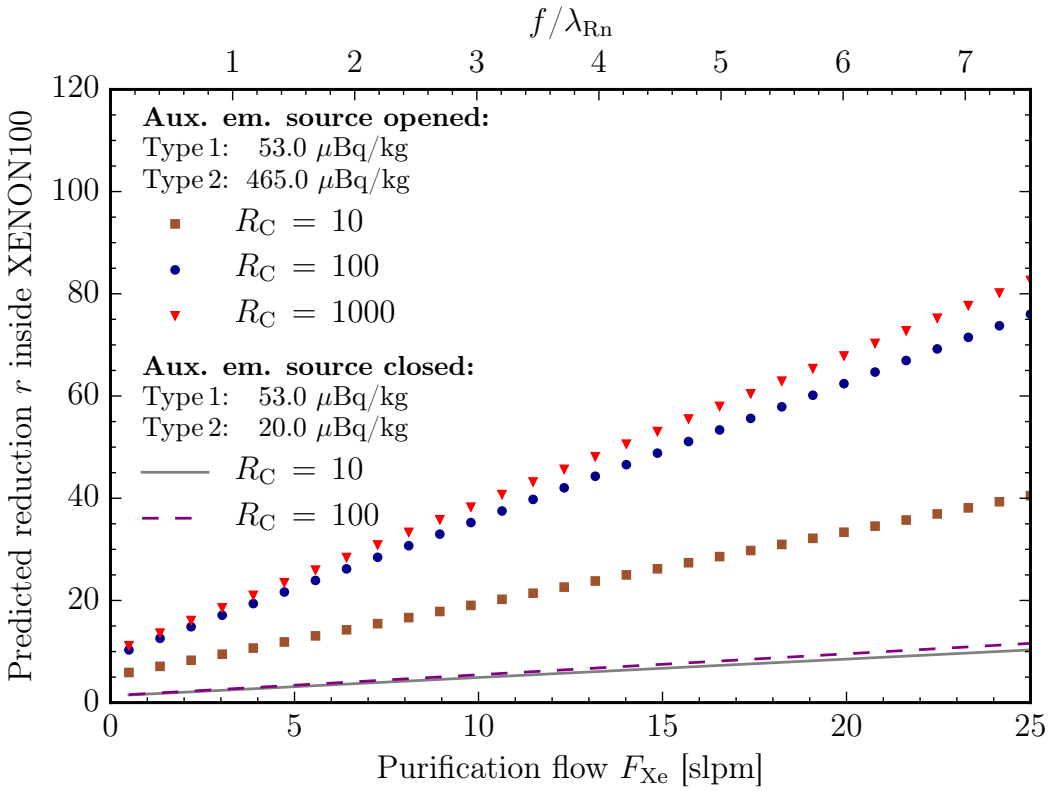


Figure 7.7: **Expected $^{222}$Rn reduction $r$ inside the XENON100 detector as a function of the purification flow $F_{\mathrm{Xe}}$:** The experiment is type 2 dominated, when the auxiliary emanation source is opened and type 1 dominated, when the source is closed. The radon removal system is more efficient for type 2 sources. The importance of a high purification flow for type 1 dominated systems in order to achieve a reasonable reduction $r$ can be observed. On the top axis, the corresponding ratio of the effective circulation rate $f$ over the $^{222}$Rn decay constant $\lambda_{\mathrm{Rn}}$ is shown, in order to directly compare the expected reduction $r$ to other experiments with different target masses.

for a scenario of a type 2 dominated system, as it was the case for the second distillation run by using the artificial source, as well as for the scenario of a type 1 dominated system, as it was the case during the first run. In the type 2 dominated case, the expected reduction $r$ yields a factor of about 76 for an increased purification flow of $F_{\mathrm{Xe}} = 25\,\mathrm{slpm}$ ($f/\lambda_{\mathrm{Rn}} = 7.5$) and a given $R = 100$. After closing the auxiliary source, resulting into $c_s = 0\,\mu\mathrm{Bq/kg}$, the XENON100 system changed into the standard dark matter search operation mode, type 1 dominated, as described before. For the same purification flow of $F_{\mathrm{Xe}} = 25\,\mathrm{slpm}$ ($f/\lambda_{\mathrm{Rn}} = 7.5$), the differences for $R = 10$ and $R = 100$ are minor, yielding a reduction $r$ between 10–12. Thus, a more efficient radon removal inside the XENON100 detector can be only achieved by a sufficiently large purification flow $F_{\mathrm{Xe}}$ for the given xenon inventory and, thus by a large ratio of $f/\lambda_{\mathrm{Rn}}$. This

is of crucial importance, when designing a radon distillation system for the large scale XENON1T or XENONnT experiments. Depending on the radon source composition of these next-generation detectors, the focus needs to be on a large process speed rather than an ideal removal capability $R_{\mathrm{C}}$.

### 7.1.5 HETP value

The height equivalent of one theoretical plate (HETP) for a radon in xenon mixture for the used package material type EX from Sulzer is unknown so far, but can be estimated by creating the McCabe-Thiele diagram with the parameters obtained from the second radon distillation run at XENON100. As described in section 3.1, the in-going mass flow $F$ is equal to the extraction flow $D$ at the top of the column, since no radon-enriched xenon is extracted at the bottom ($B = 0$). With the standard purification flow of XENON100 of 4.85 slpm, measured with the FC404 flow controller at the outlet of the column, as well as obtained from the fit, follows

$$F = D = 1.75\,\mathrm{kg/h}. \tag{7.14}$$

The inlet radon activity concentration can be determined to be 518 µBq/kg from phase V after opening the auxiliary emanation source, but before starting the second distillation run. This corresponds to a concentration of $c_F = 5.4 \times 10^{-23}$ mol/mol. Equation (7.2) in combination with the best fit value of $R_{\mathrm{C}} = 124$ yields the out-going concentration $c_D = 4.3 \times 10^{-25}$ mol/mol. By calculating the liquid xenon mass $M_{\mathrm{Xe,reboiler}}$ within the reboiler to be 3.4 kg during the second distillation run, the concentration in the bottom is computed to be $c_B = 3.6 \times 10^{-21}$ mol/mol, according to equation (3.16) in section 3.1. The evaporated xenon in the bottom, corresponding to the gaseous stream $V'$, is found to be 3.71 kg/h, calculated from an average heating power at the bottom of 95 W. In combination with the feed and extraction flow, as well as a gaseous feed ($q = 0$), the liquid and gaseous flows within the distillation system, as defined in section 3.1, can be determined as the following:

$$V = 5.46\,\mathrm{kg/h} \quad \text{and} \quad V' = 3.71\,\mathrm{kg/h}, \tag{7.15}$$

$$L = 3.71\,\mathrm{kg/h} \quad \text{and} \quad L' = 3.71\,\mathrm{kg/h}. \tag{7.16}$$

Consequently, the reflux ratio $R$ as defined in equation (3.8) at the top of the column, the ratio of the re-condensed xenon going back as liquid flow $L$ and the extracted purified flow $D$, can be concluded to be

$$R = \frac{L}{D} = 2.1, \tag{7.17}$$

while the reflux ratio $R'$ at the bottom of the system is infinity by definition in the case of radon distillation. Assuming a relative volatility of $\alpha = 0.1$ (see table 3.1), the resulting McCabe-Thiele diagram for the second radon distillation run at XENON100 is presented in figure 7.8.

In total, five theoretical plates $n_{\mathrm{TP}}$ can be drawn to meet the obtained parameters. With a length of $h = 110$ cm of the used package material inside the smaller modified column version, follows

$$\mathrm{HETP} = \frac{n_{\mathrm{TP}}}{h} = 22\,\mathrm{cm}. \tag{7.18}$$

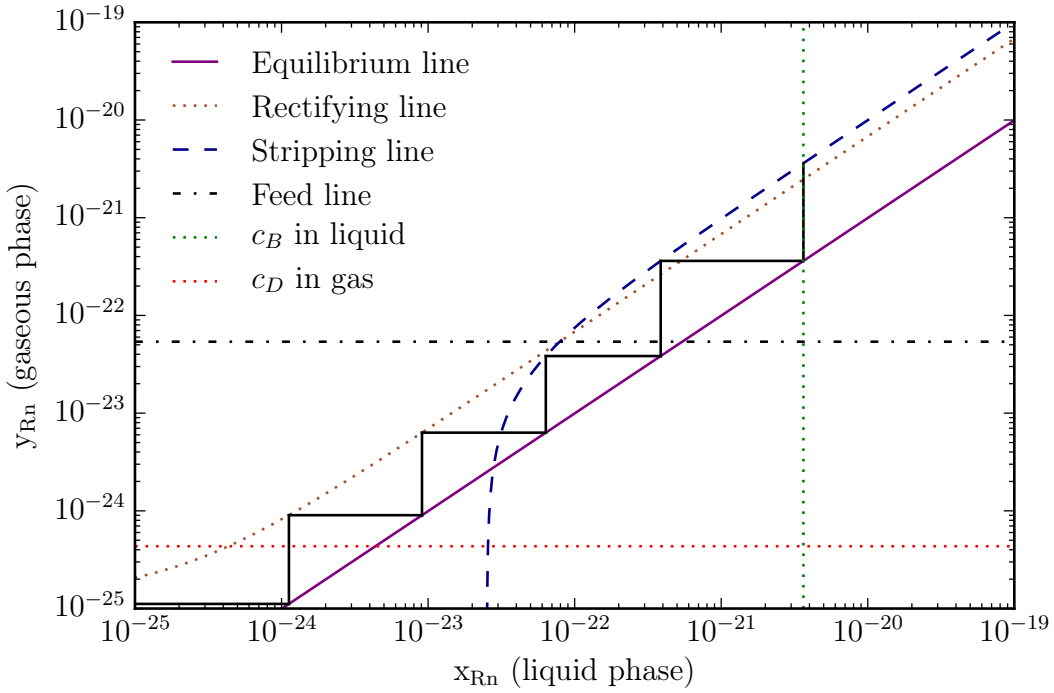


Figure 7.8: **McCabe-Thiele diagram for the second radon distillation run at XENON100:** In total, five theoretical stages are required to describe the distillation process resulting into a HETP value of 22 cm.

This is comparable to the results found for a krypton in xenon mixture. For the lower limit of the reduction capability $R_C = 73$, the corresponding diagram yields four required theoretical stages. With that, an upper HETP limit for the given system can be stated as

$$\mathrm{HETP_{Lim}} < 27.5\,\mathrm{cm}. \tag{7.19}$$

Overall, the online radon removal by cryogenic distillation was successfully demonstrated for the first time in the scope of this work. Following this campaign, the final Phase-2 distillation column was installed as a XENON1T subsystem. After the successful online krypton campaign, as presented in chapter 6, the column was modified and utilized as a radon removal system at XENON1T as well. This allowed further investigations on the reduction of the ultimate background radon, especially in perspective of the upcoming XENONnT experiment. This test is presented in the next section.

## 7.2 XENON1T

The XENON1T detector utilizes a total liquid xenon mass of 3200 kg with an active volume of 2000 kg inside the TPC. Due to the high stopping power of xenon for $\gamma$-radiation, intrinsic contaminants are the dominant source of ER background within a fiducial volume of 1000 kg. The krypton in xenon concentration was reduced by online distillation to $(360 \pm 60)$ ppq, as presented

in chapter 6. Therefore, the ultimate ER background in XENON1T is originating from $^{222}$Rn.

In order to develop radon mitigation strategies, the distribution of radon sources in the overall detector system needs to be known. Therefore, all system components were measured for their radon emanation rate [45, 102]. In XENON1T, the sources can be divided into three categories depending on their respective locations as depicted in figure 7.9.

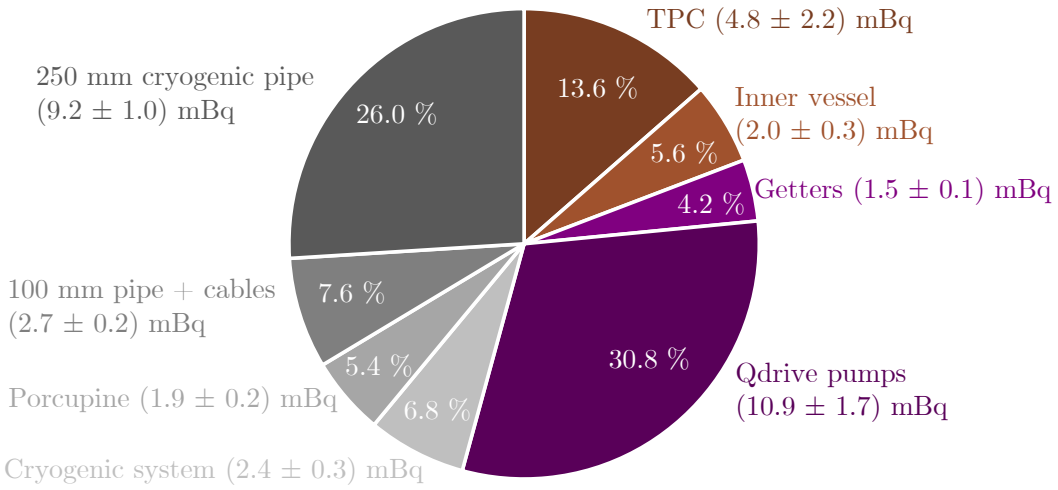


Figure 7.9: **Radon emanation sources in XENON1T:** The sources are separated by their location in the system. Sources within the cryostat are visualized in brown, sources within the cryogenic system grey and sources within the purification system are purple. The total emanation is $(35.4 \pm 6.0)$ mBq, resulting into an expected radon activity concentration of $(11.1 \pm 1.9)$ µBq/kg for a homogeneous radon distribution within 3200 kg of liquid xenon. Numbers taken from [45, 103].

The brown shaded pieces in figure 7.9 denote sources inside the cryostat such as the emanation from the inner stainless steel vessel ($(2.0 \pm 0.3)$ mBq) as well as the TPC components ($(4.8 \pm 2.2)$ mBq). As in XENON100, they are referred to as type 1 sources. They constitute 19.2 % of the total radon budget.

The grey shaded areas visualize the contribution from the cryogenic system ($(2.4 \pm 0.3)$ mBq) and parts attached to it. The porcupine ($(1.9 \pm 0.2)$ mBq) contains the PMT signal and high voltage cable feed-throughs. These cables are guided via the 100 mm-pipe ($(2.7 \pm 0.2)$ mBq) into the cryostat. The liquid and gas exchange between cryostat and the cryogenic system happens via the 250 mm diameter cryo pipe ($(9.2 \pm 1.0)$ mBq), one of the major contributors to the total radon budget. The grey shaded sources are referred to as type 1 sources since they are directly connected to the inner vessel. Therefore, no radon removal system can be installed in between cryogenic system and cryostat. The contribution is 45.8 %.

The purple shaded elements are sources within the purification system, namely the three QDrive pumps ($(10.9 \pm 1.7)$ mBq/kg) and the two getters ($(1.5 \pm 0.1)$ mBq). These sources can be referred to as type 2 since a radon removal system can be

installed in principle after the purification system and before the detector. The fraction from these sources is 35.0 %.

The total radon emanation is $(35.4 \pm 6.0)$ mBq, yielding an expected activity concentration of $(11.1 \pm 1.9)$ µBq/kg for a homogeneous radon distribution within the 3200 kg of liquid xenon. The average emanation was determined with the help of in-situ $\alpha$-spectroscopy to be $(13.5 \pm 0.2)$ µBq/kg [91], comparable to the expected value.

### 7.2.1 Mitigation strategy

One possibility to further reduce the radon induced background in XENON1T is the replacement of the three QDrives, the major contributors with 30.8 %. A magnetically coupled piston pump was developed in the Münster University in cooperation with the nEXO group at Stanford University and the nEXO/XENON group at Rensselaer Polytechnic Institute [70]. The special feature of the design is the complete isolation of the drive mechanism from the gas by magnetic coupling. The movement of a magnetic ring by a linear drive outside the cylindrical pump volume creates a movement of the magnetically coupled piston inside the cylinder. Consequently, contamination of the target material is prevented, since no lubricants of the drive are in contact with the gas. First tests showed that the new pump is capable of xenon flows up to 190 slpm with compressions of up to 1.9 bar such that it could replace the three QDrives. Additionally, all materials can be selected with respect to low radon emanation. Measurements yielded an emanation rate of $(0.33 \pm 0.06)$ mBq, a factor 33 lower than the QDrives. All details and performance measurements of the new pump are discussed in [70, 95]. The pump installation at XENON1T and the resulting radon reduction will be presented in [71]. The total radon budget of XENON1T can be lowered by at least 30 % by exchanging pumps.

Another possibility is the radon removal by cryogenic distillation, as presented in section 7.1. A possible scenario, where a distillation system would be installed in series with the purification system similar to XENON100 is discussed in the following. Here, a radon free pump is assumed to be installed behind the column in order push the xenon back to the cryostat.

Based on equations (7.5) and (7.7), the expected reduction $r_{\mathrm{Xe1T}}$ within the TPC in dependence of the purification flow $F_{\mathrm{Xe}}$ and the reduction capability $R_{\mathrm{C}}$ can be estimated for the given radon sources. The calculations are illustrated in figure 7.10 for $R_{\mathrm{C}} = 10$, $R_{\mathrm{C}} = 73$ and $R_{\mathrm{C}} = 1000$. Again, the effective circulation time $f$ depends on the total xenon inventory, and the expected reduction $r_{\mathrm{Xe1T}}$ can be expressed in units of $f/\lambda_{\mathrm{Rn}}$ for comparison to other experiments. In detail, the ratio $(f/\lambda_{\mathrm{Rn}})_{\mathrm{Xe100}} = 1.47$ is equivalent to a purification flow of about 100 slpm in XENON1T for the given xenon mass of 3200 kg. In this hypothetical scenario, a reduction $r_{\mathrm{Xe1T}} = 3.8$ can be estimated for $R_{\mathrm{C}} = 73$. The top axis in figure 7.10 indicates the ratios $f/\lambda_{\mathrm{Rn}}$ for the corresponding purification flows.

The modified Phase-1 distillation column (see section 7.1) featured a reduction capability greater 73. The separation efficiency of the larger Phase-2 system is likely to be higher. The maximum possible flow of 20 slpm ($f/\lambda_{\mathrm{Rn}} = 0.3$) of the distillation plant would result in a reduction $r_{\mathrm{Xe1T}} = 2.0$, assuming a conservative separation of 73 for the Phase-2 system. However, the difference for

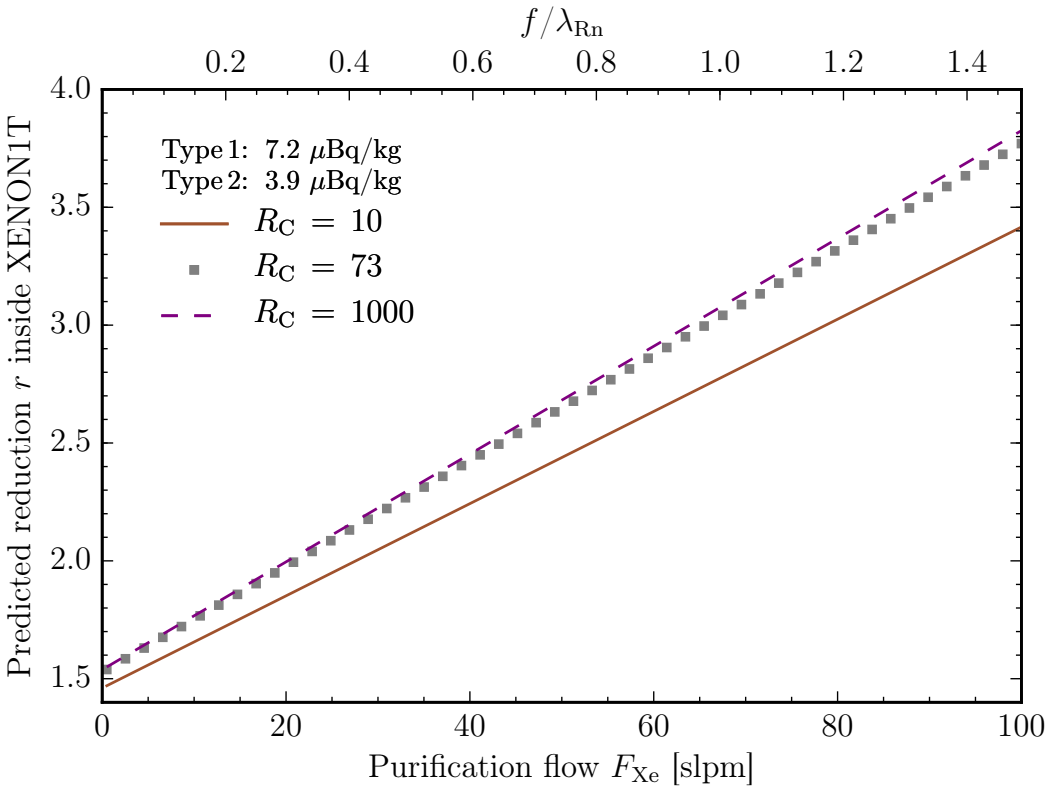


Figure 7.10: **Expected $^{222}$Rn reduction $r_{\mathrm{Xe1T}}$ inside the XENON1T detector as a function of the purification flow $F_{\mathrm{Xe}}$:** The XENON1T experiment is a type 1 dominated system. Therefore, a high purification flow is more important than a perfect radon removal. For comparison to other experiments, the ratio of the effective circulation rate $f$ over the $^{222}$Rn decay constant $\lambda_{\mathrm{Rn}}$ is indicated on the top axis.

$R_{\mathrm{C}} = 1000$ is minor. Additionally, the flow of 50 slpm ($f/\lambda_{\mathrm{Rn}} = 0.75$) during the two science runs at the purification system needs to be halved, resulting into a lower electron lifetime. Since the electron lifetime of about 610 µs was already lower than the time for one complete drift of about 700 µs, this scenario is not applicable.

For a hypothetical distillation system matching the flow of 50 slpm ($f/\lambda_{\mathrm{Rn}} = 0.75$), a reduction of $r_{\mathrm{Xe1T}} = 2.6$ could be achieved. However, the current distillation plant was not possible to be upgraded to higher flows in the time scope of XENON1T since it would require new condenser stations featuring larger cooling powers.

Therefore, a new idea was developed within this thesis: Instead of an operation in series, the krypton distillation system was operated in radon removal mode in parallel to the purification system via the same configuration as in the upgraded gas only operation during the online krypton removal, as presented in chapter 6.

### 7.2.2 Online removal

The new online radon removal method is based on the extraction of radon-enriched xenon from different parts of the cryogenic system. The radon should be removed before migrating into the liquid xenon and entering the TPC. Like that, the type 1 radon, depicted in grey in figure 7.9, would be turned into a type 2-like source.

The same three extraction ports as in the online krypton removal within the cryogenic system were exploited. One is connected to the gaseous xenon part of the 250 mm-diameter cryogenic pipe, one is connected with the porcupine, housing the cable feed-throughs, and one is split into three pipes that are installed to each of the cooling towers. Each of the three extraction points is equipped with a flow controller with a maximum flow of 1.25 slpm. For a radon extraction efficiency of 100 %, a fraction of 45.8 % from the total radon budget of XENON1T could be removed. The three lines are combined such that a summed flow of 3.75 slpm can be pushed to the inlet of the distillation plant (see also section 3.3.2 and chapter 6).

Since the radon accumulates in the reboiler in the bottom of the column and is trapped until disintegration, the purified xenon is extracted at the top. Therefore, the existing off-gas line was connected with the standard outlet pipe of the distillation system to allow a re-feeding to the inlet of the purification system. Due to the fact, that no xenon is lost in this process, no additional xenon needs to be filled into the cryostat in advance as it was the case for the online krypton removal. The main purification loop continues to operate in standard mode. A sketch of the process is illustrated in figure 7.11.

The online krypton removal finished on 12 Dec 2016. The remaining xenon was recuperated into the off-gas bottle, the column was warmed up, evacuated and pumped for three days in order to remove all trace amount of krypton before switching to radon mode.

The radon removal campaign was started on 19 Dec 2016 with the pre-cooling of the distillation plant. On 20 Dec 2016, the column was filled over the course of a few hours via the three extraction lines with xenon from the cryostat. Around 19:30, a circulation from the cryogenic system into the purification loop via the distillation column was established at 0.5 slpm. The flow was carefully increased to the operation speed of 3.75 slpm at around 19:40. As explained in section 3.3.2, the gas flow was achieved by pressure differences between the subsystems such that no additional pump was required.

In parallel to the removal campaign, a $^{220}$Rn calibration for the ER band [101] was performed from 19 Dec 2016 until 3 Jan 2017. A major earthquake near the LNGS on 18 Jan 2017 stopped the data taking and the science run 0 was forced to be ended. The distillation operation was continued, but no meaningful data could be taken. Therefore, the campaign was stopped on 2 Feb 2017, the xenon was transferred back into the cryostat and the science run 1 was started after the inspection of all critical subsystems.

After the krypton removal, $^{222}$Rn is the dominant background source, as visualized in figure 6.18. Therefore, the event rate inside the detector should change with changing $^{222}$Rn-level. The evolution of the event rate before and during the radon distillation campaign is visualized in figure 7.12. The same

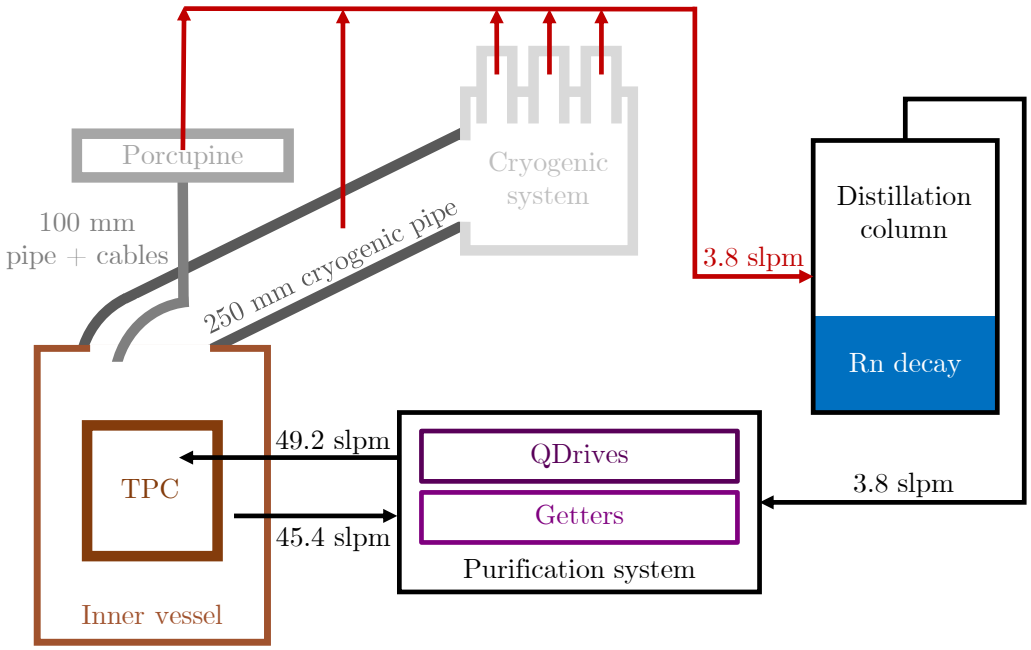


Figure 7.11: **Online radon removal in XENON1T:** The idea is to extract radon from the GXe reservoir before entering the LXe phase. Gas is extracted at a flow of 3.8 slpm from the porcupine, the cryogenic pipe, and at the three cooling towers at the cryogenic system (red arrows) and is guided to the distillation column. From here, radon-free xenon is extracted from the top and is fed back to the purification system at 3.8 slpm. This is a xenon-loss free operation, as radon disintegrates in the reboiler. The normal purification cycle operates in standard mode. The different radon contributors are visualized in their respective color, as shown in figure 7.9.

data selection criteria as in section 6.2.3 were applied.

The event rate before the radon removal was assumed to be constant and was fitted to be $(2.88 \pm 0.26) \times 10^{-4}$ events/(keV · kg · day) from 12 Dec 2016 until 18 Dec 2016. During the ER band calibration from 19 Dec 2016 until 3 Jan 2017, low energy events were introduced by β-decays from the $^{220}$Rn decay chain. Therefore, the background event rate was swarmed with additional events in the selected fiducial volume and energy interval. Consequently, the data could not be used to monitor the radon removal evolution at the beginning. However, a lower constant plateau was fitted to be $(2.28 \pm 0.17) \times 10^{-4}$ events/(keV · kg · day) from 3 Jan 2017 until 18 Jan 2017. Due to the earthquake on 18 Jan 2017, the data taking was stopped and the evolution after stopping the distillation process could not be monitored. Additionally, the detector conditions as well as the PAX version changed for the new science run 1. Therefore, the expected increase after the distillation process is not presented here. This investigation will be shown in [90].

By comparing the lower event rate during distillation to the higher rate from before the campaign, the reduction in the background rate can be calculated using the monte carlo simulation tool: In each step, the lower plateau value $c_L$ is ran-

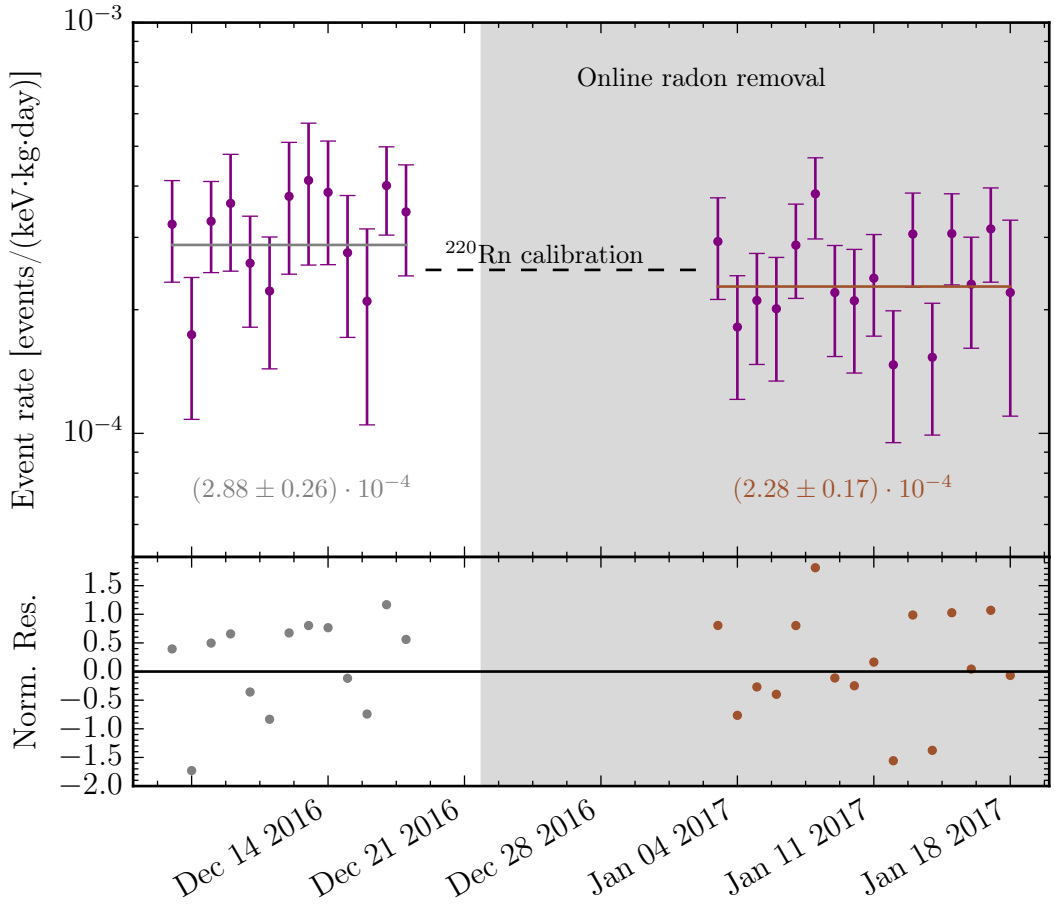


Figure 7.12: **ER event rate before and during online radon removal:** The two plateaus before (grey) and during (brown) the online radon distillation (grey shaded area) indicate a reduction by about 20 %. A $^{220}$Rn ER band calibration (black, dashed) was performed in parallel at the start of the distillation. This did not allow to monitor the evolution during this period.

domly created based on a normal distribution with $\mu = 2.28 \times 10^{-4}$ events/(keV · kg · day) and $\sigma = 0.17 \times 10^{-4}$ events/(keV · kg · day), as well as the higher level $c_{\mathrm{H}}$ with $\mu = 2.88 \times 10^{-4}$ events/(keV · kg · day) and $\sigma = 0.26 \times 10^{-4}$ events/(keV · kg · day) from before the campaign. The reduction $r$ in percent can then be calculated with

$$r = (1 - \frac{c_{\mathrm{L}}}{c_{\mathrm{H}}}) \cdot 100. \tag{7.20}$$

The distribution of $10^8$ generated reduction factors $r$ yields a decrease by $(20.8^{+8.8}_{-10.1})\%$.

Another way to check for the reduction is the in-situ $\alpha$-spectroscopy using the isotopes $^{222}$Rn and $^{218}$Po as well as the delayed coincidence analysis of $^{214}$BiPo-events. The details of both methods will be presented in [91]. Additionally to the level before and during the radon removal campaign, a plateau value during SR1 was determined. The found plateau values for each case are taken from [91] and are summarized in table 7.2. By comparing the different plateaus, an averaged

Table 7.2: Plateau values before, during and after radon distillation at XENON1T from in-situ $\alpha$-spectroscopy ($^{222}$Rn and $^{218}$Po) and $^{214}$BiPo delayed coincidence analysis. Numbers taken from [91].

| Period | $^{222}$Rn [µBq/kg] | $^{218}$Po [µBq/kg] | $^{214}$BiPo [µBq/kg] |
|---|---|---|---|
| Before distillation | 13.6 ± 0.9 | 12.4 ± 0.8 | 5.1 ± 0.5 |
| During distillation | 11.4 ± 0.7 | 10.4 ± 0.7 | 4.1 ± 0.3 |
| After distillation | 13.3 ± 0.7 | 12.6 ± 0.8 | 5.1 ± 0.5 |

reduction by $(15.2^{+7.0}_{-7.6})\%$ can be obtained from $^{222}$Rn, an averaged reduction by $(16.8^{+7.4}_{-8.1})\%$ from $^{218}$Po, whereas the BiPo analysis yielded an averaged decrease by $(19.6^{+9.1}_{-10.7})\%$. All three numbers are in agreement within their uncertainties and confirm the results from the event rate calculations.

In summary, the reduction found confirms that the new online radon removal method is working. The cryogenic system and its connected parts contribute about 46 % to the total radon budget. About half of these contributions could be removed, yielding an extraction efficiency of only about 50 %. At the moment, one limiting factor of the process are the three flow controllers at the extraction points. By installing controllers with higher possible flows, the extraction efficiency might be further enhanced. However, a new pump would have to be installed between the cryogenic and distillation system to achieve higher flows. In order to test also the extraction efficiency for the different locations, a new campaign could be started, where only one flow controller is operated at a time at different flows. For this kind of test, the detector conditions should stay the same without calibration runs in parallel for a better monitoring, especially of the evolution just after the distillation start. The new method is also applicable for the next-generation experiment XENONnT as the major components stay the same.

# Summary and Outlook 8

Several independent observations yield evidence for the existence of dark matter. Common candidates are Weakly Interacting Massive Particles, whose direct detection by scattering off xenon nuclei in a dual-phase time projection chamber is the goal of the XENON Dark Matter Project. The currently operating XENON1T experiment, located at Laboratori Nazionali del Gran Sasso in Italy, utilizes 3.2 tonnes of liquid xenon, of which about 2 tonnes are inside the TPC. Its science runs between November 2016 and February 2018 did not yield evidence for dark matter interactions within the 1 tonne × yr exposure. It set the most stringent limits on the spin-independent scattering cross section of a WIMP on nucleons for WIMP masses above $6\,\mathrm{GeV/c^2}$ with a minimum of $4.1 \times 10^{-47}\,\mathrm{cm^2}$ for $30\,\mathrm{GeV/c^2}$ WIMPs (90 % C. L.). To achieve this, a low electronic recoil background level of $(2.24^{+0.23}_{-0.12}) \times 10^{-4}\,\mathrm{events/(keV \cdot kg \cdot day)}$ was a key requirement.

In such large detector volumes, intrinsic radioactive isotopes within the liquid xenon, namely $^{85}$Kr and $^{222}$Rn, are the main background source and generate WIMP-like signals in the region of interest via β-decays, as discussed in section 2.3. In contrast to external radiation, fiducialization does not shield against the homogeneously distributed radioactive noble gases. The β-decay of anthropogenic $^{85}$Kr features an endpoint energy of 687 keV and a half-life of 10.76 y. Therefore, the $^{\mathrm{nat}}$Kr level has to be reduced to the order of 200 ppq once before the dark matter search. Starting from a few ppb of natural krypton in commercially acquired xenon, a reduction by a factor of $10^4$–$10^5$ is needed. This can be achieved through cryogenic distillation that exploits the difference in vapour pressure between krypton and xenon. To reach such high separation factors, a multi-stage package column was built, which can be modeled as a series of connected theoretical distillation stages. As evaluated in chapter 3 with the common McCabe-Thiele method, 9 to 10 of these stages are required to meet the XENON1T design values. The same principle can be applied for radon removal. As the radon is trapped until disintegration at the bottom of the column, the method was modified, allowing for the design of a potential radon distillation column for XENONnT.

One main focus of this thesis was the upgrade from the smaller Phase-1 to the final Phase-2 column. The major improvements were an elongated package tube of 2.8 m and an optimized gas collection efficiency of the two condenser stations. This enabled the processing of xenon with a high content of impurities other than krypton. Furthermore, it allows the XENON collaboration to purchase

higher contaminated xenon, reducing the price significantly. This is important as the major cost of XENON1T and the upcoming XENONnT originates from the xenon itself.

The integration into XENON1T allows for the operation of the column in offline and online distillation modes, giving access to a variety of applications. In the offline mode, xenon is transferred from one subsystem into another via the column. In the case of online distillation, the gaseous phase of the detector can be purified while the standard purification loop is operating in parallel.

The characterization of the Phase-2 system was the topic of chapter 4. The thermodynamic stability was discussed for a three day offline distillation from bottles into ReStoX. Here, the column was operated at design values: a pressure of 2 bar and a flow of 8.5 slpm (3.1 kg/h). At the same time, the krypton-enriched off-gas was extracted at a flow of 1 % of the feed flow, while 99 % of the feed were leaving the column as purified xenon. A reflux ratio of $R = 152$ at the top was calculated, which is sufficiently high for a good separation efficiency. In other offline distillation runs, stable operation at up to 18.5 slpm (6.7 kg/h) was achieved. This is more than a factor of two higher than the initial design value. Additionally, the stability during an online distillation of the detector over the span of 46 days was discussed. This was the longest operation of the distillation plant so far. It was operated at a pressure of 1.55 bar and a flow of 3.7 slpm (1.3 kg), resulting in a reflux ratio between 226 and 317. This shows the large variability of the Phase-2 system for applications beyond design.

The key properties of a distillation system are the reduction capability and the purified output concentration $c_B$. For the Phase-2 system, a reduction between inlet and outlet of $\mathrm{F_{red}} = (6.4^{+1.9}_{-1.4}) \cdot 10^5$ was measured, featuring outlet concentrations of

$$c_B < 48\,\mathrm{ppq} \quad (90\,\%\,\mathrm{C.L.}). \tag{8.1}$$

Here, the only limitation was the sensitivity of the RGMS during the measurements. This value is comparable to the lowest ever measured concentration of less than 26 ppq from Phase-1 and is about a factor four better than required for XENON1T. From the reduction factor, the output concentration and the required number of theoretical stages, the Height Equivalent for One Theoretical Plate was estimated to be 27 cm, which is significantly higher compared to the value of 15 cm stated by the Phase-1 column. One explanation could be that the description by the McCabe-Thiele method might reached its limit to be applicable for ultra-low concentrations. Another possibility could be that the measured sample with a concentration of $(730 \pm 140)$ ppq, which was used to create the McCabe-Thiele diagram, was contaminated during the extraction. However, the separation capability along with the resulting purity are unmatched world-wide and outperform the XENON1T requirements.

Cryogenic distillation was also applied for the helium removal from the ReStoX gas phase before initial filling of the XENON1T cryostat, as presented in chapter 5. The helium concentration was measured to be $c_{\mathrm{He,GXe}} = (66 \pm 2)$ ppm. The helium can potentially migrate into the evacuated housing of the PMTs and decrease their lifetime. Therefore, the gas phase of ReStoX ($\mathcal{O}(38\,\mathrm{kg})$ of xenon) was continuously cycled through the distillation column at a flow of 8.9 slpm (3.2 kg/h). The operation was approximated with an ideal online dis-

tillation model based on gas kinetics in a single liquid-gas interface. Samples were extracted and analyzed in terms of helium as well as krypton. Both concentration evolutions in time were successfully fitted with the model. It was found that the distillation column features a helium separation factor greater than 144 (90 % C.L.). This has to be interpreted as conservative lower limit as the sensitivity of the on-site RGA was a limiting factor. A helium reduction of $r_{He} = 120.9^{+11.5}_{-10.0}$ inside ReStoX was measured with the on-site RGA system after 4 days of operation. Furthermore, the fit revealed that helium is enriched by a factor of $439.9 \pm 33.7$ in the GXe phase with respect to the LXe phase in ReStoX.

Based on these results, a novel online distillation operation for the purification of the detector was developed in the scope of this thesis, while the TPC was filled and operational. This was outlined in chapter 6. As for ReStoX, the basic concept is a continuous purification of the 21.5 kg xenon in the gaseous phase of the detector in a closed loop. With this method, krypton is removed from the liquid reservoir by migration into the gas, as the krypton particle balance between the two phases is disturbed. Three different online distillation modes were tested: In the initial operation (liquid+gas), the online distillation was tested without any hardware modification of the global system. Here, a xenon mixture from the liquid and gas phase was extracted and processed by the distillation column. For the second test, the main purification loop was stopped and only gaseous xenon was distilled (gas only). After this, the global system was modified such that the xenon from the gaseous reservoir could be processed directly by the distillation column in parallel to the main purification loop (upgraded gas only). An online krypton removal model was developed that can describe the krypton change inside the gas as well as liquid at any given time in XENON1T based on the different detector operation modes, including periods with and without distillation. The krypton evolution was monitored with samples for the Residual Gas Analyzer as well as the Rare Gas Mass Spectrometer systems and by analyzing the electronic recoil event rate inside the TPC.

The novel method efficiently reduced the krypton concentration in xenon to the lowest level ever achieved in a dark matter detector. A confirmed concentration of $(360 \pm 60)$ ppq was achieved within 70 days of distillation, starting at around 3 ppb in the combined mixture of the GXe and LXe reservoir. This allowed for the initiation of the first XENON1T dark matter search two months earlier than with the standard distillation operation and allowed for taking over the leadership in the extremely competitive field of direct dark matter detection. Additionally, the method gives the possibility to further reduce the krypton induced background at any given time in XENON1T if a lower concentration is required without removing the xenon from the detector. In the last part of the chapter, the model was successfully fitted to the data revealing that the main drivers of the krypton removal from the fiducial volume are the evaporation and extraction flow. By increasing these flows, the online distillation can be further optimized.

A potential application of the online removal is the usage of light radioactive noble gases as new calibration sources. For example, the isotope $^{37}$Ar allows

to calibrate the TPC down to an energy of 2.8 keV via electron capture, but features a half-life of 35 d, which is too long to let it decay before initiating the dark matter search. However, with the distillation column it can be removed on a faster timescale. This can be predicted with the new model as well and will be tested at the very end of XENON1T's operation.

After the removal of krypton, the dominant background source in XENON1T originates from the decay of the noble gas $^{222}$Rn with a half-life of 3.8 days. In the scope of this thesis, the first successful radon removal operation using a cryogenic distillation column was demonstrated at XENON100, the predecessor of XENON1T. The details of these tests were introduced in chapter 7. A smaller modified Phase-2 column was connected to the XENON100 circulation loop via an interface gas system. This allowed for the purification at the full XENON100 flow of 4.85 slpm (1.75 kg/h) in series through the column. Two distillation runs were performed using an artificial radon source in front of the distillation plant in the second run. The XENON100 TPC acted as a radon monitor to measure the reduction over time. In the first run, an overall reduction inside the TPC of $r_{III} = 2.0 \pm 0.2$ was found, while in the second run with an opened artificial source the reduction was $r_{VI} = 22.4 \pm 0.8$. By modeling the ingoing and outgoing radon fluxes of the TPC, the reduction capability of the distillation column was determined from the second run to be

$$R_{\mathrm{C}} > 73 \quad (95\,\%\,\mathrm{C.\ L.}). \tag{8.2}$$

A McCabe-Thiele diagram was generated for the given conditions yielding the requirement of 4 theoretical distillation stages. With that, an HETP value of $\mathrm{HETP}_{\mathrm{Lim}} < 27.5$ cm was estimated. This information is of crucial importance for the design of a future radon column, as it is required to estimate the total height of the package tube. Based on the developed model, the expected reduction $r$ inside the TPC was computed for different purification flows $F_{\mathrm{Xe}}$ and reduction factors $R_{\mathrm{C}}$ of the column. For a better comparison between different experiments, the dependence can be expressed in units of $f/\lambda_{\mathrm{Rn}}$, the effective circulation rate $f$ over the $^{222}$Rn decay constant $\lambda_{\mathrm{Rn}}$. As discussed in section 7.1.4, the distillation is efficient if $f$ is large compared to $\lambda_{\mathrm{Rn}}$. Especially in systems where most of the radon is generated inside the TPC, such as XENON100, the purification flow (a large ratio of $f/\lambda_{\mathrm{Rn}}$) is more important than a perfect removal system. In order to reach the XENON100 value of $(f/\lambda_{\mathrm{Rn}})_{\mathrm{Xe100}} = 1.47$ in XENON1T, a purification flow of about 100 slpm through the column for an inventory of 3200 kg is required.

As this was not possible with the Phase-2 column, another mitigation strategy was developed in this thesis: The idea is to extract radon from the gaseous part of the cryogenic system and its connections before it migrates into the liquid. The reduction in XENON1T was monitored with the ER event rate in the TPC. A decrease during the distillation by $(20.8^{+8.8}_{-10.1})\%$ was found. This was confirmed by an independent in-situ $\alpha$-spectroscopy. The cryogenic system and its components contribute about 46 % to the total radon budget in XENON1T. About half of these contributions could be removed, yielding an extraction efficiency of about 50 %. This efficiency might be enhanced by changing the flow controllers at the cryogenic system and by adding a pump to further increase the extraction flows.

For the upcoming XENONnT experiment, a krypton concentration of 100 ppq and a radon activity concentration of 1 µBq/kg are required. In terms of krypton removal, the Phase-2 distillation system is able to provide the required purity. One scenario is to process the additional 5 tonnes of xenon in a standard offline distillation from bottles into the new storage system ReStoX-II for XENONnT. Then, the new gas can be mixed with the already purified 3.2 tonnes of XENON1T. After filling the XENONnT detector, the krypton can be further reduced to the desired level via the presented online distillation mode.

In terms of radon, all components are screened for their radon emanation before the assembly of XENONnT. In the next step, components with high radon emanation, such as the QDrive pumps, need to be exchanged. Finally, a cryogenic distillation column can be used to further reduce the radon background. The Phase-2 distillation plant will not be used for radon removal. Instead, a high-throughput radon distillation system is being developed based on the results of this thesis. The basic design of such a column is briefly discussed here as an outlook.

Following equation (7.6), the reduction of sources inside the TPC with a perfect removal system is limited by the effective circulation $f$. A reduction of the inner sources of a factor of 2 can be achieved for $f/\lambda_{\mathrm{Rn}} = 1$, while a reduction of a factor of 3 is reached for $f/\lambda_{\mathrm{Rn}} = 2$. For the given inventory of XENONnT of about 8 t, these ratios require purification flows of $F_{\mathrm{Xe}} = 170$ slpm (60 kg/h) and $F_{\mathrm{Xe}} = 340$ slpm (120 kg/h), respectively. Therefore, the new system features a throughput of 200 slpm at an operation pressure of 2 bar with the possibility to upgrade it later on. As the radon is trapped in the reboiler, the goal is to reach an enrichment factor of 1000 between the feed and bottom concentrations. This avoids leakage of radon particles from the bottom to the top. Additionally, the operation is loss-less with regard to xenon, as no off-gas is extracted. A depletion of radon at the top with respect to the feed of 100 is large enough to achieve a sufficient reduction in the detector, as it was shown in figures 7.7 and 7.10 for XENON100 as well as XENON1T. The reflux ratio $R$ was chosen to be 0.5 in order to reduce the required cooling power at the top, while keeping the number of theoretical stages low. With an activity concentration of 10 µBq/kg, a McCabe-Thiele diagram can be computed yielding 6-7 required stages. This diagram (figure 3.3) along with all parameters and the determination of $R$ was discussed in section 3.1. Together with the upper limit on the HETP-value of 27.5 cm, obtained from the second distillation run at XENON100 in section 7.1.5, a total height of the new package tube of about 150 cm is calculated for 7 stages.

In XENONnT, a liquid xenon purification loop is developed for a faster removal of electronegative impurities at flows of up to 5 liters of liquid xenon per minute (900 kg/h). A fraction of this liquid will be passed to the new radon distillation column, which will be located at the top floor of the current service building. The outlet of the column should be in liquid form as well. From this, the total required cooling and heating power can be calculated. As the xenon enters in liquid, no input condenser is used, as it was the case for the krypton column. At the top, a cooling power of about 1 kW is needed to achieve a reflux ratio of 0.5. Additionally, the gaseous radon-depleted xenon flow of 200 slpm (72 kg/h) has to be liquefied and sent back to the LXe purification loop. This requires a cooling

power of about 2 kW. Additionally, a heating power of about 3 kW at the reboiler evaporates 300 slpm of xenon to establish a stable distillation process. The total cooling power of about 3 kW is about a factor 9 larger compared to the krypton column and cannot be achieved by using cold-heads with only 250 W each. In order to reach such large cooling powers, either a industrial cooling machine or liquid nitrogen have to be used. It was decided to use liquid nitrogen, as it gives the possibility to easily scale up the throughput and it is more cost-efficient in the long run. Furthermore, a 30 kt nitrogen tank is already available next to XENON1T/XENONnT. For 3 kW of cooling, a nitrogen consumption of 1300 kg/d can be calculated. In order to reduce the required cooling power, a design was created where the reboiler doubles as a heat exchanger. A scheme of the design and a first CAD model are visualized in figure 8.1 along with the respective flows in the system.

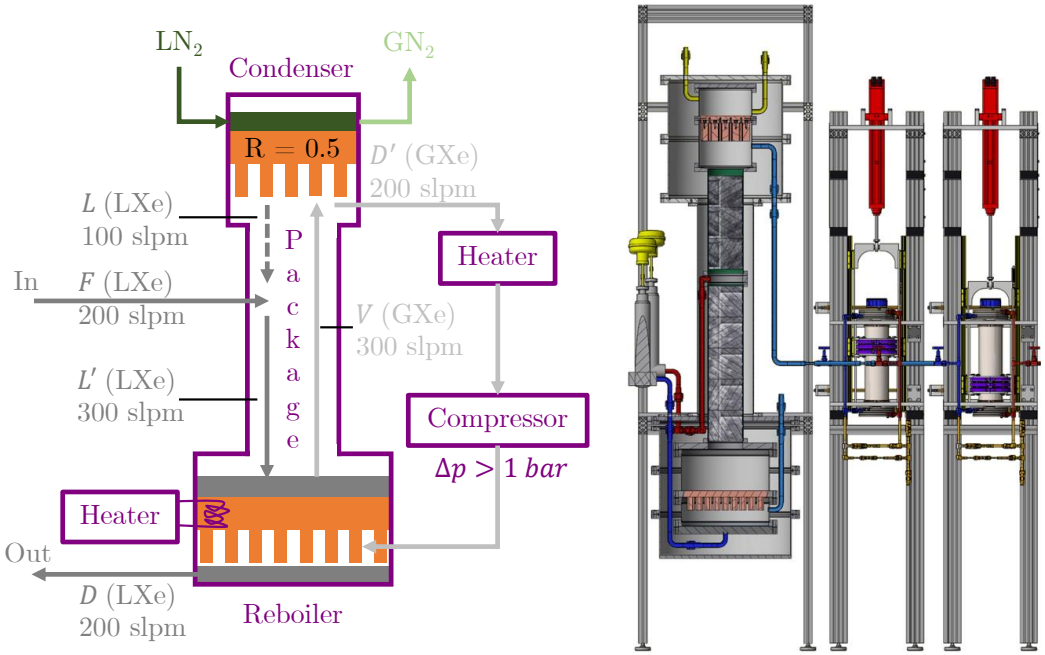


Figure 8.1: **Design and CAD drawing for a radon distillation column for XENONnT:** The new system consists of one condenser station at the top and and one at the bottom. While the top condenser is operated with liquid nitrogen, the reboiler at the bottom doubles as a heat exchanger. In this manner, the external applied cooling power is reduced from 3 kW to 1 kW. The heat exchanger only works if a high-purity, high-flow pump compresses the gaseous xenon coming from the top to achieve a pressure difference between the two phases. The purification speed is 200 slpm at an operating pressure of 2 bar with a radon reduction of 100 between feed and outlet at the top. CAD drawing by C. Huhmann.

In total, two condenser stations are required - one at the top and one at the bottom. The top condenser consists of two chambers connected via oxygen-free copper with fins, similar to the krypton column condensers, and is used to introduce a reflux to the system. Liquid nitrogen is injected on the top chamber

of the condenser, cooling the xenon on the other side of the copper. By regulating the flow of the liquid nitrogen, variable cooling powers can be achieved. The reboiler at the bottom is a condenser as well. Here, radon-depleted gaseous xenon is liquefied in the bottom chamber, while liquid xenon in the top chamber is evaporated. As the liquid in the reboiler is highly radon-enriched and the gas is highly radon-depleted, both reservoirs are only thermally in contact via a copper plate with fins. For an efficiency of 100 %, no additional cooling by liquid nitrogen needs to be applied, and the total external cooling power can be reduced to 1 kW. This reduces the nitrogen consumption to 440 kg/d. However, in order to make the heat exchanger work, a pressure difference between the two phases needs to be established. This can be achieved by a radon-free compressor that needs to be able to handle flows of up to 200 slpm and provide pressure compressions greater than 1 bar. A multi-cylinder magnetically-coupled piston pump based on the prototype in [70, 95] is under developed. This pump can be operated in a multi-stroke engine mode to achieve high and stable flows without radon emanation. As the gaseous xenon from the top of the column is at a temperature of about −100 °C, it needs to be warmed up by additional heating to room temperature, as the pump will operate outside the insulation vacuum.

The online radon removal technique, presented in section 7.2.2 for XENON1T, where radon is extracted from the gaseous part of the cryogenic system and its connections, will be applied in XENONnT as well. The xenon will be directly guided to the inlet of the new radon distillation column. With the help of an additional pump, flows of up to 20 slpm will be achieved for higher extraction efficiency from the cryogenic system. The additional cooling power required to liquefy the incoming gas is small compared to the overall cooling power.

In summary, the Phase-2 krypton distillation column, which was built, characterized and operated in a novel online removal mode in this work, in combination with the new radon distillation column, based on the demonstrated radon removal capabilities of cryogenic distillation in this thesis, will help to achieve the required ER background rate for an unprecedented sensitivity of XENONnT to potentially discover the ever elusive dark matter.

# Bibliography


[1] G. Hinshaw *et al.*, *Nine-year Wilkinson Microwave Anisotropy Probe (WMAP) Observations: Cosmological Parameter Results*, The Astrophysical Journal Supplement Series **208** (2013) (2), p. 19

[2] Planck Collaboration, *Planck 2013 results. I. Overview of products and scientific results*, A&A **571** (2014), p. A1

[3] Planck Collaboration, *Planck 2015 results - XIII. Cosmological parameters*, A&A **594** (2016), p. A13

[4] A. Einstein, *Lens-like action of a start by the deviation of light in the gravitational field*, Science **84** (1936) (2188), pp. 506–507

[5] F. Kahlhoefer, K. Schmidt-Hoberg, M. T. Frandsen and S. Sarkar, *Colliding clusters and dark matter self-interactions*, Monthly Notices of the Royal Astronomical Society **437** (2014) (3), pp. 2865–2881

[6] D. Clowe, M. Bradač, A. H. Gonzalez *et al.*, *A Direct Empirical Proof of the Existence of Dark Matter*, The Astrophysical Journal Letters **648** (2006) (2), p. L109

[7] D. Harvey, R. Massey, T. Kitching, A. Taylor and E. Tittley, *The nongravitational interactions of dark matter in colliding galaxy clusters*, Science **347** (2015) (6229), pp. 1462–1465

[8] K. G. Begeman, A. H. Broeils and R. H. Sanders, *Extended rotation curves of spiral galaxies: Dark haloes and modified dynamics*, Mon. Not. Roy. Astron. Soc. **249** (1991), p. 523

[9] P. van Dokkum *et al.*, *A galaxy lacking dark matter*, Nature **555** (2018) (7698), pp. 629–632

[10] M. Milgrom, *A Modification of the Newtonian dynamics as a possible alternative to the hidden mass hypothesis*, Astrophys. J. **270** (1983), pp. 365–370

[11] J. P. Ostriker and P. Steinhardt, *New Light on Dark Matter*, Science **300** (2003) (5627), pp. 1909–1913

[12] S. D. M. White, C. S. Frenk and M. Davis, *Clustering in a neutrino-dominated universe*, Astrophys. J. **274** (1983), pp. L1–L5

[13] G. Bertone, D. Hooper and J. Silk, *Particle dark matter: Evidence, candidates and constraints*, Phys. Rept. **405** (2005), pp. 279–390

[14] K. N. Abazajian *et al.*, *Light Sterile Neutrinos: A White Paper* (2012)

[15] G. Jungman, M. Kamionkowski and K. Griest, *Supersymmetric dark matter*, Phys. Rept. **267** (1996), pp. 195–373

[16] J. L. Feng, *Dark Matter Candidates from Particle Physics and Methods of Detection*, Ann. Rev. Astron. Astrophys. **48** (2010), pp. 495–545

[17] T. Marrodán Undagoitia and L. Rauch, *Dark matter direct-detection experiments*, J. Phys. **G43** (2016) (1), p. 013001

[18] A. M. Sirunyan *et al.*, *Search for dark matter produced with an energetic jet or a hadronically decaying W or Z boson at* $\sqrt{s}$ *=13 TeV*, JHEP **07** (2017), p. 014

[19] M. Aaboud *et al.*, *Search for new phenomena in final states with an energetic jet and large missing transverse momentum in pp collisions at* $\sqrt{s}$ *=13 TeV using the ATLAS detector*, Phys. Rev. **D94** (2016) (3), p. 032005

[20] A. M. Sirunyan *et al.*, *Search for dijet resonances in proton–proton collisions at* $\sqrt{s}$ *=13 TeV and constraints on dark matter and other models*, Phys. Lett. **B769** (2017), pp. 520–542, [Erratum: Phys. Lett.B772,882(2017)]

[21] J. Aleksić *et al.*, *Optimized dark matter searches in deep observations of Segue 1 with MAGIC*, JCAP **1402** (2014), p. 008

[22] H. Abdallah *et al.*, *Search for dark matter annihilations towards the inner Galactic halo from 10 years of observations with H.E.S.S*, Phys. Rev. Lett. **117** (2016) (11), p. 111301

[23] S. Archambault *et al.*, *Dark Matter Constraints from a Joint Analysis of Dwarf Spheroidal Galaxy Observations with VERITAS*, Phys. Rev. **D95** (2017) (8), p. 082001

[24] M. Ackermann *et al.*, *Limits on Dark Matter Annihilation Signals from the Fermi LAT 4-year Measurement of the Isotropic Gamma-Ray Background*, JCAP **1509** (2015) (09), p. 008

[25] M. G. Aartsen *et al.*, *Search for annihilating dark matter in the Sun with 3 years of IceCube data*, Eur. Phys. J. **C77** (2017) (3), p. 146

[26] S. Adrian-Martinez *et al.*, *Limits on Dark Matter Annihilation in the Sun using the ANTARES Neutrino Telescope*, Phys. Lett. **B759** (2016), pp. 69–74

[27] K. Choi *et al.*, *Search for neutrinos from annihilation of captured low-mass dark matter particles in the Sun by Super-Kamiokande*, Phys. Rev. Lett. **114** (2015) (14), p. 141301

[28] M. Aguilar *et al.*, *First Result from the Alpha Magnetic Spectrometer on the International Space Station: Precision Measurement of the Positron Fraction in Primary Cosmic Rays of 0.5˘350 GeV*, Phys. Rev. Lett. **110** (2013), p. 141102

[29] J. B. Albert *et al.*, *Improved measurement of the $2\nu\beta\beta$ half-life of $^{136}Xe$ with the EXO-200 detector*, Phys. Rev. **C89** (2014) (1), p. 015502

[30] National Institute of Standards and Technology, *www.nist.gov*

[31] E. Aprile and T. Doke, *Liquid Xenon Detectors for Particle Physics and Astrophysics*, Rev. Mod. Phys. **82** (2010), pp. 2053–2097

[32] L. Althüser, *Light collection efficiency simulations of the XENON1T experiment and comparison to data*, Master's thesis, WWU Münster (2017)

[33] S. Wittweg, *XENON100 Dark Matter Search with the PAX Raw Data Processor for XENON1T*, Master's thesis, WWU Münster (2016)

[34] W. R. Leo, *Techniques for Nuclear and Particle Physics Experiments* (Springer-Verlag, Berlin, Second revised edition, 1994)

[35] G. Heusser, *Low level counting from meteorites to neutrinos*, AIP Conf. Proc. **785** (2005), pp. 39–47, [,39(2005)]

[36] E. Aprile *et al.*, *Material radioassay and selection for the XENON1T dark matter experiment*, Eur. Phys. J. **C77** (2017) (12), p. 890

[37] D. Mei and A. Hime, *Muon-induced background study for underground laboratories*, Phys. Rev. **D73** (2006), p. 053004

[38] M. Ambrosio *et al.*, *Vertical muon intensity measured with MACRO at the Gran Sasso Laboratory*, Phys. Rev. **D52** (1995), pp. 3793–3802

[39] E. Aprile *et al.*, *Conceptual design and simulation of a water Cherenkov muon veto for the XENON1T experiment*, JINST **9** (2014), p. P11006

[40] E. Aprile *et al.*, *Physics reach of the XENON1T dark matter experiment*, JCAP **1604** (2016) (04), p. 027

[41] E. Aprile *et al.*, *The XENON1T Dark Matter Experiment*, Eur. Phys. J. **C77** (2017) (12), p. 881

[42] X. Du *et al.*, *A new method for measuring Kr-81 and Kr-85 abundances in environmental samples*, Geophys. Rev. Lett. **30** (2003), p. 2068

[43] M.-M. Bé, V. Chisté, C. Dulieu *et al.*, *Table of Radionuclides*, vol. 1 of *Monographie BIPM-5* (Bureau International des Poids et Mesures, Pavillon de Breteuil, F-92310 Sèvres, France, 2004)

[44] M.-M. Bé, V. Chisté, C. Dulieu *et al.*, *Table of Radionuclides*, vol. 4 of *Monographie BIPM-5* (Bureau International des Poids et Mesures, Pavillon de Breteuil, F-92310 Sèvres, France, 2008)

[45] S. Bruenner, *Mitigation of 222Rn induced background in the XENON1T dark matter experiment*, Ph.D. thesis, MPIK Heidelberg (2017)

[46] E. Aprile *et al.*, *The XENON100 Dark Matter Experiment*, Astropart. Phys. **35** (2012), pp. 573–590

[47] E. Aprile *et al.*, *XENON100 Dark Matter Results from a Combination of 477 Live Days*, Phys. Rev. **D94** (2016) (12), p. 122001

[48] G. Plante, *The XENON100 Dark Matter Experiment: Design, Construction, Calibration and 2010 Search Results with Improved Measurement of the Scintillation Response of Liquid Xenon to Low-Energy Nuclear Recoils*, Ph.D. thesis, Columbia U. (main) (2012)

[49] E. Aprile *et al.*, *Intrinsic backgrounds from Rn and Kr in the XENON100 experiment* (2017)

[50] S. Lindemann and H. Simgen, *Krypton assay in xenon at the ppq level using a gas chromatographic system and mass spectrometer*, Eur. Phys. J. **C74** (2014), p. 2746

[51] M. Weber, *Gentle Neutron Signals and Noble Background in the XENON100 Dark Matter Search Experiment*, Ph.D. thesis, MPIK Heidelberg (2013)

[52] J. B. Albert *et al.*, *Measurements of the ion fraction and mobility of $\alpha$- and $\beta$-decay products in liquid xenon using the EXO-200 detector*, Phys. Rev. **C92** (2015) (4), p. 045504

[53] H. M. Araujo *et al.*, *Radioactivity Backgrounds in ZEPLIN-III*, Astropart. Phys. **35** (2012), pp. 495–502

[54] E. Aprile *et al.*, *First Dark Matter Search Results from the XENON1T Experiment*, Phys. Rev. Lett. **119** (2017) (18), p. 181301

[55] E. Aprile *et al.*, *Lowering the radioactivity of the photomultiplier tubes for the XENON1T dark matter experiment*, Eur. Phys. J. **C75** (2015) (11), p. 546

[56] P. Barrow *et al.*, *Qualification Tests of the R11410-21 Photomultiplier Tubes for the XENON1T Detector*, JINST **12** (2017) (01), p. P01024

[57] E. Aprile *et al.*, *Dark Matter Search Results from a One Tonne-Year Exposure of XENON1T*, Phys. Rev. Lett. **121** (2018), p. 111302

[58] K. Abe *et al.*, *Distillation of Liquid Xenon to Remove Krypton*, Astropart. Phys. **31** (2009), pp. 290–296

[59] S. Rosendahl *et al.*, *Determination of the separation efficiencies of a single-stage cryogenic distillation setup to remove krypton out of xenon by using a Kr-83m tracer method*, Review of Scientific Instruments **86** (2015) (11), p. 115104

[60] S. Rosendahl, *Gas purification of the XENON dark matter search*, Ph.D. thesis, WWU Münster (2015)

[61] E. Aprile *et al.*, *Removing krypton from xenon by cryogenic distillation to the ppq level*, Eur. Phys. J. **C77** (2017) (5), p. 275

[62] W. McCabe, J. Smith and P. Harriott, *Unit Operations of Chemical Engineering* (7. McGraw-Hill International Edition, 2005)

[63] L. Lohrenegel, *Einfuehrung in die thermischen Trennverfahren* (Oldenbourg Verlag Muenchen Wien, 2007)

[64] M. Murra, *Set-up and test of a cryogenic distillation column for the XENON1T experiment*, Master's thesis, WWU Münster (2014)

[65] S. Bruenner *et al.*, *Radon depletion in xenon boil-off gas*, The European Physical Journal C **77** (2017) (3), p. 143

[66] Sulzer Chemtech Ltd., *Structured Packings: Energy-efficient, innovative and profitable* (2015)

[67] D. Roth, *Kalibrationsaspekte der kryogenen Destillationssaeule fuer das XENON1T-Experiment*, Bachelor's thesis, WWU Münster (2014)

[68] C. Hasterhok, *Gas Purity Analytics, Calibration Studies, and Background Predictions towards the First Results of XENON1T*, Ph.D. thesis, MPIK Heidelberg (2018)

[69] V. Pizzella, *Purity control of the XENON1T gas inventory prior to initial filling and studies of mixing properties of impurities in gaseous xenon*, Master's thesis, University of Rome Tor Vergata (2016)

[70] E. Brown *et al.*, *Magnetically-coupled piston pump for high-purity gas applications*, The European Physical Journal C **78** (2018) (7), p. 604

[71] D. Schulte, *In preparation*, Ph.D. thesis, WWU Münster (2021)

[72] J. Cardoso *et al.*, *Experience with a Slow Control system based on industrial process control hardware and software for the XENON1T dark matter search*, in *2016 IEEE-NPSS Real Time Conference (RT)* (2016), pp. 1–3

[73] E. Brown *et al.*, *In situ measurements of krypton in xenon gas with a quadrupole mass spectrometer following a cold-trap at a temporarily reduced pumping speed*, Journal of Instrumentation **8** (2013) (02), p. P02011

[74] A. Fieguth, *Investigations of impurities in xenon gas with a cold-trap-enhanced quadrupolevmass spectrometer*, Master's thesis, WWU Münster (2014)

[75] A. Dobi *et al.*, *Detection of krypton in xenon for dark matter applications*, Nucl. Instrum. Meth. **A665** (2011), pp. 1–6

[76] Z. Wang *et al.*, *Design and construction of a cryogenic distillation device for removal of krypton for liquid xenon dark matter detectors*, Rev. Sci. Instrum. **85** (2014), p. 015116

[77] K. Abe *et al.*, *XMASS detector*, Nucl. Instrum. Meth. **A716** (2013), pp. 78–85

[78] D. S. Akerib *et al.*, *Chromatographic separation of radioactive noble gases from xenon* (2016)

[79] J. Aalbers, C. Tunnell and B. Pelssers, *Processor for Analyzing XENON (PAX)* (2014),
URL: `http://xenon1t.github.io/pax/`

[80] C. T. J. Aalbers, *Handy Analysis tools for XENON (HAX)* (2015),
URL: `http://hax.readthedocs.io/en/latest/`

[81] F. Gao, *Low energy background in XENON1T*, Internal note

[82] P. Sorensen, *Anisotropic diffusion of electrons in liquid xenon with application to improving the sensitivity of direct dark matter searches*, Nucl. Instrum. Meth. **A635** (2011), pp. 41–43

[83] J. Aalbers, *Drift and diffusion in XENON1T*, Internal note

[84] M. Szydagis *et al.*, *NEST: a comprehensive model for scintillation yield in liquid xenon*, Journal of Instrumentation **6** (2011) (10), p. P10002

[85] D. S. Akerib *et al.*, *First results from the LUX dark matter experiment at the Sanford Underground Research Facility*, Phys. Rev. Lett. **112** (2014), p. 091303

[86] X. Cui *et al.*, *Dark Matter Results From 54-Ton-Day Exposure of PandaX-II Experiment*, Phys. Rev. Lett. **119** (2017) (18), p. 181302

[87] E. Aprile *et al.*, *An atom trap trace analysis system for measuring krypton contamination in xenon dark matter detectors*, Review of Scientific Instruments **84** (2013) (9), p. 093105

[88] Y. Zang, *PTR102 maximum cooling power*, Private communication

[89] Z. Greene, *XENON1T: Spin-independent WIMP dark matter results and a model to characterize the reduction of electronegative impurities in its 3.2 ton liquid xenon detector.*, Ph.D. thesis, Columbia University New York (2018)

[90] M. Vargas, *In preparation*, Ph.D. thesis, WWU Münster (2019)

[91] N. Rupp, *In preparation*, Ph.D. thesis, MPIK Heidelberg (2019)

[92] Gas Encyclopedia by Air Liquide, *www.encyclopedia.airliquide.com/krypton*

[93] Z. Greene, *Kr-85 Evolution Over SR1*, Internal note

[94] J. Naganoma, *Memo in case of leak into the system*, Internal note

[95] D. Schulte, *Upgrading and characterization of a magnetically-coupled piston pump for ultra-clean noble gas applications*, Master's thesis, WWU Münster (2018)

[96] M.-M. Bé *et al.*, *Table of Radionuclides*, vol. 7 of *Monographie BIPM-5* (Bureau International des Poids et Mesures, Pavillon de Breteuil, F-92310 Sèvres, France, 2013)

[97] S. Lindemann, *Intrinsic $^{85}Kr$ and $^{222}Rn$ Backgrounds in the XENON Dark Matter Search*, Ph.D. thesis, MPIK Heidelberg (2013)

[98] E. Aprile *et al.*, *Radon emanation measurements*, (In progress)

[99] K. Abe *et al.*, *Radon removal from gaseous xenon with activated charcoal*, Nuclear Instruments and Methods in Physics Research A **661** (2012), pp. 50–57

[100] E. Aprile *et al.*, *Online $^{222}Rn$ removal by cryogenic distillation in the XENON100 experiment*, Eur. Phys. J. **C77** (2017) (6), p. 358

[101] E. Aprile *et al.*, *Results from a Calibration of XENON100 Using a Source of Dissolved Radon-220*, Phys. Rev. **D95** (2017) (7), p. 072008

[102] N. Rupp, *On the detection of $^{222}Rn$ with miniaturized proportional counters: background, sensitivity studies and results for XENON1T*, Master's thesis, MPIK Heidelberg (2015)

[103] S. Lindeman, *Radon emanation in XENON1T*, Internal note

# Danksagung

Vielen Vielen Dank an alle, die bei dem Gelingen dieser Arbeit mitgeholfen haben.

Ich möchte mich zunächst bei Prof. Dr. C. Weinheimer bedanken, der es mir ermöglicht hat, an diesem spannenden Experiment zu arbeiten und mich während der Dissertation stets unterstützt hat. Für mich ist und war es immer etwas ganz Besonderes im größten Undergrundlabor der Welt arbeiten zu dürfen. Es hat mir sehr viel Spaß bereitet ein Mitglied der AG Weinheimer zu sein und ich freue mich auf die weitere Zusammenarbeit in den kommenden Jahren.

Herrn Prof. Dr. A. Andronic danke ich für die Übernahme der Zweitkorrektur dieser Arbeit.

Ich danke der Feinmechanischen Werkstatt und der Elektronik Werkstatt, ohne die kein einziges unserer verrückten Experimente gebaut werden könnte.

Ich möchte mich weiterhin bei einer langen Liste von Leuten bedanken, ohne die es die Arbeit in dieser Art nicht geben würde.

Fangen wir mal mit den Leuten aus der Münster Xenon Gruppe an: Ich danke StephanR, Alex, Lutz, Axel, ChristianH, SamW (minicw), Denny, Henning, Kevin, MichaelW, Miguel, Rasmus, Simon, Fabian, Julian und noch vielen anderen. In meiner Zeit habe ich einige Bachelor- und Master-Studenten betreut und angelernt. Es ist schön zu sehen, wie sie sich im Laufe der Zeit weiterentwickelt haben. Ich kann sagen, dass ich hier nicht nur Kollegen sondern auch viele Freunde gefunden habe. Ich möchte besonders unseren Ingenieur Christian Huhmann hervorheben, ohne den nichts laufen würde im Labor. Außerdem danke ich noch dem wahren Meister der Destillation Stephan Rosendahl. Schön, dass ich bei dir lernen durfte.

Besonderen Dank an Alex und Olli, mit denen ich damals vor 100 Jahren angefangen habe zu studieren. Wir haben stets zusammen gelitten. Unser Kartenhaus hat bis zuletzt Stand gehalten. Ich hoffe, dass dies auch die nächsten Jahre so bleibt, auch wenn wir uns nicht mehr so häufig sehen. Hinzu kommen noch Nils, Christopher, Sergej und Johannes! Die regelmäßigen Kaffeepausen waren eine willkommene Ablenkung.

Ich habe sehr viel Zeit am LNGS in Italien verbracht. Dort durfte ich viele interessante Charaktere aus der ganzen Welt kennenlernen. Deshalb geht as ab hier in Englisch weiter.

A big thank you to the people that I met at LNGS during the last years: Junji, Danilo, Roberto, Alfio, Marcello, Auke Pieter, Sander, Patrick de Perio (GAAAAAAIIIIIIIIIINZZZZZZZZZZZZZ!!!!!), GuillaumeP, Miguel (daschilva), Zhou, U-po-le, Evan, Shingo, Pietro, Francesco, Jean-Marie, Fei, Wulf-expert, Andrea, Jingqiang,David, Marie-Cecile, Yun, Qing, Joey, Dan, GuillaumeE,

Alfredo, Quim, Ale, Constanze, and many many many others. Sorry if I forget anyone.

I want to specially thank Danilo, Roberto, Junji and Alfio, the KEY EXPERTS on-site. I had a lot of fun with you guys. Thanks for keeping the detector running 24/7. To Alfio I can just say: "It's a shame!".

Greetings and a big thank you goes to the KNF Killers, Alex, Stefan, Ludwig and Natascha. Although we distilled radon for the first time world-wide at XENON100, we managed to kill ALL the pumps at XENON100 within a few weeks. But, whatever. We also learned that radon must be removed during Christmas!

Special Thanks to Dr. I. Cristescu, who is a brilliant expert on cryogenic distillation. He gave us very good advices on how to operate such a column on stable conditions.

Ich danke meinen Eltern Klaus und Renate und meiner Schwester Julia, die mich mein ganzen Leben lang untersützt haben. Zudem möchte ich meiner Oma Inge und meinem Opa Hermann danken. Ihr seid die Besten!

Finally, I want to thank you, Federica! I met you during my time in Italy (So thank you XENON :D). You always supported me during bad and good times. Grazie mille! Ti amo amore mio!

Für mich heißt es nun endlich wieder:
"Kabel löt ich,
Rohre schweiß ich,
manometer,
bin ich fleißig!"
- Rosendahl, 2013-